Enhanced Security Screening Using Spectral X-ray Imaging

Busi, Matteo

Publication date:
2019

Document Version
Publisher's PDF, also known as Version of record

Enhanced Security Screening Using Spectral X-ray Imaging

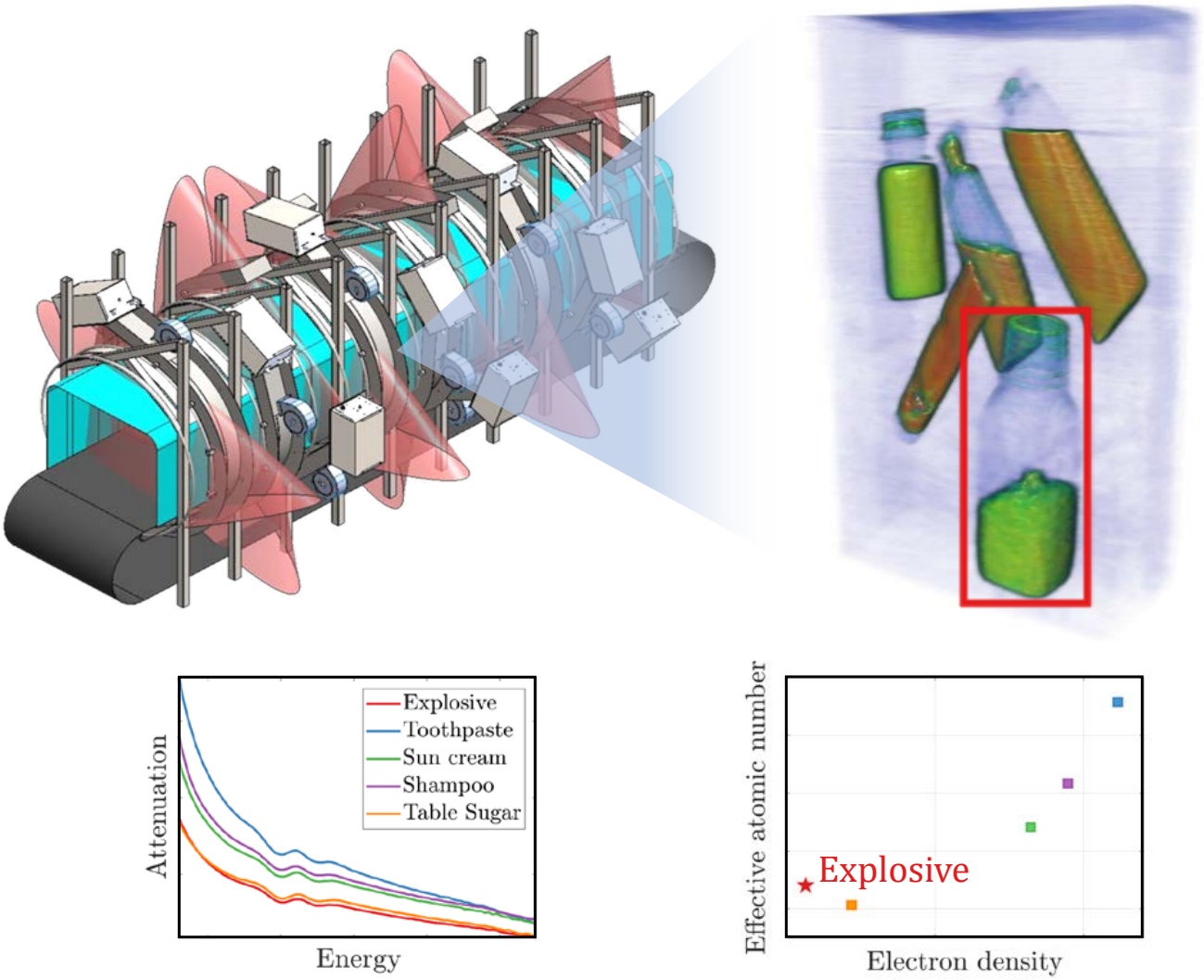

Matteo Busi
PhD Thesis
August 2019

Academic Advisors:
Kristoffer Haldrup
Ulrik Lund Olsen
Erik Bergbäck Knudsen
Jeppe Revall Frisvad

DTU Physics
Department of Physics

Contents

Abstract

X-ray image techniques are part of many security-screening systems due to their ability to produce images of the interiors of the object scanned. The classification of threats is carried out via shape recognition and the characterization of materials through the physical properties that are measurable with X-rays. In the case of X-ray Computed Tomography (CT), the measured quantity is the Linear Attenuation Coefficient (LAC), which has energy dependence. The polychromatic nature of laboratory-scale X-ray sources results in energy-dependent distortions in the retrieval of the LAC, when using conventional energy-integrating detectors.

This thesis presents spectral X-ray imaging techniques based on energy-discriminating single-photon counting detectors, with focus on Spectral X-ray CT (SCT). This technique offers the possibility to resolve the energy dependence of the LAC, in a discrete number of energy channels. Thus, it directly enables the estimation of system-independent properties as the effective atomic number, Z_{e}, and the electron density, ρ_{e}. Energy-dependent effects, such as beam hardening, are mitigated with the proposed method. However, artifacts due to scattering noise and photon starvation by metals remain to be corrected.

This work also introduces a framework for Monte Carlo simulation of SCT measurements used to generate a large amount of training data for machine learning-based correction methods. These posses the advantage of near real-time execution and not requiring *a-priori* knowledge of the sample. The proposed employs a spectral Convolutional Neural Network architecture, which can learn features from the energy domain. The corrections of real experimental datasets show promising results for both scattering noise and metal artifact removal. The drawback using this method is the introduction of blur, due to the spatial downsampling of the input images and the small size of the network that could fit the computational hardware used for this work.

Lastly, this thesis presents a benchmark study of the material classification and threat detection accuracy of 2- and 3-dimensional luggage-type objects. It is found that material features measured with spectral techniques produce better results compared to energy-integrating techniques. The accuracy is improved up to $\approx 35\%$ for the threat detection. In addition, the material classification accuracy is improved up to $\approx 55\%$.

Acknowledgements

In submitting this thesis, I would like to express my most sincere gratitude to the Innovation Fund Denmark, which covered the project expenses. The financial cost of experiments and travels to conferences where I could specialize in my field and disseminate my findings has never been an obstacle during the three years of this research project.

I would like to express my deep gratitude to Kristoffer Haldrup and Ulrik Lund Olsen, my research supervisors, for promptly introducing and guiding me into the academic world, with encouragement and critiques of this research work. I would also like to thank Erik Bergbäck Knudsen and Jeppe Revall Frisvad, also co-supervisors, for their advice and assistance, especially with software development. I could not have wished for any better supervision team.

I have appreciated much to work with Harry E. Martz and his group (Alex A. Dooraghi, K. Aditya Mohan, Kyle M. Champley and all the staff I have collaborated with) during my external project at Lawrence Livermore National Laboratory.

I am particularly grateful for the assistance given by Jan Kehres in the laboratory during the experiments, in the control of the scanning systems and the retrieval and processing of the data. Your advice and skills always helped me carrying out high-quality experiments and analysis. My grateful thanks are also extended to Christian Kehl for his help in setting up from scratch the architecture for Convolutional Neural Network correction. Without your help, a significant part of this research work would not have been possible at this time. A very special gratitude goes to Erik S. Dreier for his assistance using the detector correction algorithm, for introducing me to some of the Danish traditional ceremonies and cultural aspects and the chats on the way to the coffee machine and back to the office.

I would like to express my appreciation to all the NEXMAP section staff for the pleasant and cooperating scientific environment. I have always been proud and inspired being part of the group. I am omitting mentions because I have really much enjoyed working, having discussion and sharing lunch breaks with all of you the same way I hope you did with me. Thanks to Mads Laursen and Mario Beltran for reviewing and proof-reading parts of the final manuscript.

My sincere thanks also go to Nick and Alex Rica, of whom I had the great pleasure of being a guest during the six months of my external stay in the United States. You instantly received me as part of the family and you taught me the "American way". Your honest friendship really helped me feel at home in a place 10,000 km from my

roots.
I would also like to thank my friends of "Er Baretto" for their moral support and share of good times. Your friendship is still binding us despite the geographical distance. A note of mention goes also to the Copenhagen baseball team Urban Achievers for the friendly atmosphere and letting me play with the team altough my scarce attendance; and to the former and active members of <Flawesome> and <Low Expectations> for the fun in the free time.
Finally, I would like to deeply thank my family. You gave me total support and the absolute freedom of choice in every important (and non) life decision, my home will always be wherever I am with you. I owe you all my personal development and cultural taste, which has easily led me to where I am now.

Introduction 1

X-ray Computed Tomography (CT) is a non-destructive testing and evaluation technique that has been established for routine uses in the medical field, in the industry and many other sectors. This technique, briefly, consists in measuring the ratio between the incident and transmitted photons through an object from multiple projections. The collection of the projections is used by mathematical models to reconstruct a voxelized model of the object. While this technique has been used daily for many decades, it is still an active topic of research in the X-ray imaging domain. The reason is that the data analysis is often obscured by a reduced quality in the results of the measurement and image processing, i.e. the volume reconstruction of the object under investigation. The key factors for an optimal reconstruction are the image resolution (by means of lack of blur) and the contrast to noise ratio (that defines how well different materials are distinguishable with respect to the background image noise). For example, in the medical field, a poor resolution or contrast between suspicious and regular matter in the CT reconstructions makes it hard to perform precise diagnoses. In security screening applications, a too small contrast between different materials complicates the correct discrimination between threat and innocuous materials.

A poor quality of the reconstructions is often a consequence of mainly two aspects. Firstly, commercially available standard imaging scanners employ sources generating a polychromatic beam while they are equipped with detectors that integrate the energies of the incoming signal. Since the interactions that feature the CT measurements are energy-dependent, this leads to non-linearity in how the physical properties of matter are measured and calculated. Consequences of this aspect are typically grouped under the so-called beam-hardening effect, showing up mainly as cupping artifacts and a loss of contrast in the images. Secondly, to keep a limited X-ray dose while having a small focal spot, which is necessary to have a good spatial resolution and decrease image blur, the source parameters are set so that dense materials may drastically block the radiation resulting in photon starvation at the detectors. The consequences of this effect are typically sorted in the metal artifact category, showing up as severe streaking artifacts in the images.

The two effects introduced above are due to hardware limitations in a correct measurement of the physical interactions. Other typical artifacts are due to scanning

requirements consisting of high throughput of scanned objects and a demand for a reduced dose. For example, one may want to reduce the number of projections taken during the CT scan, resulting in so-called few-views artifacts. In other applications, the object cannot be measured from the full angular set, resulting in so-called limited-view artifacts. Finally, sample or instrument motion, as well as finite size of the source focal spot are sources of blur in the images. A detailed overview of the artifacts in X-ray CT and their causes can be found in the review by Boas and Fleischmann [1]. While several research topics in the mathematics and imaging processing domain have the overarching goal to compensate and correct for artifacts in the reconstructions and acquisitions, physical-based models can also be used to address the problem and develop correction methods. This work will focus on the enhancement of models used for the correction methods based on the study of the physical interactions between photons and matter, with an attention to security screening applications.

1.1 X-rays as a Tool for Security Screening

In security screening, the underlying goal of the technique employed is the accurate and precise detection of illicit objects or substances, typically contained in bags or luggage presenting high level of clutter. The natural choice for this task is given to X-ray imaging methods. Due to their ability to penetrate matter, X-rays reveal inner structure of objects enabling a rapid survey without a physical intervention required. Moreover, X-rays are highly sensitive to electron density variations, allowing for a characterization of materials based on their physical properties. In commercial aviation, due to the threat of hijacking, sabotage and use of Improvised Explosive Devices [2], airports are required to be equipped with X-ray scanners for the screening of customers' luggage. The first scanners implemented conventional X-ray attenuation based measuring systems, seeking to detect explosive or illicit material by the analysis of the bulk density and shapes in the images. Traditionally, the screening technology has been using simple 2D images, or radiographs, however, new regulations are imposing using 3D reconstruction from CT scans [3]. Using conventional CT however, the accurate material characterization and classification is limited mainly by two factors. Firstly, innocuous and threat materials may have very similar physical properties thus, hard to distinguish from each other. Secondly and more importantly, the measured quantity is the Linear Attenuation Coefficient (LAC), $\mu(E)$, which is described by the Lambert-Beer's law:

$$I(E) = I_0(E) \exp^{-l\mu(E)}, \tag{1.1}$$

where E is the energy and I and I_0 are respectively the transmitted and incident beam intensity passing through a sample of thickness l. The LAC is an energy-dependent property of matter. Thus, this method is system-dependent as it is determined by the source, filters and other components that make up the scanner. Moreover, this technique is prone to non-linearity in the calculation of the LAC, caused by beam

hardening as the spectrum is modulated as it passes through media. The reviewing and demand for more strict screening procedures following the 9/11 terrorist attack and the 2006 transatlantic aircraft plot [4] inspired the research for more refined techniques. To overcome the limitations in the characterization of materials, researchers have recently developed methods to estimate energy-independent physical parameters of the materials, using Dual Energy CT (DECT) scans [5, 6]. DECT is a first step towards Spectral X-ray CT (SCT), in which the LAC of materials is measured at two different mean energies (low- and high- energy pair). This is performed typically as a consecutive scan changing source parameters and filters to modify the energy distribution of the radiation or using sandwich dual energy detectors [7]. The dual LAC values are then converted into the energy-independent physical parameters of electron density ρ_e and effective atomic number Z_e, as in the System-Independent ρ_e/Z_e (SIRZ) method proposed by Azevedo et al. [8] and further developed by Champley et al. [9] While this is expected to soon be the standard acquisition method employed by airport scanners, it yet has limitations caused by the assumptions in the method. For example, materials with the presence of K-edge discontinuities in the LAC are not characterized correctly, and the beam-hardening correction depends on the accuracy of the spectral models used for the source and detectors.

1.2 Simultaneous Spectral X-ray Imaging

The groundbreaking step towards multi-energy Spectral X-ray CT and other energy-resolved imaging techniques was the development of energy-sensitive single Photon Counting Detectors (PCD). These detectors can discriminate the energy of the detected photons allowing for the simultaneous acquisition of the spectrum of energy-dependent material properties. Simulation and preliminary experimental studies on multi-energy spectral CT have demonstrated the superiority of this technique, in terms of improved contrast to noise ratio [10–13], and for enabling K-edge X-ray imaging [14, 15]. However, the lower price on the market of these detectors has grown the interest towards SCT dramatically. While techniques using PCDs are potentially superior to conventional energy integrating techniques, they require an adaptation and extension of the image processing routines and correction algorithms to compensate for the detectors' limitations in their performance and accuracy. In addition, the increased size of the data due to the supplementary energy dimension requires optimization of the algorithms, in terms of computing efficiency. This thesis presents a workflow for spectral X-ray CT, with novel scattering and metal artifact correction methods, which take advantage of the additional information provided by the energy resolution and the powerful tools from the artificial intelligence, or more specifically, deep learning field. The performance of the spectral technique for material discrimination is benchmarked against conventional energy integrating techniques. While the focus of this work revolves around the SCT technique, a few other spectral X-ray imaging techniques for security screening applications using PCDs will be introduced and discussed.

1.3 Thesis Overview

Chapter 2 provides the theoretical background of X-ray imaging with an overview of various techniques used in this thesis, and a description of the physical interactions between photons and matter. Chapter 3 introduces the concept of spectral X-ray imaging, with focus on the SCT technique and its main advantages over other techniques. This chapter presents a new material characterization method for the estimation of electron density and effective atomic number using SCT scans. Chapter 4 presents the framework adopted for the Monte Carlo (MC) X-ray tracing simulation of the interactions between photons and matter. The software package used in this thesis is McXtrace [16] and a new component for the simulation of SCT scans is developed. This toolkit is used for the estimation of the scattering noise produced by the sample and other instrument components, and for the generation of synthetic. Chapter 5 describes the SCT correction steps developed employing Convolutional Neural Network (CNN) architectures. Briefly, the networks are trained to reproduce the same output as the MC simulations but with an increase in speed of several orders of magnitude and with the advantage of not requiring complex inputs, but merely images like the ones obtained in real scanners. Chapter 6 presents the experimental results in the characterization of methods using SCT. Finally, the performance of different material properties measured using SCT are benchmarked in a material classification test for the detection of threat objects in large samples containing multiple materials.

X-ray Imaging and characterization 2

This chapter will briefly describe the theoretical framework that is at the base of X-ray imaging, with the description of the interactions between photons and matter and the different imaging techniques. A detailed documentation on the subject can be found in the literature [17, 18].

2.1 X-ray Interactions

X-rays are electromagnetic waves with the quantum entity being photons with wavelengths typically in the region of 1 Å (corresponding to 12.39 keV). Photon's energy of soft and hard X-rays extends the range respectively down to a few hundreds of eVs and up to a few MeVs. Since X-rays are electromagnetic waves, they follow the fundamental properties and relations for waves. As such, the wavenumber, k, wavelength, λ, and energy are related by the following equations: $k = \frac{2\pi}{\lambda} = \frac{E}{\hbar c}$, where $\hbar$ is the reduced Planck's constant and c is the speed of light. At a macroscopic scale, the interactions between X-rays and matter can be summarized by the refractive index, n:

$$n(E) = 1 - \delta(E) + i\beta(E). \tag{2.1}$$

Considering a planar X-ray wave $\xi_0 = e^{ikz}$, after travelling a distance z within a media with refractive index, n, the wavevector changes from k to nk and the wave can be expressed as:

$$\xi = e^{inkz} = e^{(1-\delta)kz} e^{-\beta kz}. \tag{2.2}$$

We can deduce that the first term of the Right Hand Side (RHS) of Eq. (2.2) corresponds to a phase shift of the wave, $\phi = -\delta kz$, thus, is related to refraction effects of the waves. The real part of the refraction index, δ is derived as [17]:

$$\delta(E) = \frac{2\pi\rho_e r_0}{k^2}, \tag{2.3}$$

where r_0 is the Thomson scattering length, ρ_e is the electron density.

The second term of the (RHS) of Eq. (2.2) corresponds to an exponential decay, as predicted by Lambert-Beer's law. It is derived that the imaginary part of the refraction index, β, is proportional the linear attenuation coefficient (LAC), μ of materials as:

$$\beta(E) = \frac{\mu(E)}{2k}. \tag{2.4}$$

Both changes in δ and β of materials can be measured using X-rays, employing different imaging modalities. Among the figures of merit to characterize an optimal imaging technique, contrast is one of the key factors. Contrast is defined as the value differences between two different materials in the resulting images. For two materials j and k, the contrast, $\mathcal{C}$, for the observable x can be written as:

$$\mathcal{C}(x) = \Delta x = |x_j - x_k|. \tag{2.5}$$

In the energy range suitable for laboratory-scale measurements (approximately between 5 and 200 keV), the contrast between the different materials is several orders of magnitudes higher for δ than β. Fig. (2.1) represents an example of contrast in δ and β for water (H_2O) and hydrogen peroxide (H_2O_2). This demonstrates the high

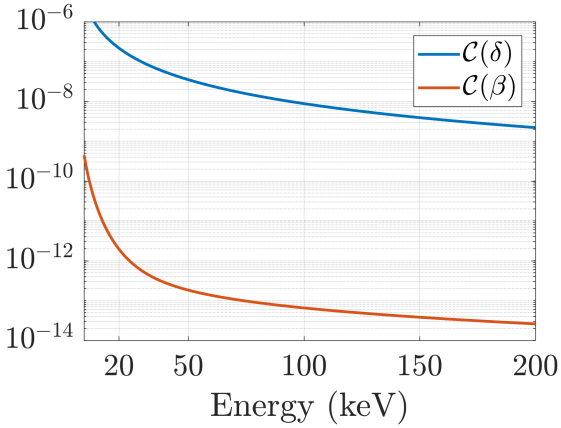

Figure 2.1: The contrast between water and hydrogen peroxide for the real, $\mathcal{C}(\delta)$, and imaginary, $\mathcal{C}(\beta)$, parts of the refractive index.

potential of phase-contrast imaging techniques, which are sensitive to the phase shift experienced by photons when passing through media, over conventional attenuation-based techniques, which directly measure the ratio between incident and transmitted photon. The disadvantage of phase-contrast imaging techniques is that they are much more experimentally demanding in terms of equipment necessary for their realization. An important property of materials in the X-ray energy range is that the refractive index difference of materials from unity (i.e. the refractive index of vacuum) is extremely small. Consequently, refraction angles are extremely small, and the registration of the phase shift require high-resolution detectors or external devices that modulate the X-ray beam. Even though the early techniques developed all required a synchrotron radiation source, recent studies demonstrated the feasibility of laboratory scale phase-contrast imaging techniques [19–22].

2.1.1 Attenuation and Photon Cross Sections

For photons with energy $E < 1.022$ MeV[1] and a single element with atomic number Z, the physical interactions are represented by photoelectric absorption, elastic scattering and incoherent scattering. Fig. (2.2) sketches these different interactions, which will be described below in separate subsection.

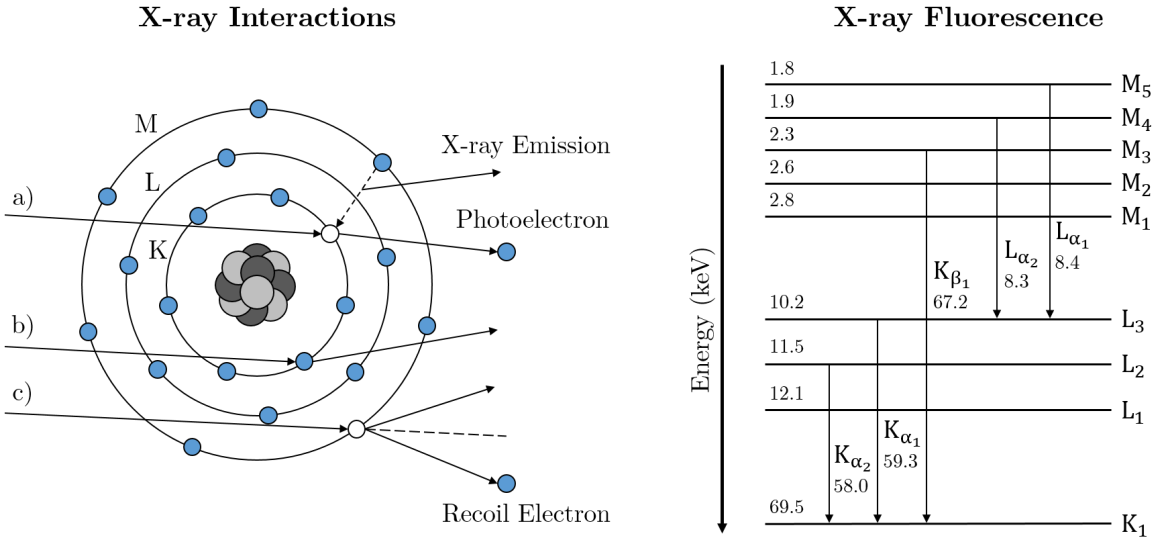

Figure 2.2: Left: a) In photoelectric absorption a photon transfers its energy to an electron of an atom, which is ejected from an electron shell as a photoelectron, producing a hole. This hole is filled by an electron of an outer electron shell and a photon is emitted (X-ray fluorescence), with energy equivalent to the difference between the binding energy of the two shells. b) In elastic scattering the photon only suffers a deviation in the direction. c) In incoherent scattering the photons transfer parts of its energy to a free-electron, which recoils away from the atom. Right: X-ray fluorescence emissions lines (Siegbahn notation) and binding energies of the electron shells for Tungsten ($Z = 74$).

These, all contribute to the imaginary part of the refractive index have been studied and tabulated in terms of cross sections, $\sigma(Z, E)$ (cm^2/g), which represent the likelihood of a certain interaction to happen. The individual cross section due to photoelectric absorption (σ_{ph}), elastic scattering (σ_{ela}), and incoherent scattering (σ_{inc}) sum up to the total mass attenuation cross section, (σ_{tot}) expressed as:

$$\sigma_{\text{tot}}(Z, E) = \sigma_{\text{ph}}(Z, E) + \sigma_{\text{ela}}(Z, E) + \sigma_{\text{inc}}(Z, E). \tag{2.6}$$

Look-up tables of the photon's cross-sections for elements of the periodic tables, compounds and mixtures can be found from multiple sources [23–25]. In this work, the photon cross-sections tables used are the ones provided by the National Institute

[1] 1.022 MeV is the energy of twice the rest mass of the electron. Above this energy, the cross-section for pair production becomes significant.

of Standards and Technologies (NIST) [26]. Fig. (2.3) illustrates the NIST energy-dependent photon attenuation cross sections of elements of the periodic table and the individual contributions, exemplified for silicon. This figure emphasizes the presence

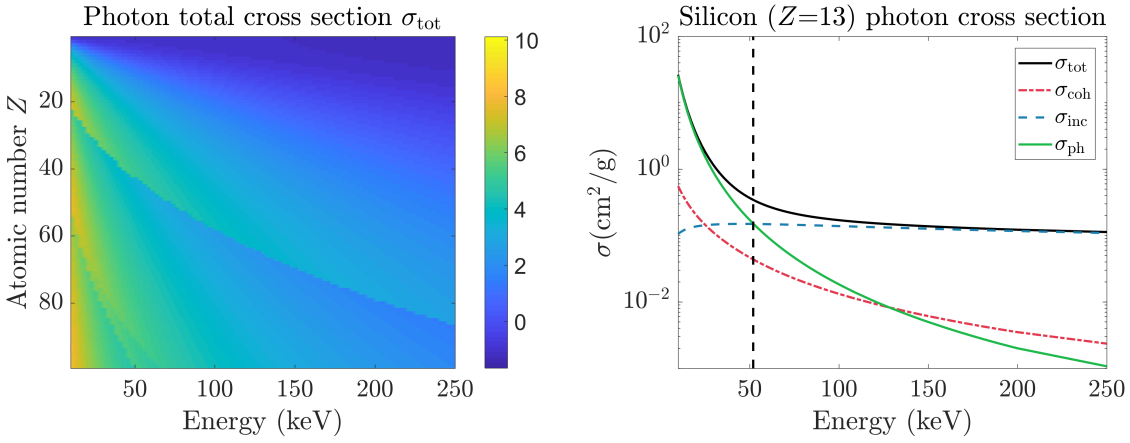

Figure 2.3: Left: Photon cross sections for the elements of the periodic table. Note that the scale of the color bar is in $\log_{10}$ unit. The K_α absorption edge boundary is clearly visible in the middle of the plot. Right: The individual cross sections tabulated by NIST, exemplified for silicon. The total attenuation cross section (solid black), is the sum of the individual photoelectric absorption (solid green), elastic (dashed red) line and incoherent scattering (dash-dotted blue) cross sections. The vertical dashed black line at approximately 60 keV marks the intersection between σ_{ph} and σ_{inc}. Note the logarithmic scale in the $y-$axis.

of an energy boundary that defines two regions, where the dominant interaction is either the photoelectric absorption or the incoherent scattering. For silicon for example, the energy boundary is found at approximately 60 keV that corresponds to the energy value in which the incoherent scattering cross section becomes larger than the photoelectric absorption cross section. The energy boundaries in which are found intersection between the cross sections increase with the atomic number Z however, the qualitative behavior of the cross sections holds the same for each element in the periodic tables (ignoring K-edges). With respect to the elastic scattering, it is observed that it has an intensity of approximately two orders of magnitude lower than the total attenuation in the photoelectric absorption regime and of approximately three orders of magnitude lower than the total attenuation in the incoherent scattering regime. Other interactions that need to be mentioned but are only possible energy above 1.022 MeV are the nuclear and electron pair production, which both result in the annihilation of the incident photon.

The linear attenuation coefficient (LAC), $\mu(Z, E)$, can be calculated from the cross section defined in Eq. (2.6), by multiplying the material's bulk density, ρ (g/cm^3), as in the following equation:

$$\mu(Z, E) = \rho\sigma_{\text{tot}}(Z, E). \tag{2.7}$$

Photoelectric Absorption

In the photoelectric absorption interaction between X-ray and matter, a photon with energy E_γ is absorbed by an atom transferring its energy to it. The atom becomes excited, ejecting a photoelectron from an electron shell with binding energy E_b. The photoelectron has energy equivalent to the difference between the photon's energy and the binding energy of the ejected electron shell: $E_{e^-} = E_\gamma - E_\mathrm{b}$. The hole generated in this process is filled very quickly (femtoseconds) by an electron belonging to an outer shell. This jump produces simultaneously the emission of a photon with energy equivalent to the difference between the two electron shells. The X-ray radiation produced by this effect is called X-ray fluorescence and is characteristic for each element of the periodic table, since the binding energy varies with the atomic number. Fig. (2.2) shows some of the different emission lines that can be produced, depending on which electron shells are involved, and their respective notation (see Siegbahn notation [27] for a full overview of the emission lines classification for X-ray spectroscopy).
The photoelectric absorption cross section is approximately proportional to the third power of the reciprocal of the energy [17], $1/E^3$, except for discontinuous sharp rises, called absorption edges. These, are found when the energy of the incident photon is equal to the binding energy of an electron shell (K, L_1, L_2, M_1, etc.) corresponding to the absorbing atom. Fig. (2.4) depicts the photoelectric absorption cross sections for iodine, cadmium, gadolinium and tungsten, where the K-edges are clearly visible. The energy corresponding to the K-edges increases with the atomic number, Z. It is found that the photoelectric absorption cross section is linearly dependent to approximately the fourth power of the atomic number, Z^4 [17]. Thus, overall the photoelectric

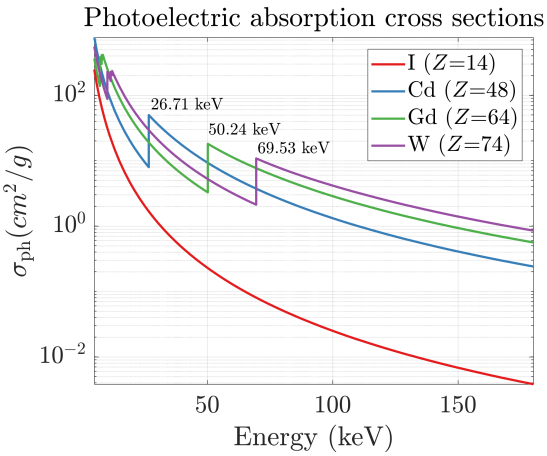

Figure 2.4: Photoelectric absorption cross sections for iodine, cadmium, gadolinium and tungsten. The K-edges are clearly visible for Cd, Gd and W at the energies of 26.71, 50.24 and 69.53 keV respectively. Additional overlapping edges visible in the low energies are L_1- and L_2-edges of gadolinium and tungsten.

absorption cross section dependence on energy can be approximated as:

$$\sigma_{\text{ph}} \propto \frac{Z^4}{E^3}. \tag{2.8}$$

Elastic Scattering

Elastic (also commonly named Rayleigh or coherent) scattering is the process by which photons with energy E are scattered by bound atomic electrons without excitation of the target atom. This process results from interference effects between waves diffracted by different parts of the atomic charge distribution. This perturbation leads to a change in the direction of the photons, which is modeled by the atomic Differential Cross Section (DCS). The elastic DCS per unit solid angle is given approximately by:

$$\frac{d\sigma_{\text{ela}}}{d\Omega} = \frac{d\sigma_{\text{Th}}}{d\Omega} F(\text{Q}, Z)^2, \tag{2.9}$$

where the first term is energy-independent and is the DCS per unit solid angle for Thomson scattering, which describes the elastic of electromagnetic radiation by a charged particle:

$$\frac{d\sigma_{\text{Th}}}{d\Omega} = r_0^2 \frac{1 + \cos^2\theta}{2}, \tag{2.10}$$

where θ is the angle between the incident and the outgoing scattered photon. The second term in Eq. (2.9) is the atomic form factor, $F(\text{Q}, Z)$, defined as:

$$F(\text{Q}, Z) = \int \rho(\mathbf{r}) e^{i\text{Q}\mathbf{r}} d\mathbf{r}. \tag{2.11}$$

The atomic form factor can be interpreted as the scattering amplitude of an electromagnetic wave by an isolated atom, seen as a charge cloud surrounding the nucleus, with density $\rho(\mathbf{r})$. In the calculation of the scattering amplitude, $e^{i\text{Q}\mathbf{r}}$ is the phase factor, which weights the contribution from each volume element $d\mathbf{r}$. A detailed framework for the description and derivation of the atomic form factor can be found in the standard textbooks [17]. For the purpose of this work, it is important to know its dependence on the magnitude of the momentum transfer, Q, which related the scattering angle to the wavelength (thus energy) as follows:

$$\text{Q} = \frac{4\pi}{\lambda} \sin(\theta). \tag{2.12}$$

It can be shown that the atomic form factor is a monotonically decreasing function, that goes from $F(0, Z) = Z$ to $F(\infty, Z) = 0$ [28]. The first limit corresponds to the phase factor approaching the unity thus, the integral simply yields the total number of electrons, Z. The second limit corresponds to X-ray wavelength becoming smaller than the scatterer size, which produced destructive interference of the scattered waves. Analytical approximations can be used to estimate atomic form factors [28–30] as a function of the momentum transfer and atomic number. Fig. (2.5) shows a polar plot

of the DCS for a carbon atom ($Z = 6$) for X-ray energies $E = \{2, 5, 15, 30, 200\}$ keV as a function of the scattering angle. It can be observed that the amount of forward scattering increases drastically with the energy, and the back-scattering becomes negligible at the photon energy of 15 keV and above. However, when materials more complex like molecules or mixtures are considered, one must consider the structure in which the atoms organize into a molecule. This can lead to oscillations or isolated peaks in the magnitude of the form factor making it unique for each material and structure. In this way, the measurement of the scattering function, which is the intensity of the scattered radiation as a function of the momentum transfer, can be used to distinguish different materials. A further analysis of the scattering function can be used to extrapolate properties of materials such as inter-atomic distances, coordination number etc.

Incoherent Scattering

Incoherent (also commonly named Compton or inelastic) scattering is the process by which a photon with energy E interacts with an electron that absorbs it and re-emits a secondary photon with lower energy $E' = \tau E$ in a new direction with an angle, θ, relative to the original direction. Part of the energy of the colliding photon is transferred to the electron, which recoils. The decrease in energy of the photon is referred to as Compton shift. The relationship between the scattering angle and the fractional energy, τ, is derived by conservation laws of energy and momentum and is

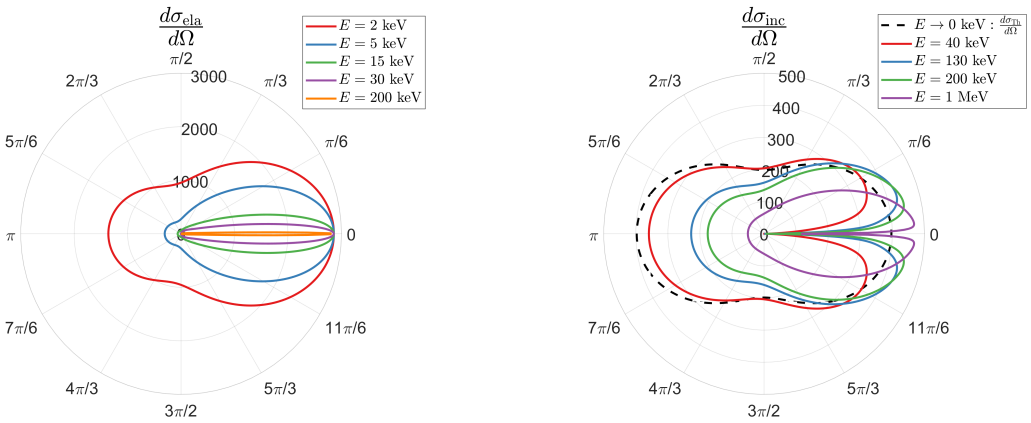

Figure 2.5: Left: Polar plot of the elastic scattering DCS (in arbitrary units) per unit solid angle, for different photon energies $E = \{2, 5, 15, 30, 200\}$ keV for carbon ($Z = 6$). The angular axis is the scattering angle, θ, of the photon undergoing elastic scattering. Right: Polar plot of the Thomson scattering ($E \to 0$ keV) and incoherent scattering DCS (in arbitrary unit) per unit solid angle, for different photon energies $E = \{40, 130, 200, 1000\}$ keV. The angular axis is the scattering angle, θ, of the secondary photon that is emitted through incoherent scattering.

given by:

$$\cos\theta = \frac{1}{\gamma}\left(\gamma + 1 - \frac{1}{\tau}\right), \tag{2.13}$$

with $\gamma = E/mc^2 = E/(511\text{keV})$. Eq. (2.13) can be rearranged in terms of the fractional energy, τ, as:

$$\tau = \frac{1}{1+\gamma(1-\cos\theta)}. \tag{2.14}$$

The fractional energy has minimum and maximum values corresponding to backward ($\theta = \pi$) and forward ($\theta = 0$) scattering respectively:

$$\tau_{\min} = \tau|_{\theta=\pi} = \frac{1}{1+2\gamma} \quad \text{and} \quad \tau_{\max} = \tau|_{\theta=0} = 1. \tag{2.15}$$

The angular deflection of the secondary photon is described by the Klein-Nishina formula [31], assuming unpolarized photons and the target electron to be free and at rest:

$$\frac{d\sigma_{\text{KN}}}{d\Omega} = \frac{r_0^2}{2} f(E,\theta)^{-2}\left[f(E,\theta) + f(E,\theta)^{-1} - \sin^2\theta\right], \tag{2.16}$$

with

$$f(E,\theta) = \frac{1}{[1+E(1-\cos\theta)]}. \tag{2.17}$$

When considering real matter, electron binding effects need to be considered as well. This is done by multiplying the Klein-Nishina formula by the incoherent scattering function of the target atom, $S(\text{Q}, Z)$ [28]. The incoherent scattering function can be computed in terms of the atomic ground state wave function and the respective form factor $F(\text{Q}, Z)$ [32]. It can be shown that $S(\text{Q}, Z)$ is a monotonically increasing function of Q that has limit values of $S(0, Z) = 0$ and $S(\infty, Z) = Z$. For practical purposes, this function can also be calculated using analytical approximations [28, 30, 33]. Overall the atomic incoherent DCS in terms of the fractional energy τ becomes:

$$\frac{d\sigma_{\text{inc}}}{d\tau} = \frac{d\sigma_{\text{KN}}}{d\tau} S(\text{Q}, Z), \tag{2.18}$$

where the first term is the Klein-Nishina DCS in terms of the fractional energy, which can be derived from Eq. (2.16). Fig. (2.5) displays the incoherent scattering DCS for carbon atom ($Z = 6$) for X-ray energies $E = \{40, 130, 200, 1000\}$ keV where it can be seen how the amount of forward scattering increases drastically with the energy of the primary photon while the back-scattering is still significant at 200 keV. Without considering the incoherent scattering function S, which is responsible of the sharp decrease of scattering intensity as the scattering angle approaches zero, in the low-energy limit the incoherent scattering DCS reduces to the Thomson formula in Eq. (2.10), where backward and forward scattering have the same likelihood.

2.2 Attenuation Imaging

Perhaps the most direct technique employed within X-ray imaging is based on the fact that the attenuation coefficient depends on material physical properties of density and atomic number, as in Eq. (2.7), resulting in a contrast in the images of materials with a difference in such physical properties. The attenuation coefficient of materials is measured using Lambert-Beer's law for a non-homogeneous sample with varying attenuation coefficient $\mu(x, y)$:

$$I(x') = I_0(x') \exp\{-\int_t \mu(x, y) dx dy\}, \tag{2.19}$$

where I_0 and I are respectively the incident and detected X-ray intensity, measured at the pixel position x', and x an y are the position coordinates within the sample. Lambert-Beer's law can be rearranged into the line integral form to define a radiograph, or projection R:

$$R(x') = -log\frac{I(x')}{I_0(x')} = -\int_t \mu(x, y) dx dy. \tag{2.20}$$

When parallel rays passing through the sample along a certain direction or angle (ω) are considered, the so called forward-projection can be described via the Radon transform [34] expressed as:

$$R_\omega(x') = \mathcal{R}\left[\mu(x, y)\right] = -\int_t \mu(x, y)\delta(x\cos\omega + y\sin\omega - x') dx dy, \tag{2.21}$$

where δ is the delta function. Fig. (2.6) illustrates a collection of projections $\{R_{\omega_n}(x'\}$ from multiple views, ω_n ($n = 1, 2, 3, \dots$), which are merged in Computed Tomography (CT) to obtain a voxelized reconstruction of the object in terms of the attenuation coefficient, $\mu(x, y)$. The first reconstruction algorithm developed for X-ray CT was the Filtered Back Projection (FBP). In this method, the back-projection is retrieved by calculating the inverse Radon transform:

$$R'_\omega(k) = \int e^{-ikx'} R_\omega(x') dx' = \int_t \mu(x, y) e^{-ik(x\cos\omega + y\sin\omega)} dx dy, \tag{2.22}$$

and integrating over the frequency domain, (k):

$$\mathrm{FBP}_\omega(x, y) = \int_{-\infty}^{+\infty} |k| R'_\omega(k) e^{ik(x\cos\omega + y\sin\omega)} dk. \tag{2.23}$$

Finally, the reconstructed volume in terms of attenuation is retrieved by summing all the filtered back projections:

$$\mu(x, y) = \sum_\omega \mathrm{FBP}_\omega(x, y). \tag{2.24}$$

Note that in Eq. (2.23) $|k|$ is an added term called Ram-Lak filter. Without this factor the inverse Fourier transform and the Fourier transform in the equation would just

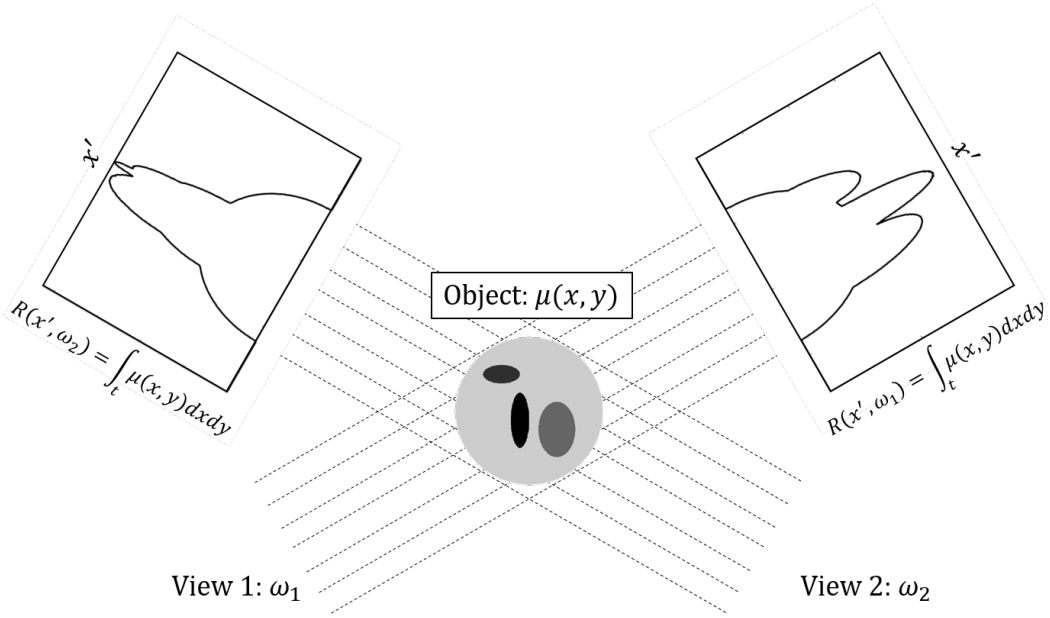

Figure 2.6: Schematic illustration of the Computed Tomography technique. Multiple projections of the sample enable the reconstruction of the object, with volumetric information of the inner materials.

cancel out and leave the back projection formula, which will not allow to recover the original function $\mu(x, y)$ but rather its smoothed version. Several different choices of filters can be found in the literature, depending on the application.
Since the data collected is discretized into pixels, so the models and the reconstruction results must be discretized. The advantage of the FBP is that it is computationally very efficient as it is analytically defined. However, it requires a relatively large number of projections, it is not robust to noise in the dataset and it requires equally spaced projections, imposing limitations in the geometrical settings for the scanning acquisitions. In iterative reconstruction algorithms, the forward projection is modeled as a linear system of equations [35] in the form of:

$$y_i = \sum_j a_{ij} x_j, \tag{2.25}$$

or in matrix form:

$$y = \mathcal{A}x \tag{2.26}$$

Therein, $\mathcal{A}$ is the projection matrix, containing the information about the geometry of the acquisitions, i.e. how the rays are passing through the sample voxels x_j and reaching the detector pixels y_i. Since the number of equations is prohibitively large, and there is randomness due to the noise, the problem is ill posed as it may have non-unique solutions. Thus, iterative approaches are required to solve the problem of the CT reconstruction. The advantage of these techniques is that they are intrinsically discretized, and they can handle noise and various geometry settings for the acquisition.

On the other hand, they are computational demanding and may require parameter optimization to yield desired results. Iterative reconstruction algorithms are subject of an ongoing active field of research, which has overarching goal to refine the quality of the results by developing model-based iterative reconstruction techniques. More details on the topic can be found in various literature publications [35–37]. In this thesis, the focus is on developing physical-based models for the correction steps in the image and signal processing.
The contrast between different materials using this technique is given by the difference between their linear attenuation coefficients. Thus, according to Eq. (2.7), it depends linearly on the difference between the bulk density ρ of similar materials and approximately on the 4th-power of atomic number Z of different materials. For this reason, this technique is very efficient in the non-destructive evaluation of objects composed of materials with different atomic number (e.g. bone/flesh, organic/metal compounds etc.). In the context of security screening however, materials often have similar physical properties making it challenging to distinguish between threat and innocuous materials.

2.3 Scattering Methods for Material Characterization

In the previous section, where the concept of attenuation imaging was presented, the scattering interactions were assumed to act in the same way as photoelectric absorption events, assuming a scattered photon does not reach the detector. Thus, in that technique the scattered radiation represents a noise element that needs to be estimated and corrected. However, as mentioned in Section 2.1.1 each material scatters photons in a unique way, making the measurement of scattering function itself a useful tool for the characterization of different materials. Fig. (2.7) sketches the X-ray Diffuse Scattering (XDS), which measures the elastic scattering intensity as a function of the momentum transfer Q, expressed in Eq. (2.9). This is typically done by illuminating a sample with an X-ray beam collimated into a pencil beam and measuring the scattering signal around the incident beam, either with a 2D flat panel detector or by translating a single pixel detector. The scattering angles, θ, can be calculated given the detector pixel position and the sample to detector distance. The wavelength, λ, is ideally a fixed value corresponding to a monochromatic radiation however, the monochromatic bandwidth depends on the source and in many cases on the monochromator crystal that are employed. Large-scale facilities such as synchrotron radiation sources, or free electron lasers, due to their extremely high brilliance are the typical choice for this technique, when high resolution is required. Time-resolved studies of the molecular dynamics using this technique have nowadays reached a time resolution of femtoseconds [38]. For security screening application however, laboratory-scale conventional sources are used, which generate a polychromatic beam. Thus, the techniques become better with

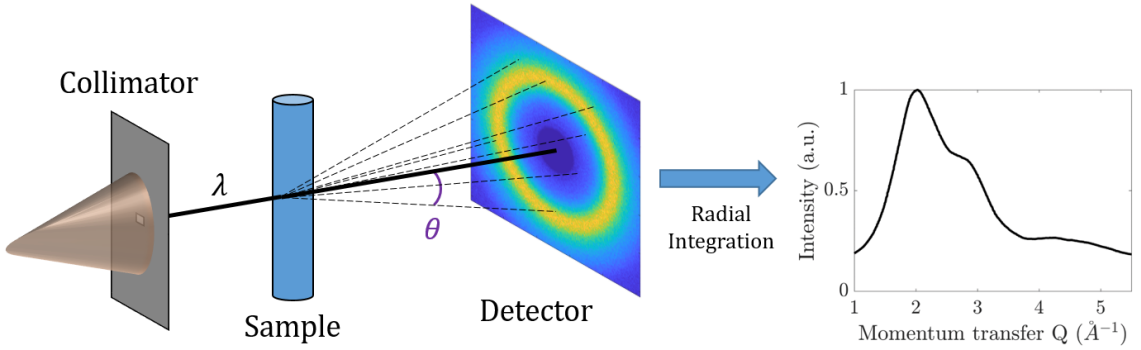

Figure 2.7: Schematic illustration of the X-ray Diffuse Scattering technique. The X-ray beam is collimated into a pencil beam, passes through a sample and the scattering signal is measured at a flat-panel 2D detector as a function of the X-ray's wavelength, λ, and the scattering angle, θ. The following azimuthal radial integration then is used to calculate the scattering signal as a function of the momentum transfer, Q.

the energy-resolving detectors that will be presented in the next section. In the context of material characterization and security screening, ED-XRD has the advantage that the material features measured, i.e. the scattering functions, have a non-monotonic or discontinuous nature. Thus, compared with attenuation-based methods, the material classification task is simplified by the detection of the scattering function peaks rather than a contrast between the attenuation coefficients of different materials. For example, different water-based mixtures in which water is the dominant material, have very similar linear attenuation coefficient values making it hard to distinguish between each other. However, an analysis of the changes in the position and shape of the scattering peaks due to different solvents in the momentum transfer domains may facilitate the material classification.

Spectral X-ray Imaging Techniques and Characterization Methods 3

This chapter introduces the concept of spectral X-ray imaging and characterization. It starts presenting the detectors that enable the spectral X-ray techniques, which rely on the simultaneous detection of the energy of the incoming photons. The chapter continues describing some of the laboratory-scale spectral X-ray imaging techniques under development with focus on Spectral X-ray CT (SCT). These techniques are described in contrast with the respective conventional ones using energy integrating detectors, to highlight the advantages as well as the limitations and the main problems faced in the data processing chain. Lastly, is described the method developed for the material characterization into system-independent physical properties.
Fig. (3.1) represents a block diagram of the overall workflow proposed for material classification applications using SCT scans and introduces the main data processing algorithms developed in this work.

3.1 Single Photon Counting Detectors

The groundbreaking step towards the emergence of spectral X-ray imaging techniques was the development of energy discriminating Photon Counting Detectors (PCD) for X-ray imaging applications. Fig. (3.2) illustrates the layout of the detector main components and the photon interactions. Assuming ideal detection, the incident photon is absorbed within the thickness of the semiconductor layer sensor that is bump-bond connected to the readout chip. The photoelectric absorption event produces electron-holes pairs, which are separated and drifted within the sensor by an electric field induced with an HV bias. The electric charge reaching the readout chip produces a pulse which is pre-amplified, shaped and counted only when the signal exceed predefined thresholds, resulting in the suppression of electronic noise. Multiple thresholds can be used to bin the signal into energy channels with number and width defined by energy thresholds [39, 40]. Semiconductor materials used for these detectors

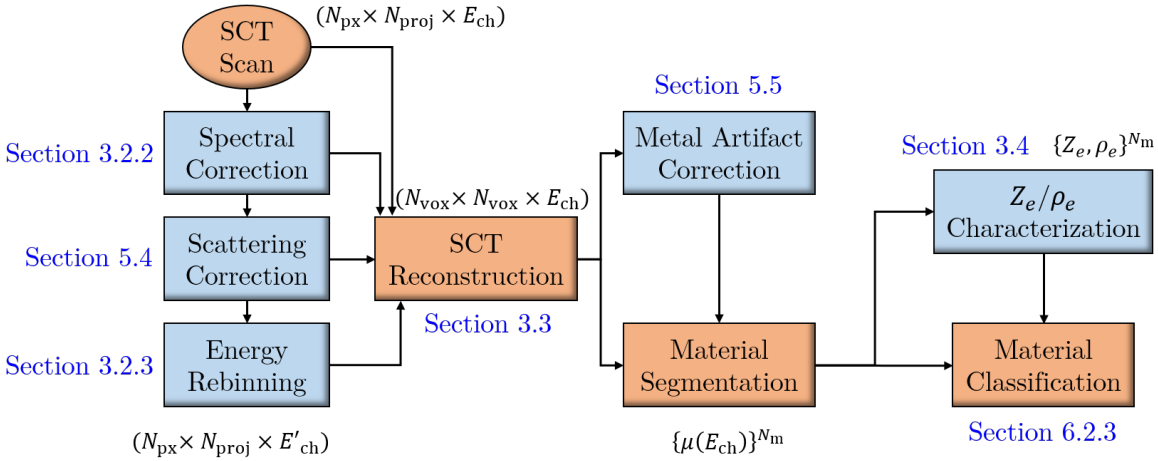

Figure 3.1: Block diagram of the overall workflow following a SCT scan, showing the individual data processing steps. Note that the orange colored blocks are the mandatory steps. In the figure's notation, N_{px} is the number of detector pixels, N_{vox} is the number of voxels in the volume/image reconstructed, N_{proj} is the number of projections, E_{ch} is the number of energy channels of the detector, N_m is the number of the materials composing the sample, $\mu(E)$ is the material's LAC and Z_e and ρ_e are the material's effective atomic number and electron density respectively.

are dense, high atomic number materials (such as CZT (CdZnTe), CdTe and GaAs) to have a higher likelihood oh photoelectric absorption. This family of semiconductor-based detectors are preferred to their main competitors in the market, which are Si-based detectors, due to their high efficiency in terms of absorbed photons for energies up to 160 keV. On the other hand, presence of high Z elements in the semiconductor layer leads to fluorescence noise signal for energies corresponding to the K-edges of such materials, if that is within the energy range of the detector. That leads to a decreased performance of the detectors at low energies, where the contrast in the LAC between organic materials is the greatest.

3.1.1 MultiX ME-100 detector

The detector adopted for the experiments in this work is the MultiX ME-100 v2 [42], developed at CEA-LETI. This detector has an energy resolution of 6.5% (8 keV at 122 keV) for X-ray fluxes up to 7 Mphotons/s for each pixel [43]. A single module of Multix-ME100, consists of an array of 1×128 pixels of size 0.8×0.8 mm^2 and each operated with 128 energy channels of width 1.1 keV, evenly distributed between 20 and 160 keV. Detector modules can be daisy-chained into detector arrays to extend the field of view. Figs. (3.3 and 3.4) depict five daisy-chained modules of the MultiX detector for a total of 640 pixels array detector and a total linear field of view of 512 mm. In imaging application daisy-chained modules lead to a gap between the pixels adjacent to the end of the linked modules that must be modeled in the reconstruction algorithm for geometry consistence. Moreover, each module is composed of 5 crystals that have

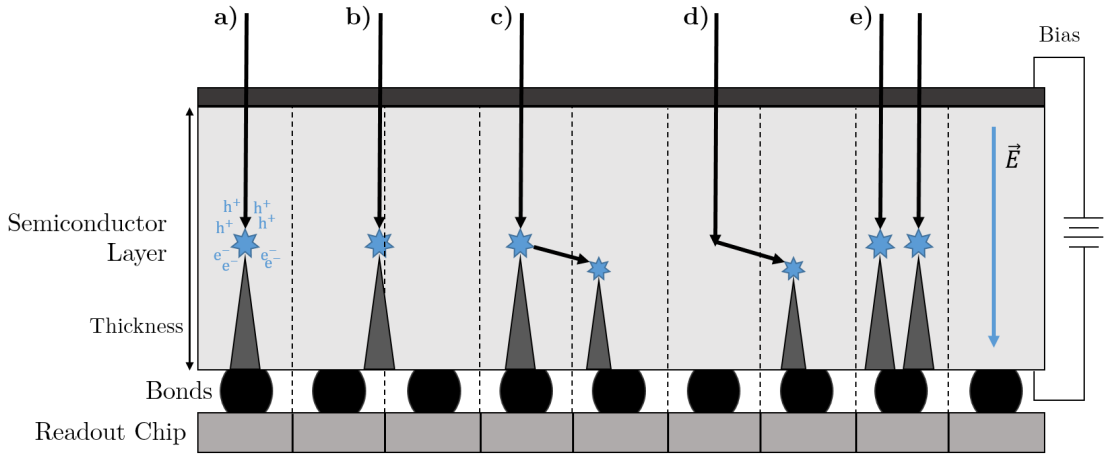

Figure 3.2: Overview of the interactions between photons and the detector device: The incident photon is absorbed by the semiconductor layer and produces an electron cloud that is drifted towards the readout chip via an electric field induced by an HV bias. a) The full electric charge is deposited into the collecting pixel. b) The photon hit the sensor at the edge of the collecting pixel and electric charge is deposited into two pixels (*charge sharing*). c) *Fluorescence* provokes a subsequent electric charge that are deposited into two different pixels. d) The incident photon undergoes a *scattering* event which deflect the trajectory and the charge is collected by a neighboring pixel. In case of inelastic scattering, an electron is released in the interaction and the photon loses energy. e) Two photons hit the sensor within the same processing chain are detected as a single photon with increased energy (*pulse pile-up*). Figure inspired by the work of Ehn [41].

a significant drop in count rate due to reduced size at their edges. This difference can be seen even following the Lambert Beer's law normalization thus, the pixels located at the crystal edges require a correction or interpolation to avoid severe ring artifacts in the reconstructions (see Fig. (5.10) for an example of an only partially corrected ring artifact). The Multix-ME100 implements fast readout electronic circuits to reach count rates of several millions counts per seconds. In SCT measurements we achieve a reasonably low noise level for integration times of only a few hundreds of milliseconds per projection. Given these characteristics, this detector is suitable for applications with high throughput demand, such as luggage inspection, where a scan of a single object must approach near real-time execution.

3.1.2 Correction Algorithm for Detector's Spectral Response

When using a PCD, the first processing routine that is recommended following the measurements and the storage of data is the correction for the detector's spectral distortions. Assuming a perfect PCD, a photon absorbed by the sensor via photoelectric absorption deposits all its energy into the sensor's respective pixel, noted as *collecting pixel*. However, in the real scenario, PCDs are subject to interactions between the photons and the detector device that can result in both a wrong energy

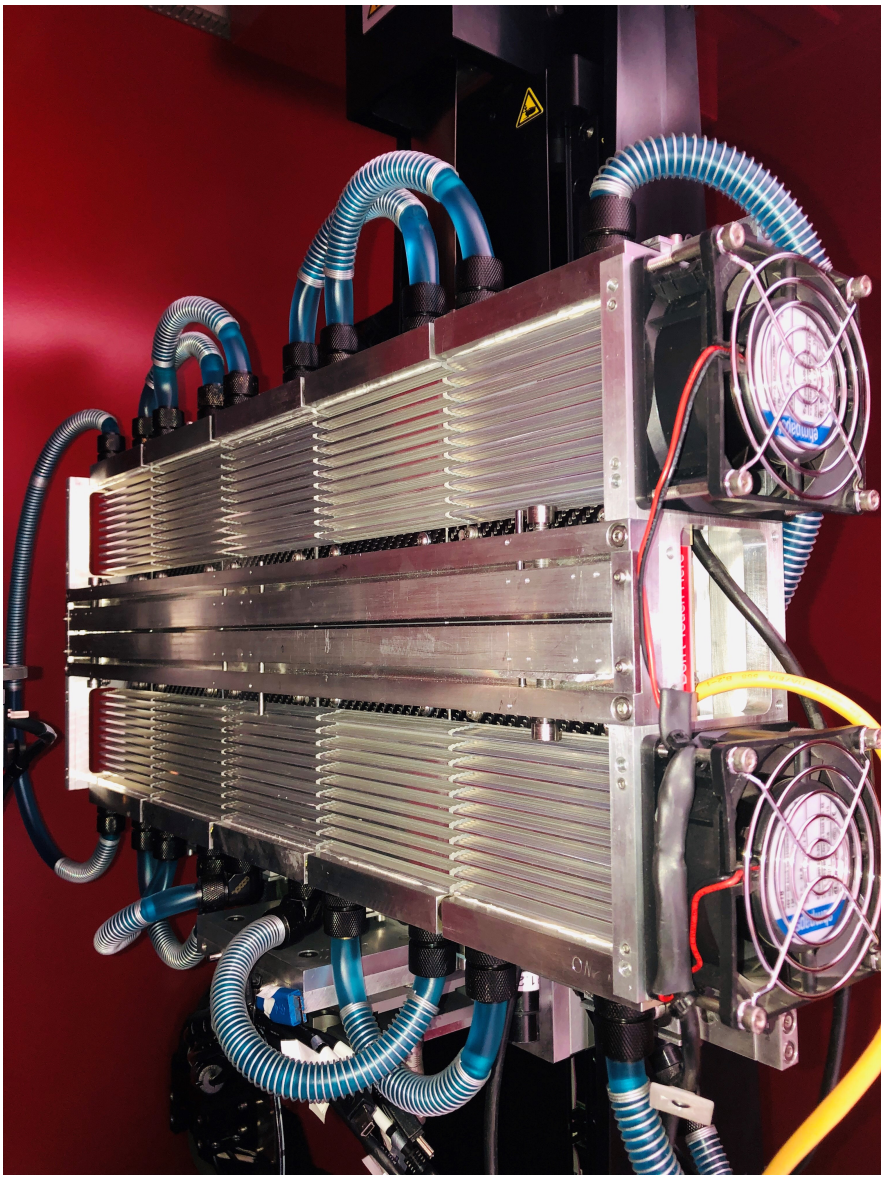

Figure 3.3: Picture of five daisy-chained MultiX-ME100 modules with the liquid cooling system and a slit with adjustable aperture size to suppress environmental and scattering noise.

determination and activation of the pixels neighboring the collecting one. Fig. (3.5) illustrates the effects on the spectrum of these interactions, which are listed and briefly described below:

- *Charge sharing* and *Weighting Potential Cross-Talk*: When a photon hits a sensor close to the edge of the collecting pixel, its charge may spread into one of the neighboring pixels. These pixels are triggered as well, and both collecting and neighboring pixels successively count a photon with reduced energy. This effect is called *charge sharing*. Similarly, the movement of the charge carriers in the collecting pixels may induce a charge in the neighboring pixels, which also count a photon with reduced energy. This is the so-called weighting

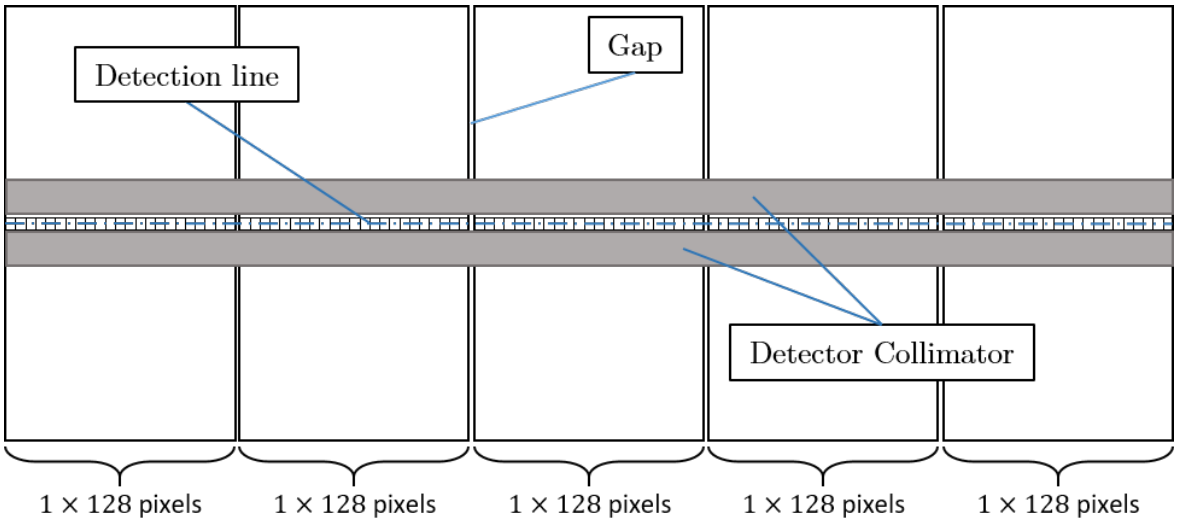

Figure 3.4: Sketch of the frontal view of the five daisy-chained MultiX-ME100 modules and the collimator slit.

potential cross-talk [44]. When polychromatic beams are considered, both these interactions result in an overall background signal in the low-energy tail of the peak corresponding to the source's emission line. In CT, when the signal is converted into linear attenuation coefficients of materials using Lambert-Beer's law, these effects cause a dampening of the LAC at low energies. This effect increases with the attenuation of materials and eventually can result in a relative maximum of the LAC in the low-energy range (see for example Fig. (3.9)), while it should be physically modeled as a monotonically decreasing function (assuming no K-edge discontinuities).

- Fluorescence radiation: When PCDs are built using semiconductors with high atomic number elements, these may have K-edges within the energy range of the source. Thus, when a photon hits the semiconductor sensor there is a chance for the fluorescence emission from the detector itself to be detected in the collecting pixel or within a few neighboring pixels. The overall spectral distortion due to by fluorescence is similar to charge-sharing effects. For example, MultiX-ME100, which is a CdTe-based PCD, is exposed to such effects due to the $K_{\alpha 1}$ and $K_{\alpha 2}$ emissions of Cd and Te respectively at approximately 23 keV and 27 keV.

- Scattering radiation: As in the case of fluorescence radiation, photons which hit the sensors can undergo scattering interactions and travel further reaching neighboring pixels before being fully absorbed. These can be due to both elastic and incoherent scattering events; however, incoherent scattering has more impact due to the higher probability of photons with scattering angles large enough to end up activating neighboring pixels.

- Pulse Pile up: When two or more photons hit the detector sensor within the same processing chain, their pulses overlap and are registered by the collecting pixel

as a single photon with energy approximately equal to the sum of the individual photon energies. When considering a polychromatic beam, this effect leads to an increase of the spectrum with the energy, in contrast to the ideal Bremsstrahlung decay to zero at the acceleration voltage setting of the source. Since the X-ray emission follows a Poisson distribution, this effect increases dramatically with the beam flux. When a material LAC measurement is concerned, this effect results in an upturn of the LAC for high energies, while it is supposed to be modeled by the photon cross section for incoherent scattering.

In addition to the effects listed above, CdTe semiconductor based PCDs (such as the MultiX-ME100) suffer from incomplete charge collection, which has the effect of skewing the spectrum toward lower energies. This is caused by the difference in the drift mobility of electrons and holes [45]. Lastly, the detector's working temperature influences the shape of the measured X-ray spectrum [46]. In X-ray CT applications, where the data is normalized by Lambert-Beer's law using the same flat field spectrum (I_0), it is important that the spectrum does not change when collecting the successive projections to avoid distortions in the measured LAC. Thus, especially in long CT scans, cooling systems are required to stabilize the detector's temperature and overcome temperature build-up due to the incident X-ray source and room temperature fluctuations.

When polychromatic beams are used, the changes in the spectrum shape are a superimposition of the effects for the individual photon energies, which complicates the modeling of the detector spectral response matrix that is typically employed for corrections [47]. To characterize the spectrum distortion due to these interactions, a synchrotron radiation source measurement was taken using the MultiX detector and a 70 keV X-ray beam. Fig. (3.5) highlights the experimental findings and the different distorting interactions. Overall, the distortion can be summarized as a broadening of the main energy peak, a background signal below the actual photon's energy and peaks around 140 keV which can be attributed to a two photons pile-up counting event.

The changes in the spectrum due to theses interaction depend on the source's spectrum shape and photon flux as well. The latter depends in turn not only on the source power, but also on the materials the X-ray passes through. For this reason, in a CT scan, where the data is normalized by taking the ratio between acquisitions with and without the sample, there is a non-linearity in the spectral response of the detector leading to wrong LAC calculation. Thus, a good spectral correction algorithm is essential in the correct quantitative characterization of materials using SCT. In this work the correction algorithm presented by Dreier et al. [48] is adopted in the data workflow (Paper II in the appendix). This method, as compared with previously presented correction algorithms, is flux dependent so that it is more flexible with respect to different source settings and samples, and robust to pile-up and other flux-dependent effects.

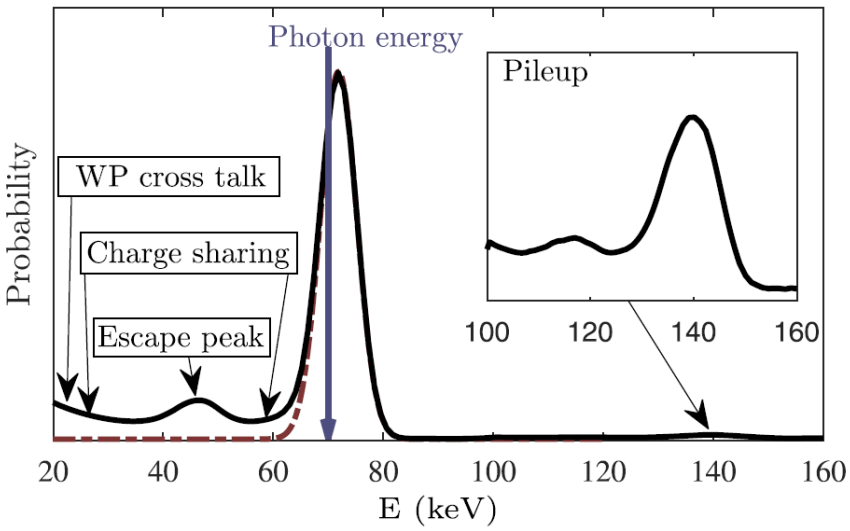

Figure 3.5: Spectral distortions suffered by a PCD measuring a 70 keV synchrotron radiation source X-ray beam. The dashed red line corresponds to the ideal detector response, considering the detector's energy resolution. Figure is taken from Paper II in the appendix.

3.1.3 Energy channels rebinning

Depending on the type of data analysis application, the number of energy channels in the spectral datasets is a parameter that can be optimized for a more efficient data processing workflow. Generally, algorithms that process datasets with fewer energy channels have faster computation time thus, the number of energy channels shouldn't increase unless there is an advantage. Moreover, wider energy channels lead to an increase of their respective photon count, which is relevant in SCT for reducing noise artifacts due to low photon statistics and for increasing the contrast to noise ratio. Most of the PCDs with a high number of energy channels (in some cases referred as hyper- or multi-spectral) offer the possibility of manually setting the thresholds, assigning an energy value to the energy channels that corresponds to the arithmetic mean between the two respective adjacent thresholds. For quantitative spectral analysis, e.g. the measurement of material's LAC, the correctness of the energy value assigned to the channel is key to an efficient data analysis, especially in cases of energy channels with relatively high energy width. Fig. (3.6) highlights the difference in the two methods for assigning the energy values to the new energy channels, exemplified for a rebinning into 8 energy channels. Clearly, the deviation between the two means gets higher as the number of new energy channels decreases due to a larger energy integration width, and the weighted means represent the real spectrum better.
When using hyper-spectral PCDs it is recommended to collect the data with the maximum number of energy channels and then, if desired, merge them into fewer channels (K) using the following procedure exemplified for MultiX-ME100, which considers the source spectrum and the detector spectral response. The merging is

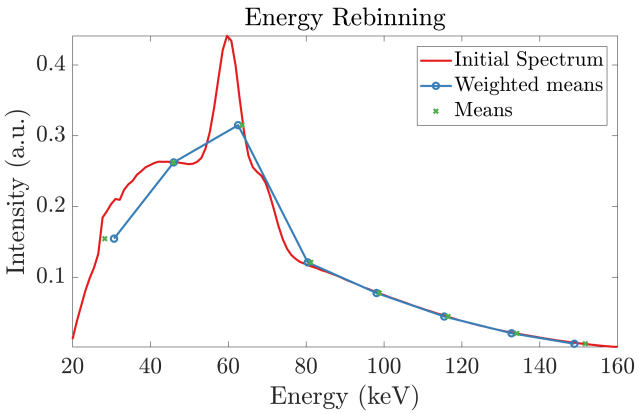

Figure 3.6: Plot of the initial spectrum measured with 128 energy channels (red line), and the spectrum resulting from the energy rebinning into 8 energy channels, with energy values defined as weighted means as in Eq. (3.2) (blue-circled line) and with arithmetic mean (green crosses).

done by summing the radiation I detected in adjacent energy channels as follows (exemplified for a rebinning from 128 to $K = 64$ energy channels):

$$I^{E'_k} = I^{E_{2k-1}} + I^{E_{2k}}, \quad k = 1, ..., K. \tag{3.1}$$

The energy values assigned to the new energy channels E'_k are calculated by taking the weighted mean according to the source spectrum as follows:

$$E'_k = \frac{I_0^{E_{2k-1}} \cdot E_{2k-1} + I_0^{E_{2k}} \cdot E_{2k}}{I_0^{E_{2k-1}} + I_0^{E_{2k}}}, \quad k = 1, ..., K. \tag{3.2}$$

Therein, I_0 is the corrected flat-field measurement, i.e. the projection without the sample being inserted, and corresponds to the source spectrum as measured by the detector (also referred to as the system's spectral response). It has to be noted that the merging procedure in Eqs. (3.1 and 3.2) can be done for a power of 2 of new energy channels (i.e. $K = 1, 2, 4, 8, 16, 32$) however, the principle can easily be adapted for any number of new energy channels.

3.2 Spectral X-ray Computed Tomography

As today, in the fields of medical imaging, Non-Destructive Testing (NDT) and generally in the industry, conventional CT scanners are made up with sources that produce a polychromatic beam and energy-integrating detectors. When only the contrast between different materials is of concern this is an efficient method. However, it is defective for quantitative characterization of materials. This is because the material property directly measured in a CT scan is the LAC, which is an energy-dependent property, whereas the energy information is lost at the detectors during the signal integration. To calculate the effective LAC of the materials, system spectral-response functions modeling the source spectrum and the detector spectral response

are required to find a pseudo-monochromatic energy point for the LAC (see Fig. (3.7 a)).
Other physical properties of matter can be extrapolated from the LAC. It has for long been known [49] that the energy-dependent LAC, $\mu(E)$, can be expressed as:

$$\mu(E) = \sum_{n=1}^{N} a_n f_n(E), \tag{3.3}$$

where $\{a_n, n = 1, 2, ..., N\}$ are the coefficients of a set of basis functions $\{f_n(E), n = 1, 2, ..., N\}$ and N is an arbitrary chosen number of basis functions. Depending on the choice of the basis functions of Eq. (3.3), several image processing algorithms for quantitative material analysis have been proposed and will be described later in this section. Still, the groundbreaking step towards techniques able to extract more information with energy-selective CT scans is the representation of the attenuation coefficient into the dual basis function decomposition by Alvarez and Macovski [5].

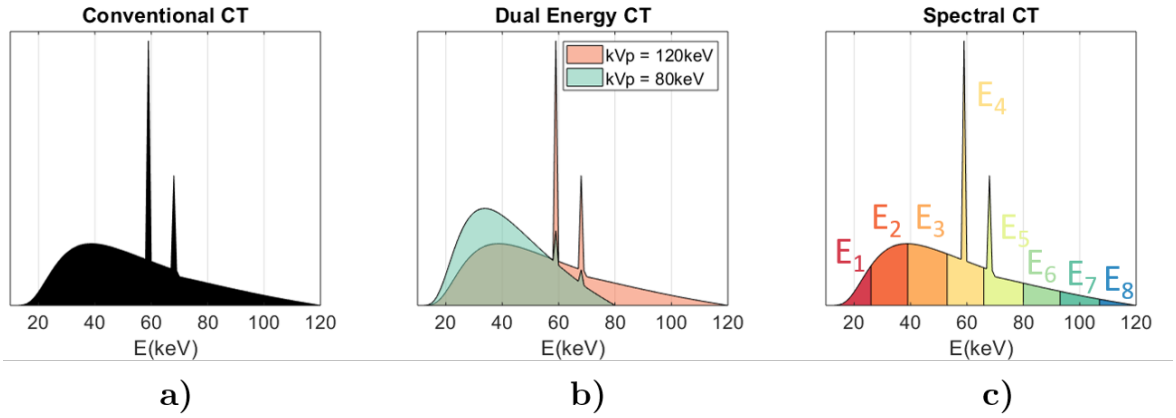

Figure 3.7: **a)** In conventional X-ray CT, the signal is integrated over all energies. Center. **b)** In Dual Energy X-ray CT, two different spectra are used to probe the sample attenuation at a low- and high- mean energy. **c)** In spectral X-ray CT, single photon counting detectors discriminate the incoming radiation in distinct energy channels with mean energy depending on the set energy thresholds.

The dual basis decomposition inspired the emergence of the Dual-Energy CT (DECT) technique, which would soon become the new state-of-the-art method for quantitative material characterization using X-ray CT. DECT (see Fig. (3.7 b)) is performed either by a pair acquisitions with energy integrating detector and two different source spectra using different filters or acceleration voltage settings, or simultaneously with a single source spectrum and employing dual-energy sandwich detectors. This technique has the advantage of contrast enhancement and enabling the material characterization into material dependent physical properties.
The first implementations of energy discriminating PCDs in X-ray imaging, however, put the concept of spectral X-ray CT under the spotlight of many research groups. Fig. (3.7 c) illustrates the so-called Spectral X-ray CT (SCT), which probes using

PCDs the linear attenuation coefficient (LAC) at multiple energies defined by the energy thresholds. In the literature, this technique can also be found named as Multi-Energy X-ray CT (MECT). For a high enough number of narrow energy channels, a SCT scan is ideally approaching a set of monochromatic scans. Thus, each projection defined in Eq. (2.20), becomes a set of energy resolved projections $\{R_{E_k}\}$:

$$R_{E_k}(\vec{x'}) = -log\frac{I^{E_k}(\vec{x'})}{I_0^{E_k}(\vec{x'})} = -\int_t \mu(\vec{x}, E_k)d\vec{x}, \quad \text{with} \quad k = 1, ..., N_E; \tag{3.4}$$

where $\vec{x'}$ is the detector pixel's position and N_E is the number of energy channels of the detector. The most direct approach with SCT is to perform reconstructions for each energy channel of the energy-resolved projections resulting in the retrieval of the energy spectrum of the materials' LAC. Since the emission of X-ray photons from the source follows a Poisson distribution and has a defined spectrum shape, each energy channel has a relative noise level that depends on the photon source flux in that energy channel. Clearly, wider energy channels integrate more photons and thus have lower noise level. Instrumental settings of a SCT scan thus have a trade-off between spectral resolution and noise level. To compensate for this, a study presented by Rigie et al. proposed to use total nuclear variation as a regularizer for reconstruction of spectral sinogram, showing greater performance than channel-by-channel reconstructions.
Most of the works in the current literature use detectors with up to eight energy channels, each of a width of several keVs, which is far from the ideal assumption of monochromatic acquisition sets. In this case, a source and detector spectral response model needs to be applied to correct for beam hardening and to assign the correct energy values to the respective energy channels in which the linear attenuation coefficients are calculated. Alternatively, one can use the basis function decomposition shown in Eq. (3.3) and substitute the LAC in a pre-reconstruction step in Eq. (3.4) resulting in the reconstruction of the object in terms of the coefficients, $a_n(x')$. Obviously, the LAC decomposition can also be performed in a post-reconstruction step. The advantage of a pre-reconstruction is that it typically reduces the computational time as the number of reconstructions is determined by the number of basis function and coefficient pairs, rather than the number of energy channels. However, the accuracy of this method depends on how well the basis function can represent all the possible materials.

3.2.1 Dual Basis Decomposition

Several choices for the basis function have been suggested however, the most influential was the one presented by Alvarez and Macovski [5]. They found good match with experimental data (without K-edges) by fitting Eq. (3.3) with a dual set of basis functions, consisting of the photoelectric absorption and Klein-Nishina functions:

$$\mu(E) = a_{\text{ph}} f_{\text{ph}}(E) + a_{\text{KN}} f_{\text{KN}}(E). \tag{3.5}$$

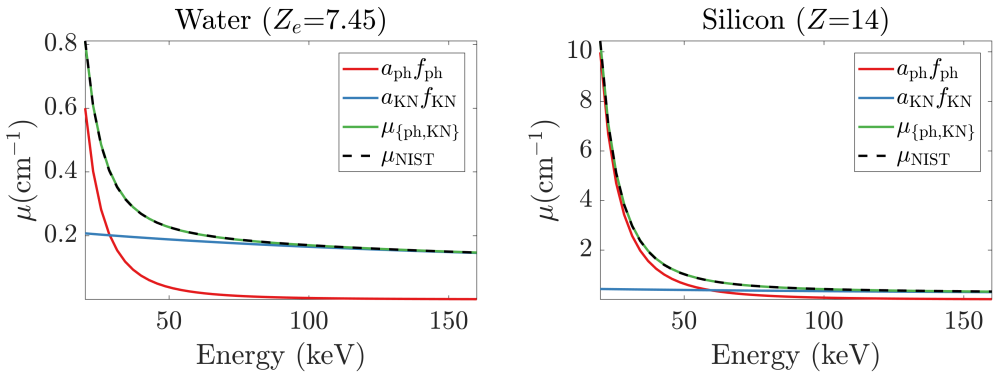

Figure 3.8: Dual basis composition of the LAC of water and silicon using the photoelectric absorption, f_{ph}, and the Klein-Nishina, f_{KN}, functions.

As discussed in chapter 2, the photoelectric absorption basis function depends on the energy as $f_{\text{ph}}(E) = 1/E^3$, whereas the Klein-Nishina function is defined by:

$$f_{\text{KN}} = \frac{1+\alpha}{\alpha^2}\left[\frac{2(1+\alpha)}{1+2\alpha} - \frac{1}{\alpha}\log(1+2\alpha)\right] + \frac{1}{2\alpha}\log(1+2\alpha) - \frac{1+3\alpha}{(1+2\alpha)^3}. \quad (3.6)$$

They also expressed the dependence of the coefficients on the physical parameters of bulk density ρ and atomic number Z:

$$\begin{aligned} a_{\text{ph}} &\approx \text{K}_1 \frac{\rho}{\text{A}} Z^n, \quad n \approx 4; \\ a_{\text{KN}} &\approx \text{K}_2 \frac{\rho}{\text{A}} Z \end{aligned} \quad (3.7)$$

where K_1 and K_2 are constants and A is the atomic weight. Fig. (3.8) features an example of the dual basis decomposition into photoelectric absorption and Klein-Nishina, exemplified for water and silicon materials. Therein, the constants that were best fitting the LACs reported by NIST were $K_1 = 28.0, K_2 = 0.40$ for water and $K_1 = 24.7, K_2 = 0.30$ for silicon, setting the exponent to $n = 4$ in Eq. (3.7).
Alvarez and Macovski showed for example, that a_{ph} and a_{KN} can be measured with a DECT scan using a pair of a low- and high- energy scans. The underlying assumption is that, since the low-energy part of the spectrum is dominated by photoelectric absorption interactions whereas the high-energy part of the spectrum is dominated by incoherent scattering events, the low/high-energy scan pairs can be used to measure the respective the coefficients pairs, $\{a_{\text{ph}}/a_{\text{KN}}\}$, in Eqs. (3.7). The energy distribution that models the source spectrum and detector response of the two scans are required to produce a pair of pseudo-monochromatic measurements. Another method, presented by Ying, Naidu and Crawford [6], extended this technique to retrieve the pair of material features $\{\mu_{\text{high}}, Z_{\text{eff}}\}$, where μ_{high} is the attenuation coefficient measured with the high-energy source spectrum and Z_{eff} is the effective atomic number. The commonly-used definition of Z_{eff}, used to approximate materials composed of different

elements into a single non-integer value for the atomic number, is found in [50]:

$$Z_{\text{eff}} = \sqrt[p]{\sum_{i=1}^{N} r_i Z_i^p}, \tag{3.8}$$

where N is the number of elements in the material and r_i is the relative electron fraction of each element, defined by:

$$r_i = \frac{n_i Z_i}{\sum_{j=1}^{N} n_j Z_j}, \tag{3.9}$$

where n is the number of atoms with the same atomic number. The exponent p is a free parameter that can be tuned depending on the set of materials and spectral region and was originally set to $p = 2.94$. As of today, the most recent, accurate and precise documentation of material characterization from DECT was presented by Azevedo et al. [8]. They proposed a new material feature space, composed by the pair of electron density ρ_{e} and a redefinition of the effective atomic number, Z_{e}. The method shows great advantage compared with the previous techniques as it estimates system-independent physical properties of materials. In this approach, the total mass cross section is converted into *electronic* cross section ($\text{cm}^2/\text{e}^-\text{mol}$), as:

$$\sigma_e(Z, E) = \frac{A(Z)}{Z}\sigma(Z, E), \tag{3.10}$$

where $A(Z)$ is the atomic mass (g/mole) of the element Z. Likewise, the bulk density ρ (g/cm^3) is converted into *electron* density ρ_{e} ($\text{e}^-\text{mol/cm}^3$), using the relation:

$$\rho_{\text{e}} = \frac{Z}{A(Z)}\rho. \tag{3.11}$$

For a compound material, consisting of a number n_i of N distinct elements i, the electronic density is extended from Eq. (3.11) as:

$$\rho_{\text{e}} = \frac{\sum_{i=1}^{N} n_i Z_i}{\sum_{i=1}^{N} n_i A_i}\rho. \tag{3.12}$$

The effective atomic number, Z_{e}, presented by Azevedo et al. [8] is a redefinition of the Z_{eff} in Eq. (3.8). It is represented by a non-integer atomic number that corresponds to an artificial element, for which the interactions are assumed to be modeled by the X-ray attenuation cross sections. The cross sections for the artificial element Z_{e} are obtained by a linear interpolation between the cross section of the two adjacent elements in the periodic table:

$$\sigma_e(Z_{\text{e}}, E) = (1 - \epsilon)\sigma_e(Z', E) + \epsilon\sigma_e(Z' + 1, E). \tag{3.13}$$

Therein, Z' is the lower adjacent element $Z' = \text{floor}(Z)$ and ϵ is the difference $\epsilon = Z' - Z$. In this feature space of the effective atomic number and electronic density, Eq. (2.7) for the linear attenuation coefficient of a material m becomes:

$$\mu^m(E) = \rho_{\text{e}}^m \sigma_e(Z_{\text{e}}^m, E). \tag{3.14}$$

This technique was shown by Azevedo et al. [8] to be superior to its precedents, with good accuracy and precision for a set of materials with $Z_e < 15$ and well known-physical parameters. The general interest is towards system-independent techniques that can be implemented in any scanner. However, the performance of these techniques depends on the choice of the pair of spectra used for the DECT acquisitions and the correct modeling and characterization of their respective system spectral responses. For these reasons, these techniques define a group of materials within a limited range of Z_e for which the characterization is accurate and precise but is inaccurate for others. For example, the same pair of spectra that was used to characterize materials with $Z_e < 15$, may not be efficiently used with highly attenuating materials as a different pair of spectra would be more proficient. Nevertheless, this dynamic range is often not required in real application. For example, in security screening, materials that cannot be characterized using this technique are often metals or alloys for which the shape detection is enough in terms of threat detection. A more concerning limitation is that the approximation of compound materials into Z_e is not valid for materials including elements with K-edge. An example of such a material is Polyvinyl Chloride (PVC), which can contain lead particles as stabilizer, for which a K-edge discontinuity is found at 88 keV. Mixture compounds and inhomogeneous materials are also not efficiently approximated by the Z_e as this feature depends on the concentration of the different materials. Similarly, granular materials yield different ρ_e values depending on the void fraction in the material.

3.2.2 Material Basis Decomposition

Material basis decomposition is a worth to note basis function decomposition of Eq. (3.3). In these methods, the basis functions are represented by energy dependent linear attenuation coefficients of reference materials f_Z, typically with very different attenuation properties. The other materials are then represented in terms of the coefficients a_Z found for the reference materials. Brambilla et al. [51] for example have used a dual function set composed of the measured energy resolved LAC of polyethylene (PE) and polyvinyl chloride (PVC), and a trial function set adding gadolinium's LAC, which presents a K-edge discontinuity at 50.2 keV. The trial basis function set can be represented in Eq. (3.3)'s form as:

$$\mu(E) = a_{\mathrm{PE}} f_{\mathrm{PE}}(E) + a_{\mathrm{PVC}} f_{\mathrm{PVC}}(E) + a_{\mathrm{Gd}} f_{\mathrm{Gd}}(E). \tag{3.15}$$

The advantage of this model is that is more flexible than the photoelectric absorption-Compton and it can be more accurate for certain applications, as the basis functions are modeled with real data from the same scanner. Moreover, it can represent the LAC of materials with K-edge discontinuities. However, this method is system-dependent as it is built upon other reference measurements.

Taking advantage of the high number of energy channels of recent PCD realizations, Babaheidarian and Castañón [52] proposed a spectral decomposition method called SPECK, that can be considered as a combination of the dual and material basis

decomposition. SPECK adds to the standard photoelectric absorption and Klein-Nishina basis functions the energy-dependent LAC of a number (K), of elements with the K-edge in the detector's energy range. These are the additional basis functions, denoted as $f_k(E)$. In this approach Eq. (3.3) can be rewritten as:

$$\mu(E) = a_{\text{ph}} f_{\text{ph}}(E) + a_{\text{KN}} f_{\text{KN}}(E) + \sum_{k=1}^{K} a_k f_k(E). \tag{3.16}$$

This choice of basis functions still has the property of being a linear independent set of functions, due to the energy dependence of the K-edge discontinuities relative to each element's atomic number Z. The advantage of using this basis function set is that it can fully represent materials exposed to K-edge discontinuities. As suggested by Babaheidarian and Castañón for example, Baratol, an explosive compound which combines barium nitrate ($Ba(NO_2)_3$) with TNT, has a K-edge for barium at 38 keV and would not be characterized correctly using either the standard dual-basis function or the approximation into effective atomic number Z_{e}.

3.2.3 K-edge Imaging

In chapter 2 it was discussed how certain materials can be exposed to discontinuities in their LAC's function of energy, due to the K-absorption edges. In conventional CT, the X-ray spectrum is integrated, and such discontinuities cannot be resolved thus, the additional information exposed by this material property is lost. However, in spectral CT, using detectors with an energy resolution that is high enough to resolve K-edge discontinuities, this represents an additional material feature that can be used for characterization and contrast enhancements. Several recent works [11, 14, 15] have proposed the use of iodine or gadolinium as a contrast agent, since their K-edge at the energies of respectively 33.16 keV and 50.23 keV is within the detectors' energy range. Using this technique, the contrast between two materials with similar attenuation coefficient properties but different K-edges can be drastically enhanced. Another work from Si-Mohamed et al. [53] demonstrated the determination, via spectral X-ray K-edge imaging, of the bio-distribution of gold nanoparticles *in vivo*. The current challenges in these techniques are mainly represented by the spectral resolution and the detection's energy range of the current PCDs that can work with relevant photon flux. For example, iodine, which is a practical and convenient contrast agent in biology studies, has the K-edge discontinuity in an energy range where CdTe based PCD has low spectral resolution due to the distortion effects discussed earlier in this chapter. Nevertheless, this technique shows great potential of improvement, both in the advance of the hardware and the data processing algorithms.

3.3 Spectral ρ_e/Z_e Estimation Method (SRZE)

In this work the focus is on a novel method developed for the estimation of the physical properties of electron density, ρ_e, and effective atomic number, Z_e, of a material from its spectral LAC measurements. The detailed description of the method can be found in the Paper III of the appendix section. Fig. (3.1) highlights the overall workflow of the data processing, which starts with the correction algorithm briefed in Section. 3.1.2 and fully detailed in Paper II for the correction of the detector's spectral response. In case of desired rebinning the data is processed using Eqs. (3.1 and 3.2) of Section. 3.1.3. The projections are then converted into the attenuation coefficient domain using Eq. (3.4) and corrected for scattering, when necessary, using the method presented below in chapter 5.

Depending on the geometry parameters of the CT scan, different reconstruction algorithms and techniques have been used. In case of slice reconstructions with fan-beam geometry and a high number of projections we used the filtered-back projection (FBP) method using LTT [54] software. With the same geometry, but a limited number of projections (below 100) we used a custom implementation of the Algebraic Reconstruction Technique with Total Variation regularization (ART-TV) presented by Sidky et al. [55] as it has shown better reconstruction quality. In case of cone-beam collimation of the source we used a GPU implementation of the Simultaneous Iterative Reconstruction Technique (SIRT) [56] using ASTRA toolbox [57] for enhanced computational speed. Note that in this work reconstruction were performed on an energy channel-by-channel basis.

The individual materials are segmented from the reconstructions in their respective Region Of Interest (ROI) surfaces or volumes using the spectral algorithm presented by Kehl et al. [58] For each material, the energy-dependent LAC and its respective error is found by calculating the median value and the standard deviation within the material's ROI for each energy-resolved reconstruction.

Energy channel thresholding

Once the LAC's mean value and standard deviation are found for each material, the analysis can start. Fig. (3.9), represents an example of silicon's LAC measured with and without the application of the detector spectral correction algorithm presented in section 3.1.2, as well as the corresponding ground truth calculated using reference values of silicon's effective atomic number and electron density. The correction algorithm helps correct the LAC towards the ground truth values at the low energies, where the contrast between organics compounds is highest. The error increases towards the low- and high-energies due to the lower photon statistics in these energy channels. Likewise, the deviation of the LAC from the reference increase towards the low- and high-energies due to a incomplete restoration of the distortions by the correction algorithm. To estimate the ρ_e and Z_e of each material, the method requires an automated selection of the low- and high-energy thresholds, E_L and E_H, which

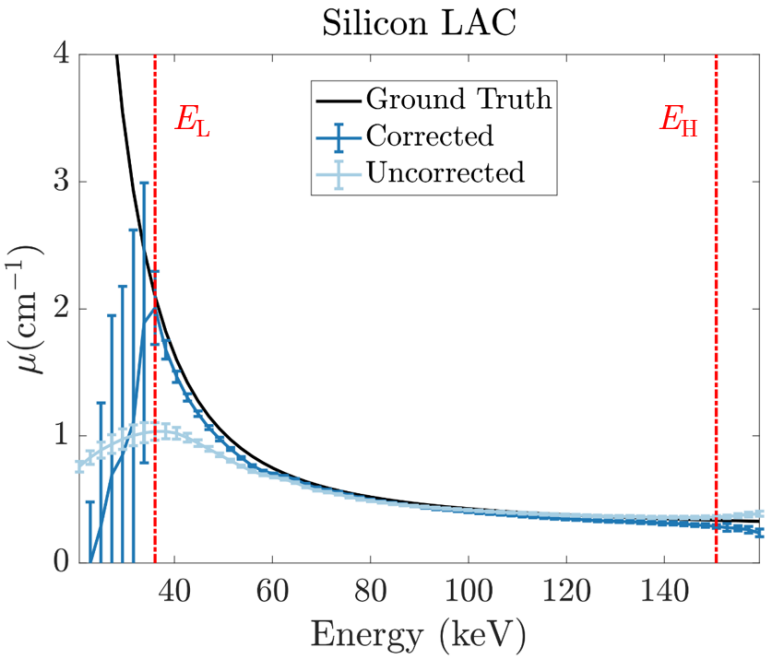

Figure 3.9: Energy resolved LAC, exemplified for Silicon. The solid black line is the ground truth obtained by using the ground truth values of ρ_e and Z_e in Table 1, using NIST cross-sections. The dark and light blue lines are the LAC calculated with and without applying the spectral correction algorithm in Section 3.1.2 respectively. The width of the error-bars represents the respective standard deviation values. The vertical red dash-dotted lines are the low- and high-energy thresholds E_L and E_H found by the energy channel thresholding step.

correspond to energy thresholds that exclude bins in which the LAC is affected by low photon statistics and pulse pile-up. For all the materials scanned in this work, these two thresholds were calculated by assuming the LAC to be monotonically decreasing, and with no inflection points in the incoherent scattering regime ($E > 60$ keV). This assumption is useful, in case of a PCD, for materials (i.e. $1 \leqslant Z_e \leqslant 42$) that do not have a K-edge within the detector's energy range. The low-energy threshold E_L is determined by taking the first derivative of the estimated LAC ($\partial\mu(E)/\partial E$) and locating the nearest zero intercept closest to the lowest-energy bin, as it corresponds to a relative maximum with a change from increasing to decreasing. The high-energy threshold E_H is determined by taking the second derivative of the estimated LAC ($\partial^2\mu(E)/\partial E^2$), and locating the bin nearest the zero intercept, closest to the highest energy bin, as it corresponds to an inflection point. Fig. (3.9) also illustrates the energy thresholds determined from the measured LAC of silicon.
The estimation is performed by solving a constrained minimization of a cost function $g(E)$:

$$\arg\min g(E). \tag{3.17}$$

The cost function is defined as $g(E) = |\tilde{\mu}(E) - \mu(E)|^2$, that is, the squared

distance between the measured LAC, $\tilde{\mu}(E)$, and its relative theoretical definition $\mu(E)$, parametrized by ρ_e and Z_e as in Eq. (3.14). Thus, for a spectral acquisition Eq. (3.17) becomes:

$$\underset{\{\rho_\mathrm{e},Z_\mathrm{e}\}}{\arg\min} \sum_{k=i}^{f} \lambda_{E_k} |\tilde{\mu}(E_k) - \rho_\mathrm{e}\sigma_e(Z_\mathrm{e}, E_k)|^2. \tag{3.18}$$

Therein, λ_{E_k} are the energy weights, computed as the reciprocal of the variance (s^2) of each material's LAC in their ROI, $\lambda_{E_k} = 1/s^2(\tilde{\mu}_{E_k})$. These can be interpreted as the weight given to each energy bin E_k into the estimation of the material's features. Note that the summation runs from the low- and high-energy thresholds E_L and E_H, found as described in the previous section. The minimization process in this work was performed with MATLAB®'s routine function FMINCON with solution boundaries $\rho_\mathrm{e} = 0 - 15$ e$^-$mol/cm^3 and $Z_\mathrm{e} = 1 - 99$ and initial guesses $\rho_\mathrm{e}^0 = 1$ e$^-$mol/cm^3 and $Z_\mathrm{e}^0 = 7$. No dependency on the starting values was observed. The runtime is approximately 1 second per LAC.

3.4 Energy-Dispersive X-ray Diffraction

In the previous chapter, the XRD method for characterization of materials was presented. The goal of the technique is to measure the intensity of the radiation undergoing elastic scattering interactions as a function of the momentum transfer Q, which is parametrized by the photon's wavelength, λ, and scattering angle, 2θ, as in the following equation:

$$\mathrm{Q} = \frac{4\pi}{\lambda} \sin\left(\frac{2\theta}{2}\right). \tag{3.19}$$

In most cases, an XRD experiment is performed at a large-scale facility, where monochromatic and powerful beams with extremely high photon flux are available. Laboratory-scale X-ray instruments on the other hand, implement X-ray tube sources that produce a polychromatic beam, which makes it impossible to correctly determine a single energy value as input of Eq. (3.19). A possible solution could be the use of monochromator components, as used for synchrotron radiation sources, which select only certain wavelength windows however, for laboratory scale photon fluxes they would reduce drastically the photon count slowing the speed of measurements. A more promising solution is the Energy Dispersive X-ray Diffraction[1] (ED-XRD) technique, which take advantage of the simultaneous spectral resolution of energy resolving PCDs. In this technique, a spectral measurement can be considered as a simultaneous scan of a set of monochromatic acquisitions, each at a defined energy that depends on the detector's specifics. For example, an ED-XRD acquisition with a PCD that discriminates into 128 energy channels, would lead to 128 individual

[1]The diffraction term is due to the notoriety and similarities with the X-ray Diffraction (XRD) technique however, it doesn't strictly require crystalline samples.

scattering functions Q(E). The individual energy-resolved scattering functions are normalized and merged in a final scattering function $\tilde{\mathrm{Q}}(E)$. While this technique can easily be applied for homogeneous materials, more complex samples including multiple materials represent a challenge due to the overlap of scattering signals from different materials within the X-ray beam's optical path. Techniques under development in the field of security screening for samples such as luggage are mainly found implementing collimators or coded aperture to resolve the scattering signal at each position along the optical path of the incident collimated beam [59]. Using a pencil-beam collimation, a raster scan throughout the sample is required for a complete investigation of the object. Alternatively, the beam can be steered to probe suspicious volumes detected in previous steps. The spectral resolution of the detectors, together with source flux, is indeed the major limitation of this method for material characterization.
For this work, ED-XRD was used for the material characterization into diffraction pattern of several innocuous and threat materials commonly found in luggage. The scans were carried out using a single pixel PCD, manufactured by AMPTEK, called XR-100CdTe. This detector is a CdTe semiconductor-based diode, with an energy resolution at 122 keV of 1.5 keV Full Width at Half Maximum (FWHM), and the possibility to threshold the photons into a maximum of 2048 energy channels of 0.0851 keV width. The high spectral resolution property of this detector is key in the success of the ED-XRD measurement in order to resolve the diffraction peaks and features, despite the relatively low field of view of 5 mm^2 × 5 mm^2, which makes it hard to implement in high-throughput industrial scanners. For these experiments, the

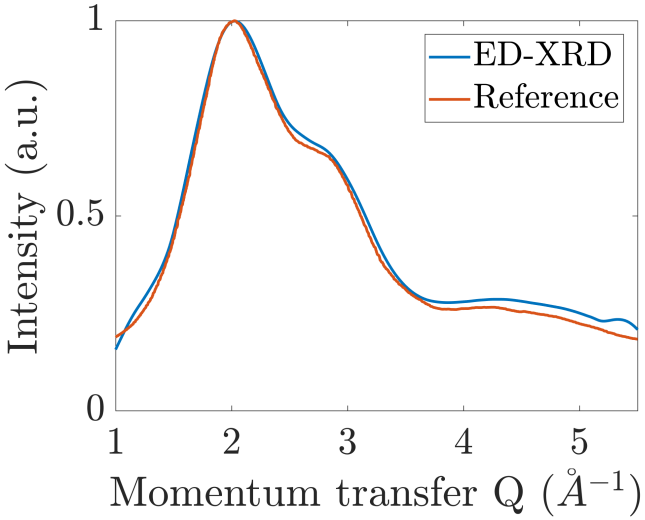

Figure 3.10: Elastic scattering signal of water, measured with an in-house ED-XRD instrument (solid blue) and a publicly available reference from synchrotron radiation source measurements (solid red).

detector was mounted on a goniometer motor able to rotate it at a fixed distance with respect to the sample position. Several scattering intensity spectra were collected at different scattering angles to equally sample the intensities at different momentum

transfer values within the relevant range. These, were normalized, merged and corrected for incoherent scattering using the analytical approximations by Pálinkás [30]. Fig. (3.10) presents an example of an ED-XRD measurement result for water. The water's diffraction pattern obtained with our in-house instrument built for ED-XRD acquisitions (section 6.1) is compared to a synchrotron radiation measurement from reference [60]. A good match was found between the two scattering functions, with a normalized root-mean-squared-error (NRMSE) of 0.03. The same technique and experiment setup were used to obtain the scattering function for the other materials, which are used in this work for modeling the elastic scattering in the simulation framework in chapter 4.

Monte Carlo Spectral X-ray Tracing Simulations using McXtrace 4

This chapter describes the software package used for the Monte Carlo (MC) X-ray tracing simulations of X-ray experiments. A new sample component is developed, which can be used to model interactions between photons and samples that can be composed of multiple different materials with a given shape. This component is used for correction steps in the SCT workflow to reconstruct and characterize the object scanned, to design the optimal parameters for the X-ray instrumentation and lastly to train the Convolutional Neural Network (CNN) architectures in the next chapter. The component, as well as other add-ons for simulation of spectral X-ray CT experiments can be found in the GitHub repository [61].

4.1 Toolkit for Simulation of Spectral X-ray CT Measurements

The simulations framework adopted for this work is McXtrace [16], a software package for MC simulation of X-ray experiments by ray-tracing methods. Rather than tracing individual photons, in this framework rays are represented by photon entities, and their interactions are simulated by probabilistic weight factors and tracing parameters such as direction, wave-vector, polarization vector and phase. The individual parts composing the instrument (e.g. sources, slits, detectors, samples, etc.) are identified as so-called *components* that can be separately implemented in comparatively few lines of code and interact with each sampled ray by applying weight factor operations or by altering their parameters. For this work, we have developed a *sample* component suitable for spectral X-ray imaging, with explicit treatment of the different physical interactions (described in chapter 2) of X-rays incident on objects composed of multiple materials of a given shape. The *sample* is initialized by loading a volumetric discretized phantom of the object that is made up of a finite number of voxels of a defined size in a 3D rectangular parallelepiped grid representing the bounding box. In this

Data: Sample's volumetric phantom and densities ρ^i, cross sections $\sigma^i(E)$ and scattering functions $I^i_{\text{ela}}(\text{Q})$ and $I^i_{\text{inc}}(\text{Q})$ for each material i.
Result: Energy resolved total and scattering signal from the interaction between X-rays and the sample.
Initialize sample and load ray parameters.;
Set the step length s_{l}.;
while *ray is within the sample* **do**
  if *ray is scattered* **then**
    if *incoherent scattering* **then**
      Sample scattering angle θ from incoherent DCS (Eq. (2.18));
      Update ray direction according to θ;
      Update energy due to Compton shift with Eq. (4.2);
    else
      Sample scattering angle θ from $I^i_{\text{ela}}(\text{Q})$;
      Update ray direction according to θ;
    end
  end
  Read photoelectric absorption attenuation $\mu(E) = \rho^i \sigma^i_{\text{ph}}(E)$;
  Ray travels the step length s_{l};
  Increment the cumulative attenuation due to photoelectric absorption along the trace: $l\mu(E) = l\mu(E) + s_{\text{l}}\mu(E)$;
end
Apply final attenuation to the ray: $e^{-\mu(E)l}$;

Algorithm 1: Pseudo-code of the McXtrace sample component.

way, samples composed of objects of complex shape require the same computational cost as simple geometries. Moreover, since the reconstruction images rendered and employed in the forward and back projections of iterative methods are discretized in the same way, the format is well suited for reconstruction algorithms and their parameter optimization. The drawback of the voxel representation, when compared with other 3D volume rendering techniques such as triangular mesh or error quadrics [62], is that it is a resource intensive method and high-resolution simulations may require an object phantom voxelization, of which the size overrides the software or hardware capabilities. For example, a 1 m^3 volume with 1 mm^3 feature resolution for an object with a relatively simple shape requires 1.2 GB in the memory while it only takes 200 kB and 1.2 MB for quadrics and triangular meshes respectively [63], due to the volumetric nature of voxelization. Depending on the application, different rendering methods have higher efficiency and one should choose accordingly. Another advantage of the voxel representation in this ray-tracing method is that the multiple scattering events, i.e. when a photon reaches the detector after more than one scattering event in the same lifetime, can be easily included in the model. Commonly in the literature, the ray tracing methods are detector driven, meaning that the scattering noise probabilities at the detector are calculated starting from the given coordinates for the detector pixels. While this can be advantageous in terms of computational cost, it limits the modeling

of multiple scattering interactions that may have a significant impact on the total scattering intensity when relatively large samples are considered. The value in each voxel holds an integer number $i = 0, 1, 2, ..., N$ which labels a specific material.
Algorithm 1 presents the pseudo-algorithm of the sample component, responsible of the tracing of the rays through the sample component.
For each material, lookup tables of various interaction likelihoods are required. The

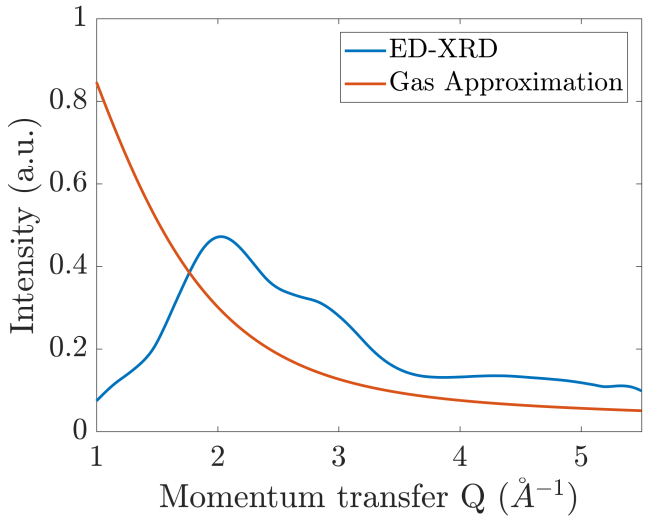

Figure 4.1: Elastic scattering function of water, measured with an in-house ED-XRD experiment (solid blue) and using analytical approximation for a gas of non-interacting atoms with the effective atomic number of water $Z_e = 7.45$.

first lookup table is composed of the energy parametrized photon cross sections for the possible interactions between the X-ray beam and the sample; i.e. photoelectric absorption $\sigma_{ph}(E)$, elastic scattering $\sigma_{ela}(E)$ and incoherent scattering $\sigma_{inc}(E)$. For X-rays spectra that go up to several MeVs, nuclear and electron pair production photon cross sections are loaded as well. These values are used to determine the likelihood of each photon interaction in the component as they pass through matter and could for instance be loaded from the database administrated by the National Institute of Standards and Technology (NIST) [64]. In a simplified approach, assuming that the scattered radiation is deflected out of the detector's range and thus, extinct at the sample, the photoelectric absorption cross section can be replaced by the total attenuation cross section ($\sigma_{tot} = \sum_i \sigma_i$), allowing the user to skip the following component's treatment of the scattering and thus, faster performance.
The remaining two lookup tables are used to sample the elastic and incoherent angular deflection of the ray trajectory when a scattering event occurs. In the case of elastic scattering, the scattering angle determination is modeled by the scattering function, i.e. the intensity of the scattering as a function of the momentum transfer. In this approach, the scattering function is treated as the probability distribution function

(PDF) of the momentum transfer $\vec{\mathrm{Q}}$, of amplitude:

$$\mathrm{Q} = |\vec{\mathrm{Q}}| = \frac{4\pi}{\lambda} \sin\left(\frac{2\theta}{2}\right) \tag{4.1}$$

where λ is the wavelength of the incident X-ray and 2θ is the detected scattering angle (i.e. between the incident and the scattered ray). The scattering vector's amplitude Q can be sampled by the inversion method [65], which involves computing the Cumulative Distribution Function (CDF) of the distribution and then inverting that function. Since the latter is discrete, the computation of the CDF is simply done by adding up the individual probabilities (normalized to sum 1) for the various points of the distribution. The detected scattering angle 2θ is derived from the sampled Q using Eq. (4.1) since the energy of the incident ray is a known parameter. Most of

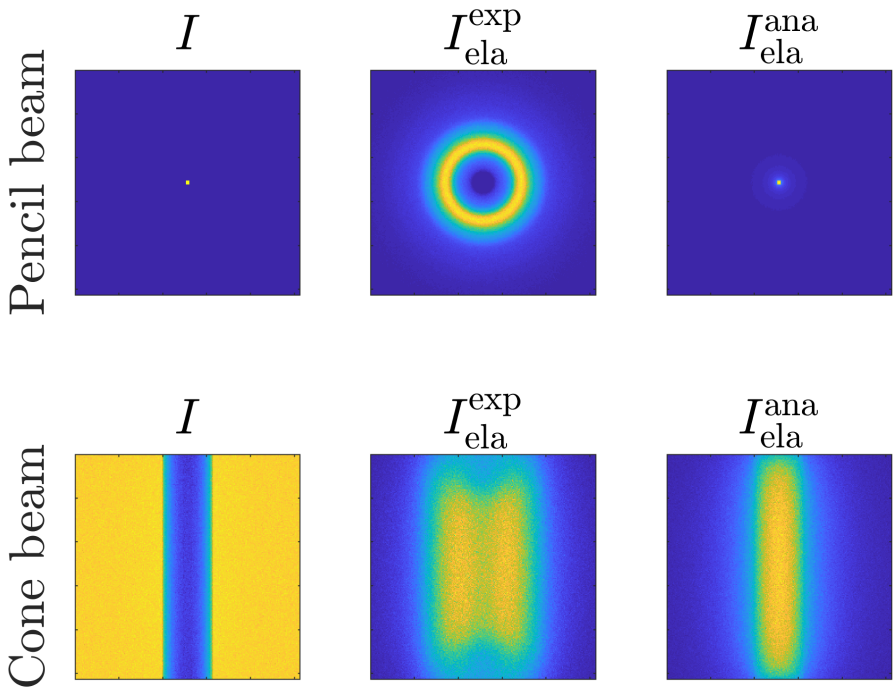

Figure 4.2: Simulation of isolated elastic scattering I_{ela} using an experimentally measured (*exp* superscript) scattering function distribution and analytical approximation (*ana* superscript). For the top row, the collimation of the beam is set to pencil beam, visible as the yellow dot in the left figure. For the bottom row, the collimation of the beam is set to cone beam, which makes the water cylinder visible.

commercially available software for X-ray tracing used for the scattering estimation use simplified models for the angular deflection due to elastic scattering, which do not consider the molecular structure of the materials. Analytical approximations such as the ones presented by Hajdu [29] are explicitly expressed for a gas of non-interacting

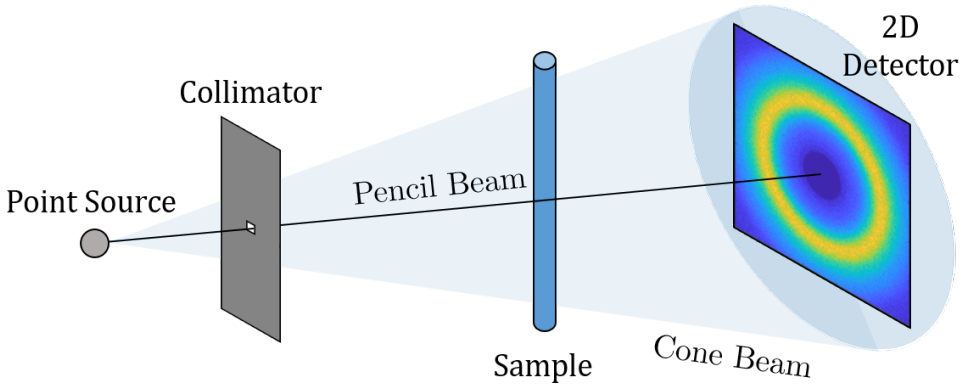

Figure 4.3: Sketch of the simulation of the XRD experiments with two different collimation settings. The first is the pencil beam (black line), obtained by using a slit collimator with small aperture size whereas the cone beam (light blue cone) is obtained by opening the slits further.

atoms, leading to a scattering function that has a maximum for forward scattering and decreases monotonically with the scattering angle. However, depending on the phase and molecular structure of materials the scattering function takes unique shapes, as discussed in chapter 2. Fig. (4.1) highlights this discrepancy, showing the elastic scattering function of water measured with ED-XRD, and calculated using Hajdu's approximation for a gas of non-interacting atoms using the effective atomic number of water $Z_e = 7.45$.

To further demonstrate the difference between the two models in imaging applications, we performed a simulation of an XRD experiment using a water filled thin cylinder as a sample. Fig. (4.2) shows the elastic scattering signal at the detector using the two different models, for two different X-ray beam geometries: pencil and divergent cone-beam geometries (see geometry sketches in Fig. (4.2)). Clearly, the simulation output using the analytical model for gas is significantly different. In general, the use of analytical approximations not considering the molecular structure leads to an overestimation of scattering within the area subtended by the sample.

In this work, the distribution for $I_{ela}(Q)$ has been experimentally determined for a list of common materials by the ED-XRD method as described by Kehres et al. [66] and stored into a feature library.

For the simulation of incoherent scattering, due to the considerable amount of backward and high scattering angles, the same models used for elastic scattering cannot be used. Firstly, the incoherent scattering analytical approximations by Hajdu [29] and the later extension by Palinkas [30] are only defined for a value range of the momentum transfer for which the elastic scattering events are relevant, as their end goal is to correct for background incoherent scattering in XRD measurements. Thus, backwards and high angle scattering events are not included in their models. Secondly, an experimental setup for measuring the incoherent scattering and obtaining an incoherent scattering

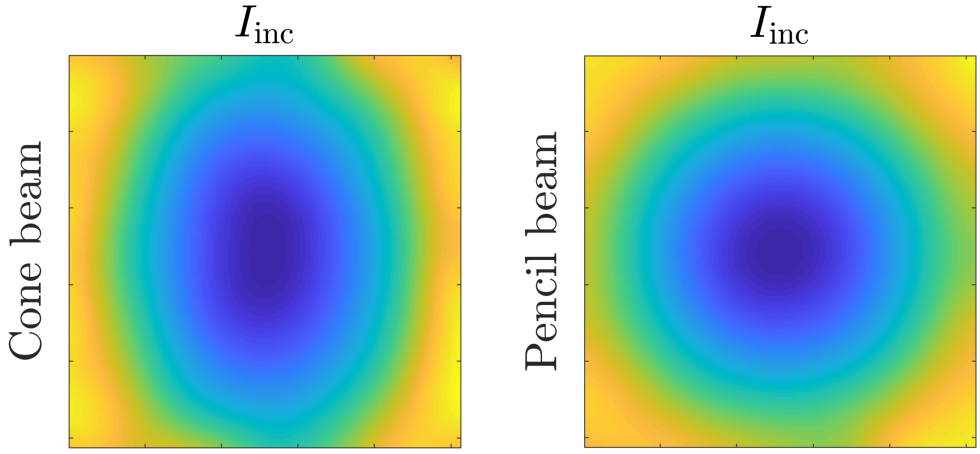

Figure 4.4: Simulation of isolated incoherent scattering I_{inc} using the scattering function model by Baró et al. [28], for the pencil- and cone-beam collimation incident on a water cylinder sample (similar to Fig. (4.2)).

function parameterized by momentum transfer is complicated by background noise from other instrument components and physical constraints in the positioning of the detectors. The scattering angles for incoherent scattering $I_{\text{inc}}(\text{Q})$, are sampled using the sampling method presented by Baró et al. [28]. In their model, the incoherent scattering function in Eq. (2.18) is determined using analytical approximations that are only dependent on the atomic number, Z. For molecules, rather than using the approximations by Baró et al. for the incoherent scattering functions, one would need to calculate molecular incoherent scattering. However, in this work's approach, molecules and compounds are approximated using an effective atomic number Z_{e}, analogous to what is done for the photon cross section in Eq. (3.13).
For both elastic and incoherent scattering, the azimuthal angle ϕ is uniformly sampled in the interval $(0, 2\pi)$, since the radiation emitted by a conventional X-ray tube is almost fully unpolarized. Finally, when the scattering event is determined to be of incoherent type, the ray's energy parameter is updated to E_{inc} according to the Compton energy shift relation [67]:

$$E_{\text{inc}} = \frac{E}{1 + \frac{E}{511\text{keV}}(1 - \cos(\theta))}. \tag{4.2}$$

4.2 X-ray Scattering Estimation in SCT using McXtrace

In X-ray CT, one of the physical interactions that leads to artifacts in the reconstructions and to a wrong characterization of the material properties is the

scattering noise. In an SCT scan, the total detected signal for each projection, $I(\vec{x'}, E)$, is a function of the pixel position $\vec{x'}$ and energy E, and can be written as:

$$I(\vec{x'}, E) = I_{\mathrm{p}}(\vec{x'}, E) + I_{\mathrm{s}}(\vec{x'}, E) + I_{\mathrm{bkg}}(\vec{x'}, E) \tag{4.3}$$

where $I_{\mathrm{p}}(\vec{x'}, E)$ is the primary signal, which is the effective radiation transmitted through the sample; $I_{\mathrm{s}}(\vec{x'}, E)$ is the scattered signal, composed of the photons being scattered by the sample, for which the scattering angle is not high enough to escape the detector. Fig. (4.5) sketches the different contributions to the total signal in a CT scan.
Lastly, $I_{\mathrm{bkg}}(\vec{x'}, E)$ is the background contribution, composed of the photons being scattered or reflected from the environment and collimating components. In this work, the latter term is not included in the simulation framework as it is highly dependent on the setup of the instrument, and the system can be optimized to minimize its contribution.

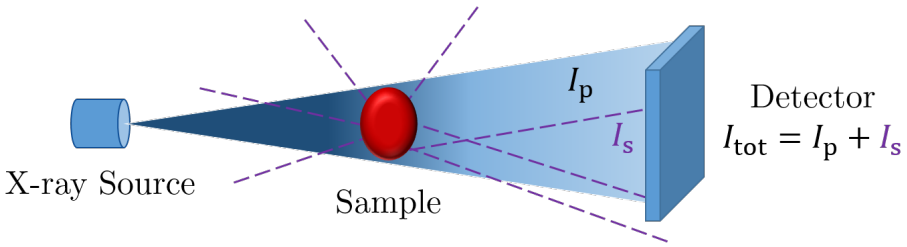

Figure 4.5: Visualization of scattering noise in X-ray CT. The total signal detected I, is a sum of the radiation transmitted through the sample (I_{p}) and the scattered photons that do not escape the detector's field of view (I_{s}).

In SCT, when the signal is converted to LAC using the Lambert-Beer's law, by considering the scattered noise radiation, Eq. (3.4) becomes:

$$R_{E_k}(\vec{x'}) = -log\frac{I^{E_k}(\vec{x'})}{I_0^{E_k}(\vec{x'})} = -log\frac{I_{\mathrm{p}}^{E_k}(\vec{x'}) + I_{\mathrm{s}}^{E_k}(\vec{x'})}{I_0^{E_k}(\vec{x'})}, \quad with \quad k = 1, ..., N_E. \tag{4.4}$$

It follows from this equation that the scattered radiation in SCT leads to a global dampening of the LAC which increases with the amount of scattering, as it shows up as an additive term to the transmission. The impact of the scattering noise in an X-ray CT measurement is quantified with the Scattering to Primary Ratio (SPR), which is the ratio between the scattering and primary signal:

$$SPR = \frac{I_{\mathrm{s}}}{I_{\mathrm{p}}}. \tag{4.5}$$

It follows from Eq. (4.5) that the SPR increases with the attenuation of the sample since this corresponds both to a decrease in the primary signal and an increase of the amount of scattering noise. Thus, the impact of scattering noise increases with the *sample size*, as higher optical paths of X-rays increase the likelihood of scattering

and absorption events. Likewise, the scattering noise depends on the *effective atomic number* and *electron density*, as both absorption and scattering cross sections increase leading to higher I_s and smaller I_p. Another instrumental parameter that affects the SPR is the distance between the sample and the detector, often referred to as *air gap*. The amount of elastic and incoherent scattering noise in X-ray CT scans depends on the air gap. Generally, smaller air gaps correspond to higher magnitude of the scattering noise as the value range of the photon's scattering angle in order to still hit the detector gets higher. The last factor is the *geometry* of the X-ray acquisition, in terms of the size of the solid angle irradiating the sample and the size of the detector. Referring to the standard geometries, a cone-beam collimation with a 2D flat panel detector is exposed to a significantly higher amount of scattering when compared with fan-beam collimation with a 1D-array detector, due to both a higher amount of scattering from the sample and a larger area of detection that allows fewer scattered photons to escape the detector. On the other hand, the latter geometry is relatively less efficient for three-dimensional evaluation of samples as it requires a translation stage either for both the X-ray source and detector array or the sample stage.

For significantly high SPR, uncorrected scattering noise leads to a loss of contrast between different materials, and a wrong material characterization due to the decrease in the calculated LAC. A scattering correction method attempts to restore the primary radiation by suppressing the scattering term in Eq. (4.4). This can be achieved with hardware solutions such as the anti-scatter grid. This component is made up of absorbing plates parallel to the incident beam direction, which block the photons reaching the detector with an incident angle due to a scattering interaction. While the anti-scatter grids suppress the scattered radiation efficiently, they have the drawback of reducing the overall relevant photon flux. Thus, employing anti-scatter grid solutions requires an increased X-ray dose at the sample to compensate and have the ideal photon statistics for optimized contrast to noise ratio (CNR). For this reason, a software implementation that can estimate and correct for the scattering noise from the projections before the reconstruction step of CT is ideally the preferred solution, as it does not introduce a trade-off between scattering suppression and an increased X-ray dose. Various methods for scattering noise estimation and their description can be found in the literature [68], which are based on the use of scattering convolution kernels applied to the transmission term. However, the gold standard method for the scattering noise estimation is using Monte Carlo X-ray tracing simulations as they explicitly model the physical interactions between photons and matter.

In this work, McXtrace and the sample component introduced in the previous section of this chapter are used to estimate the scattering noise from SCT experiments. The speed performance of the scattering estimator is similar to what has been reported in some previous recent works for a sample of similar geometrical size [69]. For the simulation of CT experiments, several projections can be simulated in parallel in multi-core architectures to increase efficiency. To reduce further the computational efforts of the MC simulations, a 3D Gaussian blurring is applied to the spectral scattering

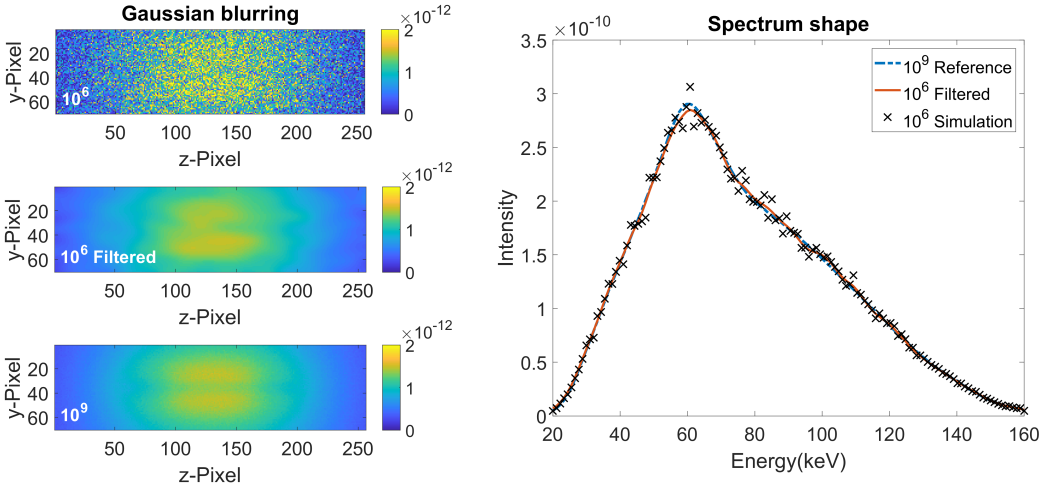

Figure 4.6: Visualization of the effect of the 3D Gaussian blurring in real-space and energy. Left: Starting from the top frame towards the bottom are shown the energy integrated scattering estimate $\tilde{S}_{\mathrm{s}}(\vec{r})$, the result of the filtering and the reference $\tilde{S}_{\mathrm{ref}}(\vec{r})$. Right: The spectral distribution of the respective spatial integrated scattering projections $\tilde{S}_{\mathrm{s}}(\vec{E})$.

projections $\tilde{S}_{\mathrm{s}}(\vec{r}, E)$, inspired by the accelerated simulation method present by Colijn and Beekman [70]. This method relies on the assumption that the scattering intensity has a smooth spatial profile and introduces a trade-off between noise and blur (variance and bias) in the simulation output using fixed bandwidth kernel density estimation with a Gaussian kernel [71]. The method implements a 3-D Gaussian kernel and vectorial form of the blurring width $\vec{\sigma} = (\sigma_z, \sigma_y, \sigma_E)$, composed of the individual blurring widths in the $z-$ and $y-$ axes of the projection image and the energy domain. The optimal choice of $\vec{\sigma}$ depends on the number of rays being sampled and the geometrical parameters of the system. For this work, the blurring widths have been found on a case-by-case basis by the minimization of the combined Root Mean Squared Error, $\mathrm{RMSE}(\sigma_z, \sigma_y, \sigma_E)$ between the simulation output, $\tilde{S}_{\mathrm{s}}(z_i, y_j, E_k)$, and a reference image, $\tilde{S}_{\mathrm{ref}}(\vec{r}, E)$, obtained by reaching simulation convergence:

$$\mathrm{RMSE}(\sigma_z, \sigma_y, \sigma_E) = \sqrt{\sum_{i=1}^{N_z}\sum_{j=1}^{N_y}\sum_{k=1}^{N_E} \frac{(\tilde{S}_{\mathrm{s}}(z_i, y_j, E_k) - \tilde{S}_{\mathrm{ref}}(z_i, y_j, E_k))^2}{N_z N_y N_E}}.$$

Therein, N_z and N_y are the numbers of pixels in the $z-$ and $y-$ direction respectively and N_E is the number of energy channels of the detector. Fig. (4.6) shows an example of this method for scattering estimation acceleration, where $\tilde{S}_{\mathrm{s}}(z_i, y_j, E_k)$, $\tilde{S}_{\mathrm{ref}}(z_i, y_j, E_k)$ and the filtering result for blurring width $\vec{\sigma} = (9, 4.14, 1.71)$ are displayed. For a better visualization of the results, the energy dimension of the scattering projections has been integrated into $\tilde{S}_{\mathrm{s}}(z, y) = \sum_{k=1}^{N_E} \tilde{S}_{\mathrm{s}}(\vec{r}, E_k)$.

4.3 Multiple Source Scattering

Applications that require a continuous and fast throughput, such as airport scanners, it is convenient to have the projections collected by multiple stationary pairs of sources and detectors lying on a mutual plane. In such a scanner, the luggage is driven through these planes with the aid of a conveyor belt. Each of these planes will be denoted in this section as *source-detector plane*. Figs. (4.7 and 4.8) display an example of a scanning

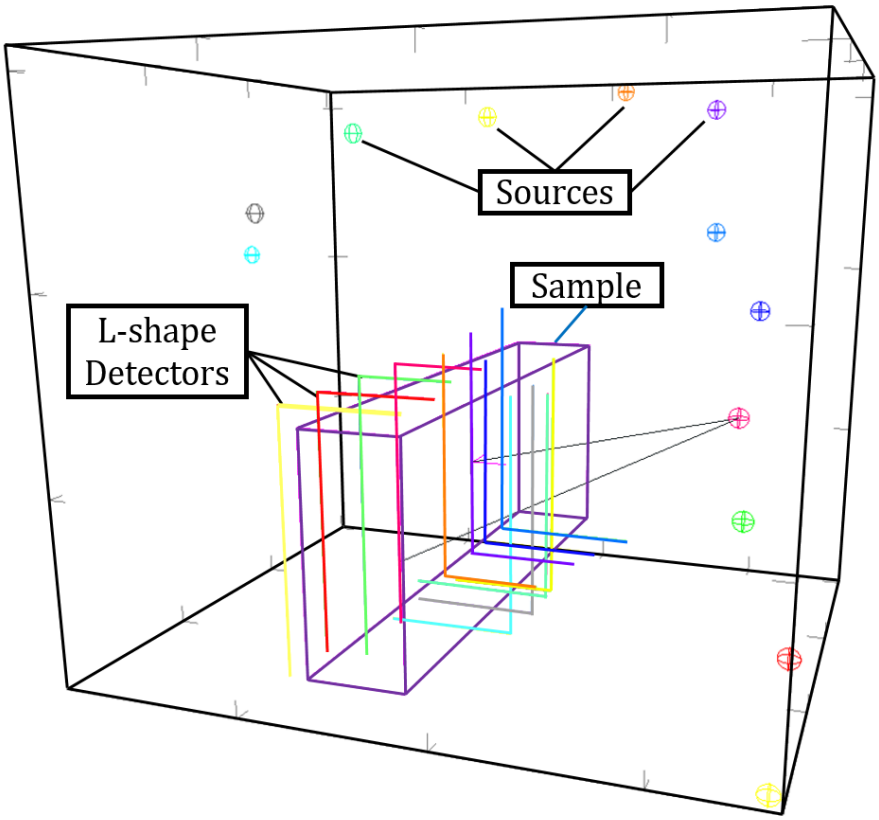

Figure 4.7: McXtrace's tracing GUI visualization of a luggage scanner composed of twelve pairs of L-shaped detectors and sources, and a parallelepiped bounding box containing the luggage phantom. Each plane containing the pair of detector and source include slits, used to collimate the beam produced by the source into a planar fan-beam, that are hidden for a better visualization of the content.

instrument with twelve source-detector planes that has been built up in the McXtrace software package. The main advantage of this type of scanning system is that a CT scan can be realized without the rotation of the sample, which would be a bottleneck in the measurement, as it would require stopping the conveyor belt transporting the objects. With this imaging mode, the individual projections are taken as the sample translates through the source-detector planes. While this system can be advantageous in terms of acquisition time per sample and building costs, it is highly exposed to scattering due to the large size of the samples and the multiple sources being active simultaneously. Each source-detector plane is exposed not only to scattering noise

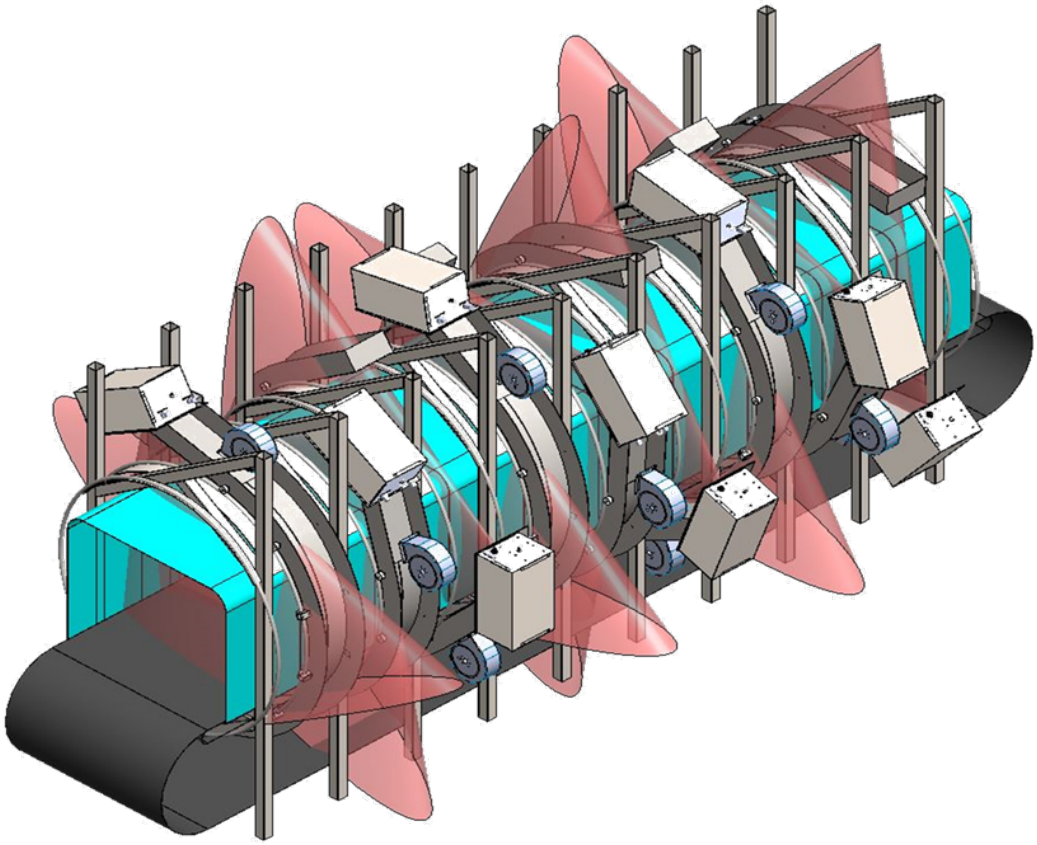

Figure 4.8: 3D-CAD drawing of the scanner built up in the McXtrace simulator in Fig. (4.7). Figure courtesy of Exruptive A/S (`https://www.exruptive.com`).

coming from the source belonging to that plane (*self-scattering*), but also from the sources lying on the other planes (*cross-scattering*). In the following simulation study, we show how the system can be optimized, in terms of scattering suppression, by the aid of the scattering estimation method presented earlier in this chapter.
To simplify the simulations' model, rather than including all the twelve source-detector planes, only two source-detector planes were considered. The sample was composed of a thin rectangular bounding box of the size of 0.5×1.2 m, enclosing a thin aluminum sheet, and four rounded objects composed of organic materials. The source spectrum was sampled using a reference spectrum measurement using the MultiX-ME100 PCD, setting the source to 160 kVp, and using a 3 mm thick aluminum filter. The individual self- and cross- scattering estimates with specific isolation of elastic and single scattering events, and the overall SPR were analyzed as a function of the following instrument parameters:

- Angle between the two sources and the sample center, γ. To find the optimal angular distribution of the sources.
- Distance between the two source-detector planes. To find the closest distance between the source-detector planes, to have a compact scanner while keeping a

low scattering noise signature.

- Aperture size of the source's and the detector's slits. To find the optimal ratio between scattering suppression and the photon flux blocked by the slits.

Fig. (4.9) exhibits these parameters, with both a lateral and a frontal view of the system. For each of these parameters a set of simulations was performed, keeping

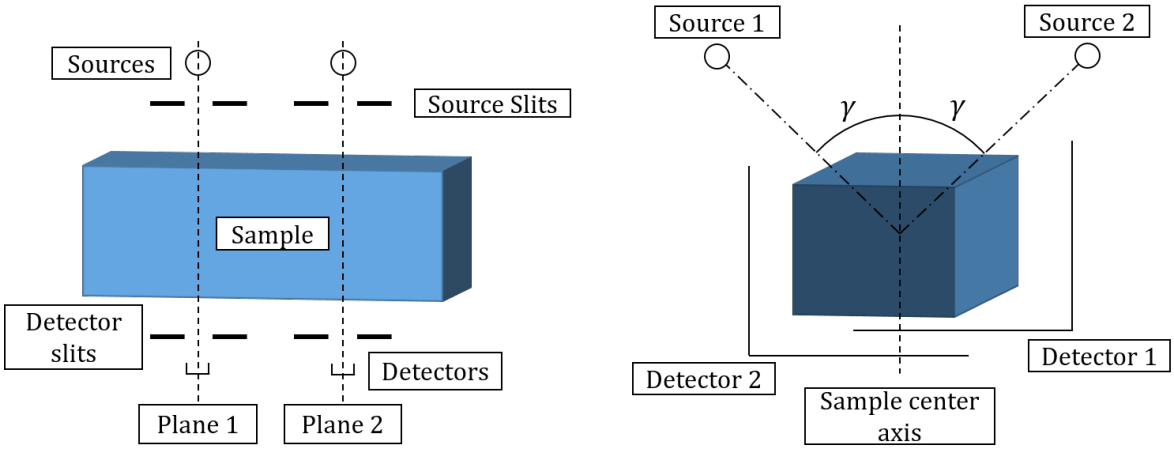

Figure 4.9: The lateral (left) and frontal (right) views of the system used in the simulations study are shown. All the parameters analyzed to optimize the SPR are shown, which are the distance between the two source-detector pair planes, the angle γ between the sources and the vertical axis of the sample and the aperture size of the detector and source slits. The detectors are *L-shaped* to keep the size of the scanner contained while having a larger field of view per source.

the other parameters to a fixed value corresponding to the distance between the two source-detector planes of 80 mm, the angle between the source and sample's vertical axis of 45°, and source and detector slit aperture size of 5 mm and 10 mm respectively. The distance between the planes was scanned for 10 values evenly distributed between 50 mm and 150 mm, the angle was scanned for 10 values evenly distributed between 0 and 90, the detector slit aperture size was scanned for 10 values evenly distributed between 1 mm and 20 mm and lastly, the source slit aperture size was scanned for 7 values evenly distributed between 1 mm and 7 mm. Fig. (4.10) represents the spectra of the scattering noise as the distance between the two source-detector planes, with their individual contribution from elastic and single scattering events. Note that the incoherent and multiple scattering profiles can be obtained as well by subtracting from the total signal the elastic and single scattering noise respectively. As expected, the self-scattering magnitude and the spectrum do not change as the distance between the two planes increases while the intensity of the cross-scattering decreases dramatically. A qualitative analysis of the self-scattering profile indicates that it is approximately evenly split into its elastic and incoherent scattering contribution, and into its single and multiple scattering event contribution. On the other hand, cross-scattering is

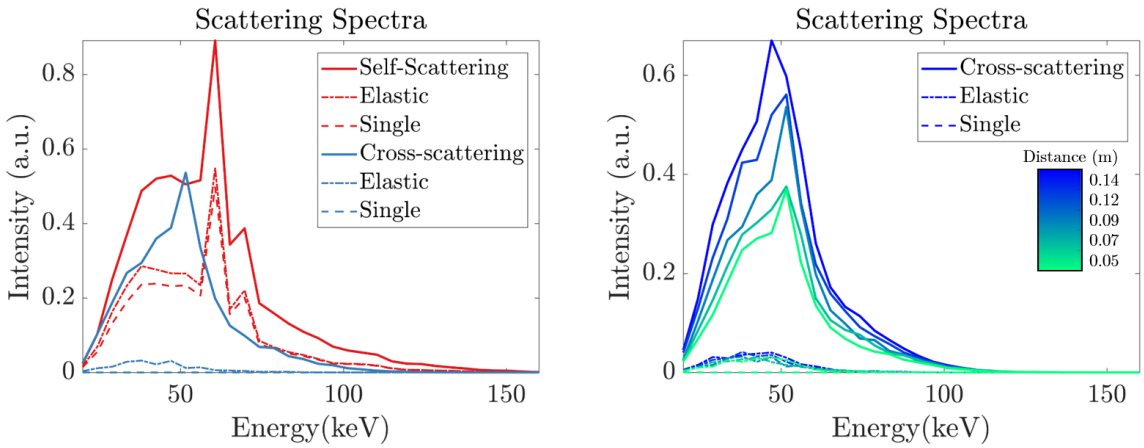

Figure 4.10: Left: Simulated scattering spectra for distance between the two source-detector planes set to 0.09 m, separated into the contribution from elastic (dashed lines) and single scattering events (dash-dotted lines) for the self-scattering (red lines) and the cross- scattering (blue lines). Right. Cross-scattering spectra as function of the distance between the two source-detector planes.

dominated by multiple and incoherent scattering events, justified by the fact that higher scattering angles are required in order to be registered at the detector, which have less likelihood in the scattering models. Moreover, cross-scattering spectra are shifted towards lower energy due to the numerous Compton energy shifts experienced by the photons undergoing incoherent scattering, and the fact that the likelihood of photon interactions with higher scattering angles increase as the energy decreases.
Fig. (4.11) represents the total SPR integrated for all energies as the individual parameters are scanned. It is observed that the SPR decrease proportionally with the distance between the source-detector planes from 9.8% to 7.5% in the value range scanned. Similarly, the SPR increases dramatically from 2.5% to 11.5% as the source slit aperture size is increased, emphasizing the importance of having this component installed in a multiple source scanner. On the other hand, the detector slit does not seem to play a major role in the scattering suppression, as the SPR only increases from 8.3% to 9.4%. Interestingly, two relative minima are found for the SPR at the angle between the source and the sample's vertical axis values of 30° and 80°. Within these two angles the SPR is contained below 9%, while it goes up to 12.6% to 11.3% respectively for angles of 0° and 90°. This study served as recommendation for the system's design in terms of scattering suppression.

4.4 Short Summary

In this chapter, I presented a simulation framework for Monte Carlo simulations of X-ray experiments. The software package was extended to be utilized for spectral X-ray techniques with focus on photoelectric absorption and elastic and incoherent scattering

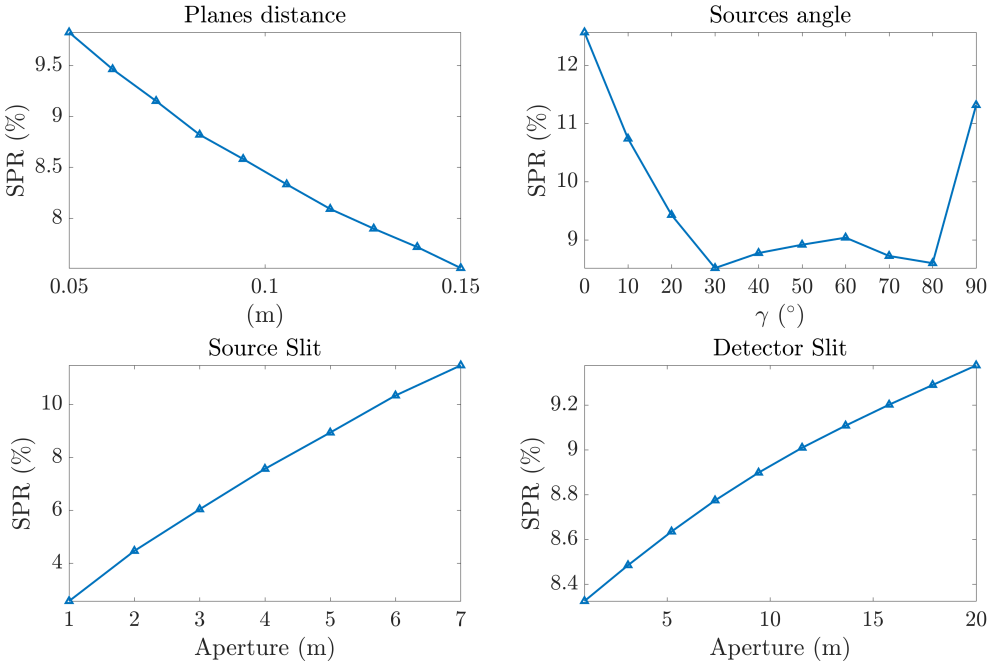

Figure 4.11: The resulting overall scattering to primary ratio (SPR) as a function of each parameter scanned: distance between source-detector planes (top left), angle between sources and sample's vertical axis (top right), source slit (bottom left) and detector slit (bottom right) aperture size.

interactions between photons and a volumetric sample, with given shape and material composition. I presented a method for the estimation of scattering in SCT acquisitions, with an application for a scanner implementing multiple X-ray sources, for which the impact of scattering in the material characterization becomes significant.
In the next chapter, the software package will be used to generate training data for machine learning architectures, with the goal of having near real-time correction methods for SCT, based on physical models of the interactions. The advantage of using a Monte Carlo simulation framework for the forward projection is that they produce results that are closer to real experiments, compared with probabilistic noise models, increasing significantly the quality of the training data.

Deep Learning Enhanced Corrections for Spectral X-ray CT

5

In this chapter, I present a brief overview of the techniques for X-ray CT image processing using tools from the field of Machine Learning and specifically the training of Convolutional Neural Networks (CNN). Specifically, I cover the architecture adopted and used in the processing of both simulated spectral X-ray CT data and experimental data. The primary focus of this chapter is to present novel correction methods for scattering and metal artifacts in SCT as well as the physical models used to generate the training data.

5.1 Related Work

Over the last decades, the development and easier accessibility of graphics cards with extremely high computing power has rapidly grown the interest of many researchers with respect of using tools and ideas from Artificial Intelligence, such as Machine Learning and more specifically Deep Learning. Machine learning can simply be explained as the practice of using algorithms that parse a bulk of input data, named *training data*, and learn from that to make predictions in a desired application. Machine learning techniques can be branched in supervised, unsupervised and reinforcement learning depending on the task. Supervised learning, which is the technique used in this work, is utilized when the training data contains the solution to the problem that is intrinsic to the input data. In unsupervised learning, the goal is to find correlation patterns and similarities in the input data, while in reinforcement learning the data is processed to maximize a given notion of a reward function. These techniques have increased in popularity due to applications such as self-driven cars[72], online fraud detection[73], product recommendation and advertisements[74], virtual personal assistants[75], image recognition[76, 77] etc.
The aforementioned deep learning branch of Machine learning, involves architectures that are inspired by a brain's network of neurons, including several layers of parameters

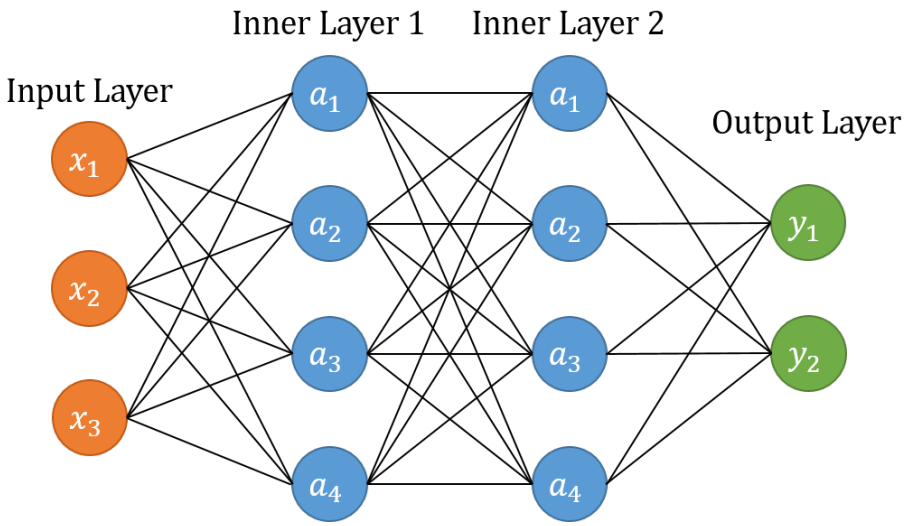

Figure 5.1: Sketch of a simplified neural network in which a pair of input, x_n, and output, y_n, training dataset is used to train the weights β_n of two inner layers. The nodes are connected through mathematical operations that vary depending on the task.

that are recursively updated by loss function optimization. The update of the parameters β can be expressed as:

$$\beta' = \arg\min_{\beta} \mathcal{L}(\beta) + \lambda\Gamma(\beta), \tag{5.1}$$

where $\lambda\Gamma(\beta)$ is the regularization (or penalty) term and $\mathcal{L}$ is the loss function:

$$\mathcal{L}(\beta) = \frac{1}{n}\sum_{i=1}^{n} L(y^i, \mathbf{f}(x(i), \beta)). \tag{5.2}$$

Therein, $\mathbf{f}$ is the activation function, which express how the input values, x^i, are related to the network predicted values, $\tilde{y}^i$. L represents the deviation between the network's prediction and the target y^i, and can be expressed in many ways (e.g. mean squared error, mean squared logarithmic error, mean absolute error etc.).
Fig. (5.1) illustrates a simplified example of a neural network. The convolutional neural network (CNN) technique that is used in this work further develops upon this architecture type, implementing convolutional filters as the tuning parameters. CNN architectures have shown a lot of success recently in fields such as computer vision and image classification and segmentation [78, 79]. In the field of X-ray CT imaging, several studies have shown promising results in the correction of metal artifacts [80], scattering [81, 82] and reconstruction in low-dose regimes [83, 84]. However, as of today, these works are contained only within the conventional energy-integrating CT. When spectral X-ray CT is considered, the architectures and algorithms that have been reported in the literature can be used individually for each energy channel. However, this method would be inefficient and neglects trends and signal coherence that are

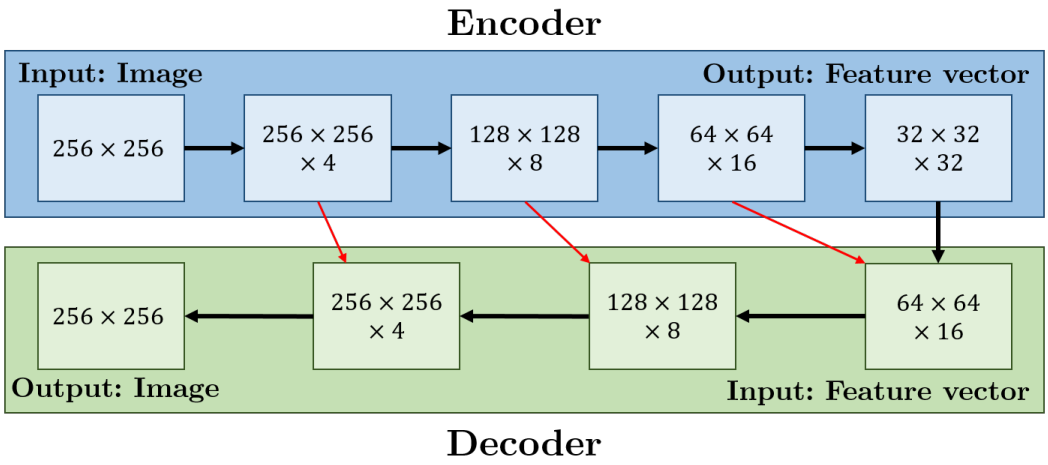

Figure 5.2: Sketch of a simplified encoder-decoder network. In the encoding part, the input image of size $(256 \times 256 \times 1)$ goes through layers of convolutional filters and pooling operations that increase the number of features (the third dimension) while reducing the image size, to avoid overfitting and keeping a reduced architecture memory size. In the decoding part, the feature vector resulting from the encoding is used to reconstruct the image in the initial input size. Skip connections (red arrows) link encoding and decoding nodes with same image size.

embedded in the spectral domain. Thus, it is preferred a spectral neural network architecture that can deal with data from spectral X-ray CT.

The CNN architecture that is adopted in this work builds on an architecture designed for biomedical image segmentation, called *U-net* [85], which is an encoder-decoder network type. Fig. (5.2) illustrates the functioning of this kind of networks. The encoder sub-network takes as input an image and recursively generates a higher dimensional feature vector, which holds the feature information about the input image. The decoder sub-network takes this feature vector and inverts the steps to reconstruct an image in the same space of the input. In the U-net, this procedure is done by applying convolutional filters to each node (increasing the third dimension) and by pooling and upsampling operations that respectively reduce and increase the image size based on its features. Skip-connections are used to connect encoding and decoding nodes with the same size in order to preserve image features at higher resolutions and speed up training convergence. In a supervised learning algorithm, such as the one used in this work, both encoder's input and decoder's output (representing the starting point and the target of the network) are provided for the training of the convolutional filters that connect all the nodes of the architecture. Fig. (5.3) illustrates how the data is provided to the CNN during the learning process. The number of training epochs, which is the times that each input training dataset (sample) is seen by the network, determines the overall time of the learning process. For each epoch, the samples are shuffled and collected into batches with a user-defined size. This determines the number of samples used by the network before the weight parameters are optimized. When the

batch size is set to 1, it is typically referred to as stochastic gradient descent. When the batch size is set equal to the total number of the samples it is referred to as batch gradient descent and lastly, when the batch size is a number in-between these two, the learning algorithm is referred to as mini-batch gradient descent. For this work, the mini-batch gradient descent showed greater performance. Batch normalization [86] can optionally be applied, which consists in shifting and scaling each batch to have man of zero and variance of one and then finding new optimal scale and shift parameters as part of the learning. A slight modification of the U-net was recently presented by

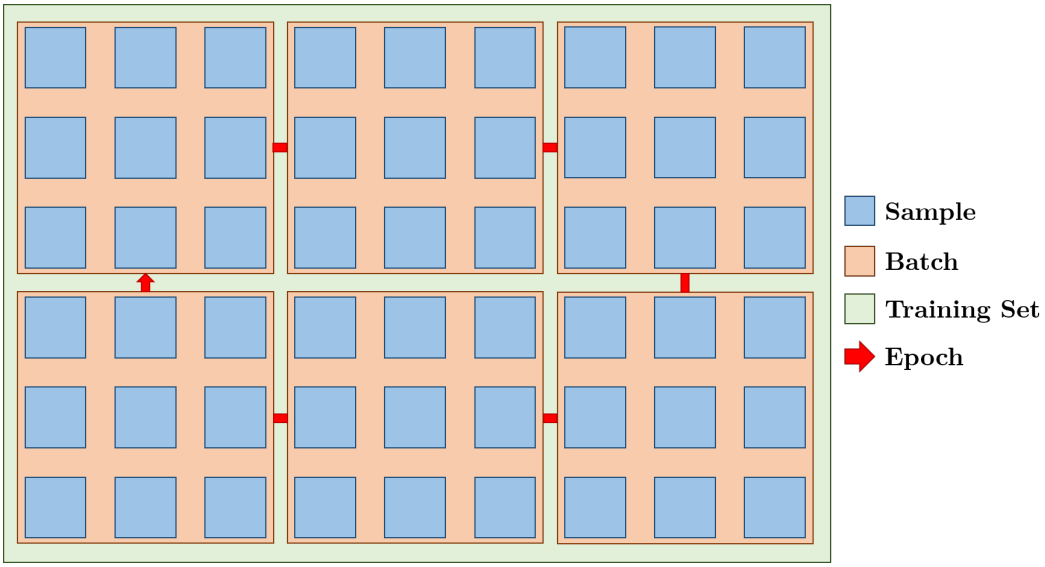

Figure 5.3: Illustration of the concepts of epoch, batch and samples used in the training. The training data samples are grouped in batches with a defined size and an epoch is completed when the network sees all the samples in a training cycle.

Maier et al. [82] for the estimation of scattering in X-ray projections. This inspired a further adaptation to deal with the additional dimension in spectral X-ray imaging given by the energy as described in section 5.2.

5.2 Spectral Convolutional Neural Network Architecture

As this work focuses on spectral X-ray imaging techniques, the U-net architecture requires an adaptation that enables the extraction of the additional information in the energy domain. Moreover, the architecture needs to be optimized to support three-dimensional data. This is a technical and conceptual challenge because the spectral images are represented as large 3D matrices (e.g. 256×256 pixels, 128 energy channels, 32-bit floating-point pixel values), each of which connected to its chain of weight maps for each network filter (i.e. the sub-unit of a layer), which have to be stored at once

in the memory of the graphics card. The architecture adopted in this work for SCT features 3D convolutional layers that can extract information from the spectral domain.

3D U-net

A U-net with 3D convolutional layers is designed to learn the combined features in the energy end spatial domains [87]. Fig. (5.4) illustrates the 3D U-net architecture built using Keras [88], a Python Deep Learning library. In this work, the initial spectral image was with size $(96 \times 96 \times 32)$ although the network can be adjusted to fit different image sizes. The image size chosen for this work was relatively small to allow for a fast check of results with modifications of the network and the training data. It is expected higher resolution of the results when increasing the image sizes. The filter types used by the CNN architecture appearing in the figure are listed and described below:

- Conv. 3D: These are layers of the network consisting of a defined number of 3D convolutional filters with defined size. These filters are the main units (or neurons) of the network as they contain all the coefficients being tuned during the training process. Note that the number of filters at each step defines the fourth dimension of the incoming dataset in Fig. 5.4. The Rectified Linear Units (ReLU) apply the function $f(x) = \max(0, x)$ to all the values in the input volume, which replaces all the negative activations with zeros. ReLU are applied after each convolutional layer to introduce nonlinearity.

- Dropout: During training, some training entities (i.e. pixels) are randomly chosen and ignored, or in other terms *dropped*. This step is introduced to avoid overfitting, as suggested by Srivastava et al. [89].

- MaxPooling: Max pooling refers to the step of applying a maximum filter to (usually) non-overlapping sub regions of the initial representation, and it is necessary to reduce the dimension of the data while preserving the features. For example, a 3D MaxPooling with size $(2 \times 2 \times 2)$ halves the size data in each of the three dimensions.

- UpSampling: Works as opposite of the MaxPooling operation. By default, this is done by padding the matrix cells with zero values. Alternatively, the upsampling can be carried out with interpolation.

- Concatenate: This step concatenates datasets along a chosen dimension. For example, the concatenation in the first layer of the CNN architecture concatenates the data preceding the MaxPooling and the data connected to the 4 filters convolutional layers, both with a size of $(96 \times 96 \times 32 \times 4)$, into a single data with size $(96 \times 96 \times 32 \times 8)$.

Patch-based training, which takes as input smaller patches of the initial images, is avoided because the image distortions and artifacts (which are corrected for) are found

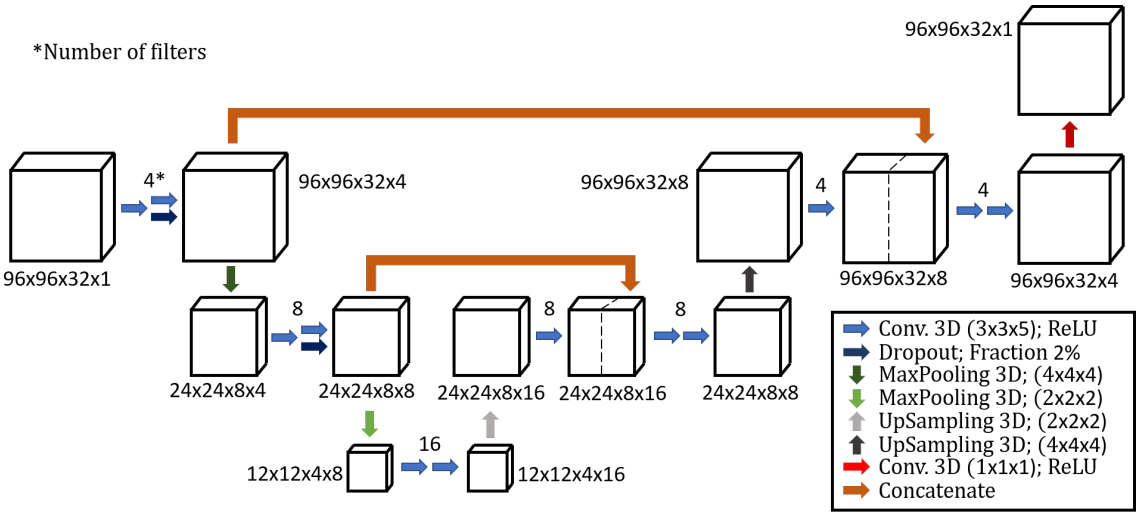

Figure 5.4: Sketch of the 3D U-net architecture, with all the building blocks and filter types. The legend inset in the lower right hand side corner shows the color code for the activation functions.

by correlations across the whole image and thus, represents non-local pixel relations. Additionally, batch normalization is not performed because the network operates with training data that has a globally variable value range. Instead, the image values are converted into either attenuation or absorption via Lambert-Beer's law. The batch size of the network itself was set to 32 to satisfy the existing hardware constraints and the number of parallel works employed for data loading and augmentation. We employed Adam [90] as optimization algorithm, with the initial learning rate set to 1.0×10^{-4} and the decay fixed at 3.0×10^{-7}. The learning rate determines how quickly the network parameters are updated at each step of the gradient descent whereas the decay represents the diminishing of the learning rate after each update. As such, the value of the learning rate changes dynamically through the training. This is preferred to have a constant value, as a too small learning rate requires many updates before reaching convergence whereas a too high learning rate causes drastic updates that lead to divergent behaviors.

The drawback of such 3D networks and their limiting factor for applications to physically measured data with large image size is the exponential computation requirement. Existing hardware limitations govern the maximal depth of a 3D U-net implementation, which prohibits the learning of higher-level logic and global data relations across the image. The hardware limitations can be overcome in trivial scenarios by increased pooling sizes thus, a more aggressive downsampling of the input image data, and a reduction in the number of learning filters. This approach has limitations in practical implementations when a given minimum observation size for imaged features is required and when a minimum number of features is to be extracted for the image correction. It is observed a significant loss of detail in the image correction, due to hardware limitation the 3D network being restricted to be relatively shallow (i.e. very few down/up sampling blocks) and with excessively coarse resolution.

A possible solution to this would be the integration and subsequent combination of alternative architectures, able to preserve resolution and detail with respect to the spatial patterns as well as spectral signal response of the data.

5.3 Training Data Generation

One of the key factors to the success of the CNN correction procedures is the quality of the training data, i.e. how well the samples generalize the problem to be solved. The image set for the hereby-presented architecture consists of a pair of distorted and ground truth spectral images corresponding in a real acquisition to the measured and desired corrected images. Depending on the difficulty, in terms of generalization, of the problems that one aims to solve using deep learning, the quantity and variety of the training data sets must be adjusted. In the literature, as a rule of thumb, a few thousands sets of training data are at the least required to model realistic, non-trivial imaging problems. Such a large number is generally achieved by relatively simple data augmentation steps, in which elementary operations such as Gaussian noise filtering, rotations and translations are applied to the input data. The training data can either be generated starting from real experimental data or simulation data, and in some cases with a combination of both. For most of the applications, experimental training data is hard and slow to generate in large amounts. In the context of security screening the major bottlenecks are in the sample preparation and replacement, as the training data must reflect the variety of different possible samples and their relative arrangement, as commonly found in bags. Moreover, it is often complex to obtain experimentally the ground truth data. For example, for CT scattering correction procedures there are no ways to directly measure the scattering noise simultaneously to the ideal CT acquisition. Likewise, for metal artifact and beam-hardening corrections the ground truths would be the results of iterative correction algorithms, or manual data correction.

In this work, the training data is generated using the Monte Carlo X-ray tracing simulation tools presented in Chapter 4. The main advantage of this method is that the ground truth is intrinsically available as it is part of the input requirements of the simulations. Secondly, the software package can be set such that it uninterruptedly generates new training data with none, or minimal operator intervention required. However, a drawback is that the execution time of a MC X-ray tracing simulation is higher compared with an experimental scan. Moreover, it can prove difficult to generate samples and training data that have the same nature and properties of real data and fit the scope of the correction correctly. When possible, it is generally recommended to use exclusively real training data, as it is the best representation of the problem to be solved. Alternatively, efficient solutions have been found by a first step training with synthesized simulation data, followed by a second training step with experimentally measured data. For the applications presented in this work, it was not possible to obtain experimental ground truth images. As such, the networks were fully trained

with simulation data and the corrections were tested on both real and synthetic data.

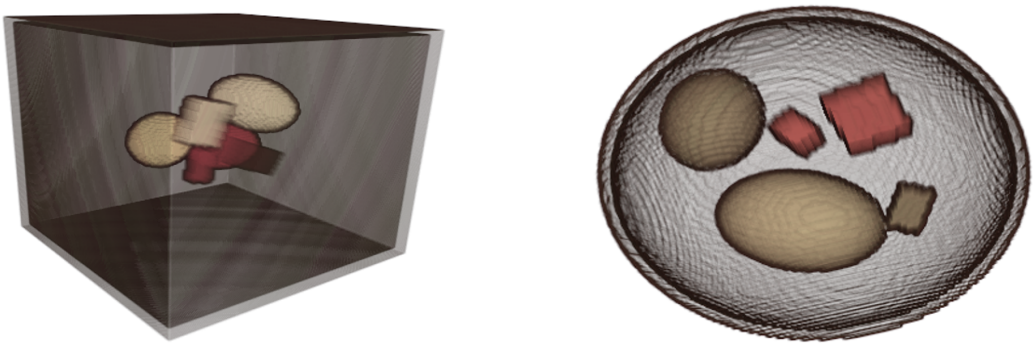

Figure 5.5: Two 3D representations of the random generated phantoms. A cuboid (left) and an ellipsoid (right) envelope, containing objects with randomly chosen shape, size, center coordinates and material composition.

The generation of the samples used in the simulations was performed by a random sample generator, which was created with the aid of a software tool for CT phantoms presented by Kazantsev et al. [91]. Using this tool, artificial samples composed of different materials were generated, using random relatively simple geometrical shapes such as ellipsoids, parallelepipeds and cubes of randomly chosen size and position. The materials used for these samples, are randomly chosen from a list of materials that can be commonly found in luggage (detailed in Table (6.5)). Fig. (5.5) shows a few realizations of random samples.
Once the full set of the training data designed for the CNN learning is generated, the datasets are split and grouped into training data, validation data and test data. The training data consists of the samples that are used by the network to fit the parameters at each epoch. The validation data is excluded from the training of the network and used after the fitting at each epoch to tune hidden-layer parameters, avoid overfitting and evaluate the convergence of the training. Similarly, the test data consists of samples that are excluded from the training and are only used at the end of the overall training of the network to analyze the performance of the trained CNN architecture in solving the assigned problem. The experts in the field typically recommend to randomly divide the dataset into 64% training data, 16% validation data and 20% test data[92].

5.4 CNN Spectral Scattering Corrections

As described in Chapter 4 the gold standard technique for the estimation of the scattering noise in SCT scans is by means of Monte Carlo X-ray tracing simulations. However, this method requires a geometrical model of the sample and its material composition, which is often not possible to define a priori (e.g. baggage, in which the content changes for each sample). A scattering correction using the MC estimation would require the reconstruction algorithm to incorporate the simulation step in an iterative approach. In this method, the sample phantom required for the X-ray tracing

is generated through a preliminary reconstruction, which is subsequently used in the simulation toolkit to estimate the scattering and correct for it. This is followed by a final reconstruction step. The purpose of the correction in most cases does not meet the speed requirement of high throughput for real scanners, since both the MC simulations and the impact on the reconstruction algorithm adds up to the total computational time of the data processing routine. As it will be shown, this gap can be closed with the aid of CNN architectures.

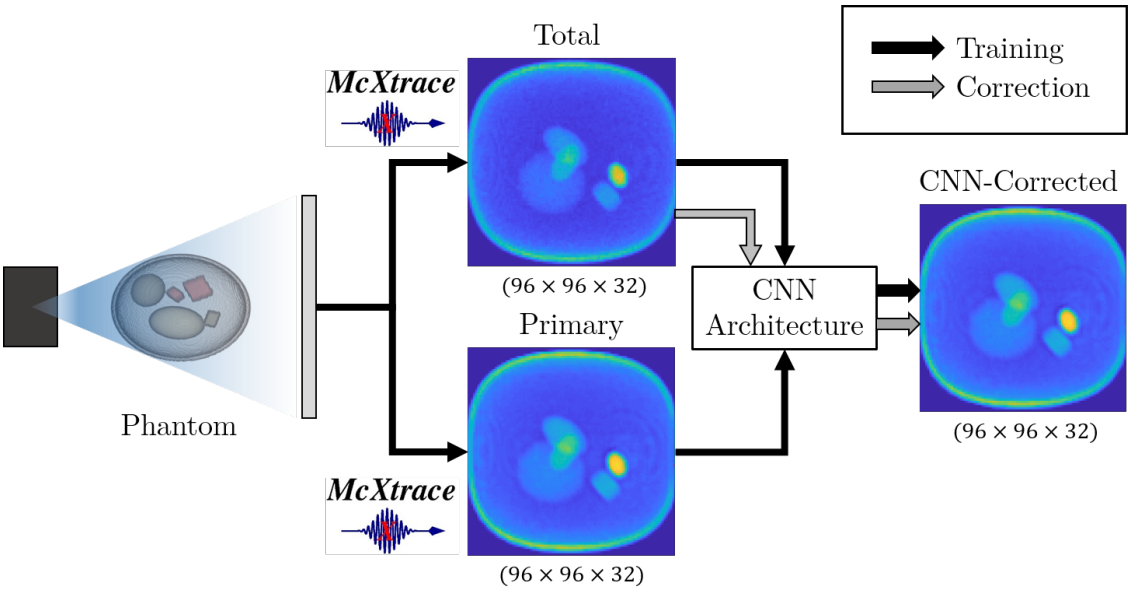

Figure 5.6: A sketch of the scattering correction using CNN. A volumetric phantom is given as input for the McXtrace software package to obtain as output the total and primary spectral projections via X-ray tracing simulations. These are given as input training data in the CNN architecture. Once trained, the CNN architecture only takes as input the total spectral projection and returns as output the primary spectral projection (corrected for scattering).

Fig. (5.6) summarizes in a block diagram the approach presented here. The CNN architecture is trained using synthetic data obtained through MC simulations as a pair of total and primary attenuation. This is done to reproduce the same scattering estimates that one would obtain by using MC X-ray tracing simulations, given attenuation projection data. Referring to Eq. (4.3), this procedure estimates the scattering noise term I_s directly from the total signal I. Since it is desired that the CNN architecture is independent of the photon flux, the training data obtained with MC simulations is normalized into attenuation using Eq. (3.4). The primary attenuation, $l\mu_p(E)$, and total attenuation, $l\mu_t(E)$, are obtained using the following relations:

$$l\mu_t(E) = -log\left(\frac{I_p(E) + I_s(E)}{I_0(E)}\right), \tag{5.3}$$

$$l\mu_p(E) = -log\left(\frac{I_p(E)}{I_0(E)}\right). \tag{5.4}$$

The CNN architecture is trained to directly estimate the primary attenuation, $l\mu_{\mathrm{p}}$, from the total attenuation, $l\mu_{\mathrm{t}}$. The advantage of using this technique for the scattering correction is that a preliminary reconstruction is not required, and it has a near-real-time operational speed once the network is trained.
For a fixed set of sample materials, the spatial and spectral distribution of the scattering signal depends highly on the air gap (i.e. the distance from the sample to the detector) and on the source spectrum, as they govern the likelihood of the different scattering interaction types and of the scattering angle amplitude. Thus, it is preferred for higher accuracy to train and utilize a CNN with fixed air gap and source spectrum that match with the data. For the scattering correction application, since the individual incoherent and elastic scattering cross sections are required for the MC simulations, the photon cross sections were obtained using as input a compound's chemical formula and its respective reference bulk density in the NIST's database. The incoherent and elastic scattering functions used are the ones described in Chapter 4 with the incoherent scattering functions modeled using the effective atomic number respective to each material. Elastic scattering functions of the different materials were taken from ED-XRD measurements when available or approximated into the water's signature when missing, as it was the best guess of the unknown material properties and shown in Chapter 4 to be more accurate than using analytical approximations for gasses.

5.4.1 Experiments

Simulation Training and Test Data

To test the performance of the CNN architecture designed for correction of the scattering noise, 900 training data sets were generated as a pair of total and primary spectral attenuation projections using McXtrace. The distance from the phantom's bounding box center to the flat panel detector was set to 20 mm, whereas the size of the phantom's bounding box was set to 274.4 mm for each side. The source spectrum in the simulations was modeled using a measurement of an X-ray spectrum with the MultiX-ME100 detector and the source set to 150 keV with a 2 mm aluminum filter. The detector's geometry was also set to match the MultiX detector, and the spectral images acquired were resized into ($96\times96\times32$) to fit the CNN. The list of materials used for the random phantoms in the simulations included aluminum, water, nitrobenzene, ethylenediamine, methanol and nitromethane for which an XRD diffraction pattern for the sampling of the elastic scattering was measured. A total of 75 random phantoms were generated, sampling for each 12 spectral projections evenly distributed between 0 and 360 degrees. The training data set was randomly divided into training, validation and test data as suggested previously in this chapter. The CNN was trained for 250 epochs for a total time of approximately 9 hours using a desktop PC equipped with NVIDIA Titan X (Pascal) and GeForce GTX 1080 GPUs, 256 GB RAM and an Intel(R) Xeon(R) E5-2637 v3 CPU. Fig. (5.7) represents the convergence of the loss function and mean squared error for the training and validation as a function of

the epochs. It is observed that they follow the expected behavior for deep learning training.

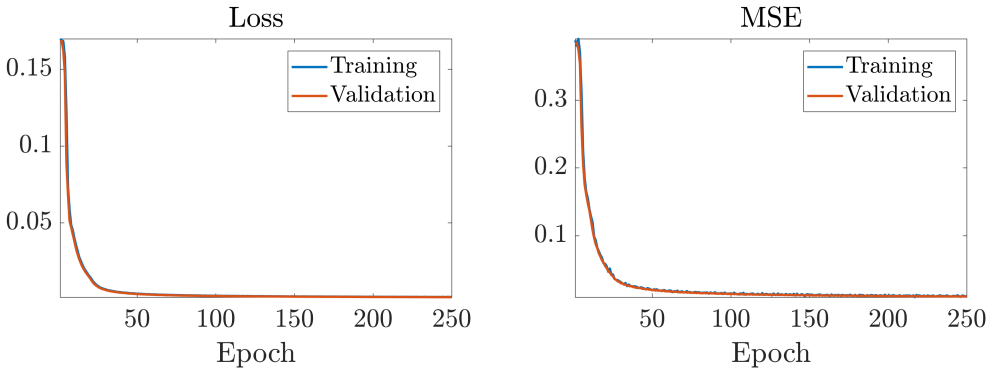

Figure 5.7: Convergence of the loss function and the mean squared error (MSE) for the training and validation data as a function of the training epochs.

Once trained, the CNN architecture was benchmarked with the simulation test datasets. Fig. (5.8) presents the correction results, exemplified for a single dataset and a specific energy channel. A visual comparison of the images highlights the restoration of the contrast between the LAC of different materials, which is confirmed by a look at the line profiles. However, the drawback is the introduction of blurring in the correction images. This can be caused by multiple factors that are under investigation. Firstly, the CNN was trained for a relatively low number of epochs, due to the large dimension of the training data and the size of the CNN architecture. Secondly, as mentioned previously, the CNN architecture is rather shallow, with few layers so that the feature resolution is already degraded severely at the second layer. In connection with that, the size of the image is of a comparably low resolution in order to fit the hardware's memory. It is expected that advances in these aspects would reduce the blurring effect of the CNN correction.
The performance of the correction is quantified in terms of the following metrics for image quality:

- Root Mean Squared Error (RMSE):

$$\mathrm{RMSE} = \sqrt{\sum_{N_{\mathrm{pix}}} \frac{(\mu^{\mathrm{gt}} - \mu^{\mathrm{CNN}})^2}{N_{\mathrm{pix}}}}, \tag{5.5}$$

  Where N_{pix} is the number of pixels in the ground truth (μ^{gt}) and CNN corrected (μ^{CNN}) energy resolved reconstructions.

- Normalized Root Mean Squared Error (NRMSE):

$$\mathrm{NRMSE} = \frac{\sqrt{\sum_{N_{\mathrm{pix}}} \frac{(\mu^{\mathrm{gt}} - \mu^{\mathrm{CNN}})^2}{N_{\mathrm{pix}}}}}{< \mu >}, \tag{5.6}$$

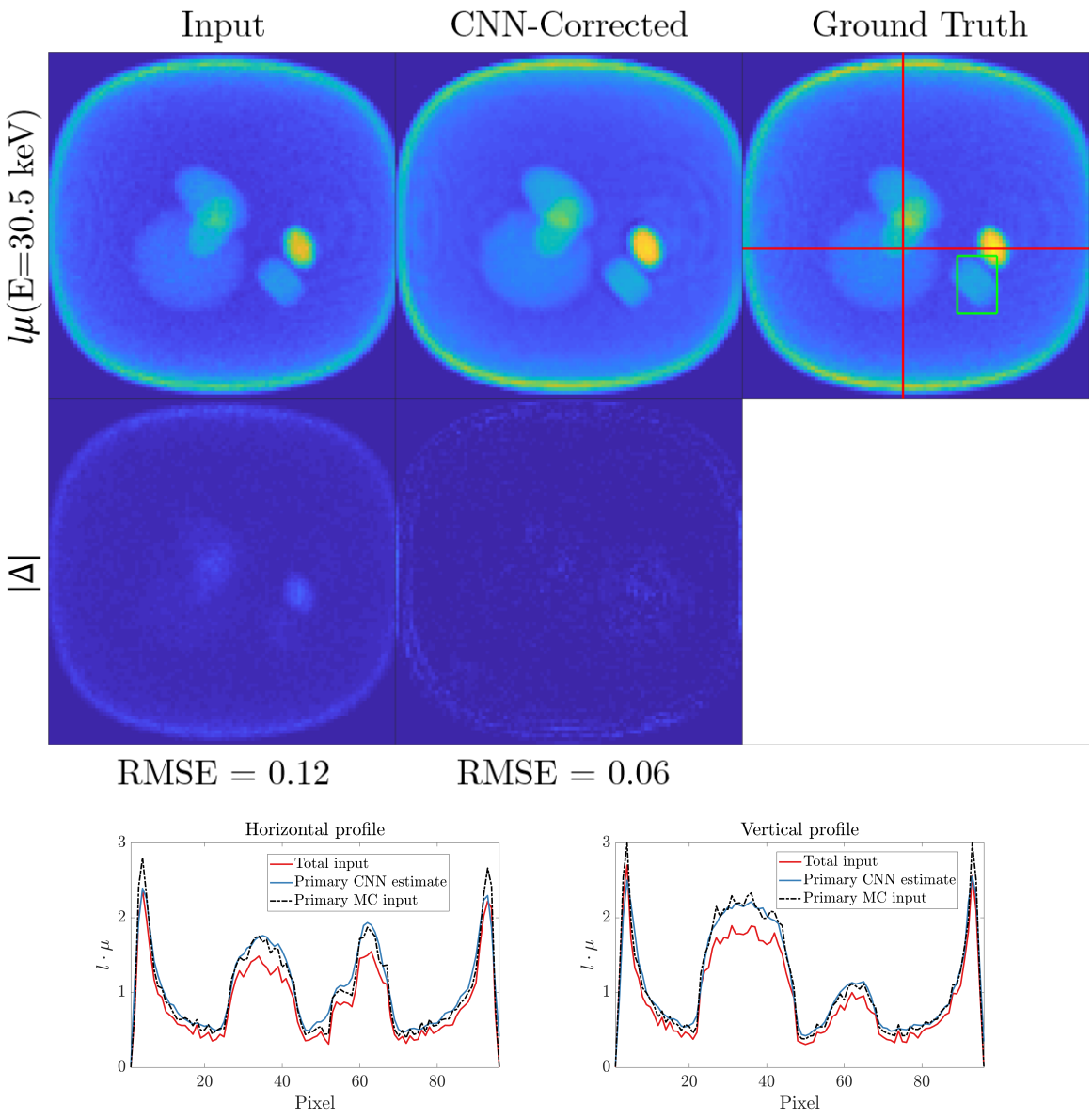

Figure 5.8: Top row: Images at a fixed energy (E=26.3 keV) of the total attenuation ($l\mu_t$), and the primary attenuation corrected using the trained CNN ($l\mu_p^{CNN}$) and estimated using Monte Carlo simulations ($l\mu_p^{MC}$). Note that the MC is the ground truth reference. Bottom row: vertical and horizontal profile of the total and primary attenuation at the marked red lines.

Table (5.1) summarizes the results for the uncorrected input and CNN-corrected, calculated as a mean RMSE and NRMSE among all the test datasets. An improvement is found in both the two indexes when considering the CNN-corrected projections.
The performance of the scattering estimation using CNN in the spectral domain was evaluated as well in terms of the energy-dependent root mean square error (RMSE(E))

Table 5.1: Performance of the CNN MAR correction measured as the RMSE and NRMSE, calculated between the input ground truth and CNN corrected data.

Data	RMSE	NRMSE
Uncorrected	0.11	0.27
CNN-Corrected	0.07	0.18

between the MC and CNN estimates:

$$\mathrm{RMSE(E)} = \sqrt{\sum_{N_{\mathrm{pix}}} \frac{(l\mu_{\mathrm{p}}^{\mathrm{MC}}(E) - l\mu_{\mathrm{p}}^{\mathrm{CNN}}(E))^2}{N_{\mathrm{pix}}}} \tag{5.7}$$

where N_{pix} is the number of pixels in each energy resolved primary attenuation projection $\mu_{\mathrm{p}}(E)$.
Fig. (5.9) shows the correction results in the spectral domain as input, corrected and ground truth attenuation calculated in the region of interest marked in Fig. (5.8). Moreover, it illustrates the RMSE(E) calculated as the mean among all the test datasets. It is observed that in the marked region of interest containing a material the CNN-correction is efficiently restoring the LAC in the full spectrum. On the other hand, the energy-dependent RMSE indicates that towards the high-energy domain the performance of CNN-correction tends to regress. The main reason for this is that the energy-resolved projections cannot be normalized in the same value range as discussed above. Thus, the training is focused on the low-energy spectrum because the LAC values are higher, hence the loss function that the CNN architecture evaluates to fit the parameter is higher. It is expected that training for more epochs will make the correction efficient towards the high-energy domain as well.

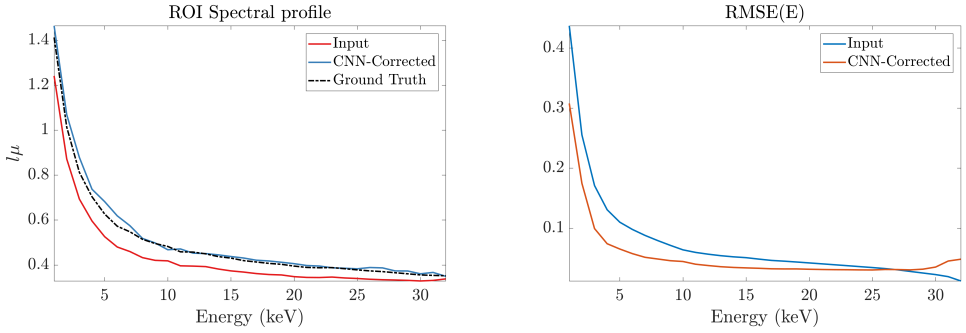

Figure 5.9: Left: Spectrum of the attenuation in the region of interest (green box) marked in Fig. (5.8). Right: Plot of the energy-resolved root mean square error calculated as the mean of RMSE of all test datasets.

Real Test Data

The same CNN architecture that was trained with MC simulation data was then tested to correct real data from an in-house SCT scan experiment (see instrumentation

in section 6.1). The sample was built up with multiple plastic materials (chemical composition and properties are listed later in Table (5.2)). The parameters for the X-ray source, the sample to detector distance and the phantom size were set up to mimic the simulations in the training data generation, in order to have the same spectrum and a comparable amount of scattering noise from the sample. The 360 projections, evenly distributed from 0 to 360 degrees, were acquired with a continuous rotation of the sample, with the detector's radiation integration time set to 0.1 s per projection. Fig. (5.10) features a 3D volume reconstruction as well as slice images including all the nine plastic materials composing the sample. The SCT scan was

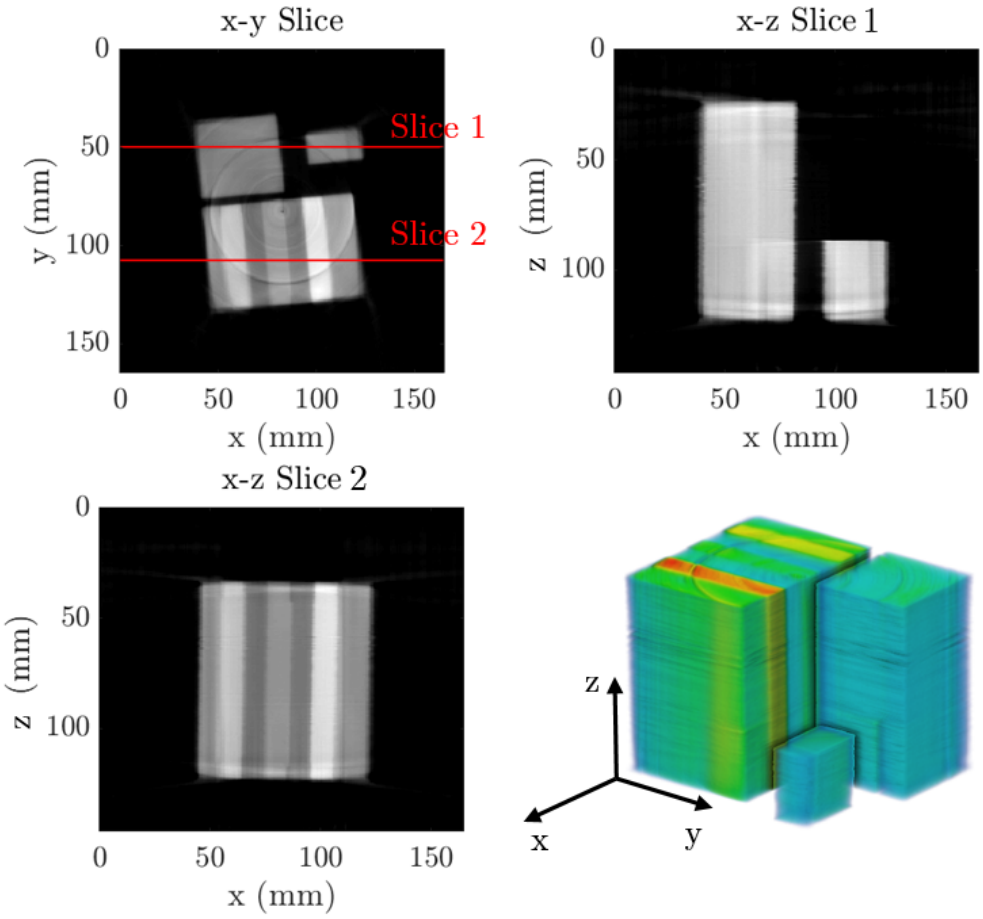

Figure 5.10: Visualization of the 3D cone-beam reconstruction of the plastics sample (bottom right frame). The top left figure shows a slice along the vertical axis containing all the plastic materials. Therein, the two red lines mark the vertical slices intersecting PMMA and PEEK (top right frame) and the other seven materials (bottom left frame) respectively. The ring artifacts visible in the images are due to the drops in attenuation at the interface between different modules of the detector array and could only be partially corrected.

performed with two different types of source collimation; one to have a scattering noise affected measurement and one to have a minimal amount of scattering. Firstly, an SCT scan with cone-beam collimation of the source, to have a significant amount

of scattering from the sample due to the large volume being irradiated. Secondly, the source was collimated into a fan-beam geometry, which is known to suppress significantly the scattering noise. Both the SCT scans were reconstructed and the individual materials LAC were extracted using the procedure described in chapter 4. The cone-beam corrected, and fan-beam LACs were then used for the evaluation of the CNN correction's accuracy. Fig. (5.11) shows the cone-beam raw and corrected

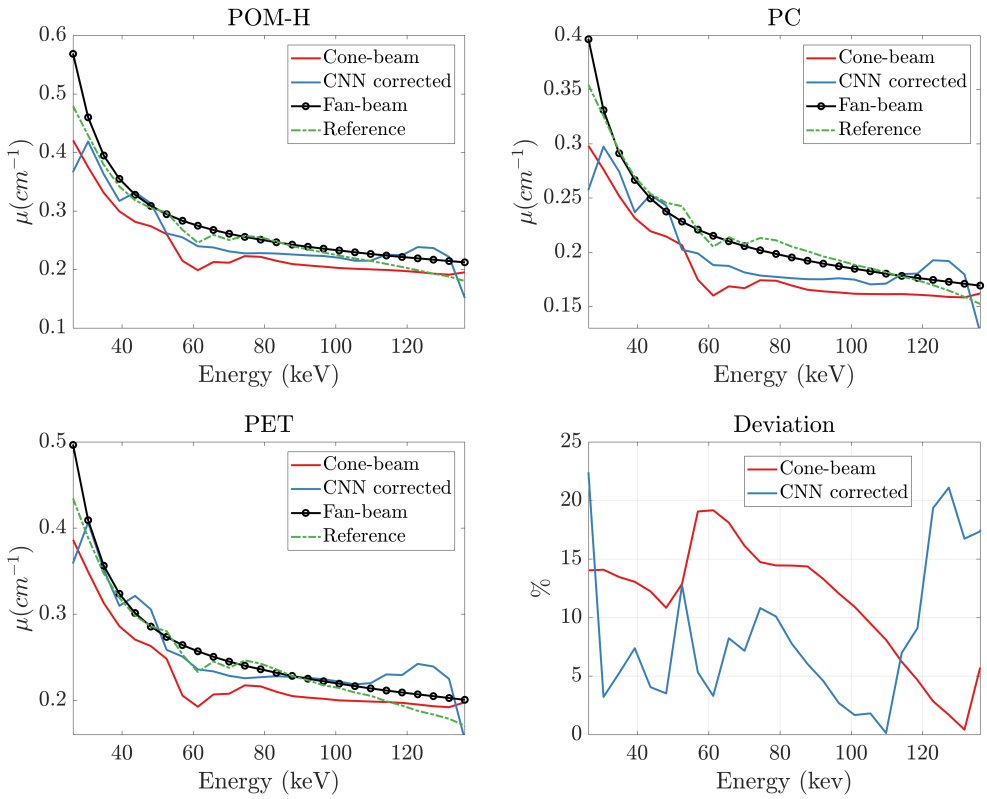

Figure 5.11: Plots of the LAC calculated for the POM-H, PC and PET materials for the cone-beam measurement, the fan-beam measurement, the CNN correction and a theoretical curve using reference values of Z_e and ρ_e. In the bottom right frame is plotted the mean percent deviation of all material between the cone-beam and the CNN-corrected LAC with respect to the fan-beam.

LACs, as well as the fan-beam and reference calculated using the expected material properties of Z_e and ρ_e. The figure confirms that the fan-beam collimation reduces the effect of the scattering noise in the calculation of the LAC. This can be observed by comparing the results of measurements with fan- and cone-beam collimation with the LAC calculated using reference tabulated values for effective atomic number and electron density. Regarding the CNN-correction, it is observed that the scattering correction pushes the LAC towards the fan-beam and reference curves, but not to a complete restoration. This can be attributed to an underestimation of the incoherent scattering in the MC simulations, arising from the interactions between X-rays and

the sample or other parts of the instrument. Another reason might be attributed to the CNN training. The convolutional filters in the CNN architecture are trained by minimizing the loss function between the total absorption projection and the scattering noise. Thus, low-energy channels which have greater values of absorption and thus, scattering have a greater weight in the training. Solutions for this effect are currently under investigation, such as an energy-dependent weight function applied to the loss function, which would ideally balance the importance for all the individual energy channels. Another factor that might lead to this mismatch is that the materials used to generate the training data have a higher attenuation range, while the materials included in the real sample are restricted to the organic low attenuating compounds. In the literature, the current corrections for X-ray CT using CNN are developed for dedicated applications such as medical or industrial scanners, in which the properties and shape of the sample do not vary much. The challenge of this correction method is that it attempts to correct for any possible material and shape that might be contained in luggage. Thus, there is a requirement for a large amount of training data to generalize for every possible material and size within a certain interval. The performance of the correction is expected to increase with a higher number and more diverse variety of training data.

Table 5.2: All the plastic materials composing the sample and their respective expected and estimated physical properties. †While most of materials are polymers, the chemical formula is reported for the composing monomer. *The mean values were calculated from the absolute values of each column.

Material	**Formula**†	$\mathbf{\Delta Z_e^{cone}}$ (%)	$\mathbf{\Delta Z_e^{CNN}}$ (%)	$\mathbf{\Delta \rho_e^{cone}}$ (%)	$\mathbf{\Delta \rho_e^{CNN}}$ (%)
*PP	C_3H_6	5.8	6.1	-11.5	-2.6
PEEK	$C_{19}H_{12}O_3$	2.0	2.5	-10.6	1.5
PC	$C_{14}O_3H_8$	-3.0	-3.0	-13.9	-6.8
PMMA	$C_5O_2H_8$	-4.3	-2.0	-14.6	-7.6
PET	$C_{10}H_8O_4$	-6.8	-3.7	-6.8	3.6
POM-C	CH_2O	-4.7	-4.5	-11.5	-2.4
POM-H	CH_2O	-5.3	-3.2	-10.0	-1.8
PVDF	$C_2H_2F_2$	-9.8	-9.2	-10.7	-1.4
PTFE	C_2F_4	-9.2	-9.2	-11.1	-0.9
Mean* $\lvert\Delta(Z_e)\rvert, \lvert\Delta(\rho_e)\rvert$	-	5.7	4.8	11.2	3.2

Nonetheless, it is found that the correction yields to a better estimate of the material properties. Using the SRZE method presented in chapter 4, the effective atomic number, Z_e, and electron density, ρ_e, were estimated from the LACs corresponding to cone-beam, CNN-corrected and fan-beam measurements. Table (5.1) reports the relative deviation, $\Delta(\%)$, between the cone-beam and CNN-corrected estimates and the

reference fan-beam estimates. It is found that the electron density, which is the main feature affected by scattering noise, is significantly restored using the CNN-correction.

5.5 CNN Spectral MAR Corrections

A notorious issue in the field of X-ray CT is Metal Artifact Removal (MAR). Metal artifacts in CT images are due to photon starvation caused by highly attenuating materials such as metals and are in most cases appearing as streaking artifacts in the reconstruction images. In the images, these streaks typically originate from a metallic object and extend further overlapping with other materials in the sample. The metal artifacts not only degrade the graphic quality of the reconstructions, but also additionally worsen the performance of segmentation and thus, the classification and characterization of materials. For these reasons, MAR is key to enhanced performance of a CT scanner both in medical and NDT fields.
The goal of a MAR algorithm is to improve the quality of the reconstructions by removing the streaks, while preserving the real features. This can be done in a pre-reconstruction approach by a correction in the sinogram domain, which is typically done by adaptive interpolation of the photon starved detector pixels in the projections. Alternatively, MAR can be done in a post-reconstruction step, by directly attempting to remove the streaks and restoring the materials' LAC values in the reconstructions. Fig. (5.12) summarizes in a block diagram the approach presented here. The overarching goal is to remove the streaking artifacts in a post-reconstruction step with the aid of CNNs from energy-resolved reconstruction obtained with spectral X-ray CT. In SCT, since the photon starvation depends on a material's LAC property it is an energy dependent phenomenon and, thus, there may be samples for which the artifacts are appearing in the low-energy reconstruction but not in the high-energy ones. This is of great value as the information regarding geometrical features, shapes and material physical properties can be extracted from the artifact-free high-energy domain and used to restore the reconstruction in the artifact-affected low-energy domain.
The generation of the training data was performed similarly to the previous case, for the scattering correction. In this case, the scattering noise is ignored and incorporated in the photon cross section attenuation to save computational time in the simulations. The materials' LACs were obtained with a combination of in-house spectral LAC measurements of materials with known density, and entries from NIST's database. In addition, each phantom includes multiple metallic objects of either copper, gold or tungsten, to force the appearance of metal artifacts in the reconstructions. Lastly, hollow object shapes were also included in the framework to simulate hollow containers such as bottles.
An issue faced when including highly attenuating materials in the training data is due to the logarithmic nature of the LAC of materials. Since the metals have a value range that is significantly superior to organic compounds, there is a biased training of the CNN architecture. That is because the training relies on the tuning of convolutional

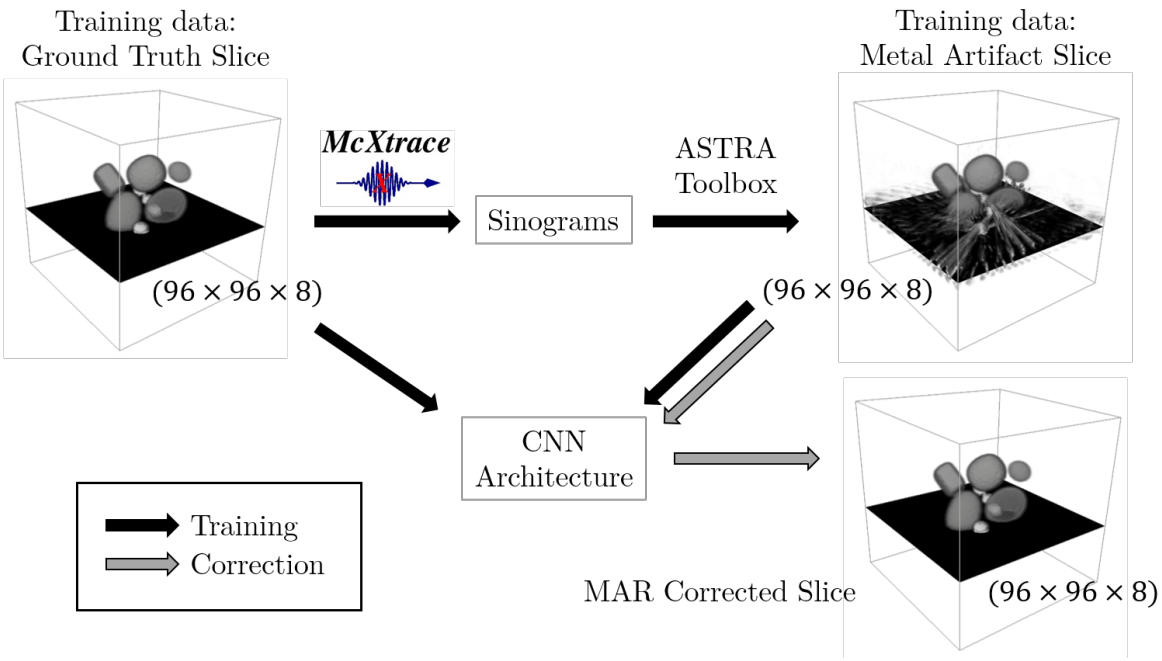

Figure 5.12: A sketch of the MAR correction using CNN. The 3D volume of the ground truth phantom of the materials is given as input of the McXtrace software package to obtain physically modeled spectral sinograms via X-ray tracing simulations. These are reconstructed into metal artifact affected volume reconstruction, using the ASTRA [93] toolbox. Each pair of the orthogonal spectral slices of the ground truth and reconstructed volumes are given as input training data in the CNN architecture. Once trained, the CNN architecture corrects the metal-artifact affected spectral slices. The metal objects are visible as the lighter gray items.

filters by minimizing a loss function, which is the deviation between the two input images. Due to photon statistic noise, the difference between the simulated and ground truth image is significantly higher for the metal, when compared with organic compounds. This results in a disappearing of the low attenuating materials from the images, as they are seen by the architecture as void noise, hence replaced with zero values. On the other hand, in most cases the overarching goal of the correction is not a mere streaking removal but a restoration of the image features of the low attenuating materials to efficiently perform further analysis routines. The solution proposed and used in this work is a high attenuation thresholding, which consists in substituting LAC values that are greater than silicon's LAC with the silicon corresponding values. This is justified by the fact that in most application the metals are not the objective of the data analysis but an intrusive material that leads to artifacts. The CNN architectures are optimized to work with data normalized in the value range $[0, 1]$ thus, the data undergoes an additional normalization step in which each individual energy dependent projection is remapped to the value range $[\min, \max] \rightarrow [0, 1]$ and it was observed to greatly improve the performance of the correction and the speed of the convergence. Note that for the scattering problem this step could not be done because the input

uncorrected and ground truth projection were on different scales due to the scattering noise, whereas in this case the features to preserve are in the same scale,
A second concern in the data generation process is that the geometrical shapes have great impact on the performance of the correction itself. Depending on the application of the CT itself, this imposes different conditions on the type of training data. For security screening scanners, ideally the CNN should have enough training data to learn all the possible geometries. Of course, this is limited by the storage and computational time to generate enough training data. In this work, the sample variation is restricted to relatively simple random geometries and few entries for the number of projections preceding the reconstruction. In an application focusing on luggage screening, objects could be scanned separately (including material characterization and segmentation) to provide the simulation inputs with realistic shapes for objects made of different materials.
A last consideration is that in the related published research, the aim of MAR is to restore the image quality by removing streaks and contrast between different materials. In this work, since the goal is the quantitative material characterization into physical properties, the focus is also on the preservation and restoration of the effective LAC values. Incorrect physical models for the generation of the training data may introduce offsets in the materials' LAC succeeding the MAR correction.

5.5.1 Experiments

Simulation Data

For the benchmarking of the spectral MAR correction using CNN, the training data was generated using McXtrace with the following procedure. The number of individual unique sample phantoms was set to 10, and a full spectral CT scan of each was done simulating randomly 120, 90, 72, 60 or 52 projections with a cone-beam geometry collimation of the source and a 256×256 flat panel 2D spectral detector with 8 energy channels, for a detection area of 204.8 mm $\times$ 204.8 mm. The source to sample and detector distances were set respectively to 816.6 mm and 1141.9 mm. This led to a relatively high sample to detector distance, in order to minimize the scattering noise from the sample for the real experiment planned as a successive step. Each energy-resolved sinogram was reconstructed into a 3D volume using the ASTRA toolbox [93] and each training dataset was extracted as a pair of orthogonal slices of input ground truth and reconstructed 3D volumes of the sample (see Fig. (5.12)). This resulted in a total of 925 training datasets split into training, validation and test as described above. Note that not every slice has visible metal artifacts due to the random composition of the phantom. Each slice pair was resized into the dimension ($96 \times 96 \times 8$) to fit the CNN architecture and followed the normalization procedure described above. The CNN architecture did not require modifications as it was compatible with the one previously presented for the scattering correction. However, one could have replaced the 3D MaxPooling and UpSampling with size ($4 \times 4 \times 4$) with an additional layer

with two 3D MaxPooling and UpSampling with size ($2 \times 2 \times 2$), increasing the amounts of features that the CNN learns. The training was carried out for 50 and 250 epochs, for a total time of approximately 2 and 8 hours respectively, to analyze the training performance against the training. Once trained each metal artifact affected slice is corrected in approximately 15 ms, satisfying the near real-time requirement of industrial applications.

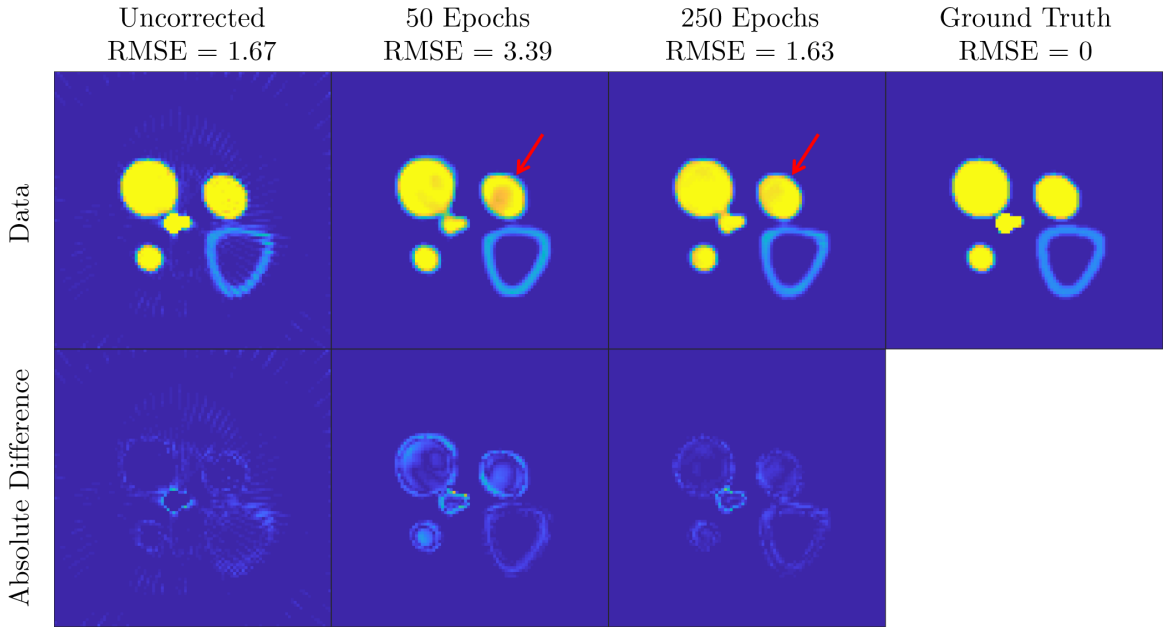

Figure 5.13: MAR correction analysis of a simulation test training data for different amounts of training epochs. The top row features the images for uncorrected data, and corrected data training the network for 50 and 250 epochs and the ground truth. The bottom row features the absolute difference between the top adjacent images and the ground truth. The red arrow indicates the cupping artifact induced by the CNN correction when the network is trained for 50 epochs. This effect disappears when the network is trained for 250 epochs.

To the indexes presented in the previous section for the assessment of the correction performance, we add for this problem one that emphasizes the image features:

- Mean Structural Similarity (MSSIM). Structural Similarity (SSIM) is a method for measuring the similarity between two images presented by Wang et al. [94]. This method returns an image with the same size as the input images, with values ranging from -1 to 1 taking maximum value when the two images are identical. In the MSSIM a single index value is calculated as the mean value over the SSIM image.

These indexes of image quality are calculated for each uncorrected and corrected (both training the CNN architecture for 50 and 250 epochs) test datasets and reported in Table 5.3. The values reported in the table are calculated as the mean between all test datasets The MSSIM increases significantly for both the 50 and 250 epochs trained

Table 5.3: Performance of the CNN MAR correction measured as the RMSE, NRMSE and MSSIM, calculated between the input ground truth and CNN corrected data. The results are reported for the uncorrected data and corrected data training the CNN for 50 and 250 epochs.

Data	RMSE	NRMSE	MSSIM
Uncorrected	0.0035	0.12	0.926
50 epochs	0.0031	0.13	0.978
250 epochs	0.0020	0.09	0.990

CNN corrections, meaning that the streaks are successfully corrected in most cases. The worse NRMSE can be caused by either lack of training data diversity or most probably due to CNN training that has not reached convergence. Fig. (5.13) features a comparison of two images after training for 50 and 250 epochs. It is observed that for a limited training, the CNN struggles to define whether an object should be full or hollow as modeled in the input data. This results in a cupping effect that is seen at 50 training epochs but disappears at 250 training epochs.
Figs. (5.14, 5.15 and 5.16) represent a few examples of the results of the MAR corrections. In these figures, the top image is consisting of metal artifact affected (Input), corrected (CNN Correction) and reference input data (Ground Truth) slice images at four of the eight energy channels, corresponding to 29.4 keV, 62.7 keV, 98.0 keV and 132.5 keV. Note that the color map in the images is identical for each energy channel (column). The red line in the ground truth frame marks the line along which the attenuation profiles are displayed in the plots at the bottom.
The first example (Fig. (5.14)) shows a slice where moderate metal artifacts are visible in the first energy channel input images and in the vertical line profiles as an increase of the LAC with respect to the ground truth. It is observed by looking at the line profiles, that the correction efficiently restores the LAC values and smoothens the noise oscillations caused by either the presence of a metal in neighboring slices or the limited number of projections. The drawback is the introduction of moderate cupping, which could be potentially solved by training the network for more epochs as discussed above. The second example (Fig. (5.15)) displays in the first energy channel a strong streaking metal artifact, which overlaps with a neighboring object provoking a partial disappearance of its geometrical features. The artifacts decrease in intensity as the energy increases, to a point where the shapes can be clearly visible. This case demonstrates the advantage of spectral X-ray CT over conventional techniques as the CNN architecture utilizes the information on the material LAC and shape in the higher energy channel to restore the image quality in the metal artifact affected low-energy channels. However, in cases like the third example (Fig. (5.16)), where the LAC values of the compounds affected by the streaks are lower (compare the LAC in the vertical axes in Figs.(5.15 and 5.15), the streaks extend to higher energy channels, challenging the performance of the MAR correction. Nevertheless, the correction still succeeds in cleaning the image from the streaks, leading to an enhanced image quality.

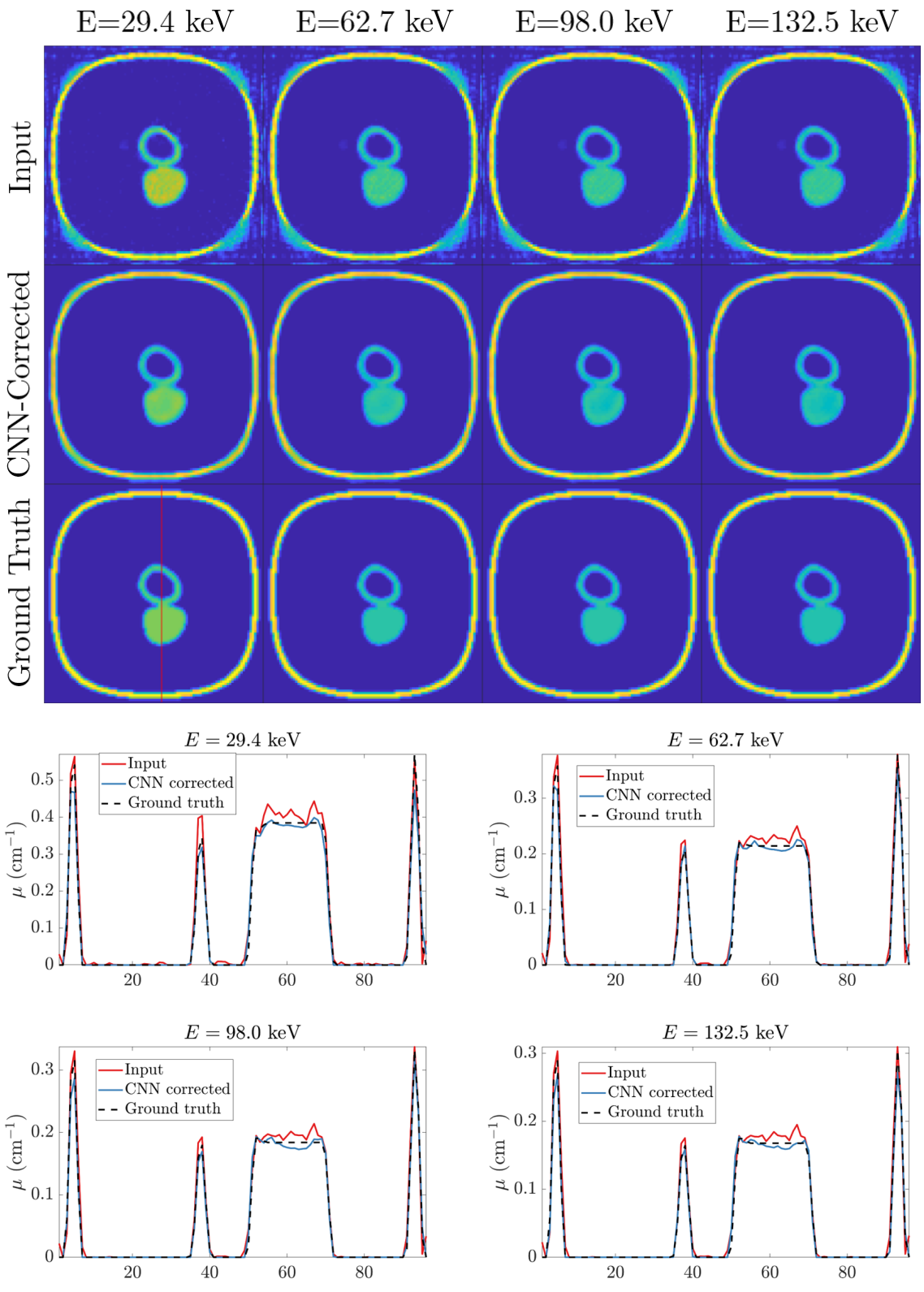

Figure 5.14: Simulation test data. **Example 1.** Orthogonal slice of the reconstructed volume for the input metal artifact affected (first row), MAR corrected (second row) and ground truth (third row) at different energy channels. Note that each column, corresponding to a fixed energy channel, have identical color map. The bottom frame shows respective line profiles at different energies along the marked red line.

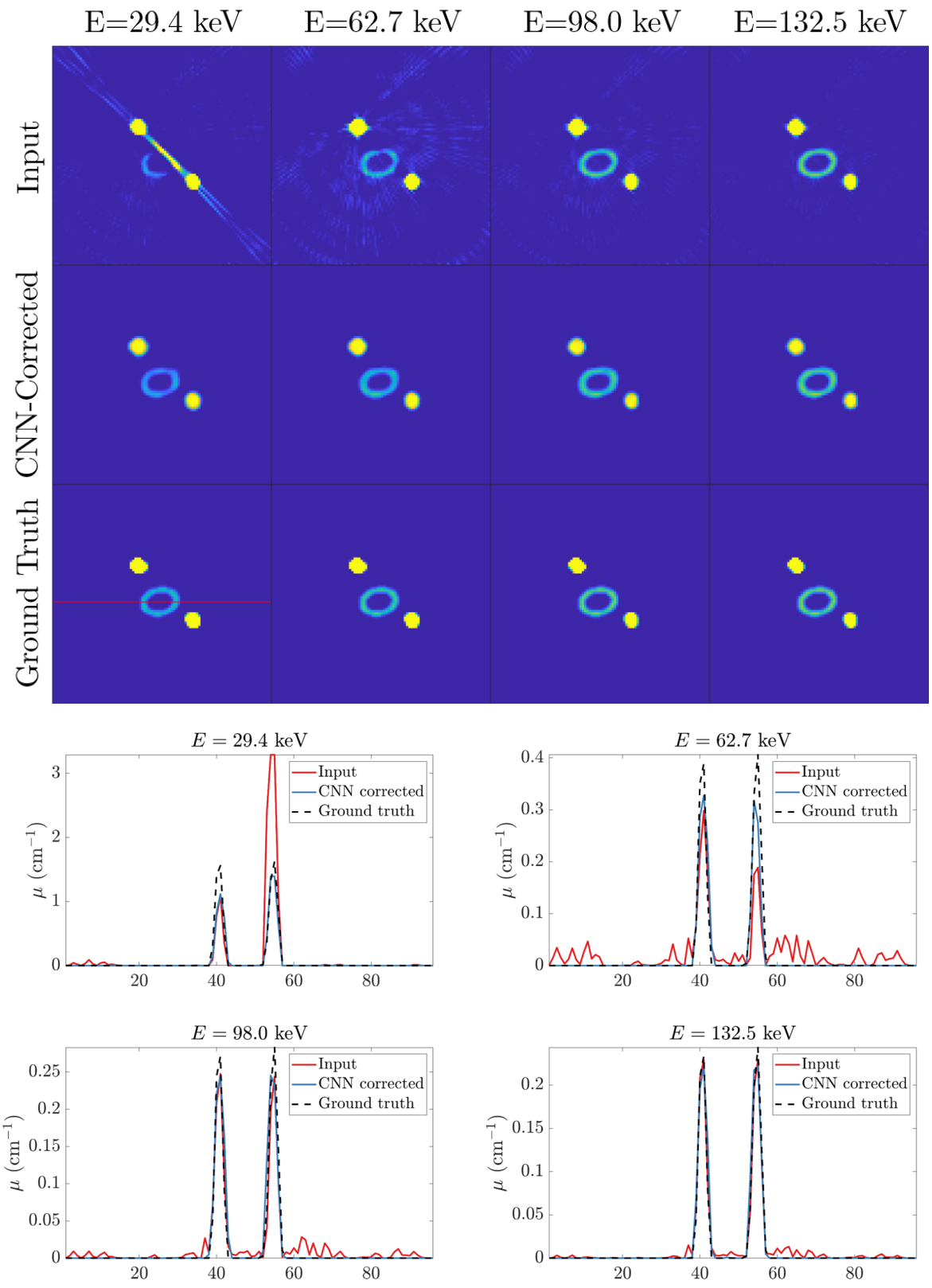

Figure 5.15: Simulation test data. **Example 2.** The object feature obscured by the metal-provoked streak artifact is restored by the CNN correction. (See Fig. (5.14) for visual notes.)

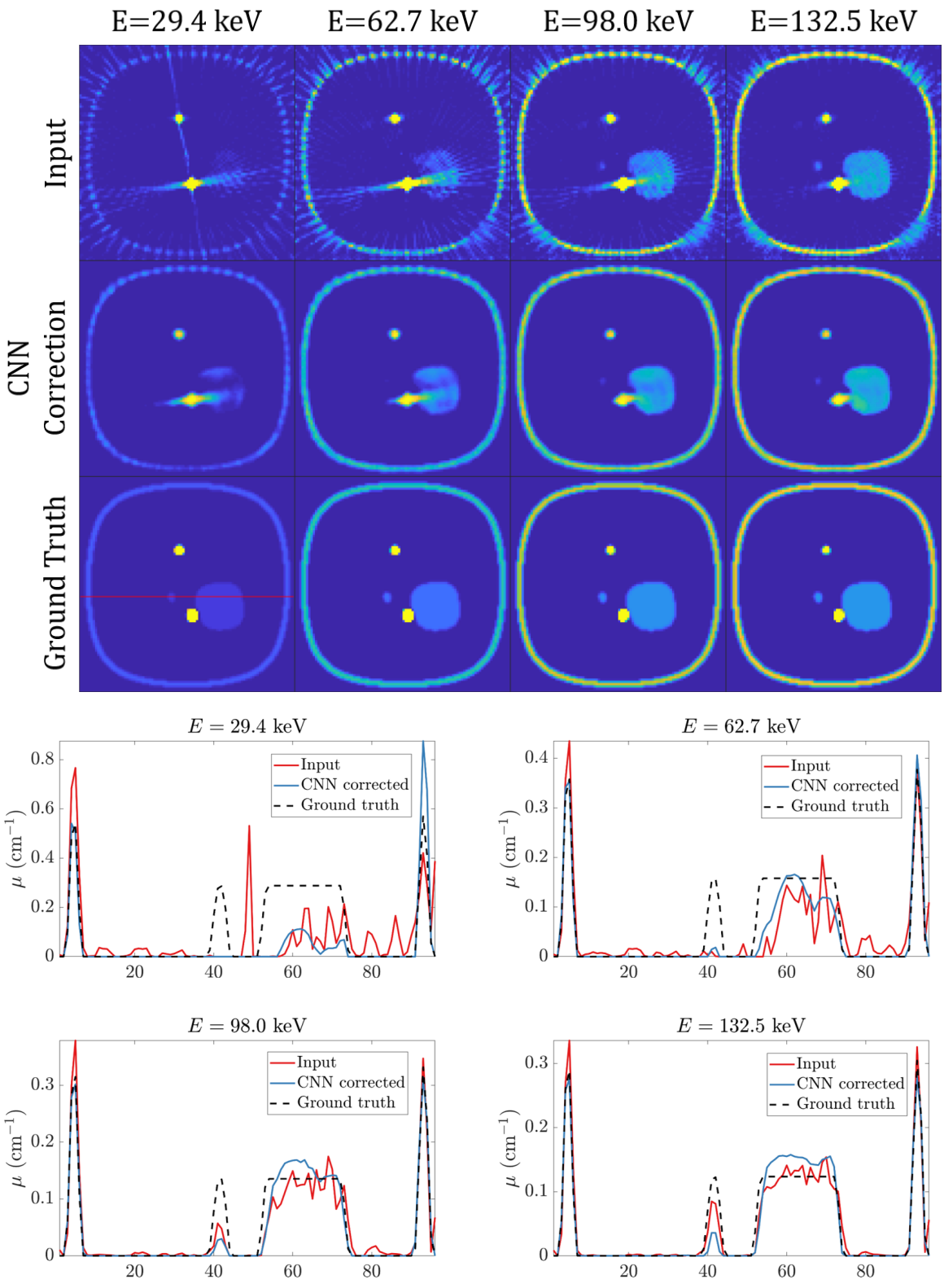

Figure 5.16: Simulation test data. **Example 3.** The object features are only partially corrected by the CNN architecture, due to severe artifacts. (See Fig. (5.14) for visual notes.)

Real data: suitcase

The same CNN architecture that was trained with MC simulation data was then tested with real metal artifact affected data (see instrumentation in section 6.1). A suitcase composed of several metal parts was filled with objects commonly found in luggage and scanned with the spectral X-ray CT technique. The geometry and source settings were set to resemble the one in the simulations to generate training data and 75 projections were taken. Differently from the simulations, the source was collimated into a fan-beam geometry to have reduced amount of scattering noise while still having streaking artifacts due to metals. Each vertical slice of the object was measured by vertically translating the sample stage. The difference between the two geometries in the reconstructions is that vertical slices from the cone-beam reconstructions may have artifacts that are caused by metals belonging to adjacent slices, whereas this is not found for fan-beam geometry. The measured data followed the SCT procedure described in Chapter 4, rebinning the energy channels into 8 to match the simulation data. The reconstruction algorithm adopted was an iterative ART with TV regularization, presented by Sidky et al. [55], which was proven particularly efficient in case of few projection CT scans. Each reconstruction slice was corrected using the CNN trained for 250 epochs and merged to reform the 3D volume stack. Figs.(5.17, 5.18, 5.19 and 5.20) display orthogonal slices and 3D volumes of the uncorrected and corrected suitcase, obtained by stacking each vertical slice.
It is observed by looking at the results, that the MAR correction efficiently cleans the reconstructions from most of the streaking metal artifacts, except for a few cases in which they are predominant in the images (see for example Fig. (5.17)). The drawback of this correction technique at its current state, is a degradation of feature resolution, which manifests as blurring and dampening of LAC values of small metallic objects, and in some cases (especially in the first energy channel) of cupping artifacts in the homogeneous materials. This could be potentially prevented by training the CNN architecture for more epochs or by including more training data with objects of more diverse shape and material composition. Alternatively, the introduction of an objective function in the loss function minimization during the CNN training could identify and segment geometrical features that are typically less artifact-prone in the intermediate energy channels and project them into the lower energy channel images. Lastly, it is noted that differently from the simulation data, the high-energy channel is dominated by noise due to low photon statistics, indicating an eventual mismatch in the spectrum modeling. Interestingly, a circle shaped artifact (marked with a red arrow) that appears in the first energy channel image of Fig. (5.17) is successfully removed by the MAR correction, possibly due to the absence of it in the higher energy channels. On the other hand, the empty plastic bottle container (marked with a red arrow in Fig. (5.18)), and suitcase border are also partially removed by the MAR correction, due to the significantly lower LAC value, compared with the other materials.
The comparison of the 3D volumes of the input and corrected suitcases in Figs. (5.19 and 5.20) highlight the overall result of the MAR correction. Note that each pair

at a fixed energy channel is shown with identical value range of the color map, to emphasize the contrast to noise comparison, as the overarching goal is the material discrimination and thus, contrast between the different objects enclosed in the suitcase. A significant improvement of the overall reconstruction quality is observed in the low-energy channel volume with only a moderate blurring drawback caused by the MAR correction (see Fig. (5.19)). On the other hand, the correction does not seem to deliver a significant improvement in the intermediate energy channel (Fig. (5.20)) as the noticeable streaking removal from the CNN architecture does not trade with the loss in feature resolution. It is expected that further developments in the architecture and eventual ad hoc tuning of the training data to be similar to real suitcases will close the gap with ideal corrections.

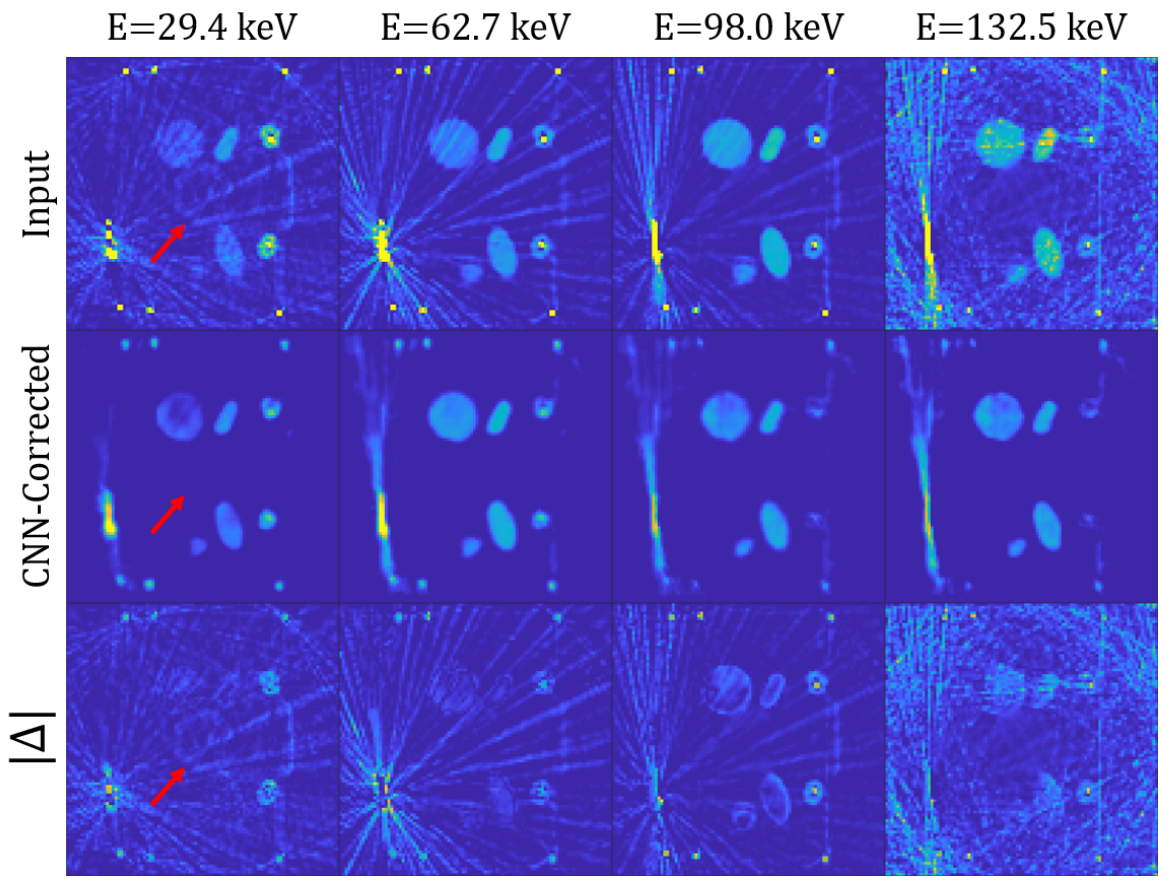

Figure 5.17: Orthogonal slice of the suitcase for the input (first row) and CNN-corrected (second row) data at different energies and the absolute difference between the two (third row). Note that each column, corresponding to a fixed energy channel, has identical color map. The red arrow indicates a hollow object look-like artifact, which does not appear in the higher energy channel and is efficiently removed by the correction.

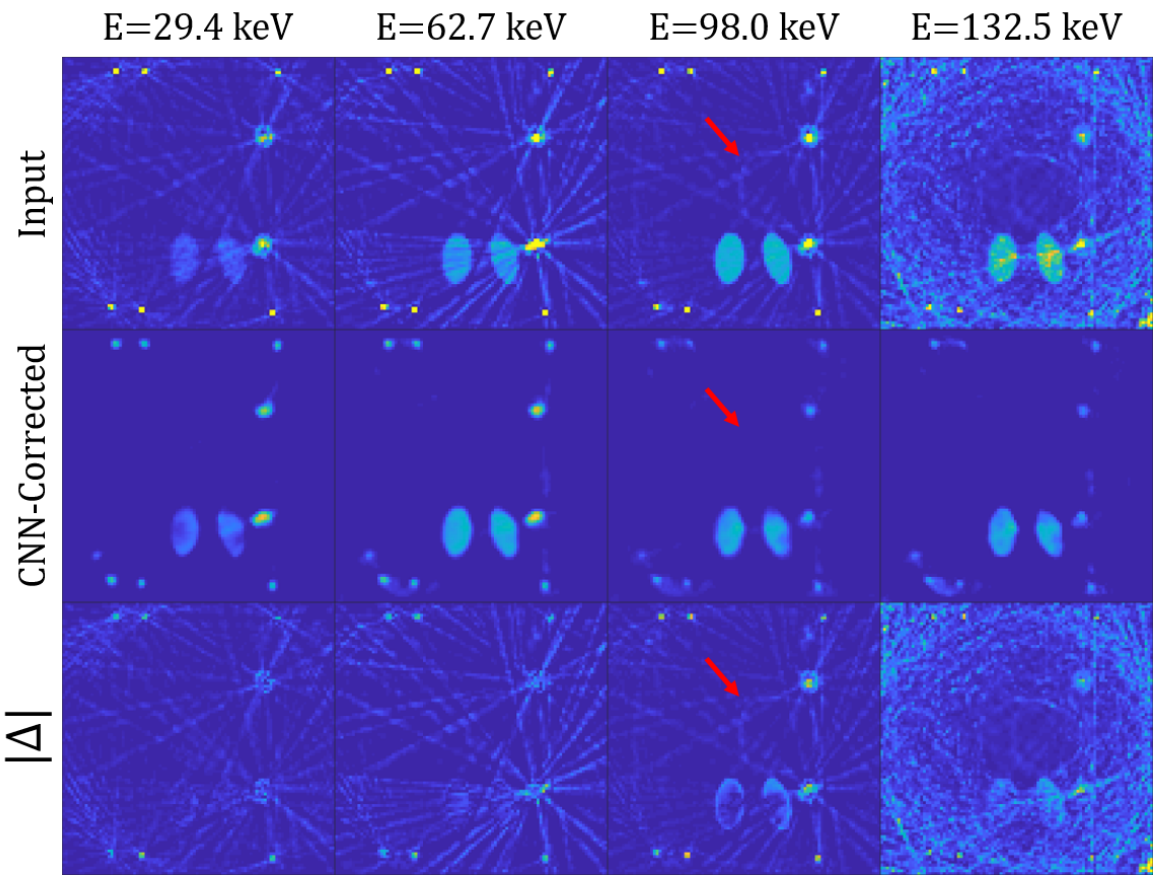

Figure 5.18: Another orthogonal slice of the suitcase as in Fig. (5.17). The red arrow indicates a real hollow object (plastic container) that is erroneously removed by the CNN correction due to its very low attenuation (especially in the low energies).

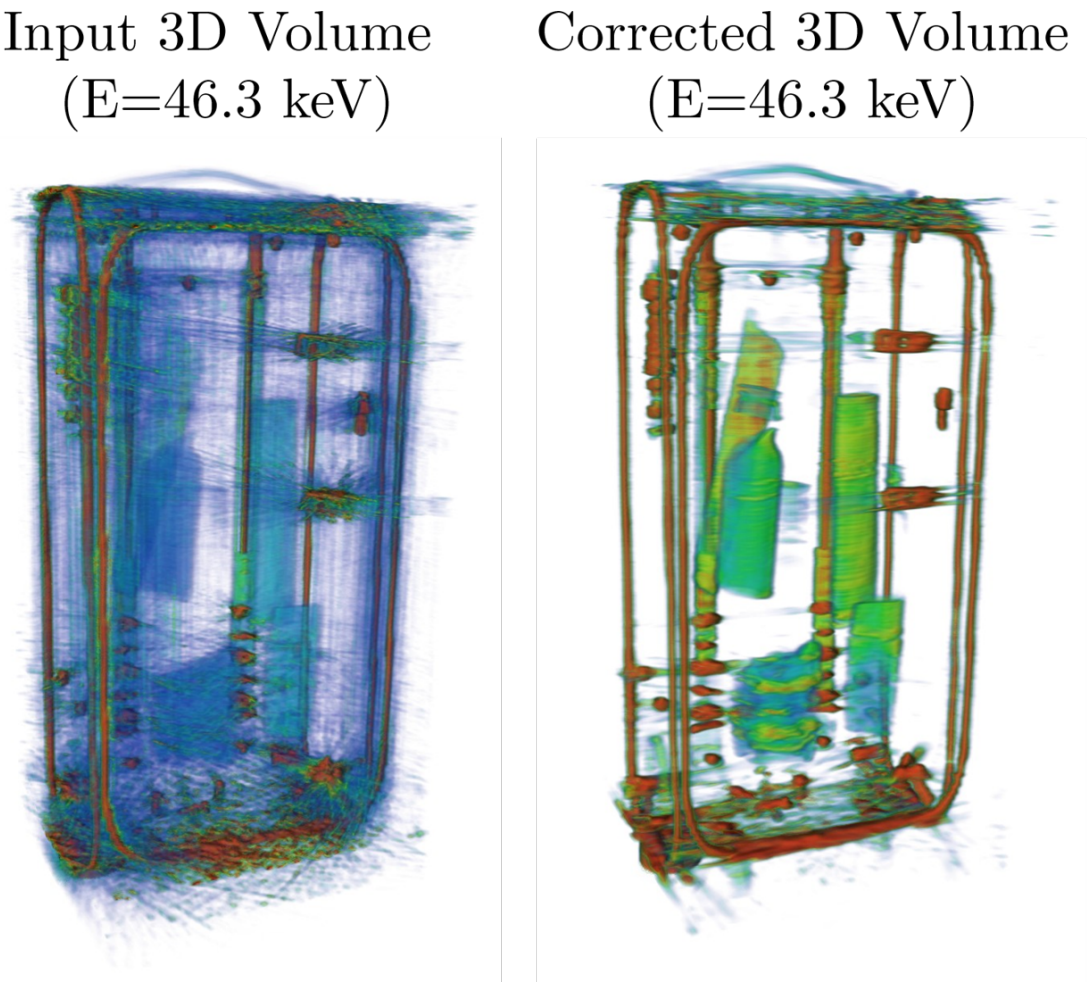

Figure 5.19: Input and MAR corrected 3D volume reconstruction of the suitcase at 46.3 keV. The CNN correction clearly removes most of the artifacts increasing dramatically the quality of the reconstruction.

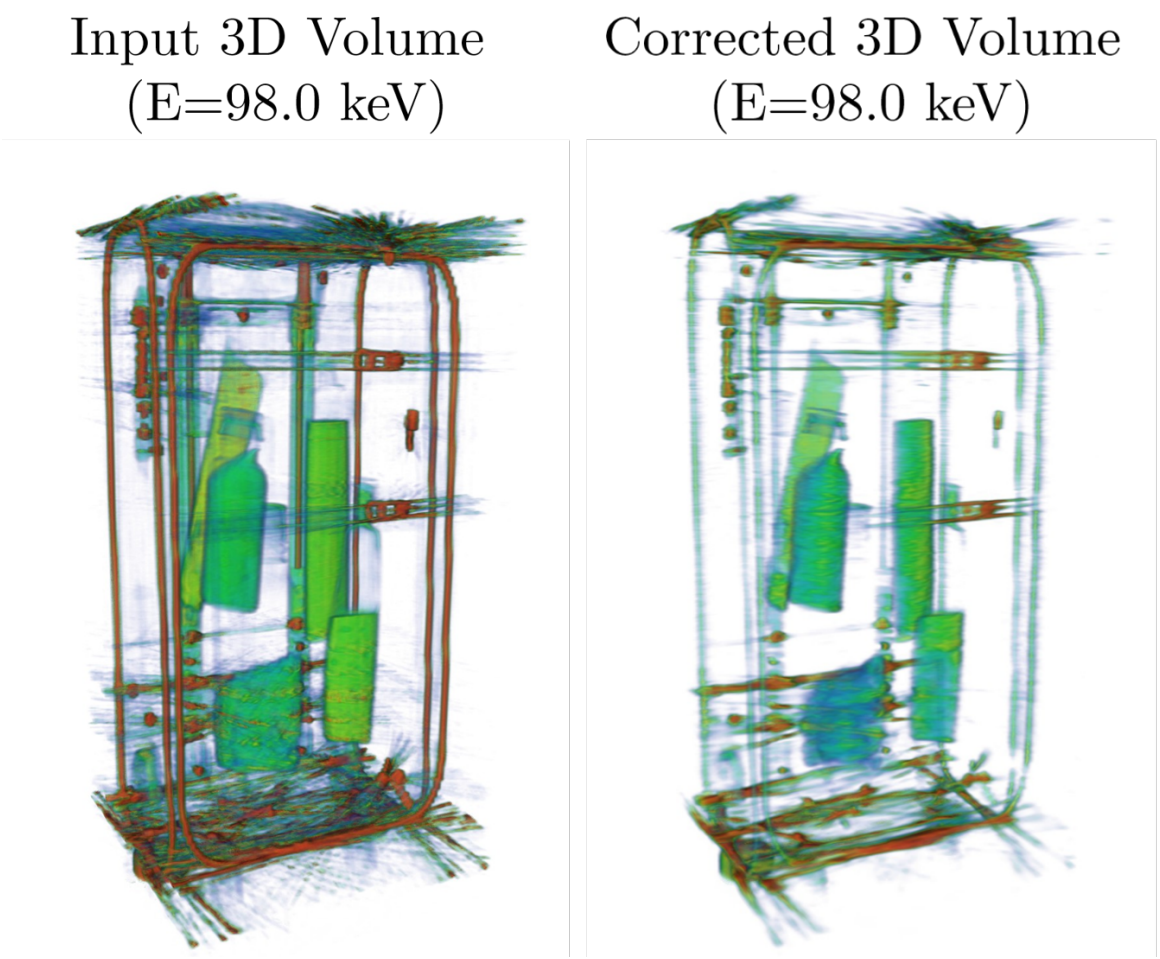

Figure 5.20: Input and MAR corrected 3D volume reconstruction of the suitcase at 98.0 keV. The CNN correction removes some of the non-severe streaking artifact introducing however, blurring of the features.

5.6 Short Summary

In this chapter, I presented a Machine Learning architecture for correction methods in SCT measurements. Specifically, the architecture was used for the direct correction of scattering from SCT projections, and metal artifacts from SCT reconstruction. The study highlighted the potential of this framework to establish near real-time corrections methods for samples for which the a-priori knowledge is scarce (e.g. luggage). It is expected that this network can be used for most of the effects producing artifacts in the reconstruction (such as beam-hardening, ring artifacts, etc.) given that the quality of the training data is good enough. Compared to related work using conventional CT techniques, this architecture can learn features from the spectral domain as well, expanding the range of the cases for which the correction is successful.

Material Characterization and Classification using Spectral X-ray CT 6

This chapter presents experimental results on the accuracy of the SRZE characterization method presented in section 3.3. It continues with a benchmarking of a material classification task of samples containing multiple objects. This is based on different material features measured using SCT.

6.1 Instrumental Setup for Spectral X-ray Measurements

Fig. (6.1) displays the instrumental setup for spectral X-ray acquisitions, which is a custom instrument mainly built by Jan Kehres in the imaging center of the Technical University of Denmark (DTU) [95]. All the experiments reported in this work were carried out using this imaging setup, unless when specified. The setup features an X-ray tube equipped with a tungsten anode (Hamamatsu Microfocus X-ray source L12161-07), mounted on a vertically translating motor. The acceleration voltage of the source can go up to 150 kV and the filament current up to 500 μA. The focal spot for these operating parameters is 50 μm. The sample stage can rotate and translate in the three orthogonal directions. The setup introduces a unit for spectral detectors on a translation stage for movement in the three orthogonal various directions. The setup also includes a tungsten slit mounted in front of the source to collimate the beam into the desired geometry, and a tungsten slit mounted in front of the detection line to suppress environmental noise. When necessary, filters can be attached to the frontal collimator to shape the source spectrum as desired. Fig. (6.2) illustrates a schematic view from the top of the setup with all the components and degrees of freedom of the translating motors. The many degrees of freedom of the components building up the instrument, makes it ideal for experimental studies, which can accommodate diverse geometry settings.

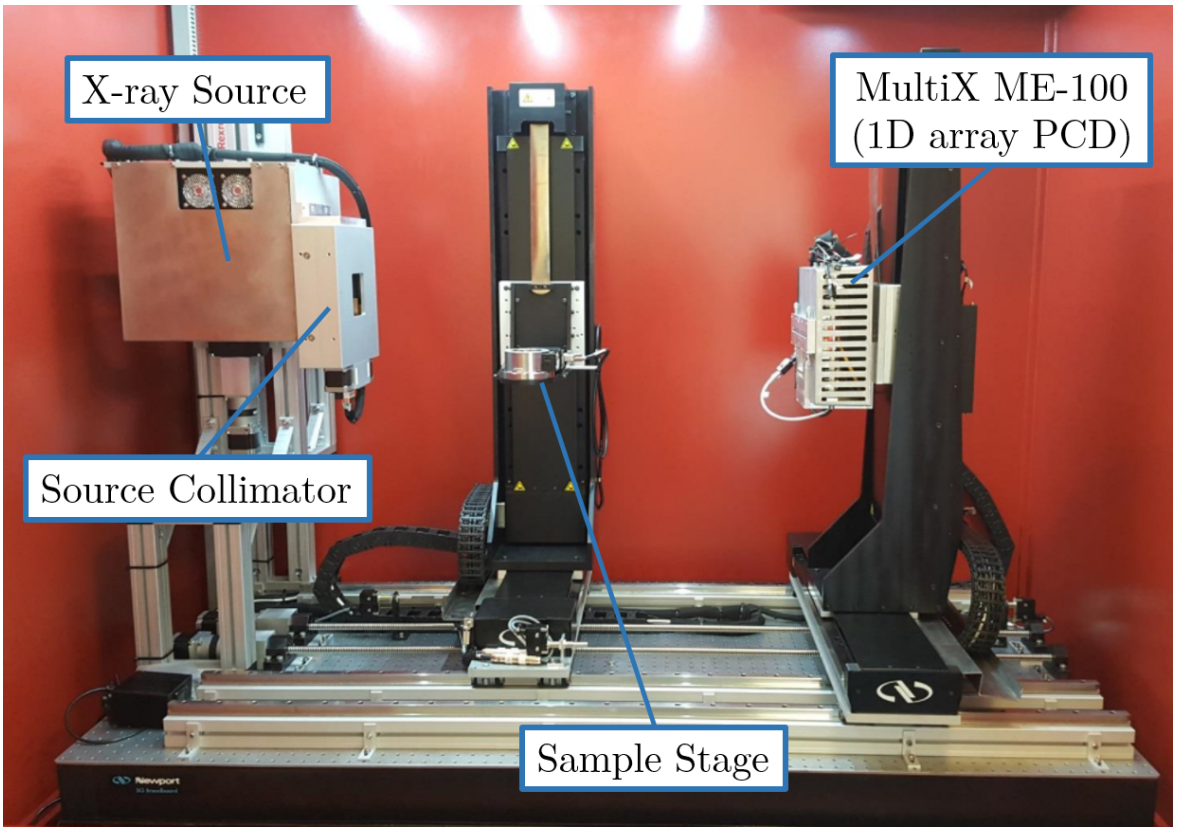

Figure 6.1: Picture of the instrumental setup for spectral X-ray acquisitions built in the imaging center of the Technical University of Denmark (DTU).

6.2 SRZE Characterization Experiments

Two experiments were carried out to evaluate the accuracy and precision of the SRZE method for the estimation of the physical properties of material. The results are reported in a table listing the expected and estimated material properties and ρ_e/Z_e scatter plot figures. In the tables, the expected values for Z_e and ρ_e were calculated with ZeCalc [96] setting the source's acceleration voltage to 160 kV with a 2 mm thick slab of aluminum filter to match experimental conditions. ZeCalc's input parameters for each material were the material's respective chemical formula and the bulk density, ρ, which was measured in the laboratory with measurements of volume and mass. Information regarding measurement uncertainties are reported in the tables as well. The Δx notation refers to relative deviation (% unit) between the expected (*exp* superscript) and the estimated (*est* superscript) values of the observable x, and is calculated as:

$$\Delta x = 100\% \quad \frac{x^{est} - x^{exp}}{x^{exp}}. \tag{6.1}$$

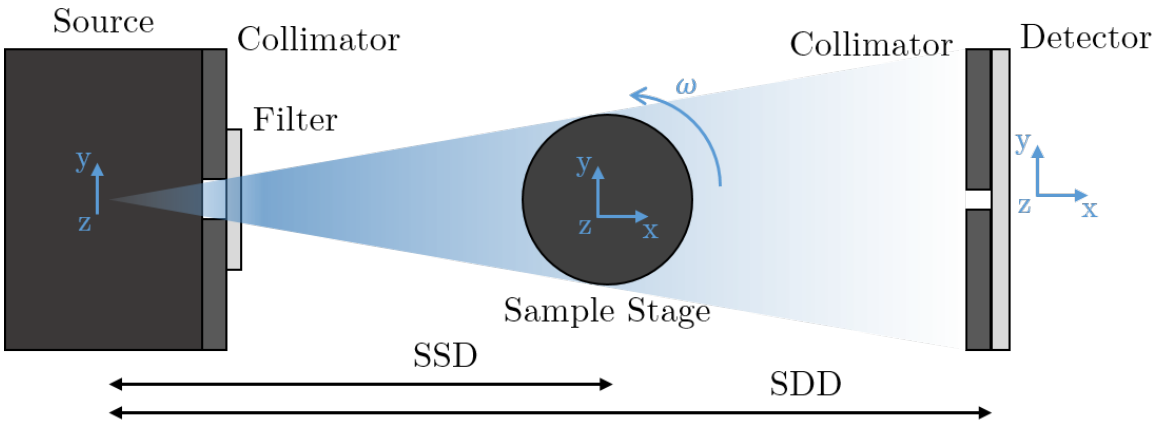

Figure 6.2: Sketch of view from the top of the instrumental setup pictured in Fig. (6.1). The SSD and SDD are the distance between the source and the sample stage and the detector respectively. The degrees of freedom of the translation motors are marked in blue.

6.2.1 Test Sample 1

The first experiment was performed at the Lawrence Livermore National Laboratory (LLNL) using the same sample reported in a previous characterization study using dual energy CT by Azevedo et al [8]. For the measurements, an YXLON 450-D11 (YXLON International, Hudson, Ohio) X-ray source was used with an acceleration voltage of 160 kV, anode filament current of 0.5 mA and 1 mm focal spot. The source spectrum was filtered with 2 mm thick slab of aluminum. The detector was made up of two daisy-chained linear array PCD MultiX ME-100 modules. For all the SCT scans performed in this work, 360 projections were acquired by rotating the sample stage at 1° increments. For each projection, the total exposure time was set to 5 s. The Source to Detector Distance (SDD) was set to 3000 mm whereas the Source to Sample Distance (SSD) was set to 2830 mm. Fig. (6.3) illustrates the first sample set, consisting of six different materials scanned simultaneously within a carousel [97]. Other materials, with larger diameter or attenuation were scanned individually. The material properties were calculated from their respective measured bulk densities ρ using the ZeCalc software [96].
Table (6.1) reports the characterization accuracy using the SRZE method. Promising results were found in the estimation of the effective atomic number, with an overall mean relative error value of 1.79%. It is observed that the estimation of Z_e worsens for smaller Z_e, due to lower performance of the detector in terms of spectral resolution at the lower-energy bins and lower contrast between LAC curves of adjacent Z_e values. Moreover, the spectral distortions in the low-energy reconstructions lead to higher standard deviations, and hence less energy weight λ_{E_k} in the estimation method. However, the highest contrast between material LACs, leading to higher differences in the features' estimation, is found at lower energies.
The estimation of ρ_e on the other hand shows a mean 4% negative bias in the mean

Figure 6.3: Picture of the carousel sample holder with six different materials in place. Figure courtesy of Dooraghi et al. [97]

Table 6.1: SRZE estimation of the material's features. †Materials placed in the six materials carousel. ‡Materials scanned individually. *The mean values were calculated from the absolute values of each column.

Material	**Formula**†	$\mathbf{Z_e^{exp}}$	$\mathbf{Z_e^{est}}$	$\mathbf{\Delta Z_e}$ (%)	$\rho^{\mathbf{exp}}$ g/cm^3	$\rho_e^{\mathbf{exp}}$ e$^-$mol/cm^3	$\rho_e^{\mathbf{est}}$ e$^-$mol/cm^3	$\mathbf{\Delta}\rho_e$ (%)
†Graphite B	C	6	5.81	-3.2	1.85	0.924	0.871	-5.7
†POM	$(CH_2O)_n$	7.01	6.87	-2.0	1.40	0.749	0.718	-4.2
†Water	H_2O	7.45	7.25	-2.7	0.99	0.554	0.516	-6.9
†PTFE	$(C_2F_4)_n$	8.43	8.32	-1.3	2.17	1.042	0.987	-5.3
†Magnesium	Mg	12	12.10	0.8	1.74	0.857	0.811	-5.4
†Silicon	Si	14	14.11	0.8	2.33	1.16	1.05	-9.5
‡Graphite A	C	6	6.17	2.9	1.70	0.846	0.842	-0.5
‡Aluminum	Al	13	13.09	0.7	2.70	1.30	1.258	-3.2
‡Titanium	Ti	22	21.74	-1.2	4.54	2.08	2.07	-0.7
Mean* $\lvert\Delta(Z_e)\rvert, \lvert\Delta(\rho_e)\rvert$	-	-	-	1.7	-	-	-	4.6

relative error value, perhaps due to an overall underestimation of the measured energy resolved attenuation coefficient. One reason for this may be due to a high amount of environmental X-ray scattering, not considered in the analysis. For these experiments, except for the titanium, aluminum, and graphite A scans, the source was not collimated into a fan-beam geometry and a large portion of the beam hit the sample stage, mostly composed of metal parts (see Fig. (6.3)). The small distance between the sample stage

and the detector permitted a large portion of the environmental scattering to reach the detectors. The large error in the estimation of silicon's electron density (ρ_e) may be due to the use of monocrystalline silicon, which is known to exhibit a different X-ray cross section than polycrystalline silicon [8, 98]. The results are in the same order of magnitude as the ones reported in a previous work using state-of-the-art Dual-Energy CT [98], except for the significant lower performance on the estimation of ρ_e, which is due to the reasons discussed above.

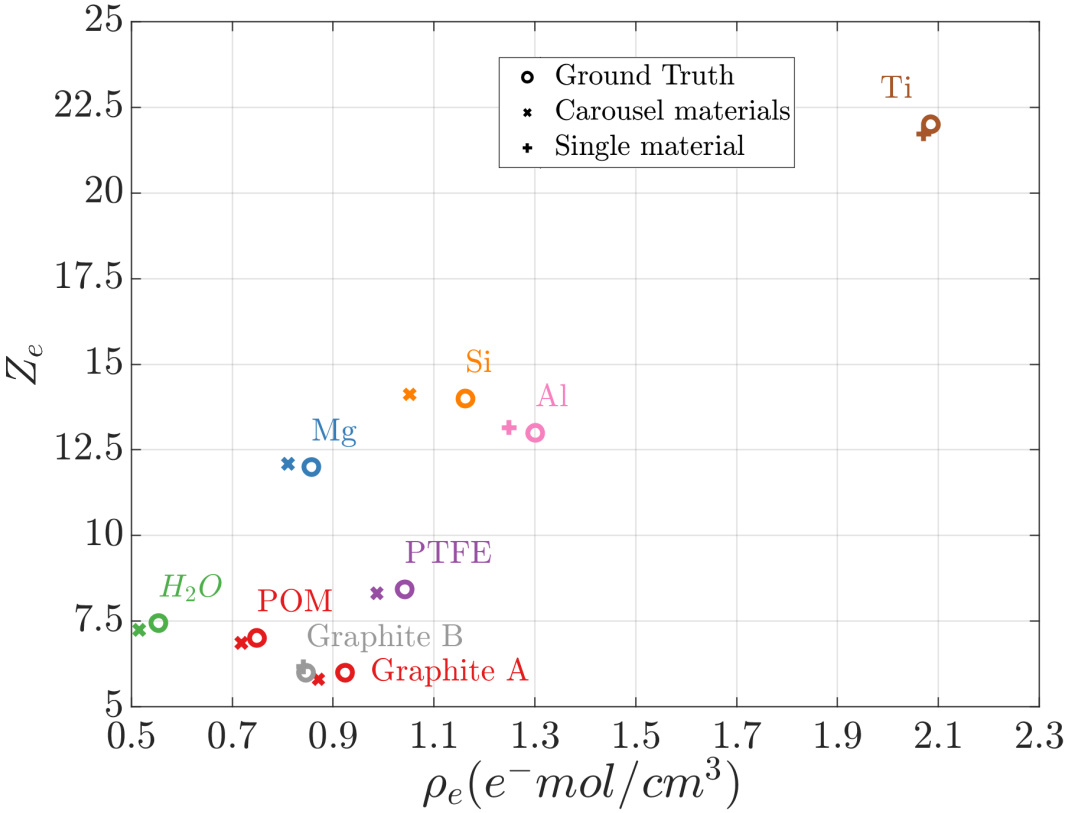

Figure 6.4: Scatter plot of the ρ_e, Z_e results obtained using the SRZE method.

6.2.2 Dependence on Number of Energy Bins

The material characterization using the SRZE method was benchmarked with respect to different numbers of new energy channels E'_k following the energy-rebinning step described in section 3.1.3. Tables (6.2 and 6.3) respectively report the results as a function of new energy channels for the carousel with six materials and for the materials scanned individually.

A first observation is that the estimation of the electron density for the carousel sample has a consistent negative bias, which is not found for the materials scanned individually. This confirms the assumption on the environmental scattering noise due to a lack of the fan-beam collimation of the source in the carousel sample scan. Another prompt observation is the significant bad results overall for the rebinning into two

Table 6.2: Estimation of Z_e and ρ_e rebinning in different numbers of energy channels, E_b, for the six materials carousel sample.

$\mathbf{\Delta Z_e}(\%)$

$\mathbf{E_b}$	**Graphite B**	**Magnesium**	**Water**	**PTFE**	**Silicon**	**POM**	$< \lvert\mathbf{\Delta Z_e}\rvert >$
2	17.7	15.5	19.0	18.0	5.7	18.4	15.7
4	4.8	4.0	7.0	6.3	-2.9	6.4	5.3
8	-1.3	0.5	0.2	0.2	-2.8	-0.2	0.9
16	-3.5	0.6	-2.0	-0.4	-1.1	-2.1	1.6
32	-3.8	1.4	-3.5	-1.5	0.2	-2.6	2.2
64	-3.9	0.8	-3.2	-1.8	0.9	-2.4	2.2
128	-3.5	0.6	-2.1	-1.2	0.8	-1.5	1.6

$\mathbf{\Delta}\rho_e(\%)$

$\mathbf{E_b}$	**Graphite B**	**Magnesium**	**Water**	**PTFE**	**Silicon**	**POM**	$< \lvert\mathbf{\Delta}\rho_e\rvert >$
2	-5.5	-10.2	-7.5	-7.2	-9.9	-4.5	7.5
4	-5.1	-5.9	-6.8	-5.8	-4.3	-3.9	5.3
8	-4.9	-4.2	-6.3	-4.8	-5.2	-3.4	4.8
16	-5.0	-4.6	-6.2	-5.0	-6.9	-3.4	5.2
32	-5.3	-5.7	-6.3	-4.9	-8.5	-3.7	5.7
64	-5.6	-5.4	-6.8	-5.1	-9.5	-4.1	6.1
128	-6.1	-5.6	-7.9	-5.8	-9.8	-4.8	6.7

energy channels. This may be because no initial energy channels of the 128 maximum energy offered by the detector MultiX ME-100 were truncated, while it is known that the detector's performance gets worse at the low- and high-energy boundaries, even though the detector response correction algorithm is applied. Thus, the integration of the signal including these troublesome energy channels leads to distortions in the calculation of the LAC. As this effect depends on the flux and photon statistics, the distortion becomes more significant as the material's LAC increases as well. The characterization of Titanium, for example, only begins to have relatively good values for 64 energy channels and yields the best results for 128 energy channels. This is because, a higher number of energy channels in the data allows truncating these energy channels through the energy thresholding step described in section 3.3. On the other hand, it is seen that for relatively low attenuating materials, as the ones in the carousel sample, the characterization is stable enough and yields best values for 8 energy channels. This suggests that the optimal number of energy channels depends on the material's attenuation properties, and that one should choose it depending on the analysis application.

Table 6.3: Estimation of Z_e and ρ_e rebinning in different numbers of energy channels, E_b, for the single material samples.

$\mathbf{\Delta Z_e}(\%)$

$\mathbf{E_b}$	**Titanium**	**Aluminum**	**Graphite A**	**Silicon**	**POM**	$< \lvert\mathbf{\Delta Z_e}\rvert >$
2	-24.8	1.5	23.5	-2.4	15.0	13.4
4	-25.6	-4.1	10.1	-7.5	2.7	10.0
8	-32.1	-2.3	2.6	-3.3	-5.3	9.1
16	-4.1	-1.1	1.9	-1.9	-7.6	3.3
32	-6.7	0.1	3.0	-1.1	-6.0	3.4
64	-3.3	0.6	1.8	-0.7	-7.6	2.8
128	-0.6	1.0	1.9	-0.6	-5.8	2.0

$\mathbf{\Delta \rho_e}(\%)$

$\mathbf{E_b}$	**Titanium**	**Aluminum**	**Graphite A**	**Silicon**	**POM**	$< \lvert\mathbf{\Delta \rho_e}\rvert >$
2	33.8	-3.7	-1.6	-4.2	-3.4	9.4
4	37.1	0.4	-0.8	1.0	-2.4	8.3
8	54.1	-1.2	0.6	-3.0	-0.3	11.9
16	5.7	-1.0	0.3	-3.5	-0.4	2.2
32	10.6	-2.6	-0.2	-4.8	-1.1	3.9
64	3.8	-3.1	0.2	-5.5	-0.4	2.6
128	-1.8	-3.9	-0.3	-5.8	-1.5	2.6

6.2.3 Dependence on Energy Thresholds Selection

To test the robustness and sensitivity of the E_L and E_H thresholds selection procedure described earlier in this chapter, the SRZE estimation method was used over a range of values for the low- and high-energy thresholds E_L and E_H. Fig. (6.5) shows the relative percent deviation of the estimated material features for aluminum as a function of the two thresholds. Note that the diagonal elements correspond to taking only two adjacent energy bins and the values below the diagonal are not calculated, as they have no physical representation. The distribution of the dark areas (corresponding to less deviation) shows that the key factor for accurate estimation of the LAC, and thus ρ_e and Z_e, is the selection of the low-energy threshold E_L. The optimal performance is reached by truncating the low-energy bins for which the spectral distortions and photon starvation cause a distortion of the measured LAC. On the other hand, choosing a higher threshold for the low-energy bins yields a poor estimation, as the bulk of the material properties is revealed by the low energy bins.

Fig. (6.5) also highlights that the selection of the high-energy threshold E_H has less impact on the estimation of the LAC, and thus ρ_e and Z_e. The large areas in which the deviation is below 2% indicate that the estimation method is overdetermined and there may be a material dependent optimal choice of the energy bins, that leads to optimized results. The difference in shape between the dark areas for ρ_e and Z_e,

suggests that there may be an independent choice of optimized thresholds for each of the two parameters characterization. On the other hand, there is a common area with low percent deviation for both parameters indicating that the characterization is moderately sensitive to errors in the determination of the thresholds.

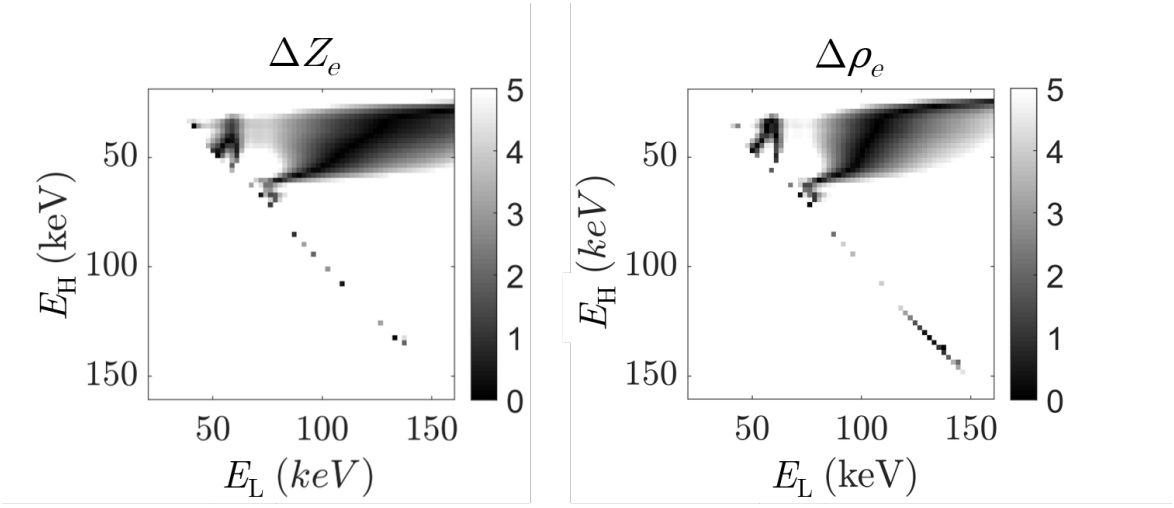

Figure 6.5: Plot of the material features estimation accuracy as a function of the E_{L} and E_{H} thresholds, exemplified for aluminum. The scale unit is the percent relative deviation (%) expressed in Eq. (6.1).

6.2.4 Plastic Samples

The second experiment was designed in order to evaluate the characterization accuracy for low attenuating plastic materials precisely. The sample was built up stacking nine plastic slabs of different material composition, which are listed in Table (6.4). A 3D visualization of the sample was shown in Fig. (5.10) of Chapter 5. A single slice fan-beam geometry SCT scan was taken with 370 projections with 0.1 s exposure time for each of them. The energy-resolved reconstructions were performed with the FBP algorithm of the LTT software. Table (6.4) and Fig. (6.7) present the characterization results obtained with the SRZE method. Except for the polypropylene (PP) material, all the relative deviations are below 3.2% with a mean deviation of 0.9% for the effective atomic number and 1.9% for the electron density. The mismatch between the characterization results for PP and the expected values are suspected to be caused by a chemical mixture with colorants, which yield a higher effective atomic number than the pure PP. For this reason, the PP results were neglected in the calculation of the mean deviations. Another observation is that the relative deviation of Z_{e} takes negative values for each material, indicating a negative bias in the estimation. Fig. (6.6) represents the expected and measured spectral resolved LAC of the PTFE material, and a comparison between the two highlights the reason for the poor Z_{e} estimation. In the low energy range, the measured LAC yields lower values due to an incomplete restoration of the spectrum by the detector correction algorithm, which leads to an

underestimation of the effective atomic number Z_e. The correction significantly extends the low energy value range in which the measured LAC follows the expectations. This is key to a correct discrimination of low attenuating materials. It is expected that both advantages in the detector's performance and the correction algorithm will increase the accuracy of the SRZE characterization method.

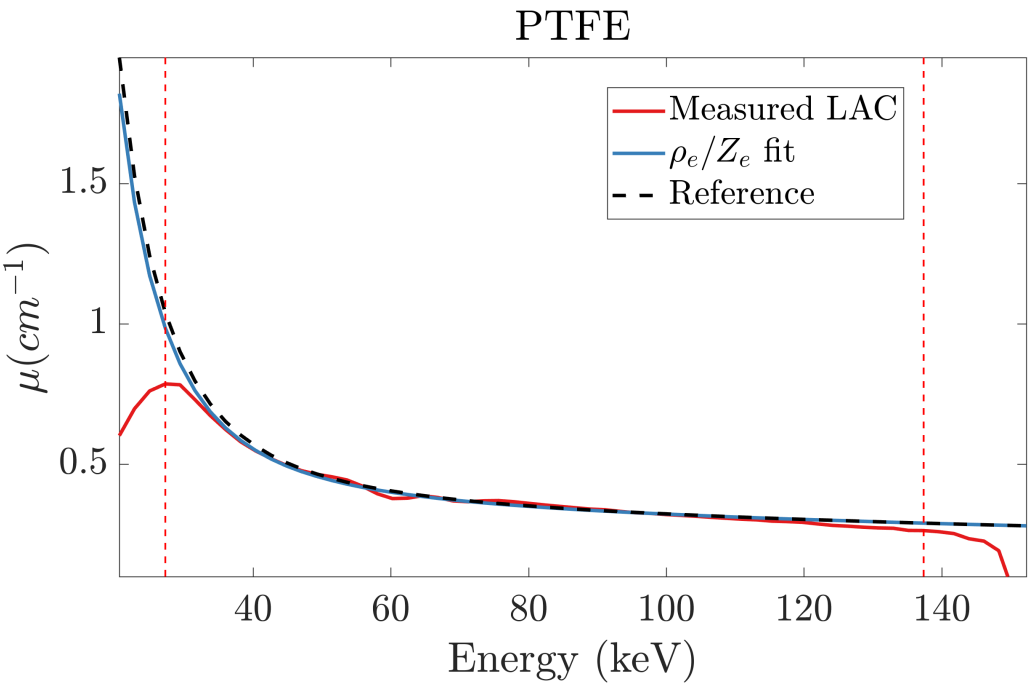

Figure 6.6: Plot of the measured LAC (red line) of the PTFE material and the LAC calculated using the estimated values (blue line) and reference (dashed black line) for effective atomic number, Z_e, and electron density, ρ_e.

6.3 Material Classification Experiments

The last part of this work is an analysis of the classification of materials based on their measured physical properties using spectral X-ray CT. The classification is performed using a large library of tabulated physical properties of materials measured individually in separate SCT scans.

6.3.1 Material Features Library

The first step of the material classification experiments was to build reference tables for the experimentally measured various physical properties of a list of materials. The library of materials, for which the physical parameters were estimated, includes innocuous materials, which are commonly found in luggage, and explosive or precursor materials, which are prohibited by airport security regulations. Note that the materials in this study are mostly organic and liquid materials without a K-edge discontinuity

Table 6.4: All the plastic materials composing the sample and their respective expected and estimated physical properties. †While most of materials are polymers, the chemical formula is reported for the composing monomer. *The mean values were calculated from the absolute values of each column, ignoring the entries for polypropylene (PP).

Material	**Formula**†	$\mathbf{Z_e^{exp}}$	$\mathbf{Z_e^{est}}$	$\mathbf{\Delta Z_e}$ (%)	$\rho^{\mathbf{exp}}$ g/cm^3	$\rho_e^{\mathbf{exp}}$ e$^-$mol/cm^3	$\rho_e^{\mathbf{est}}$ e$^-$mol/cm^3	$\mathbf{\Delta}\rho_e$ (%)
*PP	C_3H_6	5.44	7.13	31.1	0.91	0.519	0.520	0.3
PEEK	$C_{19}H_{12}O_3$	6.26	6.26	-0.1	1.30	0.677	0.653	-3.5
PC	$C_{14}O_3H_8$	6.40	6.29	-1.8	1.18	0.609	0.618	1.4
PMMA	$C_5O_2H_8$	6.49	6.47	-0.3	1.18	0.635	0.620	-2.3
PET	$C_{10}H_8O_4$	6.65	6.65	-0.1	1.38	0.721	0.699	-3.1
POM-C	CH_2O	7.02	6.95	-0.9	1.41	0.752	0.741	-1.4
POM-H	CH_2O	7.02	6.99	-0.4	1.43	0.762	0.744	-2.4
PVDF	$C_2H_2F_2$	7.94	7.83	-1.4	1.79	0.895	0.887	-0.8
PTFE	C_2F_4	8.43	8.22	-2.5	2.16	1.035	1.036	0.1
Mean* $\lvert\Delta(Z_e)\rvert, \lvert\Delta(\rho_e)\rvert$	-	-	-	0.9	-	-	-	1.9

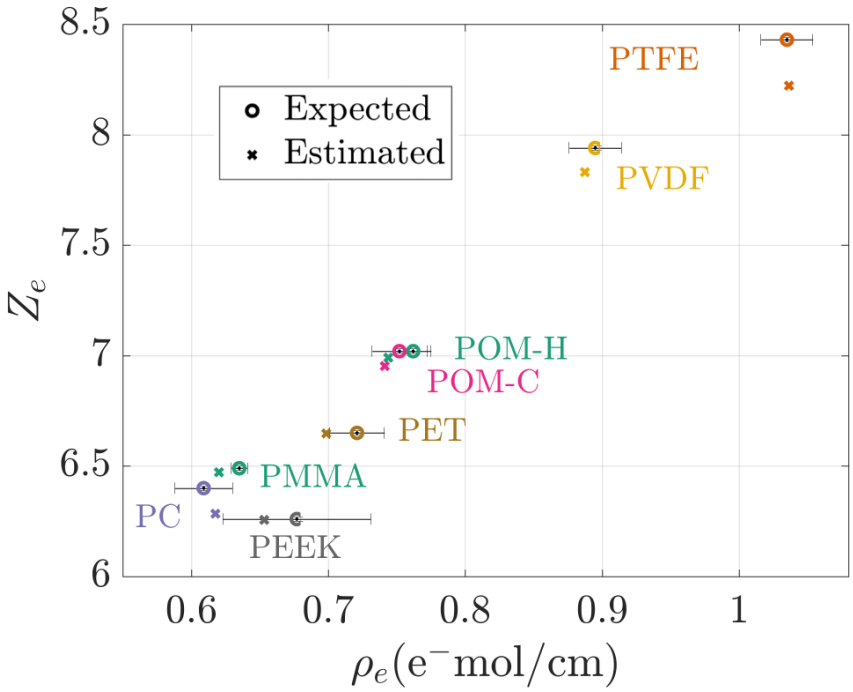

Figure 6.7: Plot of the material features estimation accuracy as a function of the E_L and E_H thresholds, exemplified for aluminum. The scale unit is the percent relative deviation (%) expressed in Eq. (6.1).

and with $6 \leq Z_e \leq 10$. Table (6.5) shows an example of such a reference table, listing all the materials characterized into effective atomic number and electron density using

the SRZE method. Similar tables were constructed for other material features such as the energy-dependent LAC, and a single value LAC obtained by integrating the signal over all the energy channels to emulate a conventional detector.

Table 6.5: The list of all the 73 materials scanned and processed through the SRZE method, and their estimated physical parameters $\rho_e(e^-mol/cm^3)$ and Z_e.

Index	Material label	Type	Z_e	ρ_e
1	2-Butanone	Threat	6.64	0.440
2	2,4-Dinitrotoluene	Threat	8.16	0.316
3	Acetone	Threat	6.12	0.442
4	Ethylenediamine	Threat	6.31	0.506
5	H_2O_2 50%	Threat	7.24	0.661
6	Hexamethylenetetramine	Threat	5.59	0.461
7	Hydrazine solution	Threat	7.07	0.575
8	Methanol	Threat	7.17	0.439
9	N,N-Dimethylhydrazine	Threat	6.36	0.454
10	Nitric acid 65%	Threat	7.21	0.744
11	Nitrobenzene	Threat	6.70	0.621
12	Nitromethane	Threat	7.09	0.586
13	Wine	Innocuous	7.16	0.557
14	Cream Liquor	Innocuous	7.19	0.580
15	Balsamic Vinegar	Innocuous	6.98	0.640
16	Bromhexin DAK	Innocuous	7.24	0.608
17	Baby Shampoo	Innocuous	7.39	0.614
18	Aftersun Lotion 1	Innocuous	6.69	0.560
19	Brandy	Innocuous	7.51	0.537
20	Hand cream	Innocuous	7.01	0.545
21	Sun Lotion 1	Innocuous	6.74	0.579
22	Body Lotion 1	Innocuous	6.93	0.566
23	Beer 1 (Wheat)	Innocuous	7.14	0.566
24	Ethanol 40%	Innocuous	6.81	0.541
25	Ethanol 96%	Innocuous	6.08	0.463
26	Shampoo	Innocuous	7.36	0.589
27	Beer 2 (Brown Ale)	Innocuous	7.35	0.564
28	Porto Wine	Innocuous	7.26	0.568
29	Aftersun Lotion 2	Innocuous	6.95	0.567
30	Sun Lotion 2	Innocuous	6.61	0.572
31	Neutral Hand Soap	Innocuous	6.50	0.585
32	Sun Lotion 3	Innocuous	7.19	0.580
33	Sun Baby Lotion	Innocuous	8.73	0.606

Continued on next page

Table 6.5 – *Continued from previous page*

Index	Material label	Type	Z_e	ρ_e
34	Antiperspirant	Innocuous	6.05	0.340
35	Beer 3 (Pale Ale)	Innocuous	7.55	0.556
36	Olive Oil	Innocuous	5.41	0.510
37	Alcohol Drink	Innocuous	7.27	0.583
38	Rapeseed Oil	Innocuous	5.40	0.516
39	Simple Eye Makeup Remover	Innocuous	7.00	0.576
40	Body Lotion 2	Innocuous	6.92	0.563
41	Sugar	Innocuous	6.49	0.524
42	Sun lotion 4	Innocuous	8.57	0.595
43	Hairspray 1	Innocuous	7.11	0.568
44	Beer 4 (IPA Ale)	Innocuous	7.35	0.563
45	Beer 5 (Danish Christmas Beer)	Innocuous	7.42	0.560
46	Whiskey	Innocuous	7.27	0.524
47	Beautifying Anti-Blemish Care	Innocuous	7.15	0.582
48	Water	Innocuous	7.05	0.562
49	Energy Drink	Innocuous	7.10	0.586
50	Hairspray 2	Innocuous	8.10	0.391
51	Shaving Foam	Innocuous	8.12	0.542
52	Toothpaste 1	Innocuous	8.19	0.665
53	Ammonia Nitrate	Threat	6.73	0.490
54	Book	Innocuous	9.74	0.419
55	C4 Simulant[1]	Threat	8.02	0.855
56	C4	Threat	6.44	0.497
57	Chocolate	Innocuous	6.68	0.700
58	Comp B	Threat	6.54	0.897
59	Crystal Sugar	Innocuous	6.63	0.531
60	DVD Bomb Simulant	Threat	7.49	0.878
61	Hard Cheese	Innocuous	7.41	0.619
62	Marzipan	Innocuous	6.47	0.648
63	Nitromethane	Threat	6.86	0.575
64	PETN Simulant[1]	Threat	7.72	0.719
65	Peanut Butter	Innocuous	6.94	0.636
66	PETN	Threat	6.73	0.839
67	Shampoo	Innocuous	7.37	0.582
68	Soap Bar	Innocuous	6.13	0.595
69	Soft Cheese	Innocuous	7.35	0.604
70	Sun Cream	Innocuous	7.32	0.571
71	TNT (chunks)	Threat	6.63	0.434

Continued on next page

[1†]We found noticeable difference in the chemical composition of the simulant materials respectively to the real threat materials.

Table 6.5 – *Continued from previous page*

Index	**Material label**	**Type**	$\mathbf{Z}_e$	ρ_e
72	Toothpaste 2	Innocuous	8.26	0.678
74	Vinegar	Innocuous	7.13	0.639

Singular Value Decomposition of Data

To confirm that the underlying model (Eq. (3.14)) adopted to estimate material physical parameters from their LAC matches with the experimental findings, the data is processed through a Singular Value Decomposition (SVD) analysis procedure, similar to the one proposed by Eger et al. [99] for synthetic data. In a first step, a matrix $\mathcal{M}$ is constructed with the energy-dependent LACs measured of all the reference materials listed in Table (6.5). The matrix $\mathcal{M}$ has dimensions $(E_b \times N_{mat})$ where E_b is the number of energy bins for which the LAC is measured and N_{mat} is the number of materials. The SVD decomposition aims to find a set of linearly independent vectors that can express the LAC, and can be represented as:

$$\text{SVD}(\mathcal{M}) \equiv \mathcal{M} = USV^T, \tag{6.2}$$

where U is a $(E_b \times N_{mat})$ matrix where each column i composes the set of linearly independent vectors $U_i(E)$, S is a $(N_{mat} \times N_{mat})$ diagonal matrix where the magnitude of each element $S_{i,i}$ describes the relative contribution of the corresponding vector U_i to the model. Fig. (6.8) represents the singular values $S_{i,i}$ and the first six singular vectors U_i. A qualitative look at these vectors indicates that the two dominant singular vectors, U_1 and U_2 are corresponding to the basis functions for incoherent scattering and photoelectric absorption, as in Eq. (3.5). These observations were confirmed by finding a linear proportionality between U_1 and the Klein-Nishina function f_{KN}, and a linear trend of the inversion $1/\sqrt[3]{U_2(E)}$. The remaining singular vectors are dominated by noise components except for the third singular vector U_3, which models the oscillations in the measured LAC due to the residuals of the detector correction algorithm around the emissions spectrum peaks of the X-ray source, as indicated by the wiggles around the energy of the K_{α_1} and K_{β_1} tungsten emission lines. This was confirmed by calculating the autocorrelation of the singular vectors, which was below the value of 0.5 [100] except for $U_{1,2,3}$ and a few more with the same behavior of U_3 but different modulation of the peaks (see Fig. (6.8) (b)). Note that the list of materials analyzed in this work do not have a K-edge in the measured LAC. Such a discontinuity in the LAC would yield an additional relevant singular value and its respective singular vector, for each of the eventual energy values of the K-edges in the library.
This suggests that for a list of materials without K-edge discontinuity such as the one analyzed here, the two dominant singular vectors contain the bulk of information about the physical properties of materials. Thus, there is no additional information which can be represented by a third feature in addition to the standard effective

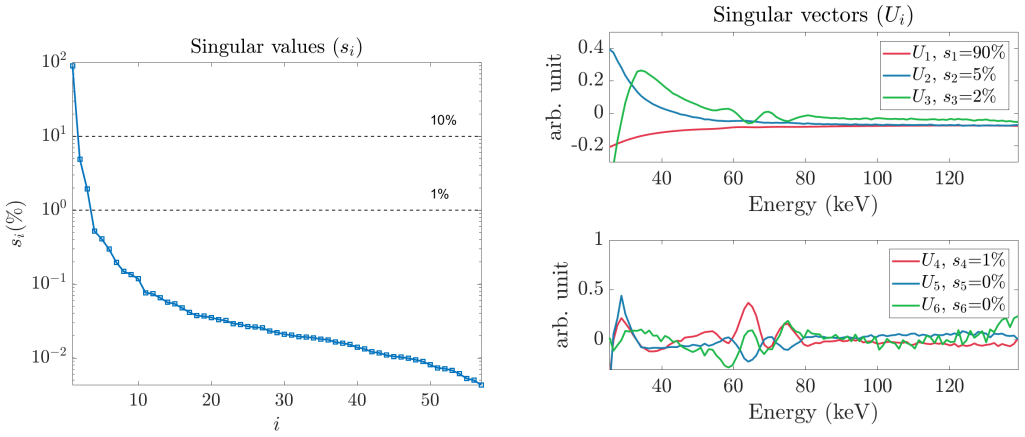

(a) **(b)**

Figure 6.8: Singular Value Decomposition analysis of the reference materials LACs. (a) Singular values of the diagonal i-elements (blue-squares). Note logarithmic scale. (b) Singular vectors U_i respective to the diagonal singular values s_i. The scale is in arbitrary unit.

atomic number and electron density $\{Z_e, \rho_e\}$ pair. Having only two dominant vectors suggests the possibility for a basis function decomposition similar to the material basis decomposition in Eq. (3.15), where the basis functions used are represented by the singular vectors, and the coefficients can be used to represent physical properties based on reference calibration measurements. This area is not investigated further in this work, as the general interest is towards a system-independent method.

6.3.2 Prediction Models

In this work, four different methods are tested for the material classification from SCT data acquisitions. In the first method, the material's feature used is the energy integrated LAC, $\tilde{\mu}(E')$, obtained by summing the signal over all the 128 energy channels of the detector. The effective energy (E') corresponding to $\tilde{\mu}$ was calculated using the source spectrum as measured by the flat field acquisition (i.e. without the sample) as a model for the detector's response. The second and third methods, utilize the energy-dependent LAC as the material's identifier, i.e. the attenuation coefficient measured at the 128 energy values corresponding to the specifics of the detector ($\mu(E_k)$ with $k = 1, 2, 3, ..., 128$), with the difference that in the third method the standard deviation is used to weight the different energy channels. In the fourth method, the materials are characterized with the SRZE characterization method described in section 3.3. For each of these methods, a look-up table library of material features such as Table (6.5), has been built by using single slice fan-beam SCT of individual materials in ideal condition (i.e. without metal artifacts and center-offset).
The classification is performed finding the closest match between the material property of all the materials in the library and the unknown material under investigation. The material *label* is thus found as follows for each method:

- Integrated LAC ($\tilde{\mu}$) classification:

$$label = \arg\min_{label} \sqrt{(\mu^{est} - \hat{\mu}^{label})^2}. \tag{6.3}$$

- Spectral LAC ($\mu(E)$) classification:

$$label = \arg\min_{label} \sqrt{\sum_{k=1}^{128} \left(\mu_{E_k}^{est} - \hat{\mu}_{E_k}^{label}\right)^2}. \tag{6.4}$$

- Weighted LAC ($w_{\mathrm{e}}\mu(E)$) discrimination:

$$label = \arg\min_{label} \sqrt{\sum_{k=1}^{128} \lambda_{E_k} \left(\mu_{E_k}^{est} - \hat{\mu}_{E_k}^{label}\right)^2}. \tag{6.5}$$

- SRZE ($\rho_{\mathrm{e}}/Z_{\mathrm{e}}$) classification:

$$label = \arg\min_{label} \sqrt{w_{Z_{\mathrm{e}}} \left(\frac{Z_{\mathrm{e}}^{est} - \hat{Z}_{\mathrm{e}}^{\,label}}{< \hat{Z}_{\mathrm{e}}^{\,label} >} \right)^2 + w_{\rho_{\mathrm{e}}} \left(\frac{\rho_{\mathrm{e}}^{est} - \hat{\rho}_{\mathrm{e}}^{\,label}}{< \hat{\rho}_{\mathrm{e}}^{\,label} >} \right)^2}. \tag{6.6}$$

The hat sign refers to the values stored in the libraries whereas the <> operator corresponds to the mean, applied to all reference values of Z_{e} and ρ_{e}. That is done to have the physical parameters in the same scale and with same importance. The energy weights λ_{E_k} are set to the reciprocal of the standard deviation respective to the LAC value, to attribute less importance wherever the uncertainty is greater. The weights $w_{\rho_{\mathrm{e}}}$ and $w_{Z_{\mathrm{e}}}$ are assigned to the individual features of Z_{e} and ρ_{e} to tune the influence given to each of them. They are calculated with the equation below:

$$\hat{s}_{Z_{\mathrm{e}}} = \frac{\max_{label}(\hat{Z}_{\mathrm{e}}^{\,label}) - \min_{label}(\hat{Z}_{\mathrm{e}}^{\,label})}{\mathrm{mean}_{label}(\hat{Z}_{\mathrm{e}}^{\,label})}; \qquad \hat{s}_{\rho_{\mathrm{e}}} = \frac{\max_{label}(\hat{\rho}_{\mathrm{e}}^{\,label}) - \min_{label}(\hat{\rho}_{\mathrm{e}}^{\,label})}{\mathrm{mean}_{label}(\hat{\rho}_{\mathrm{e}}^{\,label})}, \tag{6.7}$$

where $\hat{s}_{Z_{\mathrm{e}}}$ and $\hat{s}_{\rho_{\mathrm{e}}}$ represent the widths of the value ranges in the reference library of the effective atomic number and electron density respectively, normalized by dividing by the respective mean values. The widths are then normalized through the equations below such that their sum is equal to one, to obtain the weights:

$$w_{Z_{\mathrm{e}}} = \frac{\hat{s}_{Z_{\mathrm{e}}}}{\hat{s}_{Z_{\mathrm{e}}} + \hat{s}_{\rho_{\mathrm{e}}}}; \qquad w_{\rho_{\mathrm{e}}} = \frac{\hat{s}_{\rho_{\mathrm{e}}}}{\hat{s}_{Z_{\mathrm{e}}} + \hat{s}_{\rho_{\mathrm{e}}}}. \tag{6.8}$$

The role of these weights is to give more impact to the prediction of the feature that has more variability in the reference library. In the material classification, the prediction is successful when the individual material label is found correctly, whereas in the binary classification the discrimination is only done between innocuous and threat materials.

6.3.3 Experiments

The following scans are the tests samples, which are built shuffling a few of the tabulated materials in a sample holder or container. For each of the materials contained in the samples the classification accuracy is benchmarked, as the ratio between successful and failing predictions for the four prediction models. As a remark, note that only the materials used in the samples are extracted for building up the material reference table.

Homogeneous samples: slice reconstructions

The first set of experiments consists in 30 test samples composed of four glass bottles filled with different materials and aluminum pin of 4mm diameter placed in a sample holder. Of these samples, 10 of them were with the sample holder centered with the sample's rotation stage, 10 of them were with an offset between the sample holder and rotation stage centers, and the remainder 10 with an aluminum slab of 10×30 mm as well. Fig. (6.9) features examples of the CT reconstructions of the different groups.

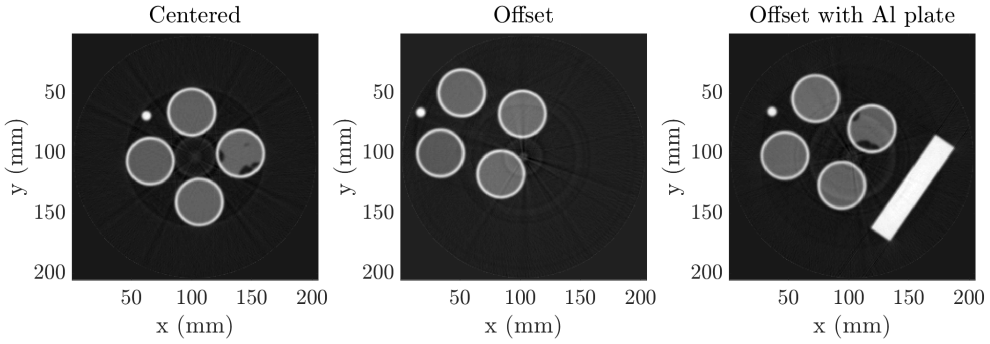

Figure 6.9: Reconstruction examples of the three types of dataset reproduced. Left: the samples are placed centered in respect to the center of rotation. Center: the samples are placed offset in respect to the center of rotation. Right: the samples are placed offset in respect to the center of rotation and an aluminum plate 10×30 mm wide is inserted to cause metal artifacts and photon starvation.

Table (6.6) reports the results of the benchmarking for the different prediction models and sample groups. Differently from the results obtained in the Paper IV of the Appendix, in this work the weighted LAC has been introduced and the weights in the SRZE classification have been calculated using Eq. (6.8), leading to $w_{Z_e} = 0.38$ and $w_{\rho_e} = 0.62$, rather than being equally set to 0.5. All the spectral characterization methods (Spectral LAC, Weighted LAC and SRZE) show an overall improved prediction accuracy when compared with the integrated LAC method

(which corresponds to conventional integrating detectors), showcasing the advantage of spectral techniques.

Table 6.6: The accuracy results (%) obtained for the different sample groups and all of them (overall column). In the exact material classification, the prediction is successful when the specific materials are classified correctly. In the binary classification, the discrimination is only performed between threats and innocuous materials. † Note that the aluminum plates and pins, which are of relatively simple classification, are counted toward the total results.

Material classification

Prediction Model	Centered	Offset	Offset with Al plate†	Overall
Integrated LAC ($\tilde{\mu}$)	24%	28.0%	40.0%	30.7%
Spectral LAC ($\mu(E)$)	80.0%	74.0%	38.3%	64.1%
Weighted LAC ($w_e\mu(E)$)	84.0%	86.0%	83.3%	84.4%
SRZE (ρ_e/Z_e)	84.0%	82.0%	75.0%	80.3%

Binary classification (Threat/Innocuous)

Prediction Model	Centered	Offset	Offset with Al plate	Overall
Integrated LAC ($\tilde{\mu}$)	60.0%	64.0%	75.0%	66.3%
Spectral LAC ($\mu(E)$)	100%	98.0%	66.7%	88.2%
Weighted LAC ($w_e\mu(E)$)	100%	100%	100%	100%
SRZE (ρ_e/Z_e)	100%	100%	83.0%	94.3%

The spectral LAC methods has better results than the integrated one, but worse than the weighted LAC and SRZE methods. This indicates that the energy channels for which the detector correction algorithm is not efficient enough or the photon statistic is too low, need to be treated carefully. This is emphasized by samples with metal artifacts induced by the aluminum plate, for which a decrease in the accuracy of the spectral LAC discrimination method is seen, whereas the accuracy increases with the weighted LAC and SRZE methods. That is because these methods allow data affected by photon starvation induced by the Aluminum plate to be disregarded by energy weights or thresholding.

It is remarked that such a relatively low accuracy in the exact material classification was expected as most of the innocuous materials in the library are water-based compounds and some of them are varieties of the same specimens (e.g. 5 types of beer, 4 sun lotions etc.). On the other hand, the SRZE method shows perfect accuracy in the binary classification for samples without the aluminum plate, and the weighted LAC yields perfect binary classification accuracy for all samples. The superior accuracy of the weighted LAC method in this case can be explained by a better efficiency in disregarding photon starvation effects using energy weights, when compared with the thresholding of the SRZE method.

To analyze the specific materials for which the classification failed a confusion matrix ($\mathcal{C}$) was build. The confusion matrix is a useful tool to determine which materials

require more attention in the classification task and is calculated as:

$$\mathcal{C} = \{c_{i,j}\} = \sum_{label} \delta_{i,j} \tag{6.9}$$

with

$$\delta_{i,j} = \begin{cases} 1, & \text{if } i = label^{real} \quad \& \quad j = label^{predicted} \\ 0, & \text{otherwise.} \end{cases} \tag{6.10}$$

Each element $c_{i,j}$ of the confusion matrix can be interpreted as the instances of the actual material corresponding to the row i that are classified into the material corresponding to the column j. Fig. (6.10) features the normalized confusion matrix for the SRZE classification method. In the normalized confusion matrix, each row is normalized to sum 1 and converted into percent (%). It is observed that from the measurements it is hard to distinguish between brandy, hand cream and water as the first two materials were classified as water. With respect to the binary classification, the shampoo has been classified as the nitromethane threat material, whereas the incorrect classification of methanol and nitromethane did not lead to wrong binary classification.

Materials filled boxes

The second set of experiments consists in 20 test samples composed of a cardboard box filled with different combinations of random threat and innocuous materials. A three-dimensional SCT of each test sample was performed with the same current settings and geometry. The source was set to 150 keV with a 2 mm aluminum filter and fan-geometry collimation of the source, with vertical height field of view at the detector corresponding to the detector's pixel size. For each of the 360 projections distributed between 0 and 360 degrees, the sample stage was continuously translated vertically to have an acquisition of the 2D projections of the sample as one would obtain with cone-beam geometry, while suppressing significantly the scattering noise from the sample. Each of the vertical orthogonal slices was reconstructed using a custom adaptation of the ART-TV reconstruction technique. Fig. (6.11) displays a 3D volume of a single sample, obtained by merging all the vertical orthogonal slice reconstructions.
Table (6.6) reports the overall results of the benchmarking for the different prediction methods. The comparison between the different material features used for the classification task is consistent with the first experiment reported, but improvement of the performance using the weighted LAC and SRZE method is lower when compared with the spectral LAC. Moreover, the weighted LAC method is not superior in both material and binary classification to the SRZE method. The overall decreased accuracy is justified by a larger amount of materials in the reference material library. Fig. (6.12) features the normalized confusion matrix for the SRZE classification method. It is found that the peanut butter, hard cheese and vinegar materials are the major responsible for the low classification accuracy as they are often the result of the prediction of other real materials.

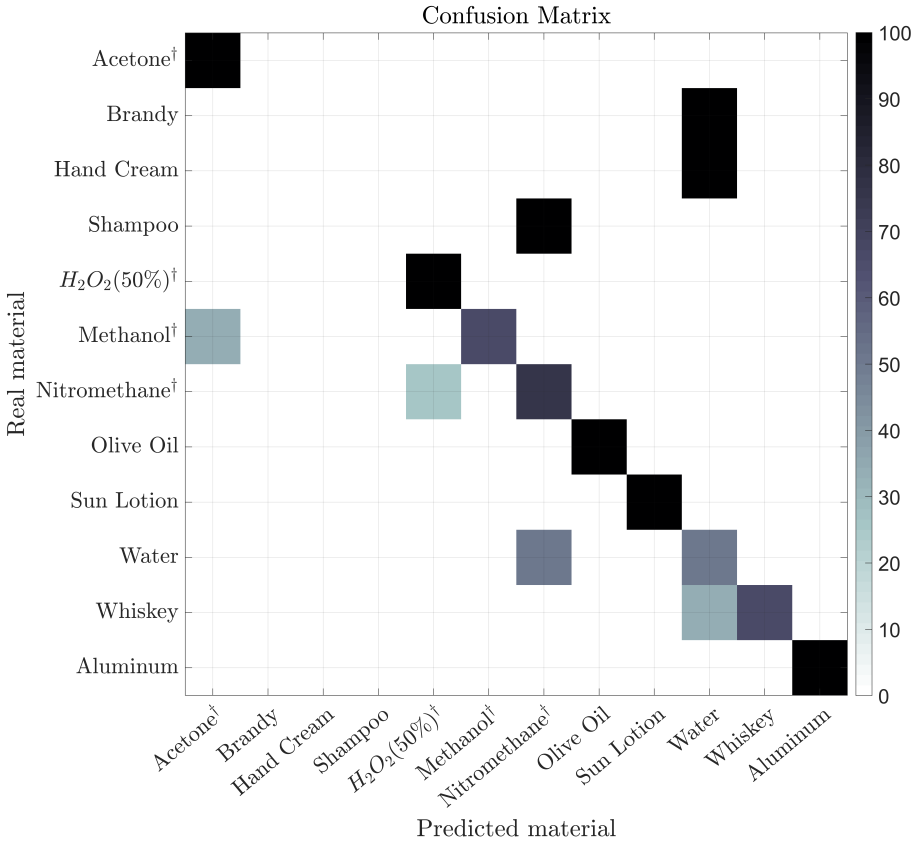

Figure 6.10: Normalized confusion matrix for the SRZE classification. The ideal confusion matrix corresponding to perfect classification is the diagonal identity matrix. The unit of the color bar is the percentage (%) of real materials (y-axis) being predicted as a material from the reference library (x-axis). †Threat materials.

Table 6.7: The accuracy results (%) obtained for the different sample groups. In the exact material classification, the prediction is successful when the specific materials are classified correctly. In the binary classification, the discrimination is only performed between threats and innocuous materials.

Prediction Model	Material Classification	Binary Classification
Integrated LAC ($\tilde{\mu}$)	18.4%	80.2%
Spectral LAC ($\mu(E)$)	36.9%	86.3%
Weighted LAC ($w_e\mu(E)$)	45.6%	86.7%
SRZE (ρ_e/Z_e)	43.7%	87.2%

6.4 Short Summary

In the first part of this chapter the SRZE method using SCT presented in Chapter 3 has been validated using sample with well-known material properties. The assumptions for the reasons producing worse electron density estimation of materials in the first

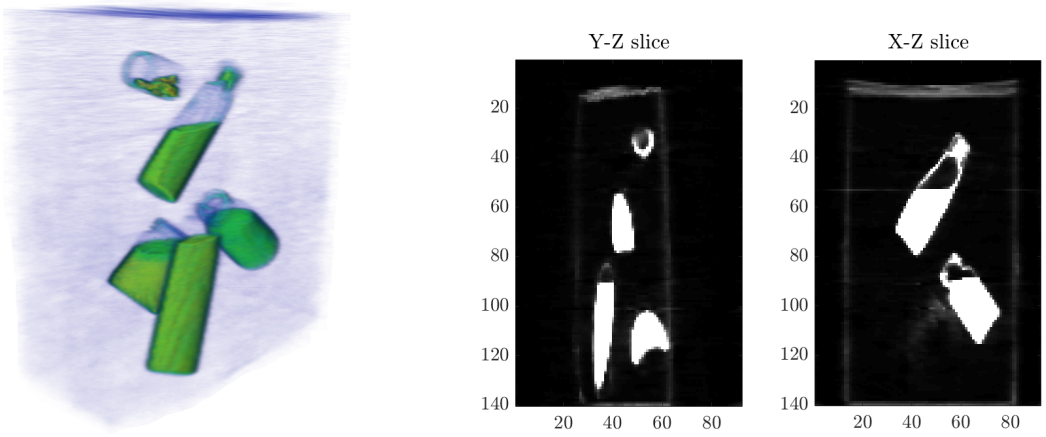

Figure 6.11: Visualization of the 3D reconstruction of a box sample filled with five different materials. To the right side are shown two vertical slices of the reconstruction in the Y-Z and X-Z planes.

experiment (Test Sample 1) were confirmed with a second scan of plastic materials. For this experiment all the estimation deviations were below 3.6%, with a mean deviation of 0.9% for Z_e, and 1.9% for ρ_e. The main advantage of this method is that due the simultaneous measurement of the spectral features it does not require system optimization to estimate high attenuating materials properties but rather, a robust truncation of photon-starved energy channels.

Finally, I have presented a benchmark study of material classification using different material features measured with SCT. All the spectral features used for the material classification produced significantly better accuracy compared with conventional energy integrating features, both in the exact material classification and in the threat/innocuous material discrimination. This study demonstrated the advantage of spectral techniques in extracting additional information on material properties from the energy domain.

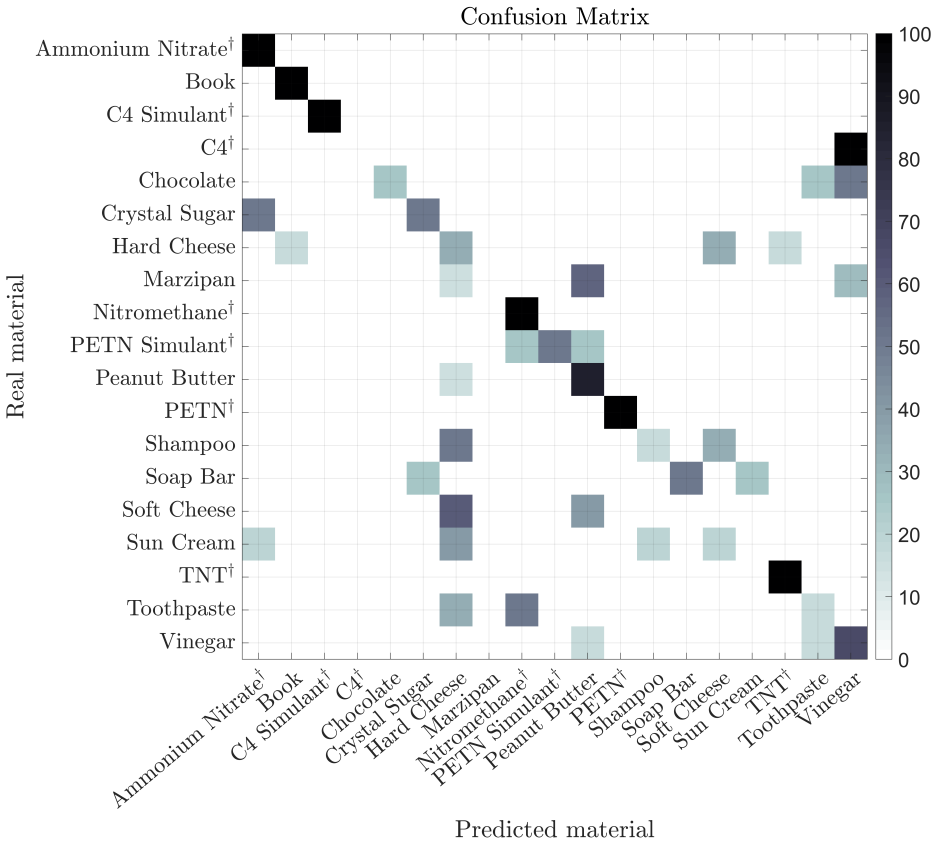

Figure 6.12: Normalized confusion matrix for the SRZE classification. The ideal confusion matrix corresponding to perfect classification is the diagonal identity matrix. The unit of the color bar is the percentage (%) of real materials (y-axis) being predicted as a material from the reference library (x-axis). †Threat materials.

Summary and Outlook 7

This thesis has presented an overview of the current state of laboratory-scale spectral X-ray imaging techniques with a focus on spectral X-ray CT. I presented an overview of the various methods and algorithms for the data processing and correction steps in the overall workflow. Although the experiments were performed to highlight the advantages that this technique offers in security screening applications, the methods and algorithms developed in this research work can also be applied in other fields, such as medical imaging and general non-destructive testing or industrial quality check inspections.

CNN-based corrections

For this research work, I have developed new correction methods for scattering and metal artifacts correction methods in the spectral image processing workflow. The methods (shown in Chapter 5) use a spectral Convolutional Neural Network (CNN) architecture from the field of machine. Compared to related work, the proposed approach learns features from the energy domain extending the range of the problems that can successfully corrected. The advantages of these methods, is that they can generalize for the problem to be solved as the prior information required for the correction is intrinsically incorporated in the training data. The correction step for real measured data is then parameter-free and with near real-time speed, satisfying requirement of real scanners. The performance of these methods depends highly on the quality of the training data and how well its variety generalizes the problem. It was shown how the fabrication of training data can be a slow and in some cases complex procedure, which needs to be tailored for the desired application. However, this aspect becomes simpler in cases where the diversity of the objects under inspection decreases. For the application cases presented in this thesis, the corrections always successfully accomplished the given task improving the results. The current limitation of this correction method is the introduction of blur in the reconstruction, which is mainly due to the computational hardware limitations. Due to the extremely large size of spectral reconstructions (3 or 4-D), the input data was downsampled in size losing high-resolution features. Likewise, the spectral CNN architecture was relatively limited in the layers depth and in the number and size of the convolutional filter (weight tensors).

For this reasons, high-resolution scanners with a large data size may require further adaptations of the architecture or fragmentation of the datasets into smaller patches followed by a successive merging. Nevertheless, it is expected that future technology and findings will overcome these limitations.

Material Characterization Methods

In Chapter 3 I have presented an overview of the different material characterization methods enabled with spectral-CT techniques. For this research work, we adopted a channel-by-channel approach for the reconstruction techniques, which preserves the energy resolution of the materials' LAC. Thus, the SRZE method we have developed for the estimation of the system-independent material properties of effective atomic number and electron density is of a post-reconstruction type. Within the security-screening field, this is justified by the high variety of the materials that can be found in the investigated objects. Nonetheless, pre-reconstruction approaches are preferred in specialized applications, where more *a-priori* knowledge of the samples is available. The SRZE method presented has shown accuracy and precision that are comparable to its state-of-the-art competitor using Dual Energy CT scans. The relative deviations from the expected ground truth, for the plastic samples experiment, were all below 3.6%, with a mean deviation of 0.9% for Z_{e}, and 1.9% for ρ_{e}. In addition, the characterization of titanium, a highly attenuating material, was possible without changes to the scanning system or the method parameters. This demonstrates the advantage of this spectral technique, in terms of the higher flexibility of the material range that can be scanned without modification of the instrument parameters. Unfortunately, it was not possible to evaluate a direct performance comparison of spectral and dual-energy CT techniques.

With respect to the overarching goal of security screening, that is the classification of material, and their discrimination into threat/innocuous material, all the spectral measured features produced significantly higher accuracy compared to the conventional energy-integrating one. The accuracy was improved up to $\approx$ 35% for the threat detection and up to $\approx$ 55% for the material classification. It was found a higher robustness when using the weighted energy-resolved LAC as the material feature for classification, compared with the ones estimated with the SRZE method. This is due to the high sensitivity of the method to the low energy channels, which are more unstable due to lower photon statistics and detector distortion effects. Nonetheless, both methods produce similar results.

Limitations and Outlook

The performance of this technique at its current state and the methods presented is limited by the relatively high cost and restricted amount of the photon counting detectors in the market, which are compulsory in the instrumentation. The accuracy

of the estimation of the material properties revealed using spectral X-ray CT highly depends on the efficiency of the detector in the measurement of the spectrum of the incoming radiation at different flux densities. While correction algorithms can overcome most of the spectrum distortions that these detectors suffer from, advances in hardware in terms of spectral resolution and performance, especially in the low energy domain, will also improve results in the accuracy and precision.
As ideas for future work, I identify and list:

- Improvement of the training data for the CNN correction methods. This can be done by including more complex and realistic shapes and more different material properties, and increasing the overall amount of training data.
- Further development of the spectral CNN architecture. This could be done by implementing energy-dependent loss functions, to overcome the fact that the value difference between images is higher at low energies due to the characteristics of the LAC. Another aspect would be the use of objective function, to incorporate material segmentation and prevent blurring and loss of feature resolution.
- Implementation of spectral reconstruction techniques, which can better utilize the additional information in the spectral domain, rather than an elementary channel-by-channel approach.
- Direct benchmarking of the characterization and classification accuracy, under the same experimental conditions, using spectral X-ray CT and the current state-of-the-art technology, Dual-Energy CT.

The first spectral X-ray applications in the literature and in industry are not older than a decade. Since the technology is at such an early stage, the results of this study demonstrate that spectral techniques are indubitably the future of X-ray imaging.

Bibliography

[1] F Edward Boas and Dominik Fleischmann. CT artifacts: causes and reduction techniques. *Imaging in Medicine*, 4(2):229–240, 2012.

[2] JL Fobes, D McAnulty, BA Klock, J Janowitz, and E Neiderman. Test and evaluation plan for the explosive device detection baseline (EDDB) study. Technical report, GALAXY SCIENTIFIC CORP MAYS LANDING NJ, 1995.

[3] Transportation Security Administration. Computed tomography. `https://www.tsa.gov/computed-tomography`.

[4] Paul Seidenstat and Francis X Splane. *Protecting airline passengers in the age of terrorism*. ABC-CLIO, 2009.

[5] Robert E Alvarez and Albert Macovski. Energy-selective reconstructions in X-ray computerised tomography. *Physics in Medicine & Biology*, 21(5):733, 1976.

[6] Zhengrong Ying, Ram Naidu, and Carl R Crawford. Dual energy computed tomography for explosive detection. *Journal of X-ray Science and Technology*, 14(4):235–256, 2006.

[7] Alvin C Silva, Brian G Morse, Amy K Hara, Robert G Paden, Norio Hongo, and William Pavlicek. Dual-energy (spectral) CT: applications in abdominal imaging. *Radiographics*, 31(4):1031–1046, 2011.

[8] Stephen G Azevedo, Harry E Martz, Maurice B Aufderheide, William D Brown, Kyle M Champley, Jeffrey S Kallman, G Patrick Roberson, Daniel Schneberk, Isaac M Seetho, and Jerel A Smith. System-independent characterization of materials using dual-energy computed tomography. *IEEE Transactions on Nuclear Science*, 63(1):341–350, 2016.

[9] Kyle M. Champley, Stephen G. Azevedo, Isaac M. Seetho, Steven M. Glenn, Larry D. McMichael, Jerel A. Smith, Jeffrey S. Kallman, William D Brown, and Harry E. Martz. Method to extract system-independent material properties from Dual-Energy X-ray CT. *Submitted to IEEE Transactions on Nuclear Science (2018)*, 2018.

[10] Polad M Shikhaliev. Energy-resolved computed tomography: first experimental results. *Physics in Medicine & Biology*, 53(20):5595, 2008.

[11] NG Anderson, AP Butler, NJA Scott, NJ Cook, JS Butzer, N Schleich, M Firsching, R Grasset, N De Ruiter, M Campbell, et al. Spectroscopic (multi-energy) CT distinguishes iodine and barium contrast material in MICE. *European radiology*, 20(9):2126–2134, 2010.

[12] Juergen Fornaro, Sebastian Leschka, Dennis Hibbeln, Anthony Butler, Nigel Anderson, Gregor Pache, Hans Scheffel, Simon Wildermuth, Hatem Alkadhi, and Paul Stolzmann. Dual-and multi-energy CT: approach to functional imaging. *Insights into imaging*, 2(2):149–159, 2011.

[13] Veronique Rebuffel, Jean Rinkel, Joachim Tabary, and Loick Verger. New perspectives of X-ray techniques for explosive detection based on CdTe/CdZnTe spectrometric detectors. *Proc. of the Int. Symp. on Digital Industrial Radiology and Computed Tomography*, 2, 2011.

[14] E Roessl and R Proksa. K-edge imaging in X-ray computed tomography using multi-bin photon counting detectors. *Physics in Medicine & Biology*, 52(15):4679, 2007.

[15] JP Schlomka, E Roessl, R Dorscheid, S Dill, G Martens, T Istel, C Bäumer, C Herrmann, R Steadman, G Zeitler, et al. Experimental feasibility of multi-energy photon-counting K-edge imaging in pre-clinical computed tomography. *Physics in Medicine & Biology*, 53(15):4031, 2008.

[16] E Bergbäck Knudsen, Andrea Prodi, Jana Baltser, Maria Thomsen, P Kjær Willendrup, M Sanchez del Rio, Claudio Ferrero, Emmanuel Farhi, Kristoffer Haldrup, Anette Vickery, et al. McXtrace: a Monte Carlo software package for simulating X-ray optics, beamlines and experiments. *Journal of Applied Crystallography*, 46(3):679–696, 2013.

[17] Jens Als-Nielsen and Des McMorrow. *Elements of modern X-ray physics*. John Wiley & Sons, 2011.

[18] Paolo Russo. *Handbook of X-ray imaging: physics and technology*. CRC Press, 2017.

[19] Alessandro Olivo and Robert Speller. A coded-aperture technique allowing x-ray phase contrast imaging with conventional sources. *Applied Physics Letters*, 91(7):074106, 2007.

[20] A Olivo, S Gkoumas, M Endrizzi, CK Hagen, MB Szafraniec, PC Diemoz, PRT Munro, K Ignatyev, B Johnson, JA Horrocks, et al. Low-dose phase contrast mammography with conventional x-ray sources. *Medical physics*, 40(9):090701, 2013.

[21] Alberto Astolfo, Marco Endrizzi, Benjamin Price, Ian Haig, and Alessandro Olivo. The first large area, high X-ray energy phase contrast prototype for

enhanced detection of threat object in baggage screening. In *Optics and Photonics for Counterterrorism, Crime Fighting, and Defence XII*, volume 9995, page 999505. International Society for Optics and Photonics, 2016.

[22] Marco Endrizzi. X-ray phase-contrast imaging. *Nuclear Instruments and Methods in Physics Research Section A: Accelerators, Spectrometers, Detectors and Associated Equipment*, 878:88–98, 2018.

[23] Martin J Berger and JH Hubbell. XCOM: Photon cross sections on a personal computer. Technical report, National Bureau of Standards, Washington, DC (USA). Center for Radiation, 1987.

[24] Lellery Storm and Harvey I Israel. Photon cross sections from 1 keV to 100 MeV for elements Z= 1 to Z= 100. *Atomic Data and Nuclear Data Tables*, 7(6):565–681, 1970.

[25] JH Hubbell. Photon cross sections, attenuation coefficients and energy absorption coefficients. *National Bureau of Standards Report NSRDS-NBS29, Washington DC*, 1969.

[26] Christopher T Chantler. Theoretical form factor, attenuation, and scattering tabulation for Z= 1–92 from E= 1–10 eV to E= 0.4–1.0 MeV. *Journal of Physical and Chemical Reference Data*, 24(1):71–643, 1995.

[27] R Jenkins, R Manne, R Robin, and C Senemaud. IUPACâ€"nomenclature system for X-ray spectroscopy. *X-Ray Spectrometry*, 20(3):149–155, 1991.

[28] J Baró, M Roteta, JM Fernández-Varea, and F Salvat. Analytical cross sections for Monte Carlo simulation of photon transport. *Radiation physics and chemistry*, 44(5):531–552, 1994.

[29] F Hajdu. Revised parameters of the analytic fits for coherent and incoherent scattered X-ray intensities of the first 36 atoms. *Acta Crystallographica Section A: Crystal Physics, Diffraction, Theoretical and General Crystallography*, 28(3):250–252, 1972.

[30] G Palinkas. Analytic approximations for the incoherent X-ray intensities of the atoms from Ca to Am. *Acta Crystallographica Section A: Crystal Physics, Diffraction, Theoretical and General Crystallography*, 29(1):10–12, 1973.

[31] Oskar Klein and Yoshio Nishina. Über die streuung von strahlung durch freie elektronen nach der neuen relativistischen quantendynamik von Dirac. *Zeitschrift für Physik*, 52(11-12):853–868, 1929.

[32] JH Hubbell, Wm J Veigele, EA Briggs, RT Brown, DT Cromer, and d RJ Howerton. Atomic form factors, incoherent scattering functions, and photon scattering cross sections. *Journal of physical and chemical reference data*, 4(3):471–538, 1975.

[33] VH Smith, AJ Thakkar, and DC Chapman. A new analytic approximation to atomic incoherent X-ray scattering intensities. *Acta Crystallographica Section A: Crystal Physics, Diffraction, Theoretical and General Crystallography*, 31(3):391–392, 1975.

[34] Johann Radon. On the determination of functions from their integral values along certain manifolds. *IEEE transactions on medical imaging*, 5(4):170–176, 1986.

[35] Per Christian Hansen. *Discrete inverse problems: insight and algorithms*, volume 7. Siam, 2010.

[36] Jiang Hsieh et al. Computed tomography: principles, design, artifacts, and recent advances. SPIE Bellingham, WA, SPIE, 2009.

[37] Lucas L Geyer, U Joseph Schoepf, Felix G Meinel, John W Nance Jr, Gorka Bastarrika, Jonathon A Leipsic, Narinder S Paul, Marco Rengo, Andrea Laghi, and Carlo N De Cecco. State of the art: iterative CT reconstruction techniques. *Radiology*, 276(2):339–357, 2015.

[38] Kristoffer Haldrup, Gianluca Levi, Elisa Biasin, Peter Vester, Mads Goldschmidt Laursen, Frederik Beyer, Kasper Skov Kjær, Tim Brandt Van Driel, Tobias Harlang, Asmus O Dohn, et al. Ultrafast X-ray scattering measurements of coherent structural dynamics on the ground-state potential energy surface of a diplatinum molecule. *Physical review letters*, 122(6):063001, 2019.

[39] Katsuyuki Taguchi and Jan S Iwanczyk. Vision 20/20: Single photon counting X-ray detectors in medical imaging. *Medical physics*, 40(10), 2013.

[40] B Henrich, A Bergamaschi, C Broennimann, R Dinapoli, EF Eikenberry, I Johnson, M Kobas, P Kraft, A Mozzanica, and B Schmitt. Pilatus: A single photon counting pixel detector for X-ray applications. *Nuclear Instruments and Methods in Physics Research Section A: Accelerators, Spectrometers, Detectors and Associated Equipment*, 607(1):247–249, 2009.

[41] Sebastian Siegfried Lukas Ehn. *Photon-counting Hybrid-pixel Detectors for Spectral X-ray Imaging Applications*. PhD thesis, Technische Universität München, 2017.

[42] A Gorecki, A Brambilla, V Moulin, E Gaborieau, P Radisson, and L Verger. Comparing performances of a CdTe X-ray spectroscopic detector and an X-ray dual-energy sandwich detector. *Journal of Instrumentation*, 8(11):P11011, 2013.

[43] A Brambilla, P Ouvrier-Buffet, Jean Rinkel, G Gonon, C Boudou, and L Verger. CdTe linear pixel X-ray detector with enhanced spectrometric performance for high flux X-ray imaging. *IEEE Transactions on Nuclear Science*, 59(4):1552–1558, 2012.

[44] Jae Cheon Kim, William R Kaye, and Zhong He. Signal modeling of charge sharing effect in simple pixelated CdZnTe detector. *Journal of the Korean Physical Society*, 64(9):1336–1345, 2014.

[45] DS McGregor and H Hermon. Room-temperature compound semiconductor radiation detectors. *Nuclear Instruments and Methods in Physics Research Section A: Accelerators, Spectrometers, Detectors and Associated Equipment*, 395(1):101–124, 1997.

[46] M Kroupa, J Jakubek, and F Krejci. Charge collection characterization with semiconductor pixel detector timepix. In *2008 IEEE Nuclear Science Symposium Conference Record*, pages 259–262. IEEE, 2008.

[47] Jochen Cammin, Jennifer Xu, William C Barber, Jan S Iwanczyk, Neal E Hartsough, and Katsuyuki Taguchi. A cascaded model of spectral distortions due to spectral response effects and pulse pileup effects in a photon-counting X-ray detector for CT. *Medical physics*, 41(4), 2014.

[48] Erik Schou Dreier, Jan Kehres, Mohamad Khalil, Matteo Busi, Yun Gu, Robert Feidenhans, and Ulrik Lund Olsen. Spectral correction algorithm for multispectral CdTe X-ray detectors. *Optical Engineering*, 57(5):054117, 2018.

[49] John A Victoreen. The absorption of incident quanta by atoms as defined by the mass photoelectric absorption coefficient and the mass scattering coefficient. *Journal of Applied Physics*, 19(9):855–860, 1948.

[50] WV Mayneord. The significance of the roentgen. *Acta Int Union Against Cancer*, 2:271, 1937.

[51] A Brambilla, A Gorecki, A Potop, C Paulus, and L Verger. Basis material decomposition method for material discrimination with a new spectrometric X-ray imaging detector. *Journal of Instrumentation*, 12(08):P08014, 2017.

[52] Parisa Babaheidarian and David Castañón. Feature selection for material identification in spectral CT. *Electronic Imaging*, 2018(15):134–1, 2018.

[53] Salim Si-Mohamed, David P Cormode, Daniel Bar-Ness, Monica Sigovan, Pratap C Naha, Jean-Baptiste Langlois, Lara Chalabreysse, Philippe Coulon, Ira Blevis, Ewald Roessl, et al. Evaluation of spectral photon counting computed tomography K-edge imaging for determination of gold nanoparticle biodistribution in vivo. *Nanoscale*, 9(46):18246–18257, 2017.

[54] Kyle Champley. Livermore tomography tools (LTT) technical manual. *LLNL, Livermore, CA, USA, Tech. Rep. LLNL-SM-687016*, 2016.

[55] Emil Y Sidky, Chien-Min Kao, and Xiaochuan Pan. Accurate image reconstruction from few-views and limited-angle data in divergent-beam CT. *Journal of X-ray Science and Technology*, 14(2):119–139, 2006.

[56] Peter Gilbert. Iterative methods for the three-dimensional reconstruction of an object from projections. *Journal of theoretical biology*, 36(1):105–117, 1972.

[57] Wim van Aarle, Willem Jan Palenstijn, Jan De Beenhouwer, Thomas Altantzis, Sara Bals, K Joost Batenburg, and Jan Sijbers. The ASTRA toolbox: A platform for advanced algorithm development in electron tomography. *Ultramicroscopy*, 157:35–47, 2015.

[58] Christian Kehl, Wail Mustafa, Jan Kehres, Anders Bjorholm Dahl, and Ulrik Lund Olsen. Multi-spectral imaging via computed tomography (MUSIC) - comparing unsupervised spectral segmentations for material differentiation. *arXiv preprint arXiv:1810.11823*, 2018.

[59] Dean S Hazineh and Joel A Greenberg. Coding versus collimation in pencil-beam X-ray diffraction tomography. In *Anomaly Detection and Imaging with X-Rays (ADIX) IV*, volume 10999, page 1099909. International Society for Optics and Photonics, 2019.

[60] Lawrie B Skinner, Congcong Huang, Daniel Schlesinger, Lars GM Pettersson, Anders Nilsson, and Chris J Benmore. Benchmark oxygen-oxygen pair-distribution function of ambient water from X-ray diffraction measurements with a wide q-range. *The Journal of chemical physics*, 138(7):074506, 2013.

[61] Matteo Busi. McXtrace CT. `https://github.com/matteobsu/mcxtraceCT`, 2019.

[62] Michael Garland and Paul S Heckbert. Surface simplification using quadric error metrics. In *Proceedings of the 24th annual conference on Computer graphics and interactive techniques*, pages 209–216. ACM Press/Addison-Wesley Publishing Co., 1997.

[63] Michael E Gehm. Simulation-based X-ray system design and analysis: past, present, and future. In *Anomaly Detection and Imaging with X-Rays (ADIX) IV*, volume 10999, page 1099902. International Society for Optics and Photonics, 2019.

[64] Martin J Berger, JH Hubbell, SM Seltzer, J Chang, JS Coursey, Ry Sukumar, DS Zucker, and K Olsen. XCOM: Photon cross sections database. *NIST Standard reference database*, 8(1):3587–3597, 1998.

[65] Reuven Y Rubinstein and Dirk P Kroese. *Simulation and the Monte Carlo method*, volume 10. John Wiley & Sons, 2016.

[66] Jan Kehres, Mark Lyksborg, and Ulrik Lund Olsen. Threat detection of liquid explosives and precursors from their X-ray scattering pattern using energy dispersive detector technology. In *Radiation Detectors in Medicine, Industry, and National Security XVIII*, page 1. SPIE, sep 2017.

[67] Arthur H Compton. A quantum theory of the scattering of X-rays by light elements. *Physical review*, 21(5):483, 1923.

[68] Ernst-Peter Rührnschopf and Klaus Klingenbeck. A general framework and review of scatter correction methods in cone beam CT. Part 2: scatter estimation approaches. *Medical physics*, 38(9):5186–5199, 2011.

[69] A. Sossin, J. Tabary, V. Rebuffel, J.M. Létang, N. Freud, and L. Verger. Fast scattering simulation tool for multi-energy X-ray imaging. *Nuclear Instruments and Methods in Physics Research Section A: Accelerators, Spectrometers, Detectors and Associated Equipment*, 802:60 – 66, 2015.

[70] A. P. Colijn and F. J. Beekman. Accelerated Simulation of Cone Beam X-Ray Scatter Projections. *IEEE Transactions on Medical Imaging*, 23(5):584–590, may 2004.

[71] Bernard W Silverman. *Density estimation for statistics and data analysis*, volume 26. CRC press, 1986.

[72] Shai Shalev-Shwartz, Shaked Shammah, and Amnon Shashua. Safe, multi-agent, reinforcement learning for autonomous driving. *arXiv preprint arXiv:1610.03295*, 2016.

[73] Tom Fawcett and Foster J Provost. Combining data mining and machine learning for effective user profiling. In *KDD*, pages 8–13, 1996.

[74] Xin Li and Hsinchun Chen. Recommendation as link prediction in bipartite graphs: A graph kernel-based machine learning approach. *Decision Support Systems*, 54(2):880–890, 2013.

[75] Nil Goksel Canbek and Mehmet Emin Mutlu. On the track of artificial intelligence: Learning with intelligent personal assistants. *Journal of Human Sciences*, 13(1):592–601, 2016.

[76] Kaiming He, Xiangyu Zhang, Shaoqing Ren, and Jian Sun. Deep residual learning for image recognition. In *The IEEE Conference on Computer Vision and Pattern Recognition (CVPR)*, June 2016.

[77] Barret Zoph, Vijay Vasudevan, Jonathon Shlens, and Quoc V Le. Learning transferable architectures for scalable image recognition. In *Proceedings of the IEEE conference on computer vision and pattern recognition*, pages 8697–8710, 2018.

[78] Tsung-Han Chan, Kui Jia, Shenghua Gao, Jiwen Lu, Zinan Zeng, and Yi Ma. Pcanet: A simple deep learning baseline for image classification? *IEEE transactions on image processing*, 24(12):5017–5032, 2015.

[79] Fausto Milletari, Nassir Navab, and Seyed-Ahmad Ahmadi. V-net: Fully convolutional neural networks for volumetric medical image segmentation. In *2016 Fourth International Conference on 3D Vision (3DV)*, pages 565–571. IEEE, 2016.

[80] Yanbo Zhang and Hengyong Yu. Convolutional neural network based metal artifact reduction in X-ray computed tomography. *IEEE transactions on medical imaging*, 37(6):1370–1381, 2018.

[81] Shiyu Xu, Peter Prinsen, Jens Wiegert, and Ravindra Manjeshwar. Deep residual learning in CT physics: scatter correction for spectral CT. In *2017 IEEE Nuclear Science Symposium and Medical Imaging Conference (NSS/MIC)*, pages 1–3. IEEE, 2017.

[82] Joscha Maier, Stefan Sawall, Michael Knaup, and Marc Kachelrieß. Deep Scatter Estimation (DSE): Accurate real-time scatter estimation for X-Ray CT using a Deep Convolutional Neural Network. *Journal of Nondestructive Evaluation*, 37(3):57, 2018.

[83] Hu Chen, Yi Zhang, Mannudeep K Kalra, Feng Lin, Yang Chen, Peixi Liao, Jiliu Zhou, and Ge Wang. Low-dose CT with a residual encoder-decoder convolutional neural network. *IEEE transactions on medical imaging*, 36(12):2524–2535, 2017.

[84] Eunhee Kang, Junhong Min, and Jong Chul Ye. A deep convolutional neural network using directional wavelets for low-dose X-ray CT reconstruction. *Medical physics*, 44(10):e360–e375, 2017.

[85] Olaf Ronneberger, Philipp Fischer, and Thomas Brox. U-Net: Convolutional Networks for Biomedical Image Segmentation. In Nassir Navab, Joachim Hornegger, William M. Wells, and Alejandro F. Frangi, editors, *Medical Image Computing and Computer-Assisted Intervention – MICCAI 2015*, pages 234–241, Cham, 2015. Springer International Publishing.

[86] Sergey Ioffe and Christian Szegedy. Batch normalization: Accelerating deep network training by reducing internal covariate shift. *arXiv preprint arXiv:1502.03167*, 2015.

[87] Özgün Çiçek, Ahmed Abdulkadir, Soeren S. Lienkamp, Thomas Brox, and Olaf Ronneberger. 3D U-Net: Learning Dense Volumetric Segmentation from Sparse Annotation. In Sebastien Ourselin, Leo Joskowicz, Mert R. Sabuncu, Gozde Unal, and William Wells, editors, *Medical Image Computing and Computer-Assisted Intervention – MICCAI 2016*, pages 424–432, Cham, 2016. Springer International Publishing.

[88] Keras Team. Keras: Deep learning for humans. `https://github.com/keras-team/keras`, 2019.

[89] Nitish Srivastava, Geoffrey Hinton, Alex Krizhevsky, Ilya Sutskever, and Ruslan Salakhutdinov. Dropout: a simple way to prevent neural networks from overfitting. *The journal of machine learning research*, 15(1):1929–1958, 2014.

[90] Diederik P Kingma and Jimmy Ba. Adam: A method for stochastic optimization. *arXiv preprint arXiv:1412.6980*, 2014.

[91] Daniil Kazantsev, Valery Pickalov, Srikanth Nagella, Edoardo Pasca, and Philip J Withers. TomoPhantom, a software package to generate 2D–4D analytical phantoms for CT image reconstruction algorithm benchmarks. *SoftwareX*, 7:150–155, 2018.

[92] Andrew NG. Machine learning. `https://www.coursera.org/learn/machine-learning`.

[93] Wim van Aarle, Willem Jan Palenstijn, Jan De Beenhouwer, Thomas Altantzis, Sara Bals, K. Joost Batenburg, and Jan Sijbers. The ASTRA Toolbox: A platform for advanced algorithm development in electron tomography. *Ultramicroscopy*, 157:35–47, oct 2015.

[94] Zhou Wang, Alan C Bovik, Hamid R Sheikh, Eero P Simoncelli, et al. Image quality assessment: from error visibility to structural similarity. *IEEE transactions on image processing*, 13(4):600–612, 2004.

[95] Technical University of Denmark (DTU). The 3D imaging center, 3DIM. `http://www.imaging.dtu.dk/`.

[96] KC Bond, JA Smith, JN Treuer, S Azevedo, JS Kallman, and HE Martz. ZeCalc algorithm details, version 6. Technical report, LLNL Tech. Rep., LLNL-TR-609327,(Jan. 2013). To request a copy of ZeCalc software, contact Mary Holden-Sanchez at holdensanchez2@ llnl. gov, 2013.

[97] Alex A Dooraghi, Brian J Fix, Jerel A Smith, William D Brown, Stephen G Azevedo, and Harry E Martz. Characterization of a spectroscopic detector for application in X-ray computed tomography. In *Developments in X-Ray Tomography XI*, volume 10391, page 103911G. International Society for Optics and Photonics, 2017.

[98] Kyle M Champley, Stephen G Azevedo, Isaac M Seetho, Steven M Glenn, Larry D McMichael, Jerel A Smith, Jeffrey S Kallman, William D Brown, and Harry E Martz. Method to extract system-independent material properties from dual-energy X-ray CT. *IEEE Transactions on Nuclear Science*, 66(3):674–686, 2019.

[99] Limor Eger, Synho Do, Prakash Ishwar, W Clem Karl, and Homer Pien. A learning-based approach to explosives detection using multi-energy X-ray

computed tomography. In *2011 IEEE International Conference on Acoustics, Speech and Signal Processing (ICASSP)*, pages 2004–2007. IEEE, 2011.

[100] Kristoffer Haldrup. Singular value decomposition as a tool for background corrections in time-resolved XFEL scattering data. *Philosophical Transactions of the Royal Society B: Biological Sciences*, 369(1647):20130336, 2014.

Papers

Paper I

Simulation tools for scattering corrections in spectrally resolved X-ray computed tomography using McXtrace.

Matteo Busi, Ulrik L. Olsen, Erik B. Knudsen, Jeppe R. Frisvad, Jan Kehres, Erik S. Dreier, Mohamad Khalil, and Kristoffer Haldrup

Optical Engineering 57(3), 037105 (March 2018)

Simulation tools for scattering corrections in spectrally resolved x-ray computed tomography using McXtrace

Matteo Busi,[a,*] Ulrik L. Olsen,[a] Erik B. Knudsen,[a] Jeppe R. Frisvad,[b] Jan Kehres,[a] Erik S. Dreier,[c] Mohamad Khalil,[a] and Kristoffer Haldrup[a]
[a]NEXMAP Section, DTU Physics, Kongens Lyngby, Denmark
[b]DTU Compute, Kongens Lyngby, Denmark
[c]Niels Bohr Institute, Copenhagen, Denmark

Abstract. Spectral computed tomography is an emerging imaging method that involves using recently developed energy discriminating photon-counting detectors (PCDs). This technique enables measurements at isolated high-energy ranges, in which the dominating undergoing interaction between the x-ray and the sample is the incoherent scattering. The scattered radiation causes a loss of contrast in the results, and its correction has proven to be a complex problem, due to its dependence on energy, material composition, and geometry. Monte Carlo simulations can utilize a physical model to estimate the scattering contribution to the signal, at the cost of high computational time. We present a fast Monte Carlo simulation tool, based on McXtrace, to predict the energy resolved radiation being scattered and absorbed by objects of complex shapes. We validate the tool through measurements using a CdTe single PCD (Multix ME-100) and use it for scattering correction in a simulation of a spectral CT. We found the correction to account for up to 7% relative amplification in the reconstructed linear attenuation. It is a useful tool for x-ray CT to obtain a more accurate material discrimination, especially in the high-energy range, where the incoherent scattering interactions become prevailing (>50 keV).
 [DOI: 10.1117/1.OE.57.3.037105]

Keywords: computed tomography; spectral computed tomography; multienergy computed tomography; x-ray scattering; Monte Carlo simulations; scattered radiation; fan-beam computed tomography; incoherent scattering.

Paper 171692P received Oct. 25, 2017; accepted for publication Feb. 14, 2018; published online Mar. 14, 2018.

1 Introduction

X-ray computed tomography (CT) is an imaging technique that has been developed since the 1970s and is used daily for many purposes, such as medical diagnostics, airport security screening, and food quality.[1–3] An x-ray CT acquisition consists in measuring the ratio between the transmitted and incident photons on an object under investigation from multiple angles. To achieve high-quality imaging of the object, it is of key importance to have a good model of the physical interactions between the x-ray photons and the sample. Most of the reconstruction techniques implemented in conventional CT scanners are based on the Bouguer–Beer–Lambert law, where the interactions are assumed to be fully described by an exponential attenuation model. Moreover, the detectors adopted by these instruments are typically based on single or dual energy methods, in which the incoming radiation signal is integrated in the full energy interval, losing the energy-dependent features. Consequently, in standard commercial x-ray CT scanners, there are two main effects deteriorating the quality of the reconstructions.

First, the x-ray source is typically emission from an anode that generates a polychromatic beam. However, materials absorb the low-energy photons more efficiently than high-energy photons, resulting in cupping and streaking artifacts in the reconstructions due to such beam hardening. Monte Carlo (MC) simulations have been used to predict and correct such effects.[4] However, it turns out to be challenging in fields, where the sample is complex and the materials have a wide range of attenuating materials. An emerging technique involves the use of single photon-counting detectors (PCDs)[5] capable of discriminating the energy of the incoming photons. In this way, under the assumption that the energy resolution is good enough, each measurement can be considered a set of monochromatic acquisitions in what is called spectral CT.

Second, the reconstruction models do not consider that the detected total signal is not only composed of the primary radiation, the photons reaching the detector along a linear path from the source, but also of the scattered radiation, the photons having undergone scattering events within the sample volume. Johns and Yaffe[6] have shown that this scattering contribution can produce significant cupping artifacts in fan-beam geometry CT acquisitions. Nevertheless, compared to the cone-beam CT, its impact is substantially decreased due to a reduced volume of the sample being irradiated and the detection solid angle being restricted to the fan-beam plane. For an overview of the recent approaches to correct for this effect, the reader is referred to a review by Rührnschopf and Klingenbeck.[7] At present, however, most of the solutions for the scattering correction adopted in commercial scanners are based on simple Poisson models of the scattering contribution, which may lead into bias artifacts in the reconstruction.

A more accurate approach is to obtain a direct estimate of the scattered radiation, based on the physical interactions between photons and matter in the CT instrument by an MC simulation of the measurement. A simulation method

*Address all correspondence to: Matteo Busi, E-mail: mbusi@fysik.dtu.dk

0091-3286/2018/$25.00 © 2018 SPIE

providing spectral scattering estimate in fast time scales has recently been developed and validated, based on a hybrid MC and deterministic approach.[8] In the latter, the scattering points in the sample are computed by MC simulations, and then deterministic calculations set the particle fractions reaching each detector pixel. Another limitation of current MC simulation methods is that samples are typically rendered as simple polygons or triangle meshes. Therefore, samples of complex shapes and overlapping between each other would dramatically increase computational costs. Last, most of the MC simulation tools proposed at present are based on energy integrating detectors, which are not compatible with spectral CT.

In this work, we present a fully stochastic MC simulation tool for spectral CT x-ray tracing featuring an estimation of the scattered radiation, based on volumetric discretized phantoms, which allows the computation of complex sample geometries without an impact on the time efficiency. Our preliminary investigations of this technique have been presented elsewhere,[9] the pseudocode for our algorithm is therefore not in the main text but deferred to the Appendix. In Sec. 2, we show the methods implemented in the simulation tool and the technique adopted to experimentally detect the scattered radiation contribution. In Sec. 3, we validate the simulation tool by comparing the scattering signal obtained by simulation and real acquisitions. Finally, in Sec. 4, we present a simulation study carried out to estimate and correct for the scattered radiation contribution to spectral CT and we draw some conclusions in Sec. 5.

2 Methods

In spectral CT, the total detected signal $S_t(\vec{r}, E)$ is a function of the pixel position $\vec{r}$ and energy E and can be written as follows:

$$S_t(\vec{r}, E) = S_p(\vec{r}, E) + S_s(\vec{r}, E) + S_{\text{bkg}}(\vec{r}, E), \tag{1}$$

where $S_p(\vec{r}, E)$ is the primary signal, which is the detected photons not undergoing interactions with the object; $S_s(\vec{r}, E)$ is the scattered signal, composed of the photons being scattered by the sample. Last, $S_{\text{bkg}}(\vec{r}, E)$ is the background contribution, composed of the photons being scattered or reflected from the environment and collimating components. In this work, the latter term is not included in the simulation framework as it is highly dependent on the setup of the instrument, and we assume that the system can be optimized to minimize its contribution. Furthermore, in spectral CT, the total signal suffers distortions of the spectral distribution due to detector effects causing the photons to be detected with a certain energy shift. Such effects (e.g., charge sharing, escape peaks, weighting potential, etc.) can be modeled using a unified detector response matrix (DRM), which is applied to each of the real acquisitions on a pixel-by-pixel basis.[10] Effects such as pile-up that depend on the flux of the x-ray beam are not efficiently accounted for by the DRM approach and need to be dealt independently.[11] Christensen et al.[12] introduced an accurate correction method, adopted in this work, for real acquisitions. This is time efficient and reliable for systems working with a high x-ray flux, up to 5 Mph/s/mm^2.

2.1 *Monte Carlo Simulation Tool*

The simulations framework adopted for this work is McXtrace,[13] a software package for MC simulation of x-ray experiments by ray-tracing methods. Rather than tracing individual photons, in this framework, rays are represented by photon entities, and their interactions are simulated by probabilistic weight factors and tracing parameters, such as direction, wave-vector, polarization vector, and phase. The individual parts composing the instrument (e.g., sources, slits, detectors, samples, etc.) are identified as so-called components that can be separately implemented in comparatively few lines of simple code and interact with each sampled ray by applying weight factors operation or altering their parameters. For this work, we have developed a sample component suitable for spectral CT with explicit treatment of the different physical interactions of x-rays incident on objects composed of multiple materials of a given shape. The sample is initialized by loading a volumetric discretized phantom of the object that is made up of a finite number of voxels of a defined size in a 3-D rectangular parallelepiped grid representing the bounding box. In this way, samples composed of objects of complex shape require the same computational cost as simple geometries. Moreover, since the reconstruction images rendered and employed in the forward and back projections of iterative methods are discretized in the same way, the format is well suited for reconstruction algorithms and their parameter optimization. The value in each voxel holds an integer number $i = 0,1,2,\ldots,N$, which labels a specific material. For each material, lookup tables are required as input, visualized in Fig. 1.

The first lookup table is composed of the energy parametrized cross-sections for the possible interactions between the x-ray beam and the sample; i.e., photoelectric absorption $\sigma^i_{\text{ph}}(E)$, coherent (Rayleigh) $\sigma^i_{\text{coh}}(E)$, and incoherent (Compton) $\sigma^i_{\text{inc}}(E)$. These values are used to determine the likelihood of each interaction in the component and could, for instance, be loaded from the database administrated by the National Institute of Standards and Technology (NIST).[14] In a simplified approach, assuming that the scattered radiation is deflected out of the detector's range, the total attenuation cross-section can be used ignoring the following component treatment of the scattering. However, as it can be observed in Fig. 1, above 50-keV incoherent scattering interaction is dominant, whereas photoelectric absorption is prevailing for lower energies. Coherent scattering is about 2 orders of magnitude lower than the total attenuation, and only influent in the low energy range.

The remaining two lookup tables are used to sample the coherent and incoherent angular deflection of the ray trajectory when a scattering event occurs and is made up of the coherent and incoherent scattering functions $I^i_{\text{coh}}(Q)$ and $I^i_{\text{inc}}(Q)$ of each material. The scattering function is treated as the probability distribution function (PDF) of the scattering vector $\vec{Q}$ of amplitude:

$$Q = |\vec{Q}| = \frac{4\pi}{\lambda}\,\sin\left(\frac{2\theta}{2}\right), \tag{2}$$

where λ is the wavelength of the incident x-ray and 2θ is the detected scattering angle (i.e., between the incident and the scattered ray). In this way, the scattering vector's amplitude Q can be sampled by the inversion method,[15] which involves

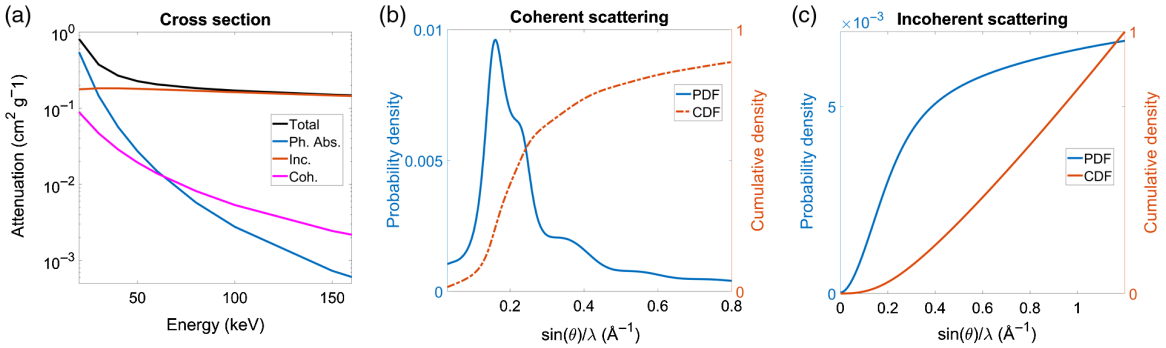

Fig. 1 The lookup tables used by the sample component, exemplified for water. (a) The NIST cross-sections are represented for each type of interaction: photoelectric absorption (Ph. Abs.), Rayleigh scattering (Coh.), Compton scattering (Inc.) and total attenuation (total), the sum of the three. Note the logarithmic scale to emphasize each contribution to the total attenuation. (b) and (c) The coherent and incoherent, respectively, scattering functions' probability distribution function (PDF) and their respective cumulative distribution function (CDF) are represented. Note the different scales for the *y*-axis.

computing the cumulative distribution function (CDF) of the distribution and then inverting that function. Since the latter is discrete, the computation of the CDF is simply done by adding up the individual probabilities (normalized to sum 1) for various points of the distribution. The detected scattering angle 2θ is derived from the sampled Q using Eq. (2) since the energy of the incident ray is a known parameter. The distributions used for $I^i_{\text{coh}}(Q)$ in this work have been experimentally determined by the energy dispersive x-ray diffraction method, as described by Kehres et al.[16] and entered into a database of common materials. The state-of-the-art coherent scattering distribution used for water, shown in Fig. 1, is the one presented by Skinner et al.[17] that was made available for download.

To model the distribution of incoherent scattering $I^i_{\text{inc}}(Q)$, we have adopted the parametrization presented by Hajdu[18] and Palinkas.[19] As an alternative, the angular deviation of scattering events can be sampled as modeled by the Thomson and Klein-Nishina functions.[20] The azimuthal angle ϕ is uniformly sampled in the interval $(0,2\pi)$, since the radiation emitted by a conventional x-ray tube is almost fully unpolarized. Finally, when the scattering event is determined to be of Compton type, the ray's energy parameter is updated to E_{inc}, according to the Compton energy shift relation:[21]

$$E_{\text{inc}} = \frac{E}{1 + \frac{E}{511\ \text{keV}}[1 - \cos(\theta)]}. \tag{3}$$

The projections' runtime of the simulations performed in the upcoming sections is 2 min on a standard laptop, equipped with i7-6600U quad-core CPUs at 2.60 GHz. The speed performance of the scattering estimator is similar and, in some instances, faster than what is reported in some previous recent works for a sample of similar geometrical size.[8] For the simulation of CT experiments, as presented in Sec 4, several projections can be simulated in parallel in multicore architectures to increase efficiency.

2.2 *Instrumentation*

The instrumentation used for the validation of the scattering estimation of the new scattering component was designed for spectral CT measurements. The x-ray beam was generated by a tungsten anode, and the acceleration voltage and filament current were set to 160 kV and 0.5 mA, respectively. For these operating parameters, the focal spot was 75 μm. The detector was made up of two 1-D PCD Multix-ME100[5] modules, composed of 1×128 pixels of size 0.8×0.8 mm^2 and each with 128 energy bins of width 1.1 keV, evenly distributed between 20 and 160 keV. The energy resolution of the detector under high x-ray fluxes is of 6.5% (8 keV) at 122 keV.[22] A 3-mm thick aluminum filter was placed in front of the source to reduce the beam hardening effects and to suppress the photons with energy below the spectral range of the detector. An energy distribution of the source, shown later in Fig. 5, was obtained by an acquisition of the direct beam (i.e., without the sample being inserted). The characteristic x-ray peaks of the tungsten target are smeared due to the limited detection energy resolution,[12,23] resulting in a smoother spectrum compared to what is theoretically expected. The source spectrum is used in the simulation as the PDF of the ray's energy parameter. In this way, we simulate a polychromatic beam with the same features as we can measure. The sample used in the work presented here was composed of four glass (SiO_2) bottles filled with, respectively, water (H_2O), hydrogen peroxide (H_2O_2), powdered sugar ($C_{12}H_{22}O_{11}$), a powdered PETN explosive simulant, and an aluminum rod. The sample, sketched in Fig. 2, was designed to highlight the challenge of automated accurate threat detection in security screening,[2] as they are innocuous and harmful materials, which have very close values of efficient atomic number (Z_{eff}) and density relative to water (ρ_{rel}).

3 Experimental Validation

The method adapted to experimentally measure the detected radiation being scattered from the sample $S_s(\vec{r}, E)$ was the collimator shadow. The latter was shown to be an accurate empirical technique[24] and suits our beam collimation choice of a fan-beam. This technique, sketched in Fig. 2, combines a fan-beam collimation with a 2-D flat detector, to obtain considerably extended surfaces in which only the scattered radiation is present. The collimation was obtained by a vertical slit composed of two tungsten blades. The 2-D flat detector was reproduced by sequentially translating in

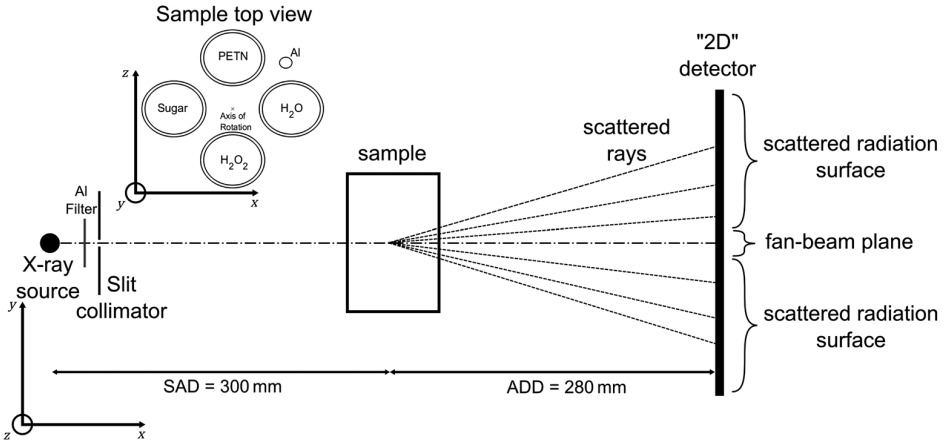

Fig. 2 Collimator shadow method: the x-ray beam is collimated into a fan-beam geometry. The sample is placed at a source-to-axis distance (SAD) = 300 mm from the detector, whereas the 1-D detector, placed at an axis-to-detector distance (ADD) = 280 mm from the sample, was composed of 256 pixels in the *z*-direction and is vertically translated in the *y*-direction to reproduce a 2-D detector. In the detector area shadowed by the collimator, the signal is only composed of the scattered radiation.

70 steps vertically our linear detector, resulting in an array of 70×256 pixels 2-D detector. We restricted the detection energy range to the interval between 40 and 160 keV to disregard energy channels with low photon statistics, as they would display accentuated distortions in the spectral shape due to insufficient signal to noise ratio.

In this technique, in the shadows cast by the collimator (i.e., outside of the fan-beam plane), the primary signal is absent, $S_p(\vec{r}, E) = 0$. Assuming absence of air scattering, the isolation of the sample scattering contribution $S_s(\vec{r}, E)$ can therefore be obtained by the subtraction between the acquisition with and without the sample, $S(\vec{r}, E)$ and $S_0(\vec{r}, E)$, respectively, to reduce the environmental noise:

$$S_s(\vec{r}, E) = S(\vec{r}, E) - S_0(\vec{r}, E) = S_s(\vec{r}, E) + S_{\text{bkg}}(\vec{r}, E) - S_{\text{bkg}}(\vec{r}, E).$$

A mathematical phantom of the sample of 150×150 vertically homogeneous voxels of size 0.667 mm was generated and loaded into the simulation component described in Sec. 2, to estimate the total signal $\tilde{S}(\vec{r}, E)$ and its respective sample scattering contribution $\tilde{S}_s(\vec{r}, E)$. The geometrical setup of the instrumentation in the simulations was set to match the experimental setup.

3.1 *Simulation Output*

The runtime for simulating each projection, sampling 10^6 rays, was 2 min. To reduce further the computational efforts of the MC simulations, we applied a 3-D Gaussian blurring to the spectral scattering projections $\tilde{S}_s(\vec{r}, E)$, inspired by the accelerated simulation method presented by Colijn and Beekman.[25] The method consists in filtering the projections with a 2-D Gaussian smoothing kernel, with standard deviation σ being the blurring width. We introduce a trade-off between noise and blur (variance and bias) in the simulation output using fixed bandwidth kernel density estimation with a Gaussian kernel.[26] We use a 3-D Gaussian kernel and vectorial form of the blurring width $\vec{\sigma} = (\sigma_z, \sigma_y, \sigma_E)$, composed of the individual blurring widths in the z- and y-axes and the energy domain. The optimal choice of $\vec{\sigma}$ depends on the number of rays being sampled and the geometrical parameters of the system. For this work, the blurring width has been found by the minimization of the combined root mean squared error, $\text{RMSE}(\sigma_z, \sigma_y, \sigma_E)$, with a reference considered as true image:

$$\text{RMSE}(\sigma_z, \sigma_y, \sigma_E) = \sqrt{\sum_{i=1}^{N_z}\sum_{j=1}^{N_y}\sum_{k=1}^{N_E}\frac{(\tilde{S}_s(z_i, y_j, E_k) - \tilde{S}_{\text{ref}}(z_i, y_j, E_k))^2}{N_z N_y N_E}},$$

therefore, $\tilde{S}_{\text{ref}}(\vec{r}, E)$ is the scattering projection used as true reference, obtained by simulating 10^9 rays; N_z and N_y are the numbers of pixels in the z- and y-direction, respectively; and N_E is the number of energy bins of the detector. Figure 3 shows $\tilde{S}_s(z_i, y_j, E_k)$, $\tilde{S}_{\text{ref}}(z_i, y_j, E_k)$, and the filtering result, for blurring width $\vec{\sigma} = (9, 4.14, 1.71)$. For a better visualization of the results, the scattering projections shown in the following figures have been energy integrated into $\tilde{S}_s(z, y) = \sum_{k=1}^{N_E} \tilde{S}_s(\vec{r}, E_k)$ and spatially integrated into $\tilde{S}_s(E) = \sum_{i=1}^{N_x}\sum_{j=1}^{N_y} \tilde{S}_s(z_i, y_j, E)$. The drop in intensity that can be observed within the fan-beam plane indicates that the photons being scattered to the fan-beam plane are less likely than the one being scattered out of it. This is the reason underlying the apparition of the two lobes of high intensity in the vicinity that would not be obtained by rather having a cone-beam collimation.

Figure 4 shows the output of the simulation, displaying the individual types of scattering events contributing to the total scattering signal, and their respective spectral and spatial distribution. It can be observed that both the incoherent and multiple scattering (i.e., when the photons are scattered more than once in the same path tracing) are heavily spread in a broad range of angles centered in the proximity of the sample, indicating that information about the geometrical structure of the sample is completely lost. A comparison between the coherent and incoherent scattering instead

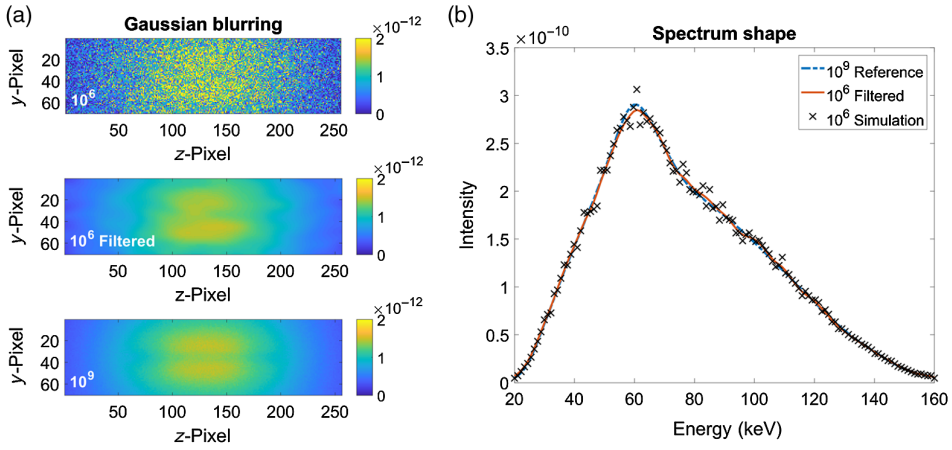

Fig. 3 Visualization of the effect of the 3-D Gaussian blurring. (a) Starting from the top frame toward the bottom are shown the energy integrated scattering estimate $\tilde{S}_s(\vec{r})$, the result of the filtering and the reference $\tilde{S}_{\text{ref}}(\vec{r})$. (b) The spectral distribution of the respective spatial integrated scattering projections $\tilde{S}_s(\vec{E})$.

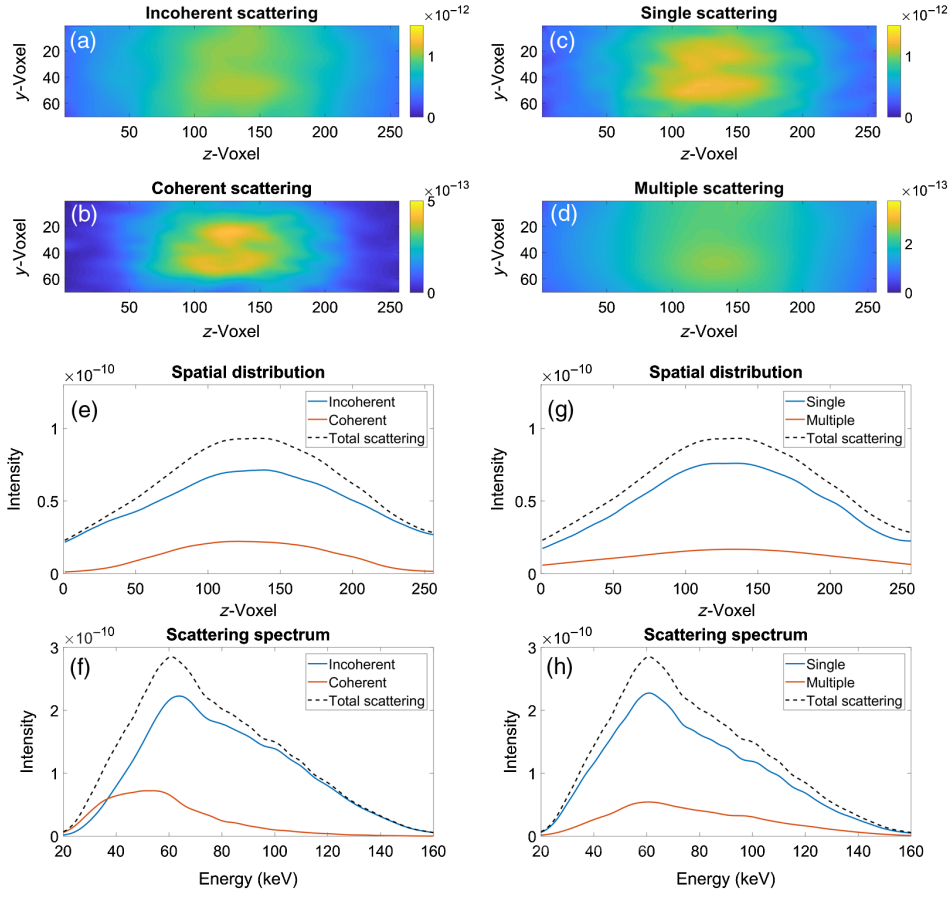

Fig. 4 Simulation output of the scattering contributions to the total signal $S_t(\vec{r}, E)$. (a)–(d) Energy integrated incoherent, coherent, single and multiple scattering profiles. (e)–(h) Spatial integrated and energy integrated distribution of the individual x-ray scattering profiles. The dashed black line is the total scattering signal, whereas the blue and red lines are its incoherent and coherent contributions in (e,f), and its single and multiple contributions in (g,h). Note that the intensity scale of (b) is three times lower than (a), whereas the intensity scale of panel (d) is four times lower than panel (c).

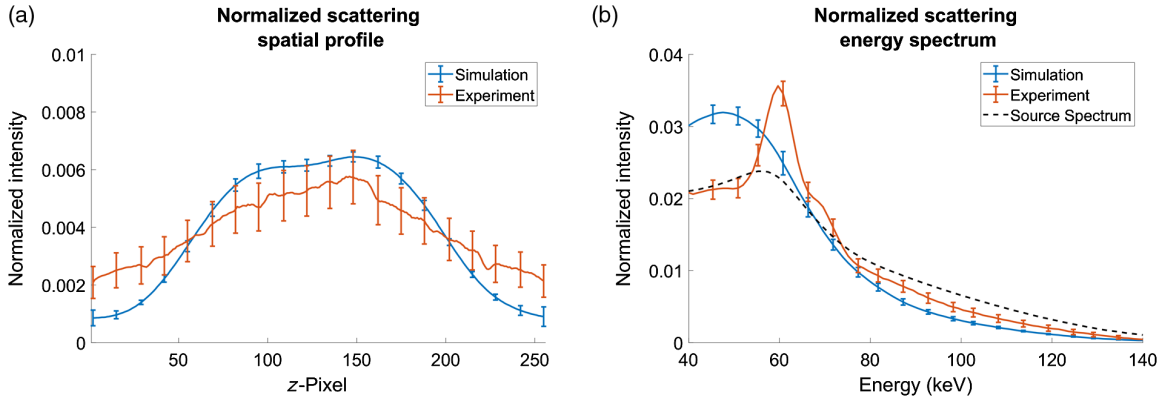

Fig. 5 Validation of the simulation tool. (a) The normalized estimated (simulation) and measured (experiment) scattering signal, integrated over the energy and the *y*-axis area shadowed by the collimator are plotted. (b) Their respective spectral distribution and the source spectrum (source spectrum) are plotted. The error bars are shown every 20th point.

suggests that the former contributes largely to the low-energy part of the energy spectrum and, despite that, is heavily centered toward the small angles compared to the latter. It is also evident that above 50 keV, the scattering profile is dominated by the incoherent scattering events. A look at the multiple scattering profiles suggests that it can be treated as a constant offset relative to the single scattering, if the purpose is to employ fast and simplified computational models. Last, it should be noted that the simulation output is on an arbitrary scale since it is a probability map. Therefore, the data should be interpreted after it has been properly rescaled according to the beam flux, which could be, for example, determined by placing a virtual monitor before the sample. However, for most applications, this procedure is not necessary as it is the case of the reconstruction techniques, in which the datasets are normalized in the preprocessing of the attenuation $A(\vec{r}, E)$ according to Eq. (4):

$$A(\vec{r}, E) = -\log \frac{S(\vec{r}, E)}{S_0(\vec{r}, E)}. \tag{4}$$

3.2 *Comparisons*

Figure 5 displays the comparisons of the scattered radiation obtained by both the simulation and experiment, and their respective spatial and energy profiles. The spatial profile of the two signals shows a qualitative good match, which does not completely hold for the energy distribution. A visual comparison of the experimental and simulated spectral distributions indicates an overestimation of the high-energy and, thus, supposedly the incoherent scattering events. Concurrently, the experimental spectral distribution displays sharper peaks centered around the characteristic peaks of tungsten. This indicates a relatively large environmental noise in addition to the scattering signal, which can be caused, for example, by the scattering of the slits used for the front collimation of the beam since they are made of tungsten. That can be due to direct beam reflection or scattering from other parts composing the instrument. Therefore, we attribute the reason for the discrepancy to the experimental complexity in achieving the ideal collimation of a fan-beam and in reducing the background radiation incoming from the system environment. A more accurate detection of the spectral distribution of the scattered radiation could be achieved by a better shielding of the background radiation, which was beyond the purpose of this work.

Another limitation of the simulation tool is the dependence on the quality of the models used for the coherent scattering angular deviation sampling. For certain samples, for instance, the noise removal can be challenging due to the relatively low count rate of the technique, leading to imprecisions in the measured distribution. Furthermore, the instrumental constraints prevent the determination of the coherent scattering functions $I^i_{\mathrm{coh}}(Q)$ in the low-Q limit, due to the presence of the direct beam. Last, the analytical approximations used for the incoherent scattering functions are required to satisfy the validity range $\sin(\theta)/\lambda < 1.2$[18,19] posing a limit to the high angles.

4 Computed Tomography Scattering Correction

In the last part of the work, we have simulated a spectral CT experiment of 101 projections evenly distributed between $\omega = (0, 2\pi)$. For each projection, 10^6 rays are traced followed by the Gaussian blurring of the scattering projections. The specifications of the instrumentation and of the sample are sketched in Fig. 2 and described in Sec. 2. The reconstruction method adopted was simultaneous iterative reconstruction technique (SIRT), implemented in the ASTRA reconstruction toolbox.[27] The latter maps the attenuation simulated projections into volumetric representation of the linear attenuation of the sample $\mu(\vec{r}, E)$. To assess the impact of the scattered radiation, we have performed slice reconstructions $\mu_t(\vec{r}, E)$ and $\mu_p(\vec{r}, E)$ of, respectively, the total attenuation projections $A_t(\vec{r}, E)$ and of the scattering corrected primary attenuation projections $A_p(\vec{r}, E)$. These are obtained by inserting the simulated total signal $\tilde{S}_t(\vec{r}, E)$ and primary radiation $\tilde{S}_p(\vec{r}, E) = \tilde{S}_t(\vec{r}, E) - \tilde{S}_s(\vec{r}, E)$, respectively, in Eq. (4). It must be noted that following Eqs. (1) and (4), since the total signal is corrupted by the scattered radiation, the total attenuation yields a lower value compared to the true attenuation.

The reconstructions shown in Fig. 6 were carried out by first merging the energy channels between 92.7 and 160 keV. That is a considerably high-energy interval, such as the

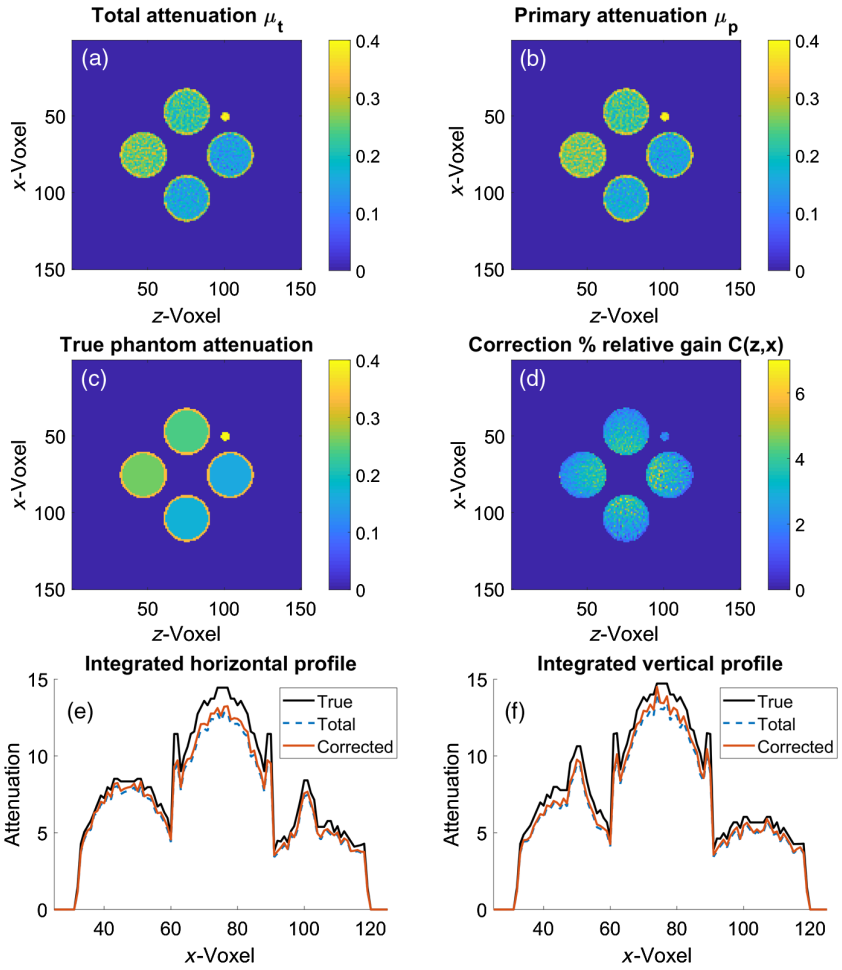

Fig. 6 (a,b) SIRT reconstruction of the total and scattering corrected primary attenuation. (c) Sample phantom used in the simulations. The color scale in frames (a–c) represents the linear attenuation μ value held by the voxel. (d) Percentile amplification of the reconstruction value using the corrected attenuation. (e,f) Spatially integrated horizontal and vertical profiles of the images, obtained by summing the values of each row and column, respectively.

ones often implemented in dual-energy CT techniques for nondestructive testing and security applications, especially for the retrieval of a material's electron density ρ_e.[28] The simulation method holds valid for lower energies, even though the correction impact becomes less significant due to a reduced number of scattering events. In Fig. 6, the attenuation profiles have been spatially integrated in a similar way as the scattering projections for a better display of the results. Since the corrected attenuation $\mu_p(\vec{r}, E)$ should always be greater than the uncorrected $\mu_t(\vec{r}, E)$, we have introduced a correction percentile relative gain $C(\vec{r}, E)$:

$$C(\vec{r}, E) = 100\% \frac{\mu_p(\vec{r}, E) - \mu_t(\vec{r}, E)}{\mu_t(\vec{r}, E)}, \tag{5}$$

to quantify the relative change of the scattering correction in the reconstruction of the linear attenuation value $\mu(E)$.

4.1 *Discussion of Results*

It was found that for this energy interval, the correction $C(x, y)$ accounts for an amplification in $\mu(E)$ that can be up to 7% and increases as the center of mass of the entire sample is approached. It was also observed that it becomes slightly higher for liquid materials, due to their lower linear attenuation, as compared to other materials composing our sample. This indicates that treating the scattering contribution as a mere scaling factor applied to the total attenuation may lead to artifacts, especially in the high-energy range, where the scattering influence becomes increasingly relevant. It is also evident that, by comparing the aluminum and the glass content values, the scattering contribution is highly dependent on the volume covered by each object. Despite the fact that the larger objects of the sample are subject to more significant loss of contrast, the reconstructions do not exhibit the otherwise commonly occurring cupping artifacts. The reason for this is the relatively limited size of the sample and the collimation of the fan-beam.

To evaluate the impact of the scattering correction in the energy domain, we have performed a slice reconstruction of each individual energy channel. The surface covered by each material i was segmented and used to retrieve energy resolved mean linear attenuation $\mu^i(E)$ reconstructed by

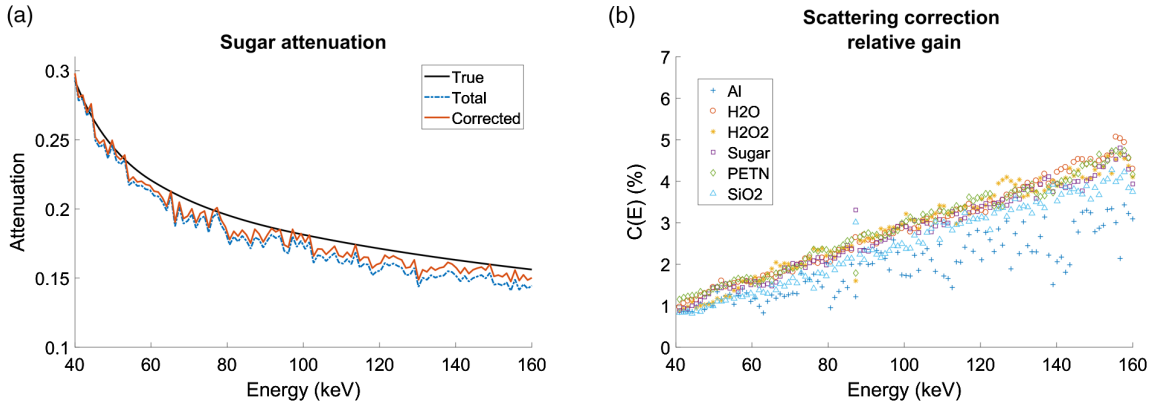

Fig. 7 (a) Mean value of the energy resolved reconstructed attenuation value in the sugar surface, using the total attenuation (total), the primary attenuation (corrected), and the theoretical expected attenuation (true). (b) Spectral profiles of the correction relative gain for each material.

using the total and scattering corrected primary attenuation. Both energy distributions are shown in Fig. 7 for powdered sugar and compared to its respective tabulated values, used in the look-up tables. It was observed that the correction aids in reconstruction of the linear attenuation μ, as it is brought closer to the tabulated linear attenuation. It has to be noted, however, that the scattering signal subtraction correction method used here is merely a preliminary procedure. A more refined approach would include the scattering estimator in the forward model of iterative reconstruction techniques. In this way, the illposedness of the reconstruction problem would be reduced and the gap observed in Fig. 7, which is due to counting statistics and missing data, will be further closed leading to a more robust solution.

The energy distribution of the correction relative gain $C(E)$ was then derived for each material and is shown in Fig. 7. A comparison between the correction relative gain $C(E)$ for aluminum and the glass contents suggests that larger volumes are more subject to scatter artifacts. Furthermore, the latter increases with the energy reaching values up to 6%, indicating that CT scanners operating in high-energy regimes require scattering correction algorithms for an adequate reconstruction of the linear attenuation. On the other hand, CT reconstruction of low-energy projections with fan-beam collimation seems to be only slightly influenced by the scattered radiation, regardless of the volume and composition of the material.

5 Conclusions

We have presented a fully stochastic simulation tool for x-ray spectral CT, featuring a computationally fast estimate of the scattered radiation, which is particularly compatible with objects of complex shape. The tool is open access and runs in the well-established McXtrace software package.[13] It has been validated by an experiment designed to detect the radiation being scattered by the sample only. We have discussed the current limitations of the simulation tool and possible strategies to overcome them. In a preliminary approach, we have shown how the scattering estimate can improve the attenuation reconstruction by a restoration of the primary radiation $\tilde{S}_p(\vec{r}, E)$, performed as a simple subtraction of the estimated scattering contribution $\tilde{S}_s(\vec{r}, E)$. It was found that especially at high energies, where the incoherent scattering events are dominant, the correction is useful to reconstruct a more accurate linear attenuation value and, therefore, improves the contrast between different materials. This is expected to aid the automated segmentation procedures leading to an advance in the material

Algorithm 1 Pseudocode of the McXtrace object component.

Data: Object's phantom and material densities ρ^i, cross sections $\sigma^i(E)$ and scattering functions $I^i_{\text{coh}}(Q)$ and $I^i_{\text{inc}}(Q)$

Result: Energy resolved total and scattering signal from the interaction between x-rays and the object

initialize system's geometry and variables;

set the step length s_i;

while *ray is within the object* **do**

  if *ray is scattered* **then**

    if *Compton scattering* **then**

      sample scattering angle θ from $I^i_{\text{inc}}(Q)$;

      update ray direction according to θ;

      update to Compton energy with Eq. (3);

    else

      sample scattering angle θ from $I^i_{\text{coh}}(Q)$;

      update ray direction according to θ;

    end

  end

  read photoelectric absorption attenuation $\mu(E) = \rho^i \sigma^i_{\text{ph}}(E)$;

  ray travels the step length s_i;

  increment the cumulative photoelectric absorption attenuation along the trace $\mu(E)l = \mu(E)l + \mu(E)s_i$;

end

apply final photoelectric absorption attenuation to the ray: $e^{-\mu(E)l}$;

classification. In future work, we aim to incorporate the scattering estimation in the forward model of a model-based iterative reconstruction technique, to improve even further the efficiency of the algorithm. This could be done, for instance, by, after a certain iteration number of the CT reconstruction, retrieving a preliminary volumetric representation of the object. The latter would be then used by the MC simulation tool to obtain the direct estimate of the scattering contribution.

Appendix: Sample Component Pseudocode

The pseudocode of the sample component developed for McXtrace is shown in Algorithm 1. Therefore, the step length s_l represents the rate at which the interaction probabilities are checked while the ray is traced through the sample up to the final length l. In our simulations, s_l was set to a value three times smaller than the voxel size. At the first step of each ray traced, the step length was additionally multiplied by a random generated number to reduce artifacts induced by the tracing regularity.[29] $\mu(E)$ represent the photoelectric absorption linear attenuation, whereas ρ^i and $\sigma^i_{\mathrm{ph}}(E)$ are, respectively, the density relative to water and the photoelectric absorption cross-section of each material.

In this method, the photoelectric absorption interaction is taken into account by incrementing at each step the outgoing photoelectric linear absorption. The scattering interaction type is determined by generating a random number $\xi = U(0,1)$, with $U(-n,n)$ being the uniform distribution between $-n$ and n, and comparing it with the tabulated scattering cross-sections:

$$\text{Scattering type} = \begin{cases} \text{Compton}, & \text{if } \xi < \left[1 - e^{-\rho \cdot s_l \cdot \sigma^i_{\mathrm{inc}}(E)}\right] \\ \text{Rayleigh}, & \text{if } \left(1 - e^{-\rho \cdot s_l \cdot \sigma^i_{\mathrm{inc}}(E)}\right) < \xi < \left[1 - e^{-\rho \cdot s_l \cdot (\sigma^i_{\mathrm{coh}}(E) + \sigma^i_{\mathrm{inc}}(E))}\right] \end{cases}.$$

Acknowledgments

The authors would like to acknowledge Innovation Fund Denmark for financing their respective work. The authors have no relevant financial interests in the manuscript and no other potential conflicts of interest.

References

1. W. A. Kalender, "X-ray computed tomography," *Phys. Med. Biol.* **51**, R29–R43 (2006).
2. K. Wells and D. A. Bradley, "A review of x-ray explosives detection techniques for checked baggage," *Appl. Radiat. Isot.* **70**, 1729–1746 (2012).
3. H. Kraggerud et al., "X-ray images for the control of eye formation in cheese," *Int. J. Dairy Technol.* **62**, 147–153 (2009).
4. M. Thomsen et al., "Prediction of beam hardening artefacts in computed tomography using Monte Carlo simulations," *Nucl. Instrum. Methods Phys. Res., Sect. B* **342**, 314–320 (2015).
5. A. Gorecki et al., "Comparing performances of a CdTe x-ray spectroscopic detector and an x-ray dual-energy sandwich detector," *J. Instrum.* **8**(11), P11011 (2013).
6. P. C. Johns and M. Yaffe, "Scattered radiation in fan beam imaging systems," *Med. Phys.* **9**(2), 231–239 (1982).
7. E.-P. Rührnschopf and K. Klingenbeck, "A general framework and review of scatter correction methods in x-ray cone-beam computerized tomography. Part 1: scatter compensation approaches," *Med. Phys.* **38**(7), 4296–4311 (2011).
8. A. Sossin et al., "Fast scattering simulation tool for multi-energy x-ray imaging," *Nucl. Instrum. Methods Phys. Res., Sect. A* **802**, 60–66 (2015).
9. M. Busi et al., "A Monte Carlo simulation of scattering reduction in spectral x-ray computed tomography," *Proc. SPIE* **10388**, 103880P (2017).
10. G. Bootsma, F. Verhaegen, and D. Jaffray, "Spatial frequency spectrum of the x-ray scatter distribution in CBCT projections," *Med. Phys.* **40**(11), 111901 (2013).
11. J. Cammin et al., "A cascaded model of spectral distortions due to spectral response effects and pulse pileup effects in a photon-counting x-ray detector for CT," *Med. Phys.* **41**(4), 041905 (2014).
12. E. D. Christensen et al., "Spectral correction algorithm for multispectral CdTe x-ray detectors," *Proc. SPIE* **10393**, 103930H (2017).
13. E. Bergbäck Knudsen et al., "McXtrace: a Monte Carlo software package for simulating x-ray optics, beamlines and experiments," *J. Appl. Crystallogr.* **46**(3), 679–696 (2013).
14. M. J. Berger and J. H. Hubbell, "XCOM: photon cross sections on a personal computer," No. NBSIR-87-3597, Center for Radiation Research, National Bureau of Standards, Washington, DC (1987).
15. R. Y. Rubinstein and D. P. Kroese, *Simulation and the Monte Carlo Method*, Vol. **10**, John Wiley & Sons (2016).
16. J. Kehres, M. Lyksborg, and U. L. Olsen, "Threat detection of liquid explosives and precursors from their x-ray scattering pattern using energy dispersive detector technology," *Proc. SPIE* **10393**, 1039302 (2017).
17. L. B. Skinner et al., "Benchmark oxygen-oxygen pair-distribution function of ambient water from x-ray diffraction measurements with a wide Q-range," *J. Chem. Phys.* **138**, 074506 (2013).
18. F. Hajdu, "Revised parameters of the analytic fits for coherent and incoherent scattered x-ray intensities of the first 36 atoms," *Acta Cryst. A* **28**(3), 250–252 (1972).
19. G. Palinkas, "Analytic approximations for the incoherent x-ray intensities of the atoms from Ca to Am," *Acta Cryst. A* **29**(1), 10–12 (1973).
20. J. Baró et al., "Analytical cross sections for Monte Carlo simulation of photon transport," *Radiat. Phys. Chem.* **44**(5), 531–552 (1994).
21. A. H. Compton, "A quantum theory of the scattering of x-rays by light elements," *Phys. Rev.* **21**(5), 483–502 (1923).
22. A. Brambilla et al., "Fast CdTe and CdZnTe semiconductor detector arrays for spectroscopic x-ray imaging," *IEEE Trans. Nucl. Sci.* **60**(1), 408–415 (2013).
23. A. A. Dooraghi et al., "Characterization of a spectroscopic detector for application in x-ray computed tomography," *Proc. SPIE* **10391**, 103911G (2017).
24. A. Akbarzadeh et al., "Measurement of scattered radiation in a volumetric 64-slice CT scanner using three experimental techniques," *Phys. Med. Biol.* **55**, 2269–2280 (2010).
25. A. P. Colijn and F. J. Beekman, "Accelerated simulation of cone beam x-ray scatter projections," *IEEE Trans. Med. Imaging* **23**, 584–590 (2004).
26. B. W. Silverman, *Density Estimation for Statistics and Data Analysis*, Vol. **26**, CRC Press (1986).
27. W. van Aarle et al., "The ASTRA toolbox: a platform for advanced algorithm development in electron tomography," *Ultramicroscopy* **157**, 35–47 (2015).
28. S. G. Azevedo et al., "System-independent characterization of materials using dual-energy computed tomography," *IEEE Trans. Nucl. Sci.* **63**(1), 341–350 (2016).
29. M. Pauly, T. Kollig, and A. Keller, "Metropolis light transport for participating media," in *Proc. of EGWR, Rendering Techniques*, pp. 11–391, Springer (2000).

Matteo Busi is a PhD student at Technical University of Denmark (Kgs. Lyngby, Denmark). He received his BS degree in physics from the Universitá degli Studi di Parma (Parma, Italy) and his MS degree in mathematics and physics from the Universitetet i Stavanger (Stavanger, Norway) in 2014 and 2016, respectively. He is a member of SPIE.

Ulrik L. Olsen is a senior research engineer at DTU physics since 2013. Funded by Innovation Fund Denmark to develop applications using high flux multispectral x-ray detection technology and currently project leader on CIL2018, a multidisciplinary effort made to reduce the human operator involvement by 50% for checked-in luggage. He was previously employed at National Laboratory RISØ, Denmark, as PhD (2005) and later postdoc working with developments of x-ray sensors.

Erik B. Knudsen is a research engineer at DTU Physics (Kgs. Lyngby, Denmark). He received his PhD degree in photonic crystal

fiber optics. His main research interests are x-ray and neutron scattering computer simulations with emphasis on coherent x-rays and polarized neutrons, as well as x-ray telescope simulations. He is a core developer of McXtrace and McStas simulation packages (since 2007).

Jeppe R. Frisvad is an associate professor at Technical University of Denmark (DTU). He received his MSc (Eng) degree in applied mathematics (2004) and PhD degree in computer graphics (2008) from DTU. His research interests are mainly material appearance modeling, realistic rendering, and light scattering. As a highlight, his work includes development of the first diffusion dipole for subsurface scattering based on ray sources.

Jan Kehres is a research engineer at DTU physics (Kongens Lyngby, Denmark). He received his PhD for in operando investigation of catalyst nanoparticles using x-ray scattering and continued in this field of research as a postdoctoral researcher. His current field of research is the application of energy dispersive detectors for x-ray scattering and advanced imaging modalities with a focus on material identification of illicit materials for security applications.

Erik S. Dreier is a PhD student at the Niels Bohr Institute, University of Copenhagen (Denmark). He received both his BS (2013) and MS (2016) degrees in physics from the University of Copenhagen. His research is focused on finding possible new applications and characterization of novel single photon counting x-ray detectors. He is a member of SPIE.

Mohamad Khalil is a postdoctoral researcher at Technical University of Denmark (Kgs. Lyngby, Denmark). He received his MS degree in high-energy physics from University Paris Pierre et Marie Curie (Paris, France) in 2011 and his PhD degree from University Paris Denis Diderot (Paris, France) and University of Ferrara (Ferrara, Italy) in December 2014.

Kristoffer Haldrup obtained his PhD degree from Niels Bohr Institute in 2007, working at Risø National Laboratory in Denmark. He then worked as a postdoc at the Centre for Molecular Movies located at the University of Copenhagen. In 2011 to 2012, funded by the VKR/Carlsberg foundations, he worked at Argonne National Laboratory near Chicago. He is now a senior scientist at Technical University of Denmark, working on methodologies for X-FEL experiments and new tomographic imaging modalities.

Paper II

Spectral correction algorithm for multispectral CdTe X-ray detectors.
Erik Schou Dreier, Jan Kehres, Mohamad Khalil, Matteo Busi, Yun Gu, Robert Feidenhans'l, and Ulrik Lund Olsen

Optical Engineering 57(5), 054117 (May 2018)

Spectral correction algorithm for multispectral CdTe x-ray detectors

Erik Schou Dreier,[a,*] Jan Kehres,[b] Mohamad Khalil,[b] Matteo Busi,[b] Yun Gu,[b] Robert Feidenhans'l,[c] and Ulrik Lund Olsen[b]
[a]University of Copenhagen, Niels Bohr Institute, Copenhagen, Denmark
[b]Technical University of Denmark, Department of Physics, Lyngby, Denmark
[c]European XFEL GmbH, Schenefeld, Germany

Abstract. Compared to the dual-energy scintillator detectors widely used today, energy-resolved photon-counting x-ray detectors show the potential to improve material identification in various radiography and tomography applications used for industrial and security purposes. However, detector effects, such as charge sharing and photon pileup, distort the measured spectra in pixelated, photon-counting detectors operating under high flux. These effects result in a significant performance degradation of the detectors when used for material identification where accurate spectral measurements are required. We have developed a semianalytical, postdata acquisition, computational algorithm that corrects the measured attenuation curve for severe spectral distortions caused by the detector. The calibration of the algorithm is based on simple attenuation measurements of commercially available materials using standard laboratory sources, enabling the algorithm to be used in any x-ray setup. The algorithm is developed for correcting spectral data acquired with the MultiX ME100 CdTe x-ray detector but could be adapted with small adjustments to other photon-counting, energy-resolved detectors with CdTe sensors. The validation of the algorithm has been done using experimental data acquired with both a standard laboratory source and synchrotron radiation. The experiments show that the algorithm is fast, reliable at x-ray flux up to 5 Mph/s/mm^2 and greatly improves the accuracy of the measured spectrally resolved linear attenuation, making the algorithm useful for both security and industrial applications where photon-counting detectors are used. [DOI: 10.1117/1.OE.57.5.054117]

Keywords: CdTe detectors; compensation of spectral distortions; photon-counting detector; MultiX ME100 detector; pulse pileup correction; charge sharing correction.

Paper 180289P received Feb. 23, 2018; accepted for publication May 9, 2018; published online May 25, 2018.

1 Introduction

Photon-counting x-ray detectors with spectroscopic properties (multispectral x-ray detectors) and CdTe sensors show great potential for improving material identification in hard x-ray applications,[1] and methods to utilize the increased information obtained with multispectral data are still under development.[2,3] This has led to a large interest in multispectral detectors within security[4,5] and medical applications.[6–8] These applications typically require a large field of view, a difficulty which has been addressed by the development of multilevel polycrystalline (thin film) detectors[9,10] as well as detectors with a line array of multiple single crystals.[8,11]

However, detector effects, such as charge sharing and pulse pileup, severely distort the measured spectrum of multispectral detectors.[6] Spectral distortion might be mitigated through the implementation of advanced digital pulse processing techniques in the field-programmable gate array.[12,13] However, the recorded spectra from commercially available multispectral detectors are still severely distorted.

A common spectral correction approach is to empirically determine a photon flux density-dependent fitting function, which translates each energy bin's measured signal into a corrected signal.[14] Unfortunately, this method typically corrects the count rate of each energy bin independently of the others, whereas the spectral distortion, such as pulse pileup,[15] effect on an energy bin's count rate is largely correlated with the count rate in all other energy bins. Therefore, the empirical fitting function-based approach is not ideal for applications, such as luggage screening, where large variations in density and effective atomic number among the measured objects result in large variation in the measured x-ray spectra. An alternative method is to correct the recorded spectra using analytical or empirical models of the individual spectral distorting effects. Comprehensive models of the spectral distortion in multispectral x-ray detectors have been proposed numerous times,[16–19] and algorithms that correct the measured spectrum for the specific effects of pulse pileup and escape peaks based on analytical models are already in use.[15,20] Furthermore, it has been shown that using a comprehensive model to add distortions to the expected x-ray spectrum improves the ability to estimate the thickness of attenuating materials in simulated experiments.[21]

In this paper, we present a comprehensive semianalytical correction algorithm (CA) that directly corrects recorded x-ray spectra for charge sharing, weighting potential (WP) cross talk, pulse pileup, incomplete charge collection (ICC), and x-ray fluorescence, with the purpose of improving the accuracy of the measured material x-ray attenuation coefficients. Our CA is designed with the primary scope to correct data acquired with the MultiX ME100 v2 CdTe

*Address all correspondence to: Erik Schou Dreier, E-mail: erik.dreier@nbi.ku.dk

0091-3286/2018/$25.00

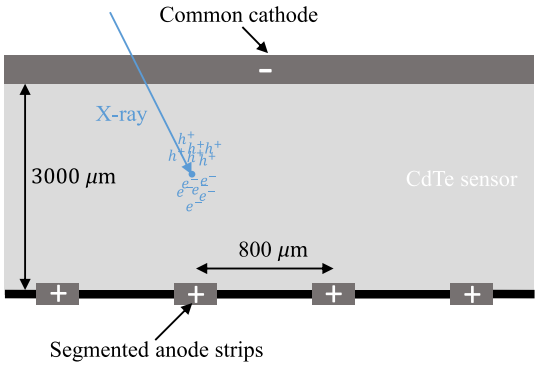

Fig. 1 Simplified layout of the MultiX detector.

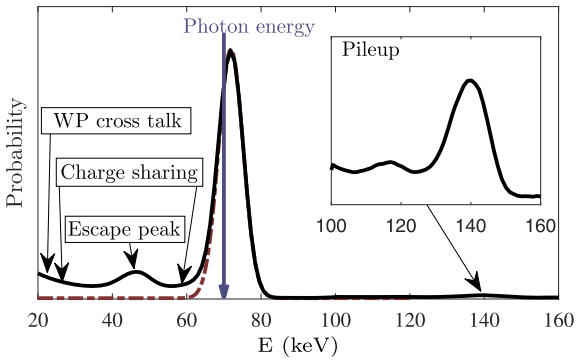

Fig. 2 The spectrum recorded with a MultiX ME100 v2 detector irradiated with a monochromatic x-ray beam of $E = 70$ keV. The "pileup box" shows a zoom-in on the pileup peak at double energy of the primary peak. The dashed red line shows the ideal response of the MultiX ME100 detector with a finite energy resolution. The primary peak's center is placed at slightly higher energy than the expected due to a slightly wrong energy calibration of the detector.

line array detector,[22] which suffers from severe spectral distortion.[11] However, the CA is based on spectral distortion models that with small adjustment could be applied to any pixelated, multispectral CdTe detector. We aim with this CA to gain the possibility to correct the measured x-ray attenuation coefficient for distorting effects in an efficient, fast, and reliable way making the CA applicable in nondestructive testing (NDT) and security applications.

The MultiX ME100 detector was chosen for this study, as it is suitable for security and NDT applications where a high flux, large field of view, and sensitivity for x-ray energies between 20 and 160 keV are required. Furthermore, the detector has shown to improve material identification as compared to conventional dual-energy sandwich detectors.[23–26] The MultiX's read-out architecture is constructed to perform well at high count rates (>1 Mph/s/mm^2) and is capable of reconstructing the measured x-ray spectra in up to 256 energy bins.[12,27] The detector has a 3-mm-thick CdTe sensor with a collective cathode on the photons' incident side of the sensor and a segmented anode on the backside as shown in Fig. 1. A single MultiX detector has 128 pixels with a pitch of 800 μm and is made up of an array of 4 sensor crystals with each 32 pixels. The detectors can further be daisy chained in up to 20 modules forming a more than 200-cm-long detector array.

In the rest of the paper, we will first introduce our CA in Sec. 2. In Sec. 3, we validate and adjust the CA's individual correction models based on experimental data from a monochromatic synchrotron source; next, we will show how the CA is calibrated using laboratory experiments in Sec. 4. Finally, we will validate the effectiveness of the full CA in Sec. 5, before discussing in Sec. 6 and concluding in Sec. 7, on our work.

2 Correction Algorithm for Spectral Distortion

The spectral response of multispectral, pixelated, CdTe detectors is typically severely distorted by a range of effects, as illustrated by the MultiX detector's recorded spectrum when irradiated by a monochromatic beam in Fig. 2. To correct for the spectral distortion, we follow the method proposed by Cammin et al.[18] and separate our distortion models into flux-dependent and flux-independent models. In our CA, we first correct the spectrum for the flux-independent phenomena, such as charge sharing, WP cross talk, etc. Next, we correct for the pulse pileup and then ICC, which as we shall show later is clearly flux dependent. Last, we recalibrate each pixel's energy scale. In the rest of this section, the models constituting our CA are presented.

2.1 *Flux-Independent Correction—The Simulated Detector Response Matrix*

Our CA aims to correct the spectrum for the following flux-independent effects:[15,16,28]

- X-ray fluorescence: Due to the high photon energy of the K-shell fluorescence in CdTe, the self-absorption length is so large that it is probable for the fluorescence photons to escape into a neighboring pixel or even to escape the detector's sensor crystal altogether. When such an escape occurs, the incident photon is registered by the detector at an energy lowered by the energy of the fluorescence photon.
- Charge sharing: If an x-ray photon is absorbed close to a pixel border, the created electron charge cloud can split onto both pixels resulting in the absorbed photon being counted as two photons with lower energy. This gives rise to a broad continuum of counts with an energy lower than the actual photon energy.
- WP cross talk: Charge carriers that are solely recorded by one pixel-anode might still induce a signal in the neighboring anode. The effect is seen as an upturn in the spectrum at low energies (seen at $E < 30$ keV in Fig. 2).
- Other flux-independent effects: In addition to the WP cross talk, charge sharing, and escape peaks, other effects, such as Compton scattering of the incident photon in the sensor crystal and electronic noise,[27] can contribute to the background.

To perform a fast correction of these flux-independent effects, we create an inverse detector response matrix $\mathbf{M}_C$ of dimension $E_b \times E_b$, where E_b is the number of energy bins. When $\mathbf{M}_C$ is applied to a raw spectrum from N pixels, described as a matrix $\mathbf{I}_R$ of dimension $E_b \times N$, it results in the corrected spectrum for each pixel described by the matrix

$$\mathbf{I}_C = \mathbf{M}_C \cdot \mathbf{I}_R. \tag{1}$$

The inverse response matrix is found from a simplified simulation of the detector's response to x-ray irradiation. To simplify the simulation, the WP cross talk, charge sharing, and electronic noise/Compton scattering are calculated independently. Therefore, this approach results in three response matrices, which all show to be numerically invertible, and hence

$$\mathbf{M}_C = (\mathbf{D}_C \cdot \mathbf{D}_E \cdot \mathbf{D}_{\mathrm{WP}})^{-1}, \tag{2}$$

where $\mathbf{D}_C$, $\mathbf{D}_E$, and $\mathbf{D}_{\mathrm{WP}}$ are the detector response matrices due to charge sharing, electron noise and Compton scattering, and WP cross talk, respectively. Applying $\mathbf{M}_C$ according to Eq. (1), we first correct for the WP cross talk, then the electronic noise and Compton scattering, and last the charge sharing. The order was chosen to remove the low-energy distortion effects before correcting for charge sharing.

The full detector response matrix is computed through a Monte Carlo simulation of a single pixel's response to x-ray irradiation as function of position and energy of the incoming photon. The simulation computes x-ray fluorescence before calculating $\mathbf{D}_C$, $\mathbf{D}_E$, and $\mathbf{D}_{\mathrm{WP}}$ matrices independently.

The amount of charge shared between two pixels is calculated by assuming that the excited charge clouds have a Gaussian charge density distribution.[29] The charge cloud width σ_t at the anode is calculated taking the charge diffusion and the charge repulsion perpendicular to the electric field into account. Combined with the initial width of the excited charge cloud σ_i that is assumed to be 5 μm,[30] the total width of the electron cloud is given as

$$\sigma_t = \sqrt{2\frac{k_B T z d}{qU} + \left(\frac{zdNq}{10\pi\epsilon U}\right)\frac{1}{\sqrt{5}\sigma_i} + \sigma_i^2}, \tag{3}$$

where z is the electron cloud position above the anode, d is the depth of the crystal layer, and U is the bias voltage. The number of charges per photon is given as $N = E_e/\Delta_E$, where $\Delta_E = 4.43$ eV/ehp[31] is the energy per electron–hole pair (ehp) for CdTe and E_e is the energy deposited in the detector by the absorbed photon.

The amount of WP cross talk between the irradiated and neighboring pixel is based on the model described by Guerra et al.,[16] which assumes that the charge cloud has no geometric expansion. In the model, the anode is assumed rectangular with a and b being the width and length of the anode, respectively.

Both Compton scattering and electronic noise should contribute with a small signal in the low-energy part of the spectrum, which should increase with incoming photon energy. The detector response matrix, $\mathbf{D}_E$, that accounts for these two effects is calculated through a simplified model that is based on synchrotron experiments as described in Sec. 3.

In the simulation of the MultiX ME100 detector, the pixel is set to an area of 0.8×0.8 mm^2, with an active crystal layer thickness of 3 mm,[23] and a bias voltage of around 1200 V.[27] The energy range of the simulation is set to 20 to 160 keV corresponding to the energy bin interval of the MultiX ME100. The WP cross talk model's anode size parameters a and b are found from finding the best correction of the experimental data as described in Sec. 4. The combined response matrix $\mathbf{M}_C = \mathbf{D}_{\mathrm{WP}} \cdot \mathbf{D}_E \cdot \mathbf{D}_C$ is shown in Fig. 3.

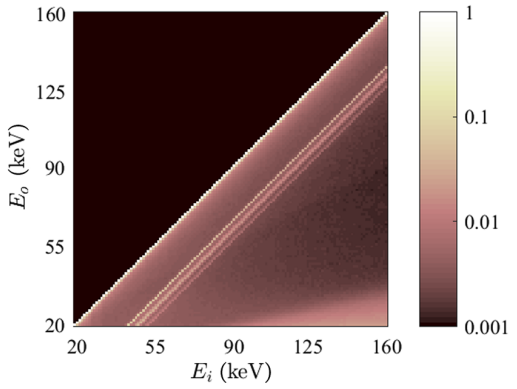

Fig. 3 The simulated detector response matrix $\mathbf{D}_{\mathrm{WP}} \cdot \mathbf{D}_E \cdot \mathbf{D}_C$ as function of the incoming photon's energy E_i and the recorded energy E_o. The color scale shows the probability density of recording an event.

A more detailed description of the simulation and models can be found in Appendix A.

2.2 *Incomplete Charge Collection*

CdTe suffers from a large difference in the drift mobility of the electrons, $\mu_e = 1000$ cm^2/V, and holes, $\mu_h = 80$ cm^2/V.[31] To mitigate this problem, CdTe detectors typically take advantage of the small pixel effect, where the ICC is reduced by having the segmented anode pads significantly smaller than the depth of the detector crystal. This minimizes the holes contribution to the signal formation and, thereby, reduces the problem with ICC due to trapping of the slow holes.[32] Despite this, ICC still occurs resulting in photons being registered with lower energy than their actual one, causing a skew of the measured spectrum toward lower energy.[20] Furthermore, effects such as polarization from the buildup of charge over time will cause ICC as well.[33]

A common description of the ICC's effect on the recorded spectrum of an incoming photon with energy E_i comes from modeling it as[20]

$$S(E) = H(E) * K(E), \tag{4}$$

where $H(E)$ is a Gaussian function with mean equal to E_i and standard deviation equal to the spectral resolution of the detector. The convolution kernel is given as

$$K_{E_k}(E) = \left[\mathrm{erf}\left(\frac{E - E_k}{\sqrt{2}\sigma_{\mathrm{ICC}}}\right) + 1\right] \cdot \chi_0(E), \tag{5}$$

for which $E_k = \mathrm{median}(E)$ and $\chi_0(E) = \begin{cases} 1, & \text{if } E \le E_k \\ 0 & \text{Otherwise} \end{cases}$.

σ_{ICC} is a scalable constant found empirically from laboratory data, which we show in Sec. 3, and is flux dependent.

2.3 *Pulse Pileup Model*

Pulse pileup occurs due to the overlapping of electrical pulses generated in an anode by two photons arriving close in time in the same pixel. To correct for the effect of pulse pileup, we use the iterative model developed by Plagnard,[15]

as described in Appendix B. To account for the photon flux-dependent pileup probability, Plagnard uses a coefficient C_{PU}, which is determined by the operator. We instead propose an automatic fitting approach using the attenuation curve of aluminum to find C_{PU}. This approach is described in Sec. 4.

2.4 *Energy Calibration*

Fluctuations in the measured energy in the order of a few keV might occur between the pixels in the detector. To calibrate the detector for these variations, the spectrum of the radioactive isotope ^{57}Co was measured. For each pixel's measured spectrum, the peak center of the primary and secondary radiation lines of the isotope as well as the escape peaks can be found. By fitting a first-degree polynomial to the expected peak centers as a function of the measured peak centers, a conversion from the measured to the actual energy is found.

3 Synchrotron Experiments

The synchrotron experiments presented in this paper were conducted at the materials science beamline ID11 at the European Synchrotron Radiation Facility (ESRF). The aim of these experiments was to evaluate our models' prediction of the distorting effects. At the ID11 beamline, the MultiX ME100 detector's response to monochromatic x-ray radiation was measured at 8 different energies between 24 and 138 keV. The x-ray energy selection was provided by double-bent crystal monochromator operating in horizontal focusing Laue geometry. The MultiX detector was mounted on the camera stage in the EH3 hutch allowing for movement in the plane perpendicular to the beam. The beam size onto the detector was controlled using slits placed just in front of the EH3 sample stage, and the beam position on the detector was changed by moving the detector stage. To obtain a reference measurement to validate the energy of the monochromatic beam, a high-energy resolution Amptek XR100T CdTe PIN-diode detector was mounted on the sample stage. The monochromatic x-ray beam's energy distribution FWHM was determined to be below the 1.4-keV resolution limit of the Amptek detector. An x-ray beam energy distribution FWHM of 1.4 keV is well below the energy resolution of the MultiX detector (estimated to be 8 keV at $E = 122$ keV at fluxes below 2 Mph/s/mm^2).[27]

3.1 *Evaluating the Flux-Independent Models*

The MultiX ME100's response to a monochromatic x-ray beam of FWHM 5×5 μm^2 was measured as a function of beam position on the detector. The detector was moved parallel and perpendicular to the pixel array in steps of $\sim$20 μm. The scan parallel to the pixel array was made across two pixels starting from approximately the center of a pixel. The detector response was measured for 2 s at each beam position before moving the detector. In Fig. 4(a), the result of a scan at $E = 123$ keV can be seen as a function of beam position and recorded energy.

The detector response of different sensor crystals (each MultiX module has 128 pixels and uses 4 tiled CdTe crystals) was evaluated by making an additional scan across 50 pixels with 5 steps per pixel. The result of this scan showed no significant change in spectral behavior among the individual pixels, except for the 2 pixels closest to the MultiX sensor crystal borders. In these border pixels, the count efficiency drops and the measured spectrum is pushed toward lower energies. In the rest of this paper, we, therefore, exclude the spectra of the 2 pixels closest to the crystal borders from all experiments and expect each of the remaining pixels to behave alike.

To evaluate the flux-independent models of our CA, the pencil beam position scan was simulated by adjusting the position and area of the simulated incoming photons' position in accordance with the experiment. The result of the simulation is shown in Fig. 4(b).

In the center of the pixel ($x \sim 585$ μm), the experimental result in Fig. 4(a) shows a tail on the primary peak ($E \sim 123$ keV) toward lower energy and a small signal at $E < 50$ keV.

To incorporate the low-energy signal in the center of the pixel in the simulation, an additional noise term was required on top of charge sharing, WP cross talk, and x-ray fluorescence. As explained in Sec. 2, we assume that Compton scattering of the incoming photon in the sensor crystal as well as electronic noise can generate such a low-energy noise signal. Hence, the new noise term was collected in the response matrix $\mathbf{D}_E$. To simulate this effect, a very simple model

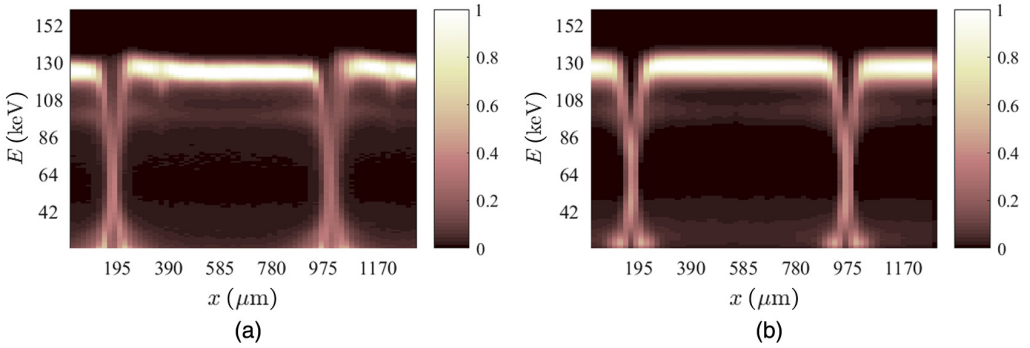

Fig. 4 The (a) measured and (b) simulated detector response as function of readout energy and the position of the monochromatic ($E = 123$ keV) pencil beam on the detector. Both simulation and experiment show two pixel border crossings positioned at $x \approx 195$ and 975 μm. The simulated spectra were convolved with K_{E_k} described in Eq. (5) to account for the peak broadening and ICC. Both color scales are normalized to peak intensity.

was developed. The effect is assumed to be position independent and modeled by including a probability, P_n, for a charge signal to be recorded subsequent to a photon being recorded. The charge signal is assumed to be a fraction of the charge deposited by the absorbed photon, with a probability distribution modeled as Gaussian with mean μ_n and width σ_n. This is done to ensure that the noise contribution's importance will increase as the photon energy increases, providing that the amount of excited charge is proportional to the absorbed energy.

The low-energy noise seen in the center of the pixel in the simulated detector response in Fig. 4(b) solely comes from the detector response matrix $\mathbf{D}_E$. We notice that the simulation overestimates the low-energy signal slightly. The value of the parameters used for this model was found from laboratory experiments as shown in Sec. 4.

The tailing effect on the primary peak shown in Fig. 4(a) was included in the simulated spectrum by convolving the simulation result with the kernel K_{E_k}, described in Eq. (5). We notice that this model slightly underestimates the extent of the primary peak's energy tail as best seen from the difference between estimated and measured signal at $E \sim 80$ keV.

Figure 4 clearly shows the incorrect recorded energy around the pixel borders due to the effect of charge sharing, x-ray fluorescence, and WP cross talk. To evaluate the simulation models, we take the sum of the measured intensity of each pixel at each position, as shown in Fig. 5(a) for a monochromatic beam with $E = 123$ keV. For each border, the cross talk intensity, i.e., the intensity that is measured in the neighboring pixel to the one being irradiated, can be fitted with a double Gaussian distribution

$$g(x) = A_{g,1} \exp\left[\frac{(x-\mu_g)^2}{2\sigma_{g,1}^2}\right] + A_{g,2} \exp\left[\frac{(x-\mu_g)^2}{2\sigma_{g,2}^2}\right], \quad (6)$$

where the identical mean of the two Gaussian distributions μ_g is forced equal to the border position, and the height $A_{g,i}$ and width $\sigma_{g,i}$ are scalable fit variables. Similar fits were made for all eight energies for both of the two pixel borders reached in the parallel scans. The resulting widths $\sigma_{g,1}$ and $\sigma_{g,2}$ are shown for all energies and both borders in Fig. 5(b).

Figure 5(b) shows that the narrowest width of the Gaussian distribution $\sigma_{g,2}$ corresponds to the expected charge cloud size estimated from Eq. (3). The broad distribution $\sigma_{g,1}$ seems to be well accounted for by the simulated extent of the WP cross talk and fluorescence photons into the neighboring pixel. However, a discrepancy is seen at energies below the K-edge of cadmium ($E_{\mathrm{Cd}} = 26.7$ keV), where a long ranged cross talk of the order of 100 μm is seen in the experimental result but not refound in the simulated model.

As a final remark, we notice that the read-out energy of the primary peak in Fig. 4(a) is shifted slightly across the pixel as function of position, an observation that was reproduced in the neighboring pixels as well. This effect was found to become more pronounced at low energies but was not studied further.

3.2 *Flux-Dependent ICC*

The flux dependence of the MultiX detector was evaluated using flux scans at ID11 at different energies with a beam positioned at the center of a pixel. The flux scans were made through increasing the beam cross section by opening the slits in steps from 5×5 μm^2 to 65×65 μm^2. In Fig. 6(a), the result of such a scan is shown for a $E = 50$ keV monochromatic beam. From the position scans and simulation in Fig. 4, it was estimated that the cross talk among pixels did not extend far enough into the pixel to affect the flux dependence measurement, and that Compton scattering and electronic noise were negligible at incoming photons with $E < 90$ keV. In Fig. 6(a), the escape peak around $E = 25$ keV and the main pulse pileup peak at $E = 100$ keV are clearly seen. As expected, the relative amplitude of the main peak decreases as the pileup peak increases with flux.

In Fig. 6(a), the spectra are clearly distorted toward lower energies as the beam flux is increased. This resembles the expected distortion from ICC, described by Eq. (4), and it, therefore, seems that the ICC increases with flux. To evaluate this effect, the main peak of the raw spectrum was fitted with $S(E)$ described by Eq. (4), with σ_{ICC} being the only parameter allowed to change with increased flux. Due to the possibility of a highly noisy spectrum, deconvolving the image with the full $S(E)$ is numerically difficult due to the Gaussian function. However, it is possible to correct for the skewness of the peak by deconvolving each spectrum with $K(E_e)$ using the σ_{ICC} found from fitting $S(E)$. The deconvolution was done using MATLAB™'s[34] built-in

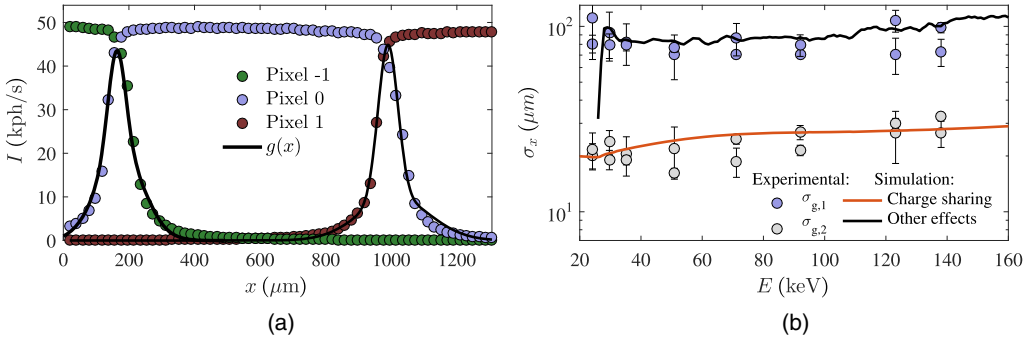

Fig. 5 Evaluating the spatial extent of the pixel cross talk. (a) The summed measured intensity of each pixel (numbered −1, 0, and 1) as function of the incoming monochromatic ($E = 123$ keV) pencil beam's position fitted with $g(x)$, Eq. (6), around the pixel borders ($x \approx 200$ and 975 μm). (b) The obtained widths $\sigma_{g,1}$ and $\sigma_{g,2}$ of $g(x)$ plotted as function of incoming photon energy with the theoretical estimated charge cloud width (charge sharing), and the width of the WP cross talk's and x-ray fluorescence's intensity distribution (other effects) superimposed.

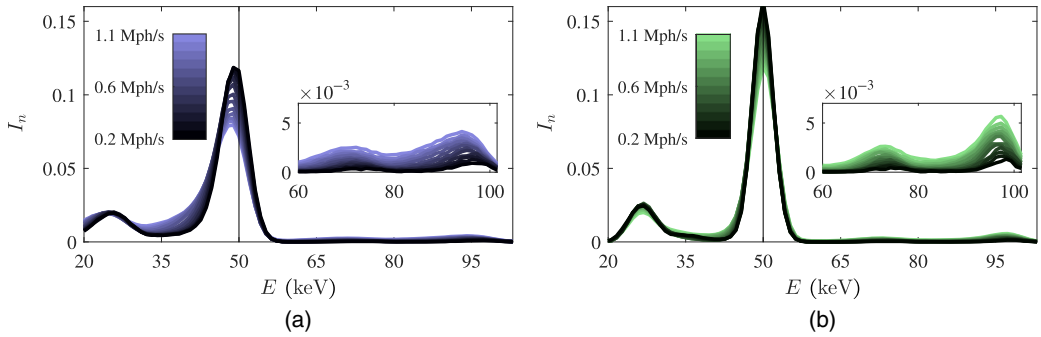

Fig. 6 Deconvolving the measured spectrum at different detector count rates (color scale) with a $K(E_e)$ kernel presented in Eq. (5). (a) The raw normalized spectrum I_n was fitted with $S(E)$, Eq. (4), from which the parameter σ_{ICC} was acquired. (b) Using the found σ_{ICC} for each spectrum, the spectral skew effect described by $K(E_e)$ can be removed through a Richardson–Lucy deconvolution and a corrected spectrum obtained. The inset box shows a zoom-in on the pileup peaks at $E = [60,100]$ keV.

Richardson–Lucy algorithm.[35,36] The result of a Richardson–Lucy deconvolution is shown in Fig. 6(b). The deconvolution works well in correcting the spectra for the peak skew as function of flux, as seen when comparing Figs. 6(a) and 6(b). To utilize this deconvolution in a correction model, a lookup table of σ_{ICC} as function of flux needs to be made. In Sec. 4, we show how this is done using the attenuation of aluminum measured with a laboratory source.

4 Laboratory Experiments

In this section, we show the laboratory measurements necessary for calibrating our CA. The x-ray laboratory experiments presented in this paper were performed in the energy dispersive x-ray diffraction (EDXRD) setup at Technical University of Denmark (DTU),[37] with a COMET MXR-160HP/11 tube that has a tungsten (W) target and a COMET MXR generator capable of operating with a voltage up to 160 kVp at a power of up to 1800 W. The x-ray flux from the source was adjusted by changing the current. Tungsten slits were used to collimate the beam and reduce the sample and environment scattering background. The scattering background from the sample in this setup was estimated to be insignificant using the simulation model described in Ref. 38.

4.1 *Optimizing the Flux-Independent Models*

The CA's flux-independent models, collected in the response matrix $\mathbf{M}_C$ presented in Eq. (2), were optimized through a simple experiment. A series of x-ray spectra were acquired by changing the source voltage and inserting different filters to attenuate the beam. For all generated spectra, the x-ray flux was kept low ($\Phi < 0.4$ Mph/s/mm^2) to minimize the effect of the flux-dependent distortions. As a reference, the same spectra were measured with the Amptek XR100T CdTe PIN-diode detector (at a count rate <10 kph/s), which due to its high-energy resolution at low count rates can be assumed to describe the true x-ray spectra. The flux-independent models contain the scalable parameters a and b in Eq. (18), as well as μ_n, σ_n, and P_n, which are used for the low-energy noise response matrix $\mathbf{D}_E$. The optimal flux-independent correction of the MultiX data was found by varying these parameters in a randomized search for the minimum χ^2 value between the corrected MultiX data and the Amptek reference data.

The best correction of the MultiX data was found for $a = b = 0.72$ mm; $P_n = 22.2\%$, $\mu_n = 0.174E_i$, and $\sigma_n = 0.2E_i$, where E_i is the simulated incoming photon energy. At these values, the low-energy noise model predicts that a recordable signal ($E > 20$ keV) from this contribution first exceeds 10% of the primary signal at incoming photon energies above 90 keV.

Two corrected spectra are shown in Fig. 7. The Amptek spectrum is convoluted with a Gaussian kernel of width $\sigma = 4$ keV corresponding to the upper energy resolution of the MultiX ME100 detector, to compare the two detectors' recorded spectra. As shown in the figure, the correction showed good correspondence to the reference measurement. Qualitatively, this was the case for all spectra we tested.

4.2 *Optimizing the Flux-Dependent Coefficients*

The proposed flux-dependent coefficients C_{PU} and σ_{ICC} presented in Eqs. (5) and (19), respectively, need to be identified from experiments. To do this, we used a measurement of the linear attenuation coefficient given as

$$\mu(E) = -\frac{1}{x}\log\left[\frac{I(E)}{I_0(E)}\right], \tag{7}$$

where $I(E)$ is the measured x-ray spectrum of the x-ray beam that has passed through the material, $I_0(E)$ is the incident spectrum measured at the detector (flat field), and x is the thickness of the material. Since the linear attenuation coefficient is a material constant independent of thickness, it can be used as a reference measure of how well the CA performs.

The measurement of the linear attenuation was done by placing aluminum plates of six different thicknesses between the detector and the source. An example of the result from such an experiment is shown in Fig. 8. The experiment was repeated for four different incident fluxes. By adjusting C_{PU} and σ_{ICC} for both $I(E)$ and $I_0(E)$ spectra, we obtain a best-fit between any measured attenuation curve of aluminum and the theoretically expected curve,[39] using the χ^2 value as a measure of the quality of the fit. The measured linear attenuation is fitted to the theoretical for the n different thicknesses of aluminum for each flat field flux. By doing so, n C_{PU} and σ_{ICC} values are obtained for both the flat field and attenuated

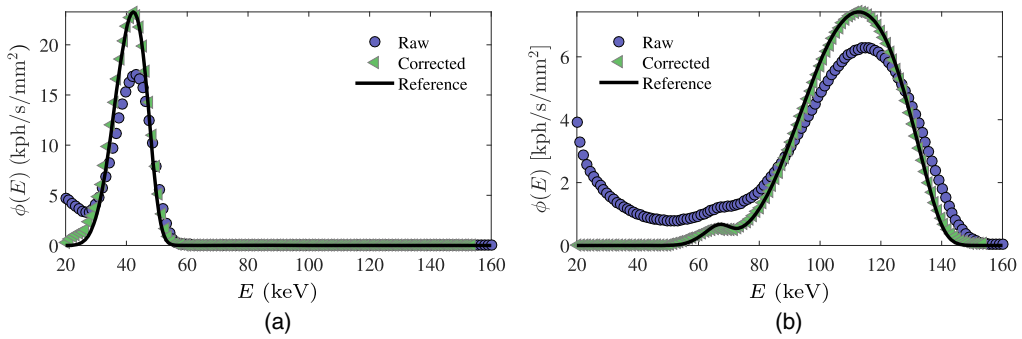

Fig. 7 Comparison between a MultiX spectrum corrected with the CA (corrected), a raw MultiX spectrum (raw), and a reference spectrum obtained with Amptek XR100 (reference). The reference spectrum is scaled to fit the corrected data. The shown spectra were obtained using (a) a filter of 19.9-mm aluminum at a source voltage of $U = 50$ kV and (b) 5.96-mm copper and 0.2-mm tantalum at $U = 140$ kV.

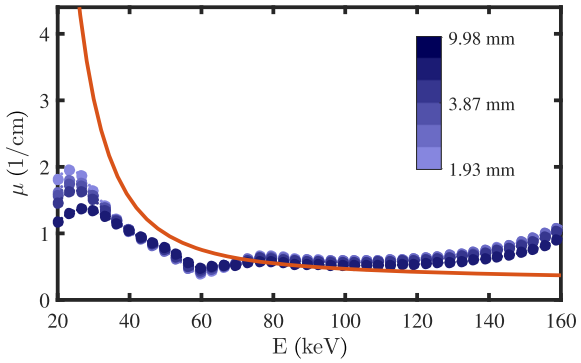

Fig. 8 Comparison between the measured linear attention curves (blue circles highlight every third point) of aluminum at different thicknesses given in the color scale, and the theoretical expected[39] (solid red line). The flat field flux was 3.7 Mph/s/mm^2.

spectra. Afterward, the n different flat field C_{PU} and σ_{ICC} are averaged. The linear attenuation fitting is then repeated, but this time using the average C_{PU} and σ_{ICC} to correct the flat field spectrum as an initial guess. Repeating this procedure ensures that the flat field spectrum correction is similar for all thicknesses.

In Fig. 9, the C_{PU} and σ_{ICC} values that result in the best-fit between measured and theoretical linear attenuation coefficient are shown for 28 spectra from 4 sets of measurement, each containing a flat field spectrum $I_0(E)$ and 6 attenuated spectra $I(E)$. The C_{PU} and σ_{ICC} coefficients are fitted with a first-order polynomial. The polynomials are used to generate fast lookup tables for correcting the spectra.

5 Final Validation of the Full Correction Algorithm

To test the full CA, a second dataset was acquired in the EDXRD setup at DTU, containing the measured linear attenuation coefficient of different thicknesses of PVC, aluminum, copper, and tantalum at different flat field fluxes. By applying the CA to the flat field and attenuated spectra and calculating the linear attenuation coefficient from these, we obtain the corrected linear attenuation curve. The measured and the corrected linear attenuation curves can be seen for a flat field flux $\Phi_0 = 4.7$ Mph/s/mm^2 in Fig. 10. In the figure, it can be seen that correcting the attenuation curve for spectral distortion improves the similarity between the measured and the theoretical expected attenuation. Particularly, at $E < 50$ keV, the CA clearly gives a much better fit between theory and data. It has to be noted that the corrected curves do not extend to 20 keV for the heavier elements,

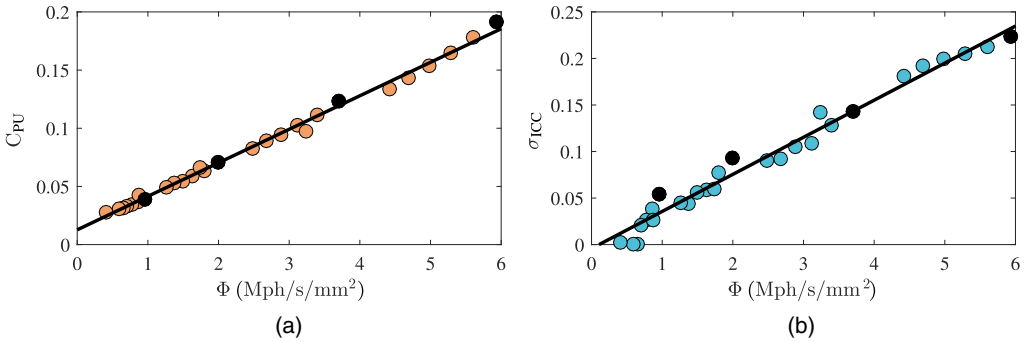

Fig. 9 (a) Pileup, C_{PU} and (b) ICC, σ_{ICC} coefficients found from fitting the linear attenuation curve of aluminum measured with the MultiX ME100 to the theoretical expected. Each point represents a corrected spectrum. The colored circles represent the correction coefficient used for the 4×6 attenuated spectra from the 6 different thicknesses of aluminum at 4 different flat field fluxes. The black circles represent the coefficients used for the 4 flat field spectra. The black lines are the C_{PU} and σ_{ICC} lookup tables, explained in the main text.

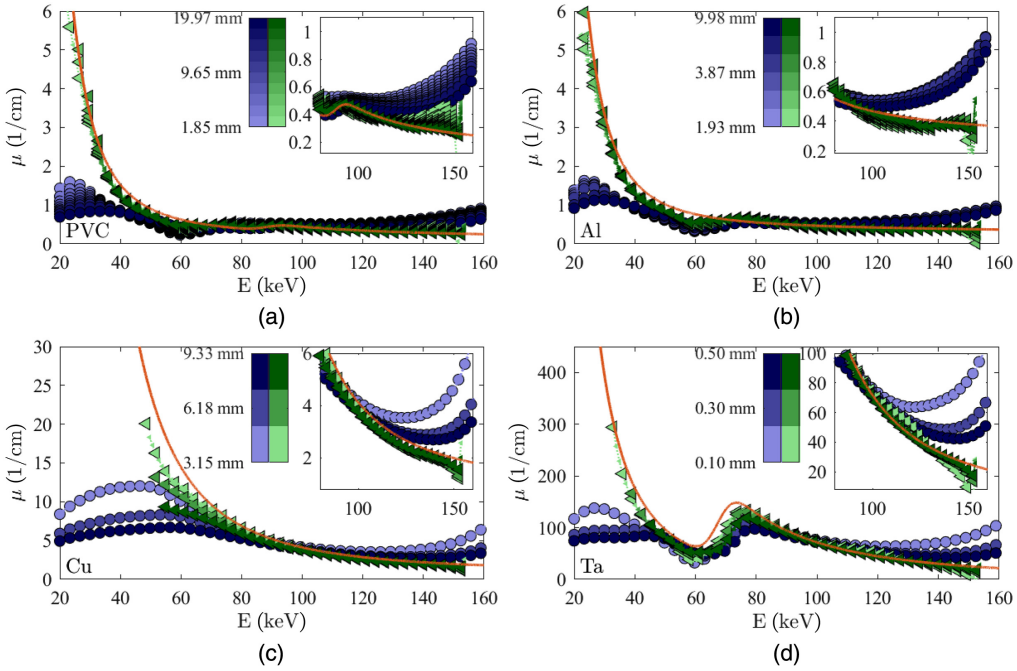

Fig. 10 Comparison between raw (blue circles) and corrected (green triangles) attention curves of (a) PVC, (b) aluminum, (c) copper, and (d) tantalum at a flat field flux of $\Phi_0 = 4.7$ Mph/s/mm^2. Every fifth data point is highlighted with a large marker. The color scales of the raw (left) and corrected (right) attenuation curves show the thickness of the measured material. The theoretical curves (solid red) are convoluted with a Gaussian kernel with $\sigma = 4$ keV.

copper and tantalum. This is due to the signal-to-noise ratio converging to zero when the corrected energy bins contain close to zero photons.

The performance of the CA is quantified by calculating the weighted correlation coefficient among the different curves. To account for statistical noise, the correlation weights were set equal to the inverse variance of the raw attenuation curve as measured by the variation between different pixels' data for both the raw and the corrected data. In Fig. 11, each material's average weighted self-correlation coefficient among the N attenuation curves is shown as function of flat field flux. Using Fisher's transform to compute the average correlation,[40] we define the average weighted self-correlation as $\overline{r}_{1,j} = \tanh\left[\frac{1}{N-1}\sum_{j=2}^{N}\tanh^{-1}(r_{1,j})\right]$, where $r_{1,j}$ is the correlation coefficient between the thinnest sheet of material, 1, and the j'th thickest. Furthermore, the figure also shows the average correlation coefficient between theory $\overline{r}_{t,j} = \tanh\left[\frac{1}{N}\sum_{j=1}^{N}\tanh^{-1}(r_{t,j})\right]$ and the j'th thickest sheet. To compare raw and corrected data equally, in both cases, the correlation coefficient is only calculated in the energy range, where the corrected data contain noninfinite values due to zero counts in the attenuated spectra. As can be seen from the figure, the average correlation coefficient of the corrected data with theory decreases very little across the full range of flat field flux, whereas the correlation between the raw curves and theory falls with increasing flux. Further, the average correlation coefficient between theoretical attenuation and the attenuation curves from the corrected data remains above, or in the case of tantalum close to, 0.95 even at high flux. Likewise, the average self-correlation coefficient of the corrected attenuation curves remains above 0.95, whereas this is only the case for aluminum in the raw dataset.

6 Discussion

The CA presented in this paper is made to correct the x-ray attenuation coefficient measured with the pixelated, multispectral detectors for multiple spectral distorting effects. The CA corrects the attenuation curve by correcting the measured flat field and attenuated x-ray spectra with the use semianalytical interpretations based on the physical origin of the different effects. Figure 10 clearly shows that the CA qualitatively improves the linear attenuation compared to theory. In particular, the CA improves the low-energy part of the attenuation, which is typically important for material identification.

In Fig. 11, we quantified that the CA improves the measured attenuation curve, both in respect to the correlation between measured and theoretical expected, but more importantly, the self-correlation between curves of different thicknesses. The latter means that the CA gives a more consistent result of the linear attenuation coefficient between different material thicknesses compared to the raw data. Furthermore, the results shown in Fig. 11 show that the CA improves the measured attenuation curves across a range of thicknesses, effective atomic number, and flat field fluxes up to at least 5 Mph/s/mm^2. This shows that the algorithm is reliable in security and other NDT applications, where unknown and largely varying samples are measured.

6.1 *Possible Improvements of the CA*

The individual models of our CA can easily be adjusted independently of each other if better models are found for any of

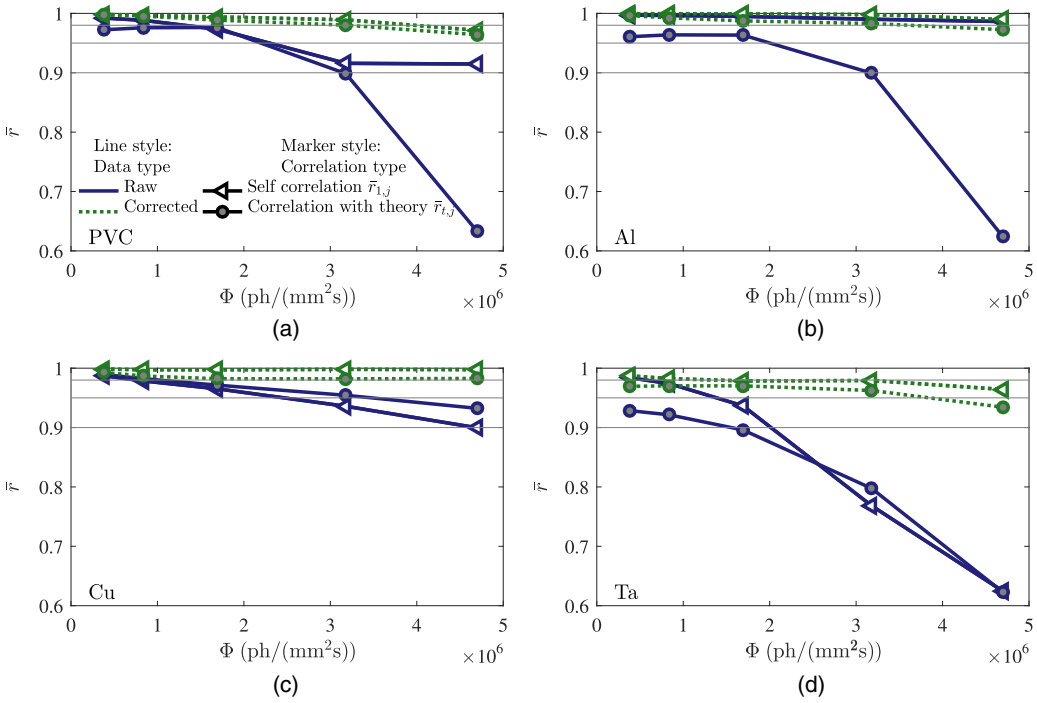

Fig. 11 The average weighted correlation coefficient as function of flat field flux, for both corrected and raw linear attenuation curves of (a) PVC, (b) aluminum, (c) copper, and (d) tantalum. The figure shows both the average weighted self-correlation coefficient between measured attenuation curves from different thicknesses of material and the average weighted correlation coefficient between the curves and the theoretical expected. Both correlation coefficients are explained in the main text. The gray straight lines mark $\bar{r} = 0.9$, $\bar{r} = 0.95$, and $\bar{r} = 0.98$.

the effects. Even though the CA clearly improves the measured attenuation curve, several of the CA's models do not fully describe the measured distortions and could be improved.

A significant distortion that is not correct by our CA is the clear drop in attenuation coefficient around $E = 59$ keV and the smaller drop around $E = 65$ keV observed in both Figs. 8 and 10. The two coincide with the tungsten K_α and K_β peaks ($E_\alpha = 59.3$ keV and $E_\beta = 67.2$ keV, respectively)[41] from the source. We expect that the drop in attenuation is due to a distortion of the tungsten peaks from the flux-dependent ICC and a general decrease of energy resolution with photon flux.[27]

Figure 4 showed that the expected MultiX detector response function could not fully account the distortion's effect in the center of the pixel. A better model than our simple empirical model of the Compton scattering in the sensor crystal and electronic noise could be added to the CA to improve the modeling of these effects. Such a new model might be part of the MultiX detector simulation and include the angular cross section of the Compton scattering and a model of the readout electronics. It is likely that Compton scattering could contribute with a loss of recorded energy of the incoming photon, resembling an ICC in addition to the recorded low-energy Compton electron signal.

The CA presented in this paper corrects the pixels spectra independently, assuming that the incident flux on two neighboring pixels is similar. The model could be improved by taking the neighboring pixels' intensity into account in cross talk models. In addition to this, the CA could be improved by developing a correction method applicable to the pixels surrounding the sensor crystal borders. In the present model designed for the MultiX ME100 detector, 4 pixels are removed for every crystal (32 pixels) corresponding to 12.4%.

6.2 *Computation Time*

The CA is based on MATLAB™ R2016a, and an extensive optimization of computing time has not yet been performed. The algorithm takes advantages of MATLAB™'s fast matrix multiplication, meaning that correcting multiple spectra together is faster than correcting them individually. At present, using a standard laptop equipped with an Intel i7-6600U quad-core CPUs at 2.60 GHz, the CA is capable of correcting the spectra of a full MultiX ME100 detector (128 pixels) in 50 ± 0.5 ms whereas a single pixel correction takes 7 ± 1 ms. It is in particular the two flux-dependent, ICC and the pileup correction, models that add to the computation time. The ICC and pileup models take around 42.7% and 42.3% of the computational time, respectively. There is, therefore, a great potential to reduce the computation time by optimizing these two flux-dependent models of the CA.

Furthermore, the present algorithm could easily be run in parallel, correcting each pixel independently, which without any further optimization would reduce the correction time to that of a single pixel, i.e., 7 ± 1 ms. By correcting a batch of acquisition frames, e.g., 50 frames of each 1 ms, the correction time could be reduced to <0.5 ms per frame. This means

that the present CA, if run in parallel, could correct the measured spectra in real time even at a frame rate of 1 ms and, hence, be used in applications where material identification needs to be fast, e.g., luggage screening in airports.

6.3 *Setup Compatibility*

The CA presented in this paper is optimized and tested for the MultiX ME100 v2, but the models are directly convertible to any CdTe line array detector and could with small adjustments be used for two-dimensional (2-D) CdTe flat panel or even CZT detectors. The calibration of the CA only requires a measurement of the attenuation coefficient of a well-defined material, such as aluminum, at different thicknesses and at different flat field fluxes. This means that the CA can easily be used in other experimental setups. In addition to this, an energy calibration measurement might be needed. This can be done with x-ray fluorescence from metals or a well-known radioactive isotope source.

7 Conclusion

We have in this paper shown an effective algorithm for correcting the material-dependent x-ray attenuation for effects, such as charge sharing, WP cross talk, pulse pileup, etc. The presented algorithm is designed and tested on data acquired with the MultiX ME100 but could be adapted to other formats of pixelated CdTe and CZT detectors with small adjustments. Using synchrotron and laboratory sources, the different correction models have been verified and the algorithm has been tested. The results from calculating the linear attenuation curves from the corrected flat field and attenuated spectra indicate that a better correspondence to data from theoretical reference tables is possible if the CA is applied to the raw data. Furthermore, the corrected measurements give significantly more consistent data, which should enable a more reliable material identification in various applications. The algorithm is applicable in any setup requiring only a few calibration measurements using easily accessible materials. The present algorithm is reasonably fast, correcting 128 pixels' spectra (contain 128 energy bins) in 50 ± 0.5 ms, and it could easily be improved by one or two orders of magnitude, making it useful in application, such as luggage screening in airports and other high-throughput NDT setups.

Appendix A: Simulating the Response Matrix

In the following, the simulation of the detector response due to escape peaks, charge sharing, electronic noise and Compton scattering, and WP cross talk is presented in detail. The models are designed to account for one-dimensional (1-D) pixelarray detector but could be extended to 2-D flat panel detectors.

The simulation is based on a single-photon Monte Carlo simulation of a pixel irradiated with x-rays. The photon's absorption position as a function of depth in the crystal is simulated according to the probability distribution given by the expected attenuation of CdTe.[39]

A.1 Escape Peak and X-Ray Fluorescence

The effect of escape peaks is taken into account by including x-ray fluorescence in the simulation. X-ray fluorescence occurs when the energy of the photon is larger than the K 1s shell binding energy ($E_{\mathrm{Cd}} = 26.711$ keV for Cd and $E_{\mathrm{Te}} = 31.814$ keV for Te[42]). The refilling of the K-shell results the emission of a photon as either K_α or K_β fluorescence, with a probability given by the fluorescence yield. The energy of the fluorescence lines is for cadmium $E_\alpha = 23.2$ keV and $E_\beta = 26.1$ keV and tellurium $E_\alpha = 27.5$ keV and $E_\beta = 31.0$ keV.[42] In the simulation, each absorbed photon with energy E_i and absorption location $\mathbf{r}_i$ has a probability to emit a K_α or K_β fluorescence photon from either Cd or Te with energy E_f governed by the value of E_i compared to the energy of the K 1s shell of Cd and Te:

- $E_i < E_{\mathrm{Cd}}$: No fluorescence photon is emitted.
- $E_{\mathrm{Cd}} < E_i < E_{\mathrm{Te}}$: A fluorescence photon is emitted with an 84% probability equaling the fluorescence yield of cadmium.[43] The energy E_f of the created fluorescence photon is set to either $E_f = 23.2$ keV ($P_f = 0.18$) or $E_f = 26.1$ keV ($P_f = 0.82$), where P_f is the probability of each energy.
- $E_i > E_{\mathrm{Te}}$: A fluorescence photon is created with probability of 85.8% equaling the average fluorescence yield of cadmium and tellurium.[43] The energy of the created fluorescence photon is set to $E_f = 23.2$ keV ($P_f = 0.09$), $E_f = 26.1$ keV ($P_f = 0.41$), $E_f = 27.5$ keV ($P_f = 0.09$), or $E_f = 31.0$ keV ($P_f = 0.41$).

The K_α or K_β fluorescence probability for the cadmium and tellurium used above is calculated according to the values reported in Ref. 43. In the simulation, the fluorescence photons are emitted in a random direction and absorbed at $\mathbf{r}_f$. The fluorescence photon's travel distance before absorption $|\mathbf{r}_f - \mathbf{r}_i|$ is simulated according to the probability distribution function given by the attenuation in CdTe. If a fluorescence photon is emitted, the energy deposited at $\mathbf{r}_i$ is set to $E_d = E_i - E_f$ and the remaining energy E_f is absorbed in $\mathbf{r}_f$, else $E_d = E_i$. If $\mathbf{r}_f$ lies outside the detector volume, the energy contained in the fluorescence photon is removed from the simulation and, hence, not detected. This creates an escape peak.

In the simulation, the initially absorbed photon and the fluorescence photon will be recorded at the same time, meaning that the recorded energy will be the sum of the energy deposited in a pixel from both photons.

A.2 Charge Sharing

The final $\mathbf{D}_C$, $\mathbf{D}_{\mathrm{WP}}$, and $\mathbf{D}_N$ response matrices are calculated by making 2-D histograms of all simulated photons' recorded and their respective incoming energy. The calculation of charge sharing and WP cross talk both result in an amount of energy being recorded on the pixels neighboring the center pixel where the photon was initially absorbed. Energy recorded in a neighboring pixel will be included in the final response matrices, by including them as separate events in the histograms. In the following, the energy deposited in a location $\mathbf{r}_0 = (x_0, y_0, z_0)$ will be denoted E_0 (and is either $E_0 = E_d$ or $E_0 = E_f$). Pixelated, multispectral CdTe detectors typically have a segmented anode collecting the electrons responsible for the spatial resolution of the detector and a common cathode collecting the holes. Therefore, the charge sharing and WP cross talk are in the simulation

assumed to be coursed only by the drift of the excited electrons.

The amount of electrons shared between two pixels is calculated for each photon by assuming that the excited electron cloud is a 1-D Gaussian distribution parallel to the pixel array. In this model, the deposited energy recorded in the neighboring pixels to the "left" or "right" of the primary pixel is given by[29]

$$E_{\text{right}} = \frac{E_0}{2}\left[1 - \text{erf}\left(\frac{d_x/2 - x_0}{\sigma\sqrt{2}}\right)\right],$$
$$E_{\text{left}} = \frac{E_0}{2}\left[1 - \text{erf}\left(\frac{d_x/2 + x_0}{\sigma\sqrt{2}}\right)\right], \tag{8}$$

where d_x is the width of the pixel and σ is the standard deviation of the electron cloud distribution. The energy recorded in the center pixel is given by $E_{\text{center}} = E_0 - E_{\text{right}} - E_{\text{left}}$. It is noted that in the simulation $\mathbf{r}_0$ will be confined to the central pixel for the original absorbed photon, but in the case of fluorescence photon, it can be in either the left or right neighbor pixel. The electron cloud at the anode, where the electrons are recorded, is assumed to be given by

$$\sigma = \sqrt{\sigma_t^2 + \sigma_i^2}, \tag{9}$$

where $\sigma_i = 5\ \mu\text{m}$[30] is the initial width of the excited charge cloud and σ_t can be calculated from the diffusion equation

$$\sigma_t^2 = 2D\tau, \tag{10}$$

where D is the diffusion constant and τ is the charge carrier lifetime.[28] To include the charge repulsion in this model, an effective diffusion constant is used[30]

$$D_{\text{eff}} = D + \frac{1}{15}\left(\frac{3\mu_e Nq}{4\pi\epsilon}\right)\frac{1}{\sqrt{5}\sigma_i}, \tag{11}$$

where μ_e is the electron mobility, q is the elementary charge, and ϵ is the permittivity. The number of charges per photon is given by $N = E_e/\Delta_E$, where $\Delta_E = 4.43$ eV/ehp[31] is the energy per ehp for CdTe and E_e is the energy deposited in the detector by the absorbed photon. The additional contribution to the charge cloud distribution due to reabsorbed fluorescence photons creating two cloud centers is thereby not taken into account. This choice was made to simplify calculations of the charge sharing effect.

By combining Eqs. (10) and (11), we obtain an expression for the cloud width due to repulsion and diffusion

$$\sigma_t = \sqrt{2\tau D + \frac{2\tau}{15}\left(\frac{3\mu_e Nq}{4\pi\epsilon}\right)\frac{1}{\sqrt{5}\sigma_i}}. \tag{12}$$

According to the Einstein relation $D = \frac{\mu_e k_B T}{q}$, where T is the temperature and k_B is the Boltzmann's constant. Assuming parallel plate electrodes with bias voltage U, we can rewrite the drift time in terms of detector depth d and interaction point compared to the anode z, such that $\mu_e\tau = \frac{zd}{U}$.[44] By combining the latter with Eqs. (9) and (12), we find

$$\sigma_t = \sqrt{2\frac{k_B T z d}{qU} + \left(\frac{zdNq}{10\pi\epsilon U}\right)\frac{1}{\sqrt{5}\sigma_i} + \sigma_i^2}. \tag{13}$$

A.3 WP Cross Talk

According to the description presented in Ref. 12, the WP cross talk originates from current induced in the neighboring pixels to the pixel where the excited charge cloud is moving. The induced current in neighboring pixels integrates to zero along the charge clouds drift path; however, if the induced current becomes large enough, it might still trigger a signal in the detector. The induced charge $Q(\mathbf{r})$ on an electrode due to moving charges in the active detector volume is described by the Shockley–Ramo theorem[28,45,46]

$$Q(\mathbf{r}) = N_0 \cdot q \cdot \phi(\mathbf{r}), \tag{14}$$

where N_0 is the number of charge carrier, q is the charge of the carriers, and $\phi(\mathbf{r})$ is the WP. The WP cross talk induced from each photon is in our simulation modeled by rewriting Eq. (14) into

$$\Delta E = E_0 \cdot \Delta\phi_j(\mathbf{r}_0), \tag{15}$$

where ΔE is the recorded energy from the charge induced in pixel j, and E_0 is the energy of the photon absorbed in pixel $j+1$, and $\Delta\phi_j$ is the difference in the WP of pixel j from the start of the charge drift path at the absorption point $\mathbf{r}_0$ to the point where the maximum charge is induced (i.e., where the current reverses on the j pixel). The model is a simplification as it assumes a point shape charge cloud containing all charge induced from a photon.

A simple model of the WP $\phi_j(\mathbf{r})$ is described in Ref. 16, where it is assumed that the detector consists of two infinite parallel plates. This model is taken as a simple approximation of the WP cross talk in the MultiX ME100, and it is repeated here for the ease of the reader. The model uses the method of mirror charges, where the WP can be described by an infinite sum of charge mirrors

$$\phi_j(\mathbf{r}) = \sum_{k=-\infty}^{\infty} \phi_0(x, y, z - 2kd, a, b), \tag{16}$$

where d is the depth of the CdTe crystal, and a and b are the dimensions of the anode pad, which is assumed rectangular. Under this assumption, the mirror potential is given by

$$\phi_0(x, y, z) = \frac{1}{2\pi}\left[\arctan\left(\frac{(a-\xi)(b-\eta)}{z\sqrt{(a-\xi)^2 + (b-\eta)^2 + z^2}}\right) + \arctan\left(\frac{(a-\xi)\eta}{z\sqrt{(a-\xi)^2 + \eta^2 + z^2}}\right) + \arctan\left(\frac{\xi(a-\xi)}{z\sqrt{(\xi^2 + (b-\eta)^2 + z^2}}\right) + \arctan\left(\frac{\xi\eta}{z\sqrt{\xi^2 + \eta^2 + z^2}}\right)\right], \tag{17}$$

with

$$\xi = \frac{(x - x_1)(x_2 - x_1) + (y - y_1)(y_2 - y_1)}{a},$$
$$\eta = \frac{-(x - x_1)(y_2 - y_1) + (y - y_1)(x_2 - x_1)}{b}. \quad (18)$$

In the above, the corners of the anode are placed at (x_i, y_i) for $i = 1 \ldots 4$ and x, y, z, are the simulated interaction points of the charge above pixel $j - 1$ with respect to the center of anode j. A way to determine a and b is described in Sec. 4 in the main paper. Equation (16) should be evaluated as an infinite sum, however, in the simulation, the sum is only evaluated in $k = [-2,2]$, as it has been shown to be a reasonable approximation.[47]

A.4 Compton Scattering and Electrical Noise

As explained in the main text, the detector response due to Compton scatter and electronic noise, contained in the response matrix $\mathbf{D}_E$, is calculated through a simplified model.

In the model, we assume that either the Compton electron or the scattered photon is recorded in the same pixel, i.e., the recorded energy will be equal to the incoming photon's energy or the scattered photon escapes the detector leaving only the Compton electron to be recorded. There is a finite probability that the Compton electron and the scattered photon will be recorded in different pixels, resulting in the scattered photon being recorded with energy lower than its incident when entering the crystal. This effect is not included in the model. However, this effect resembles that of the ICC, which is corrected for by the ICC model, and, hence, mitigates the effect of Compton scattering on the primary recorded photon energy.

Both the Compton scattering cross section and Compton edge (maximum energy transferred to the scattered electron) increase with energy.[28] The Compton edge becomes larger than 20 keV at photon incoming energies $E_i > 82$ keV. Hence, the low-energy spectrum is only affected by the photon above 82 keV. In addition to this, electronic noise, which arises as example from fluctuations in the leakage current, can contribute with a signal at low energies as well. To include these effects, we assume that the absorption of a photon would generate an electronic noise or Compton scattering charge signal with a probability P_n, described by a distribution modeled as Gaussian with mean μ_n and width σ_n. As the noise is added as a fraction of the original charge deposited in the detector, the noise contribution's importance will increase as the photon energy increases, since the amount of charge excited by the absorbed photon energy is proportional to the absorbed energy. Thereby, the noise term will have almost no importance at low energy where it will create a signal below the detection limit of the MultiX ME100 of 20 keV. The exact values of the parameters used to describe the noise term were found empirically as described in the experimental section.

Appendix B: Pulse Pileup Model

To correct for pulse pileup, we use the method developed by Plagnard,[15] which we present below for the ease of the reader. The model is based on the assumption that two photons with energy E_1 and E_2 will be counted as one with the combined energy of the two $E_t = E_1 + E_2$, if the time between the two is small enough. The effect of the pulse pile up on the measured spectrum $I_R(E)$ is described by the pileup spectrum $I_{PU}(E_{nx})$. The pileup correction model needs to calculate $I_{PU}(E_{nx})$ for all values of E_n and E_x, with E_n and E_x being the center energy of the MultiX ME100's n and x energy bin, respectively. For each n, the pileup spectrum is calculated for the whole range of x by

$$I_{PU}(E_{nx}) = \frac{I_R(E_n)}{\sum_e \bar{I}_R(E_e)} \cdot C_{PU} \cdot \bar{I}_R(E_x). \quad (19)$$

Afterward, the obtained spectrum $I_{PU}(E)$ is subtracted from the raw spectrum, and the summed contribution is added to $I_C(E_n)$ of the n energy bin to obtain the corrected spectrum

$$I_C(E) = I_R(E) - I_{PU}(E),$$
$$I_C(E_n) = I_C(E_n) + \sum_e I_{PU}(E_e). \quad (20)$$

At this point, n is increased and the procedure is repeated. Plagnard lets the coefficient C_{PU} in Eq. (19) be determined by the operator.

Acknowledgments

The authors would like to thank Exruptive for financing the ESRF beam time, through the initiative LINX (Linking Industry with Neutrons and X-rays) funded by Innovations fund Denmark. Furthermore, we thank Jon Wright from ID-11 for assistance during the beam time. The authors acknowledge Innovation Fund Denmark for financing this work. Preliminary results of this study have been presented at the SPIE Optical Engineering + Applications Conference on Radiation Detectors in Medicine, Industry, and National Security XVIII (2017) and published in the conference proceedings.[48]

References

1. G. Beldjoudi et al., "Multidimensional data processing methods for material discrimination using an ideal x-ray spectrometric photon counting detector," *IEEE Trans. Nucl. Sci.* **58**(6), 3190–3203 (2011).
2. Y. Yuan, B. Tracey, and E. Miller, "Robust x-ray based material identification using multi-energy sinogram decomposition," *Proc. SPIE* **9847**, 98470V (2016).
3. N. Kimoto et al., "Development of a novel method based on a photon counting technique with the aim of precise material identification in clinical x-ray diagnosis," *Proc. SPIE* **10132**, 1013239 (2017).
4. V. Rebuffel et al., "New perspectives of x-ray techniques for explosive detection based on CdTe/CdZnTe spectrometric detectors," in *Proc. of the Int. Symp. on Digital Industrial Radiology and Computed Tomography*, Vol. 2 (2011).
5. L. Martin, "Enhanced information extraction in the multi-energy x-ray tomography for security," PhD Thesis, Boston University (2014).
6. K. Taguchi and J. S. Iwanczyk, "Vision 20/20: single photon counting x-ray detectors in medical imaging," *Med. Phys.* **40**, 100901 (2013).
7. N. Anderson and A. Butler, "Clinical applications of spectral molecular imaging: potential and challenges," *Contrast Media Mol. Imaging* **9**, 3–12 (2014).
8. P. Shikhaliev, "Soft tissue imaging with photon counting spectroscopic CT," *Phys. Med. Biol.* **60**, 2453–2474 (2015).
9. E. I. Parsai, D. Shvydka, and J. Kang, "Design and optimization of large area thin-film CdTe detector for radiation therapy imaging applications," *Med. Phys.* **37**(8), 3980–3994 (2010).
10. D. Shvydka, X. Jin, and E. I. Parsai, "Performance of large area thin-film CdTe detector in diagnostic x-ray imaging," *Int. J. Med. Phys. Clin. Eng. Radiat. Oncol.* **2**(3), 98–109 (2013).
11. E. S. Jimenez et al., "Developing imaging capabilities of multi-channel detectors comparable to traditional x-ray detector technology for industrial and security applications," *Proc. SPIE* **9969**, 99690A (2016).

12. A. Brambilla et al., "CdTe linear pixel x-ray detector with enhanced spectrometric performance for high flux x-ray imaging," *IEEE Trans. Nucl. Sci.* **59**(4), 1552–1558 (2012).
13. L. Abbene et al., "Digital fast pulse shape and height analysis on cadmiumzinctelluride arrays for high-flux energy-resolved x-ray imaging," *J. Synchrotron Radiat.* **25**, 257–271 (2018).
14. H. Ding and S. Molloi, "Image-based spectral distortion correction for photon-counting x-ray detectors," *Med. Phys.* **39**, 1864–1876 (2012).
15. J. Plagnard, "Comparison of measured and calculated spectra emitted by the x-ray tube used at the Gustave Roussy radiobiological service," *X-Ray Spectrom.* **43**, 298–304 (2014).
16. P. Guerra, A. Santos, and D. G. Darambara, "Development of a simplified simulation model for performance characterization of a pixellated CdZnTe multimodality imaging system," *Phys. Med. Biol.* **53**, 1099–1113 (2008).
17. J. C. Kim, W. R. Kaye, and Z. He, "Signal modeling of charge sharing effect in simple pixelated CdZnTe detector," *J. Korean Phys. Soc.* **64**, 1336–1345 (2014).
18. J. Cammin et al., "A cascaded model of spectral distortions due to spectral response effects and pulse pileup effects in a photon-counting x-ray detector for CT," *Med. Phys.* **41**(4), 041905 (2014).
19. J. E. Fernandez, V. Scot, and L. Sabbatucci, "A modeling tool for detector resolution and incomplete charge collection," *X-Ray Spectrom.* **44**, 177–182 (2015).
20. R. H. Redus et al., "Characterization of CdTe detectors for quantitative x-ray spectroscopy," *IEEE Trans. Nucl. Sci.* **56**, 2524–2532 (2009).
21. J. Cammin et al., "Evaluation of models of spectral distortions in photon-counting detectors for computed tomography," *J. Med. Imaging* **3**, 023503 (2016).
22. "Multix—x-ray spectrometry in transmission for security, food, recycling," http://www.multixdetection.com/ (26 April 2018).
23. A. Gorecki et al., "Comparing performances of a CdTe x-ray spectroscopic detector and an x-ray dual-energy sandwich detector," *J. Instrum.* **8**, P11011 (2013).
24. M. Kheirabadi et al., "Multispectral x-ray CT: multivariate statistical analysis for efficient reconstruction," *Proc. SPIE* **10391**, 1039113 (2017).
25. A. Brambilla et al., "Basis material decomposition method for material discrimination with a new spectrometric x-ray imaging detector," *J. Instrum.* **12**, P08014 (2017).
26. I. M. E. Fulladosa and P. Gou, "Effect of dry-cured ham composition on x-ray multi energy spectra," *Food Control* **70**, 41–47 (2016).
27. A. Brambilla et al., "Fast CdTe and CdZnTe semiconductor detector arrays for spectroscopic x-ray imaging," *IEEE Trans. Nucl. Sci.* **60**(1), 408–415 (2013).
28. G. F. Knoll, *Radiation Detection and Measurement*, 3rd ed., John Wiley and Sons, Inc., New York (1999).
29. X. Wang et al., "Micro CT with energy-resolved photon-counting detectors," *Phys. Med. Biol.* **56**, 2791–2816 (2011).
30. L. A. Hamel et al., "Optimization of single-sided charge-sharing strip detectors," in *IEEE Nuclear Science Symp. Conf. Record* (2006).
31. D. S. McGregor and H. Hermon, "Room-temperature compound semiconductor radiation detectors," *Nucl. Instrum. Methods Phys. Res. Sect. A* **395**, 101–124 (1997).
32. H. H. Barrett, J. D. Eskin, and H. B. Barber, "Charge transport in arrays of semiconductor gamma-ray detectors," *Phys. Rev. Lett.* **75**(1), 156–159 (1995).
33. H. Toyama et al., "Quantitative analysis of polarization phenomena in CdTe radiation detectors," *Jpn. J. Appl. Phys.* **45**(11), 8842–8847 (2006).
34. "MATLAB processing toolbox," The MathWorks, Natick, Massachusetts (2016).
35. D. S. C. Biggs and M. Andrews, "Acceleration of iterative image restoration algorithms," *Appl. Opt.* **36**(8), 1766–1775 (1997).
36. R. J. Hanisch, R. L. White, and R. L. Gilliland, "Deconvolution of Hubbles Space Telescope images and spectra," in *Deconvolution of Images and Spectra*, 2nd ed., P. A. Jansson, Ed., pp. 310–360, Academic Press, Inc., Orlando, Florida (1996).
37. J. Kehres, M. Lyksborg, and U. L. Olsen, "Threat detection of liquid explosives and precursors from their x-ray scattering pattern using energy dispersive detector technology," *Proc. SPIE* **10393**, 1039302 (2017).
38. M. Busi et al., "Simulation tools for scattering corrections in spectrally resolved x-ray computed tomography using McXtrace," *Opt. Eng.* **57**(3), 037105 (2018).
39. NIST, "X-ray form factor, attenuation, and scattering tables," http://physics.nist.gov/PhysRefData/FFast/html/form.html (6 August 2017).
40. D. M. Corey, W. P. Dunlap, and M. J. Burke, "Averaging correlations: expected values and bias in combined Pearson rs and Fisher's z transformations," *J. Gen. Psychol.* **125**(3), 245–261 (1998).
41. NIST, "X-ray transition energies by element," http://physics.nist.gov/PhysRefData/XrayTrans/Html/search.html (6 August 2017).
42. A. Thompson and D. Vaughan, *X-Ray Data Booklet*, Lawrence Berkeley National Laboratory, Berkeley, California (2009).
43. W. Bambynek et al., "X-ray fluorescence yields, Auger, and Coster–Kronig transition probabilities," *Rev. Mod. Phys.* **44**(4), 716–813 (1972).
44. K. Iniewski et al., "Modeling charge-sharing effects in pixellated CZT detectors," in *IEEE Nuclear Science Symp. Conf. Record* (2007).
45. W. Shockley, "Currents to conductors induced by a moving point charge," *J. Appl. Phys.* **9**, 635–636 (1938).
46. S. Ramo, "Currents induced by electron motion," *Proc. IRE* **27**(9), 584–585 (1939).
47. A. Castoldi, E. Gatti, and P. Rehak, "Three-dimensional analytical solution of the Laplace equation suitable for semiconductor detector design," *IEEE Trans. Nucl. Sci.* **43**(1), 256–265 (1996).
48. E. D. Christensen et al., "Spectral correction algorithm for multispectral CdTe x-ray detectors," *Proc. SPIE* **10393**, 103930H (2017).

Erik Schou Dreier is a PhD student at the Niels Bohr Institute, University of Copenhagen, Denmark. He received both his BS and MS degrees in physics from the University of Copenhagen in 2013 and 2016. His research is focused on finding possible new applications and characterization of innovative single-photon-counting x-ray detectors. He is a member of SPIE.

Jan Kehres is a research engineer at Technical University of Denmark (DTU) Physics, Kongens Lyngby, Denmark. He received his PhD in operando investigation of catalyst nanoparticles using x-ray scattering and continued in this field of research as a postdoctoral researcher. His current field of research is the application of energy-dispersive detectors for x-ray scattering and advanced imaging modalities with a focus on material identification of illicit materials for security applications.

Mohamad Khalil is a postdoctoral researcher at DTU, Kongens Lyngby, Denmark. He received his MS degree in high-energy physics from the University Paris Pierre et Marie Curie, Paris, France, in 2011 and his PhD from the University Paris Denis Diderot, Paris, France, and University of Ferrara, Ferrara, Italy, in December 2014.

Matteo Busi is a PhD student at DTU, Kongens Lyngby, Denmark. He received his BS degree in physics from the Universit degli Studi di Parma, Parma, Italy, and his MS degree in mathematics and physics from the Universitetet i Stavanger, Stavanger, Norway, in 2014 and 2016, respectively. He is a member of SPIE.

Yun Gu was a postdoctoral researcher at DTU, Kongens Lyngby, Denmark from 2014 to 2017. She received her PhD from the University of Copenhagen, Copenhagen, Denmark, for advanced structural characterization of organic films specializing in x-ray diffraction technologies, and her master's degree in physics from the University of Siegen, Siegen, Germany.

Robert Feidenhans'l received his master's degree in physics and his PhD both from the University of Aarhus in 1983 and 1986, respectively. He has worked at Ris National Laboratory from 1986 to 2005. In 2005, he became a professor at the Niels Bohr Institute, University of Copenhagen. In January 2017, he became the managing director of the European XFEL, Hamburg. He has been working in the field of x-ray synchrotron radiation and free electron lasers his entire career.

Ulrik Lund Olsen is a senior research engineer at DTU Physics since 2013. He was funded by Innovation Fund Denmark to develop applications using high flux multispectral x-ray detection technology, and currently, he is the project leader on CIL2018, a multidisciplinary effort made to reduce the human operator involvement by 50% for checked-in luggage. He was previously employed at National Laboratory RISØ, Denmark, as PhD candidate in 2005 and later postdoc working with developments of x-ray sensors.

Paper III

Method for System-Independent Material Characterization from Spectral X-ray CT.

Matteo Busi, K. Aditya Mohan, Alex A. Dooraghi, Kyle M. Champley, Harry E. Martz, and Ulrik L. Olsen

NDT and E International 107 (2019) 102136

Contents lists available at ScienceDirect

NDT and E International

journal homepage: www.elsevier.com/locate/ndteint

Method for system-independent material characterization from spectral X-ray CT

Matteo Busi[a,b,*], K. Aditya Mohan[b], Alex A. Dooraghi[b], Kyle M. Champley[b], Harry E. Martz[b], Ulrik L. Olsen[a]

[a] Technical University of Denmark, DTU Physics, 2800, Kgs. Lyngby, Denmark
[b] Lawrence Livermore National Laboratory, Livermore, CA, 94551, USA

ARTICLE INFO

Keywords:
spectral X-ray CT
Quantitative X-ray characterization
Effective atomic number
Electron density
Photon counting detectors
Security screening

ABSTRACT

We propose a method for material characterization using Spectral X-ray Computed Tomography (SCT). Our SCT method takes advantage of recently-developed MultiX ME 100 photon counting detectors to simultaneously measure the energy dependence of a material's linear attenuation coefficient (LAC). Relative electron density (ρ_e) and effective atomic number ($\boldsymbol{Z_e}$) are estimated directly from the energy-dependent LAC measurements. The method employs a spectral correction algorithm and automated selection and weighting of the energy bins for optimized performance. When examining materials with $\boldsymbol{Z_e \leq 23}$, this method achieves accuracy comparable to traditional dual-energy CT, which is often realized through consecutive data acquisitions, and is compatible with any spectral detector. The method disregards data in photon starved energy channels improving the detection of highly attenuating materials, compared to techniques that use energy integrating detectors.

1. Introduction

Laboratory or industrial based X-ray radiography and Computed Tomography (CT) provide structural images of an object (airline baggage, human body, etc.), but do not typically measure quantitative material properties such as electron density or effective atomic number [1,2]. One reason is because the polychromatic nature of the incident X-rays obscures quantification due to non-linearities in how the radiation is attenuated. Moreover, analysis using the effective linear attenuation coefficient (LAC) to classify materials may result in a system-dependent solution [3]. Recently, a method was presented for material characterization using dual-energy computed tomography (DECT), called System Independent ρ_e/Z_e (SIRZ) [4], which demonstrated accurate and precise results for a set of materials with $\boldsymbol{Z_e}$ between 6 and 20. The results were shown to be consistent between different DECT systems used to perform the acquisitions. However, this method requires collection of two distinct datasets, and includes a set of reference materials for calibration of the detector's spectral response.

Advances in cadmium telluride (CdTe) energy-discriminating pixelated detectors have enabled the possibility of Spectral X-ray Computed Tomography (SCT) which incorporates spectroscopic information into CT. Theoretical and experimental studies examining photon counting detectors (PCDs) have suggested that SCT outperforms conventional energy-integrating CT in material discrimination and detection tasks [5–10]. MultiX ME100 (MultiX, Neuilly-sur-Seine, France) is a PCD that has been shown to be able to efficiently handle photon fluxes up to **7 Mphotons/pixel** [10], making it a suitable candidate for real scanning applications. Brambilla et al. presented a basis material decomposition method using MultiX ME100 PCD [11]. The method requires a calibration step in which a set of reference material (polyethylene and polyvinyl chloride) is measured. The scanned objects are characterized into thicknesses relative to the reference materials. From these, the effective atomic number, $\boldsymbol{Z_e}$, of the unknown materials is interpolated or extrapolated. In this work, we present a new method for the estimation of system independent material features (ρ_e and Z_e) from SCT acquisitions. The method estimates material features directly from measured energy resolved LACs. The formulation of the method makes it compatible with an arbitrary number of energy bins.

2. Materials and methods

In this section, we define the system-independent physical properties we have used to characterize materials. We then describe the instrumentation and the samples used to conduct the experiments. Lastly, we present the algorithm to estimate the system independent features from experimental data.

* Corresponding author. Fysikvej 307 R251, 2800, Kgs. Lyngby, Denmark.
E-mail address: mbusi@fysik.dtu.dk (M. Busi).

https://doi.org/10.1016/j.ndteint.2019.102136
Received 14 November 2018; Received in revised form 23 April 2019; Accepted 2 July 2019
Available online 08 August 2019
0963-8695/

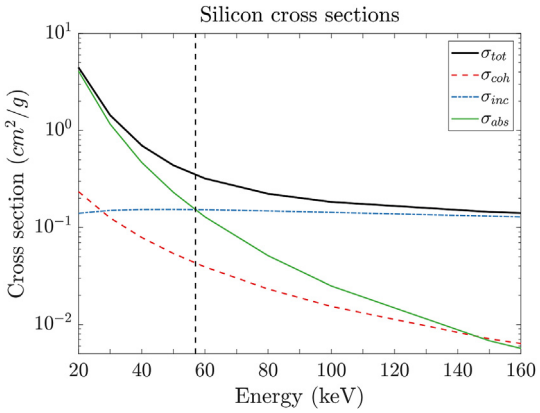

Figure 1. The NIST cross sections look-up tables, exemplified for silicon. The total cross section (solid black), is the sum of the individual photoelectric absorption (solid green), coherent (dashed red) line and incoherent scattering (dash-dotted blue) cross sections. The vertical dashed black line near **60 keV** denotes the intersection between σ_{abs} and σ_{inc}. Note the logarithmic scale in the $y-$ axis.

2.1. Physical properties of materials under investigation

The interactions between photons with energy $E < 1.022$ MeV and a single element with atomic number Z are described in terms of total mass attenuation cross section, $\sigma(Z, E)$ (cm^2/g), which consists of contribution from the photoelectric absorption (σ_{abs}), coherent scattering (σ_{coh}), and incoherent scattering (σ_{inc}) [12]. An illustration of the relative contribution of each component of the mass attenuation cross sections as a function of energy is shown in Fig. 1. Note that for the elements commonly found in organic compounds (C, H, N, O), the photoelectric absorption is the dominant contribution for energies below 60 keV; however, the photo-electric absorption increases with Z_e. Also at energies below 60 keV coherent (Rayleigh) scattering is present and accounts for a contribution to the total attenuation of approximately **10%**. Above these energies, incoherent (Compton) scattering becomes predominant.

We convert total mass cross section into *electronic* cross section (cm^2/e$^-$mol), as:

$$\sigma_e(Z, E) = \frac{A(Z)}{Z}\sigma(Z, E), \tag{1}$$

where $\boldsymbol{A(Z)}$ is the atomic mass (**g/mole**) of the element Z. Likewise, we convert the bulk density ρ(g/cm^3) into *electron* density ρ_e (e$^-$mol/cm^3), using the relation:

$$\rho_e = \frac{Z}{A(Z)}\rho. \tag{2}$$

For a compound material, consisting of a number n_i: of N distinct elements i, the electronic density is extended from eq. (2) as:

$$\rho_e = \frac{\sum_{i=1}^{N} n_i Z_i}{\sum_{i=1}^{N} n_i A_i}\rho. \tag{3}$$

To approximate the atomic number of such a compound we use the definition of effective atomic number, $\boldsymbol{Z_e}$, presented by Azevedo et al. [4] defined as a non-integer atomic number that corresponds to an artificial element, for which the interactions are assumed to be modeled by the X-ray attenuation cross sections. The cross sections for the artificial element $\boldsymbol{Z_e}$ are obtained by a linear interpolation between the cross section of the two adjacent elements in the periodic table:

$$\sigma_e(Z_e, E) = (1 - \varepsilon)\sigma_e(Z', E) + \varepsilon\sigma_e(Z' + 1, E). \tag{4}$$

Therein, $\boldsymbol{Z'}$ is the lower adjacent element $Z' = floor(Z)$ and ε is the difference $\varepsilon = Z' - Z$.

Table 1
All the materials composing the samples and their respective physical properties. Note that the values of $\boldsymbol{Z_e}$ were calculated with ZeCalc [13], setting the kV to **160 kV**. Measurement uncertainties were $\pm$ 0.15% for ρ, leading to uncertainties of about $\pm$ 0.5% for ρ_e and $\boldsymbol{Z_e}$ The density measurement were taken from Ref. [4] as the same materials were used. † Materials placed in the six samples carousel. ‡ Materials scanned individually.

Material	Formula	Diameter (mm)	ρ (g/cm^3)	ρ_e (e$^-$mol/cm^3)	Z_e
‡Graphite A	C	50	1.70	0.846	6
†Graphite B	C	12.7	1.85	0.924	6
†POM	$(CH_2O)_n$	12.7	1.40	0.749	7.01
†Water	H_2O	12.7	1.00	0.554	7.45
†PTFE	$(C_2F_4)_n$	12.7	2.17	1.042	8.43
†Magnesium	Mg	12.7	1.74	0.857	12
‡Aluminum	Al	25	2.70	1.300	13
†Silicon	Si	12.7	2.33	1.162	14
‡Titanium	Ti	12.7	4.54	2.085	22

In terms of the effective atomic number and electronic density presented above, we express the LAC of a material m as:

$$\mu^m(E) = \rho_e^m \sigma_e(Z_e^m, E). \tag{5}$$

Investigated materials are tabulated in Table 1. The material properties were calculated from their respective measured bulk densities ρ using the paper by Bond et al. [13]. Note that a set of materials was scanned simultaneously within a carousel [14], while a set of other materials, with larger diameter or attenuation were scanned individually. The material features listed in Table 1 will be considered as the ground truth for the remainder of the paper.

2.2. MultiX ME 100 V2 detector array

The MultiX ME 100 V2 consists of a linear array of CdTe-based photon-counting X-ray detectors capable of recording energies from 20 to **160 keV** in **1.1 keV** energy bin increments, maximum number of energy bins $N_E = 128$. Optionally, for custom applications, two to six independently tunable energy bins can be specified within the full energy range. In this alternative mode, bins can be separated by a gap or they can overlap. Each module consists of 4 continuous pixelated CdTe crystals approximately **2.5 cm** in length. Each crystal is divided into 32 detector elements. Each detector element is **3 − mm** thick, **0.8 − mm** wide and **0.8 − mm** high. Up to 20 modules can be daisy-chained to form a **200 − cm** linear detector array. An interface board connected to a host computer acquires and transfers the data from the modules via an Ethernet link. The detectors can have integration times from **0.5 ms** to **100 ms** (in 10 μs increments). MultiX ME100 V2 is a pulse-counting detector, thus each count measured in the image refers to one detected photon. The energy resolution of the detector under high X-ray fluxes is of **6.5%** (**8 keV**) at **122 keV**. A lead collimator built into the module and surrounding the detector elements provides some X-ray collimation and radiation shielding. To implement a robust experimental tool, an enclosure was designed to hold and align, as well as safely store and transport, the detector modules.

For system control and acquisition of the MultiX radiography and CT data, we developed an automated software utility. The manufacturer provided an Application Programming Interface (API) to enable control of the detector array that was then incorporated into the software. To accommodate the need for computed tomography capabilities, the software was designed to control a Newport XPS motion controller driving a rotary stage (Newport Corporation, Irvine, California). An API from Newport was used to interface the software with the motion controller. Individual digital line radiographs using selected integration times can be acquired and saved in a raw binary file format. The software allows for a computed tomography scan over a selected angular range and integration time to be automatically

acquired and saved for later analysis.

2.3. Experimental setup

An YXLON 450-D11 (YXLON International, Hudson, Ohio) X-ray source was used with an acceleration voltage of **160 kV**, anode filament current of **0.5 mA** and **1 mm** focal spot. The spectrum was filtered with **2 mm** of aluminum. The detector was made up of two linear array PCD MultiX ME100 modules. For all the SCT scans performed in this work 360 projections were acquired, by rotating the sample stage at 1° increments. For each projection, the total exposure time was set to **5 s**. The source to detector distance (SDD) was set to **3000 mm** whereas the source to sample distance (SOD) was set to **2830 mm**.

2.4. Correction steps

The raw data collected by photon counting detectors is distorted by physical interactions such as charge sharing, weighting potential, escape peaks, pulse pile-up and insufficient charge collection [14–18]. These effects lead to a skewing of the measured spectrum from the central energies towards low- and high-energy tails. Since these effects are energy and flux dependent, different samples yield different distortions, and hence, errors in their LAC retrieval. To correct for these distortions, we employ a correction algorithm presented by Dreier et al. [19]. In contrast to other algorithms, this approach is flux dependent and fast (milliseconds per pixel), making it a suitable candidate for applications with high throughput demand. A plot of the X-ray source spectrum, before and after the correction has been applied is shown in Fig. 2.

Another relevant source of distortions in data acquisition is the radiation scattered by the sample and the environment. Low angle scattered photons which do not escape the detectors contribute to the transmitted radiation in Lambert-Beer's law resulting in a lowering of the measured LAC. The effect in the reconstructed volumes is a global loss of contrast between different materials and can lead to severe cupping artifacts. The influence of the scattered radiation on the acquisition depends on the size of the detectors and samples, material composition of the sample and the distance between the sample and the detectors. Lastly, it depends on the source spectrum and the materials' scattering cross sections. In an SCT acquisition, where the source's potential is typically set up to **160 kV**, scattering becomes the dominant interaction of high-energy photons (see Fig. 1), lowering the attenuation measured at the high-energy bins of the PCD. It is therefore important to adopt methods to suppress X-ray scattering. In this work, the X-ray scattering was estimated using a deep learning convolutional neural network (CNN) introduced by Maier et al. [20]. The training

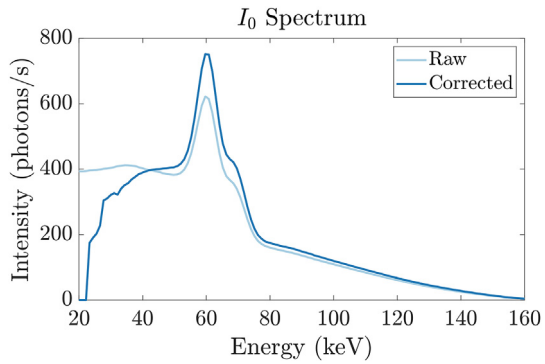

Figure 2. The raw (solid light blue) and spectral corrected (solid dark blue) X-ray source spectra, as measured by the MultiX ME100. The mean flux density per pixel was approximately **26000 Photons·s^{-1}/pixel**. Note that for this flux density the pile-up effect is not visible in the spectra but appears in the measured LAC (see Fig. 4).

datasets were obtained with a Monte Carlo (MC) simulation framework for scattering estimates presented by Busi et al. [21] A random sample generator was created with the aid of a software tool presented by Kazantsev et al. [22], to reproduce artificial samples composed of different materials. In contrast with the gold standard MC simulation, once trained, the CNN can provide scattering estimates in a few hundreds of milliseconds, while MC simulations usually take at least several minutes to converge, depending on the desired resolution. Note that the environmental X-ray scattering is not included in the model.

2.5. LAC volume reconstruction and energy selection

After the spectral and scattering corrections are performed on the spectra of each projection of the CT scan, the data is rebinned from $N_E = 128$ energy bins into $N_E = 64$ to increase photons statistics of each energy bin, while preserving flexibility in the energy selection and spectral resolution. The merging is done by summing the radiation I detected in pairs of adjacent energy bins as follows:

$$I^{E'k} = I^{E2k-1} + I^{E2k}, \quad k = 1, \ldots, 64. \tag{6}$$

The energy values assigned to the new energy bins E'_k are calculated by taking the weighted mean according to the source spectrum as follows:

$$E'_k = \frac{I_0^{E2k-1} \cdot E_{2k-1} + I_0^{E2k} \cdot E_{2k}}{I_0^{E2k-1} + I_0^{E2k}}, \quad k = 1, \ldots, 64. \tag{7}$$

Therein, I_0 is the corrected flat-field measurement, i.e. the projection without the sample being inserted, and corresponds to the source spectrum as measured by the detectors, also referred as the system's spectral response. We note that the merging procedure similarly can be done for a power of 2 of new energy bins (i.e. N_E = 1,2,4,8,16,32). For the remainder of the paper we denote the new energy bins as $E_k \equiv E'_k$, for practical reasons.

The energy resolved projections I are converted to linear attenuation coefficients, μ, using the Lambert-Beer's law:

$$\mu^{E_k}(\vec{x}) = -log\frac{I^{E_k}(\vec{x})}{I_0^{E_k}(\vec{x})}, \quad k = 1, \ldots, 64; \tag{8}$$

where $\vec{x}$ is the detector pixel array. Note that in this work we perform 2D slice reconstructions with fan-beam collimation since the detector is a linear array. The slice reconstructions are performed individually for each energy bin using the Filter Back Projection (FBP) routines included in Livermore Tomography Tools, a software package developed at LLNL [23]. An example of the slice reconstructions at four different energies is shown in Fig. 3. The reconstruction at $E_k = 27.3$ keV shows strek artifacts induced by photon starvation from the high attenuation of silicon at low energies. We also note that the contrast between the different materials varies as a function of energy. For example, the contrast between graphite and magnesium is higher at **44.8 keV** than **139.6 keV**, whereas the opposite behavior is found in the contrast between graphite and POM.

For each material, the LAC mean value and standard deviation within a region of interest (ROI) are calculated for each energy resolved reconstruction. In Fig. 4, we show an example of silicon's LAC measured with and without the correction steps discussed in Section 2.4, as well as the corresponding ground truth.

The correction algorithm helps correct the LAC towards the ground truth values at the low energies, where the contrast between organics compounds (e.g. PTFE and POM) is highest. The error increases towards the low- and high-energies due to spectral distortions, which cannot be completely restored by the correction algorithms. At certain energies, the LAC values deviate from the expectation due to complete attenuation of the radiation by the sample, resulting in photon starvation. To estimate the ρ_e and $\boldsymbol{Z_e}$ of each material, the method requires an automated selection of the low- and high-energy thresholds, $\boldsymbol{E_i}$ and $\boldsymbol{E_f}$,

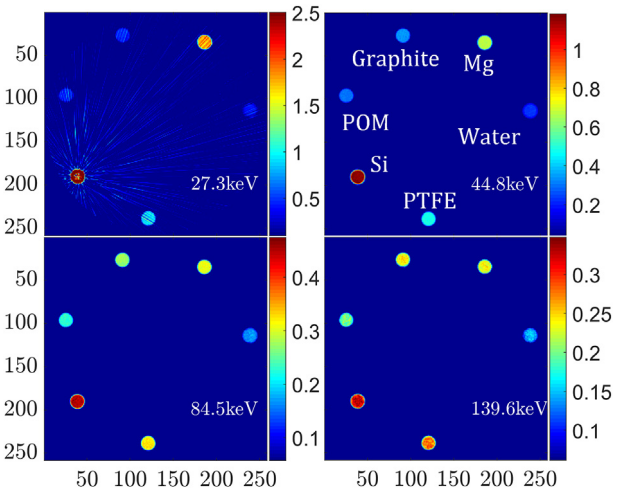

Fig. 3. Four individual energy LAC resolved slice reconstructions of the materials in the carousel, at the energies E_k = 27.3, 44.8, 84.5, 139.6 keV. The axes' unit corresponds to the pixel size (**0.8 mm**). The scale unit is the linear attenuation (cm^{-1}).

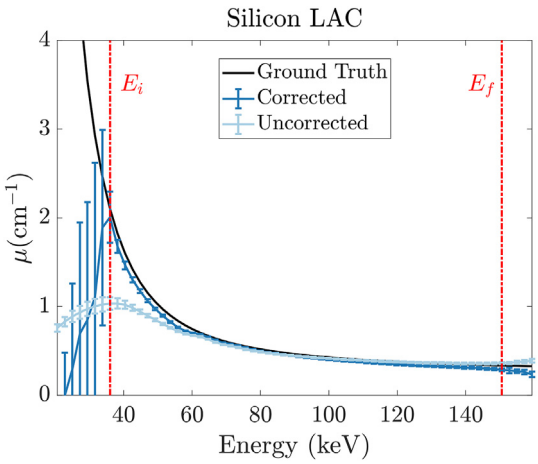

Figure 4. Energy resolved LAC, exemplified for Silicon. The solid black line is the ground truth obtained by using the ground truth values of ρ_e and $\boldsymbol{Z_e}$ in Table 1, using NIST cross-sections. The dark and light blue lines are the ROI mean LAC calculated as described in Section 2.5, with and without the correction steps of Section 2.4 being applied respectively. The error-bars represent the respective standard deviation values. The vertical red dash-dotted lines are the low- and high-energy thresholds $\boldsymbol{E_i}$ and $\boldsymbol{E_f}$ found by the energy selection step given in Section 2.5.

which correspond to energy thresholds that exclude bins in which the LAC is affected by low photon statistics and pulse pile-up. For all the materials scanned in this work, these two thresholds were calculated by assuming the LAC to be monotonically decreasing, and with no inflection points in the incoherent scattering regime ($E > 60$ keV). This assumption is useful, in case of a PCD, for materials (i.e. $1 \leq Z_e \leq 42$) that do not have a K-edge within the detector's energy range. For MultiX ME100 that is between 20 and **160 keV**. The low-energy threshold ***Ei*** is determined by taking the first derivative of the estimated LAC ($\delta\mu(E)/\delta E$) and locating the nearest zero intercept closest to the lowest-energy bin, as it corresponds to a relative maximum with a change from increasing to decreasing. The high-energy threshold ***Ef*** is determined by taking the second derivative of the estimated LAC ($\delta^2\mu(E)/\delta E^2$), and locating the bin nearest the zero intercept, closest to the highest energy bin, as it corresponds to an inflection point. The determination of the energy thresholds is illustrated in Fig. 4 for silicon.

2.6. Spectral ρ_e/Z_e estimation (SRZE)

We introduce a method that estimates the physical properties (ρ_e and $\boldsymbol{Z_e}$) of a material from its corrected LAC measurements. The estimation is performed by solving a constrained minimization of a cost function ***g(E)***:

$$\arg\min g(E). \tag{9}$$

We define the cost function $g(E) = |\tilde{\mu}(E) - \mu(E)|^2$, as the squared distance between the measured LAC, $\tilde{\mu}(E)$, and its relative theoretical definition $\mu(E)$, parametrized by ρ_e and $\boldsymbol{Z_e}$ as in eq. (5). Therefore, for a spectral acquisition eq. (9) becomes:

$$\arg\min_{\{\rho_e, Z_e\}} \sum_{k=i}^{f} \lambda_{E_k} \, |\tilde{\mu}(E_k) - \rho_e \sigma_e(Z_e, E_k)|^2. \tag{10}$$

Therein, λ_{E_k} are the energy weights, computed as the reciprocal of the variance ($\boldsymbol{s^2}$) of each material's LAC in their ROI, $\lambda_{E_k} = 1/s^2(\tilde{\mu}_{E_k})$. These can be interpreted as the weight given to each energy bin $\boldsymbol{E_k}$ into the estimation of the material's features. Note that the summation runs from the low- and high-energy thresholds $\boldsymbol{E_i}$ and $\boldsymbol{E_f}$, found as described in the previous section. The minimization process in this work was performed with MATLAB®'s routine function FMINCON with solution boundaries $\rho_e = 0 - 15$ e^-mol/cm^3 and $Z_e = 1 - 99$ and initial guesses $\rho_e^0 = 1$ e^-mol/cm^3 and $Z_e^0 = 7$. No particular dependency on the starting values was observed. Note that in the case of materials presenting a K-edge in the attenuation coefficients, the energy bins below the edge would be truncated making it compatible with estimation method, however none of the materials presented here have a K-edge within the energies in the PCDs range.

3. Results and discussion

In this section we present the experimental results obtained with the SRZE method presented in Section (2.6), for all the materials scanned (see Table 1). The accuracy of the estimation is calculated as the percent relative deviation from the ground truth for the effective atomic number as:

$$\Delta Z_e^{rel} = 100\% \cdot \frac{Z_e^{est} - Z_e^{gt}}{Z_e^{gt}}, \tag{11}$$

and similarly, for the electron density by substituting $\boldsymbol{Z_e}$ with ρ_e, where superscripts *est* and *gt* refer to estimated and ground truth, respectively. The ground truth values for the material features are listed in Table 1. All the results are plotted in Fig. 5 and listed with comparisons to the results reported in a previous study [24] in Table 2.

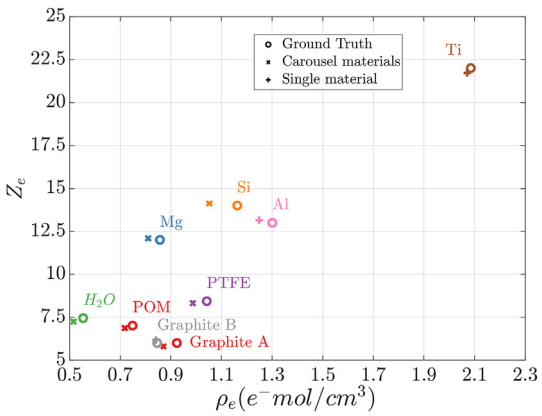

Fig. 5. Scatter plot of the ρ_e, Z_e results obtained using the SRZE method.

Table 2
SRZE estimation of the material's features. SIRZ-2 values reported are taken from Ref. [24]. The SIRZ-2 results for titanium are unpublished. †Materials placed in the six samples carousel. ‡Materials scanned individually. *The mean values were calculated from the absolute values of each column.

Material	ρ_e^{gt} (e⁻mol/cm³)	SRZE ρ_e^{rel}(%)	SIRZ-2 ρ_e^{rel}(%)	Z_e^{gt}	SRZE ΔZ_e^{rel}(%)	SIRZ-2 ΔZ_e^{rel}(%)
‡Graphite A	0.85	−0.5	0.3	6	2.9	0.5
†Graphite B	0.92	−5.7	1.5	6	−3.2	−0.8
†POM	0.75	−4.2	0.3	7.0	−2.0	−1.3
†Water	0.55	−6.9	−0.2	7.4	−2.7	−0.4
†PTFE	1.04	−5.3	−0.1	8.4	−1.3	−1.1
†Magnesium	0.86	−5.4	−0.2	12	0.8	−0.4
‡Aluminum	1.30	−3.2	1.8	13	0.7	−2.0
†Silicon	1.16	−9.5	−0.5	14	0.8	−4.4
‡Titanium	2.08	−0.7	–	22	−1.2	–
*Mean	–	4.6	0.6	–	1.7	1.4

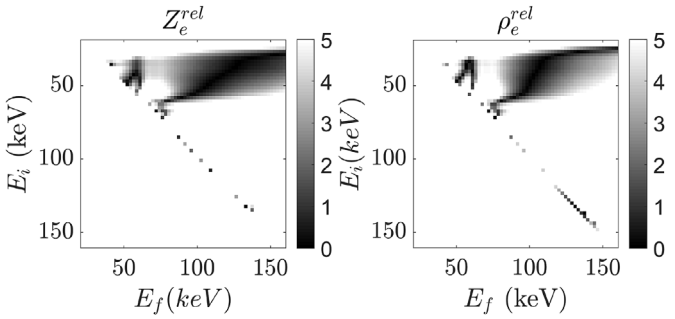

Fig. 6. Plot of the material features estimation accuracy as a function of the E_i and E_f thresholds, exemplified for aluminum. The scale unit is the percent relative deviation (%) expressed in eq. (11).

3.1. Discussion of results

The accuracy of the SRZE method in Fig. 5 and Table 2 shows promising results in the calculation of the effective atomic number, with an overall mean relative error value of **1.79%**. It is observed that the estimation of Z_e worsens for smaller Z_e, due to lower performance of the detector in terms of spectral resolution at the lower-energy bins and lower contrast between LAC curves of adjacent Z_e values. Moreover, the spectral distortions in the low-energy reconstructions lead to higher standard deviations, and hence less energy weight λ_{E_k} in the estimation method. However, the highest contrast of low-Z_e materials is found at lower energies.

The estimation of ρ_e on the other hand shows a **4%** negative bias in the mean relative error value, perhaps due to an overall underestimation of the measured energy resolved attenuation coefficient, also visible in Fig. 4. One reason for this may be due to a high amount of environmental X-ray scattering, not considered in the analysis. For these experiments, except for the titanium, aluminum, and graphite A scans, the source was not collimated into a fan-beam geometry and a large portion of the beam hit the sample stage, mostly composed of metal parts. The small distance between the sample stage and the detector permitted a large portion of the environmental scattering to reach the detectors. The large error in the estimation of silicon's electron density (ρ_e) may be due to the use of monocrystalline silicon, which is known to exhibit a different X-ray cross section than polycrystalline silicon [4,24]. The results are comparable to the ones reported in a previous work using state-of-the-art Dual-Energy CT [24], besides the significant lower performance on the estimation of ρ_e, which is due to the reasons discussed above.

3.2. Energy selection analysis

To test the robustness and sensitivity of the E_i and E_f thresholds selection procedure described in Section 2.5 we ran the SRZE estimation method over a range of values of the low- and high-energy thresholds E_i and E_f. Fig. 6 shows the relative percent deviation of the estimated material features for aluminum. Note that the diagonal elements correspond to taking only two adjacent energy bins and the values below the diagonal are not calculated as they have no physical representation. The thick dark areas show that the key factor for accurate estimation of the LAC, and thus ρ_e and Z_e is the selection of the low-energy threshold E_i. The optimal performance is reached by truncating the low-energy bins, for which the spectral distortions and photon starvation cause a distortion of the measured LAC. On the other hand, choosing a higher threshold for the low-energy bins yields a poor estimation, as the bulk of the material properties is revealed by the low energy bins.

It is also shown in Fig. 6 that the selection of the high-energy threshold E_f has less impact on the estimation of the LAC, and thus ρ_e and Z_e. The large areas in which the accuracy is below **2%** indicate that the estimation method is overdetermined and there may be a material dependent optimal choice of the energy bins, that would lead to optimized results. The difference, in shape, between the dark areas for ρ_e and Z_e, suggests that there may be an optimized choice of energy bins for an independent estimation of ρ_e and Z_e.

4. Conclusions

We have presented a method for the estimation of system-independent physical properties of materials, from Spectral CT measurements. In contrast to other methods, this does not require a calibration step using reference materials and can be used with any number of energy bins. However, it relies on the accurate measurement of the energy dependence of the attenuation coefficients. We found the method to be more robust to the variety of material samples using 64-energy bins, followed by a detection and truncation of the low- and high-energy bins where the spectral distortions cannot be fully corrected. Our assumption for the selection of the energy bin thresholds is supported by the physical properties of the attenuation coefficients of materials not presenting a K-edge, however the method is expected to be able to operate in this condition as well. The accuracy results are comparable to the ones obtained with the state-of-the-art techniques employing dual-energy CT scans, while our method is done with a single scan and it has a better performance for highly attenuating materials. Photon counting detectors are still under development therefore, improvements in the detector's response will lead to a better estimation of the material's features. Further experiments will test the robustness of the method to materials with larger range of effective atomic number Z_e, and presence of K-edges. Additional experiments will test the precision and accuracy of the method using different scanning parameters such as source potential, filament current and different source filters as well as better environmental X-ray scattering reduction.

Acknowledgments

The author would like to thank Innovation Fund Denmark for funding the project. The authors also acknowledge Bill Brown and Brian Fix (LLNL) for their efforts in the early implementations of the MultiX ME100 hardware and software in the CT scanning system.

References

[1] Martz HE, Logan CM, Schneberk DJ, Shull PJ. X-ray Imaging: fundamentals, industrial techniques and applications. CRC Press; 2017.
[2] Ying Z, Naidu R, Crawford CR. Dual energy computed tomography for explosive

detection. J Xray Sci Technol 2006;14(4):235–56.
[3] Wells K, Bradley D. A review of X-ray explosives detection techniques for checked baggage. Appl Radiat Isot 2012;70(8):1729–46.
[4] Azevedo SG, Martz HE, Aufderheide MB, Brown WD, Champley KM, Kallman JS, Roberson GP, Schneberk D, Seetho IM, Smith JA. System-independent characterization of materials using dual-energy computed tomography. IEEE Trans Nucl Sci 2016;63(1):341–50.
[5] Wang AS, Harrison D, Lobastov V, Tkaczyk JE. Pulse pileup statistics for energy discriminating photon counting x-ray detectors. Med Phys 2011;38(7):4265–75.
[6] Ding H, Molloi S. Image-based spectral distortion correction for photon-counting x-ray detectors. Med Phys 2012;39(4):1864–76.
[7] Shikhaliev PM. Energy-resolved computed tomography: first experimental results. Phys Med Biol 2008;53(20):5595.
[8] V. Rebuffel, J. Rinkel, J. Tabary, L. Verger. New perspectives of X-ray techniques for explosive detection based on CdTe/CdZnTe spectrometric detectors. Proc. of the int. Symp. on digital industrial radiology and computed tomography;vol. 2.
[9] Zimmerman KC, Sidky EY, Schmidt TG. Experimental study of two material decomposition methods using multi-bin photon counting detectors, Medical Imaging 2014. Phys Med Imaging 2014;9033:90333G.
[10] Brambilla A, Ouvrier-Buffet P, Rinkel J, Gonon G, Boudou C, Verger L. CdTe linear pixel x-ray detector with enhanced spectrometric performance for high flux x-ray imaging. IEEE Trans Nucl Sci 2012;59(4):1552–8.
[11] Brambilla A, Gorecki A, Potop A, Paulus C, Verger L. Basis material decomposition method for material discrimination with a new spectrometric x-ray imaging detector. J Instrum 2017;12(08):P08014.
[12] Chantler CT. Theoretical form factor, attenuation, and scattering tabulation for Z = 1–92 from E = 1–10 eV to E = 0.4–1.0 MeV. J Phys Chem Ref Data 1995;24(1):71–643.
[13] Bond K, Smith J, Treuer J, Azevedo S, Kallman J, Martz H. ZeCalc algorithm details, version 6, Tech. rep., LLNL Tech. Rep., LLNL-TR-609327,(Jan. 2013). To request a copy of ZeCalc software, contact Mary Holden-Sanchez at holdensanchez2@ llnl. gov. 2013.
[14] Dooraghi AA, Fix BJ, Smith JA, Brown WD, Azevedo SG, Martz HE. Characterization of a spectroscopic detector for application in x-ray computed tomography. Developments in X-ray tomography XI, vol. 10391. International Society for Optics and Photonics; 2017. p. 103911G.
[15] Guerra P, Santos A, Darambara D. Development of a simplified simulation model for performance characterization of a pixellated CdZnTe multimodality imaging system. Phys Med Biol 2008;53(4):1099.
[16] Redus RH, Pantazis JA, Pantazis TJ, Huber AC, Cross BJ. Characterization of CdTe detectors for quantitative X-ray spectroscopy. IEEE Trans Nucl Sci 2009;56(4):2524–32.
[17] Cammin J, Xu J, Barber WC, Iwanczyk JS, Hartsough NE, Taguchi K. A cascaded model of spectral distortions due to spectral response effects and pulse pileup effects in a photon-counting x-ray detector for CT. Med Phys 2014;41(4).
[18] Plagnard J. Comparison of measured and calculated spectra emitted by the X-ray tube used at the gustave roussy radiobiological service. X Ray Spectrom 2014;43(5):298–304.
[19] Dreier ES, Kehres J, Khalil M, Busi M, Gu Y, Feidenhans R, Olsen UL. Spectral correction algorithm for multispectral CdTe x-ray detectors. Opt Eng 2018;57(5):054117.
[20] Maier J, Sawall S, Knaup M, Kachelrieß M. Deep scatter estimation (DSE): accurate real-time scatter estimation for X-ray CT using a deep convolutional neural network. J Nondestruct Eval 2018;37(3):57.
[21] Busi M, Olsen UL, Knudsen EB, Frisvad JR, Kehres J, Dreier ES, Khalil M, Haldrup K. Simulation tools for scattering corrections in spectrally resolved x-ray computed tomography using McXtrace. Opt Eng 2018;57(3):037105.
[22] Kazantsev D, Pickalov V, Nagella S, Pasca E, Withers PJ. TomoPhantom, a software package to generate 2D–4D analytical phantoms for CT image reconstruction algorithm benchmarks. SoftwareX 2018;7:150–5.
[23] Champley K. Livermore tomography tools (LTT) technical manual LLNL-SM-687016 2016. p. 1–165.
[24] Champley KM, Azevedo SG, Seetho IM, Glenn SM, McMichael LD, Smith JA, Kallman JS, Brown WD, Martz HE. Method to extract system-independent material properties from dual-energy X-ray CT. IEEE Trans Nucl Sci 2019;66(3):674–86.

Paper IV

Effective atomic number and electron density determination using spectral X-ray CT.

Matteo Busi, Jan Kehres, Mohamad Khalil, and Ulrik L. Olsen

Invited Paper

Effective atomic number and electron density determination using spectral x-ray CT

Matteo Busi[a,b], Jan Kehres[a], Mohamad Khalil[a], and Ulrik L. Olsen[a]

[a]Technical University of Denmark, DTU Physics, Fysikvej 311, 2800 Kgs. Lyngby, Denmark

ABSTRACT

We present Spectral X-ray Computed Tomography (SCT) estimations of material properties directly from energy-dependent measurements of linear attenuation coefficients (LAC). X-ray Computed Tomography (CT) is commonly utilized to characterize the internal properties of an object of interest. Dual-Energy X-ray CT allows material characterization into energy-independent physical properties such as Z_e and electron density ρ_e. However, it is not robust in presence of dense materials and metal artifacts. We report on the performance of a method for system-independent characterization of materials that introduces a spectroscopic detector into X-ray CT, called spectral ρ_e/Z_e estimation (SRZE). We benchmark the SRZE method against energy-integrated measurements in material classification tests, finding superior accuracy in the predictions. The advantage of this technique, over other methods for material characterization using x-ray CT, is that it does not require a set of reference materials for calibration. Moreover, the simultaneous detection of spectral features makes it robust to highly attenuating materials, since the energy intervals for which the attenuation is photon limited can easily be detected and excluded from the feature estimation.

Keywords: Spectral X-ray CT, X-ray Characterization, Effective atomic number, Electron density, MULTIX-ME100, Threat Detection, Security Screening

1. INTRODUCTION

For decades, X-ray Computed Tomography (CT) has been adopted as one of the standard techniques for non-destructive tests and evaluations, for example in the screening of luggage for threats.[1] Since laboratory-scale X-ray sources generate a polychromatic beam (Fig. 1), conventional CT does not measure a single-energy value of the linear attenuation coefficient (LAC), but measures but its weighted average through multiple energies. Therefore, using this technique the characterization of a material's LAC is complicated by polychromatic effects such as beam hardening[2] and photon starvation from metals or dense materials,[3] and require an accurate model of the detector's spectral response. Moreover, different materials yield different contrast, in terms of intensity values in the reconstructions, when probed at different mean energies; therefore their classification might be not optimized depending on the choice of the source parameters of kilovoltage peak and filtration.

To overcome these limitations, researchers have recently developed methods to estimate energy-independent physical parameters of the materials, using Dual-Energy CT (DECT).[4,5] With a DECT acquisition, the LAC of materials is probed at two different X-ray spectra (as the low- and high- energy pair in Fig. 1) and converted into the energy-independent physical parameters of electron density ρ_e and effective atomic number Z_e, as in the System-Independent ρ_e/Z_e (SIRZ) method proposed by Azevedo et al.[6] and further developed by Champley et al.[7] This can be technically achieved, for example with a consecutive scan with different source filtration and kilovoltage peaks, or using dual-energy sandwich detectors.[8] However, the performance of these techniques depend on the choice of the pair of spectra used for the DECT acquisitions and the estimation of their respective detector spectral responses. These techniques will be accurate and precise for a group of materials within a limited range of Z_e, but will have lower performance for materials outside this range. This limitation can be overcome using spectral X-ray CT (SCT). SCT can be considered as an extension of DECT where the signal is simultaneously collected in multiple non-overlapping energy ranges. This would extend the range of materials for which the characterization is accurate.

Further author information: (Send correspondence to Matteo Busi)
Matteo Busi: E-mail: mbusi@fysik.dtu.dk, Telephone: +45 71 70 60 90

Anomaly Detection and Imaging with X-Rays (ADIX) IV, edited by Amit Ashok, Joel A. Greenberg, Michael E. Gehm, Proceedings of SPIE Vol. 10999, 1099903

With the advent of single photon counting detectors (PCD) able to discriminate the energy of the detected photons (Fig. 1), the interest towards spectral X-ray CT (SCT) has grown significantly, for the superior contrast to noise ratio[9–13] and for enabling k-edge CT.[14,15] In this work we use an extension of the SIRZ method for SCT, called Spectral ρ_e/Z_e Estimation (SRZE),[16] to estimate the physical parameters of a large dataset of innocuous materials commonly found in checked-in luggage, and threat materials which we want to be able to detect. The SRZE characterization's impact on the classification task accuracy is benchmarked against more direct methods for a set of different samples with including both innocuous and threat materials in a random order. For all cases studied in this work, we found superior accuracy in the classification task when using SRZE method for material characterization.

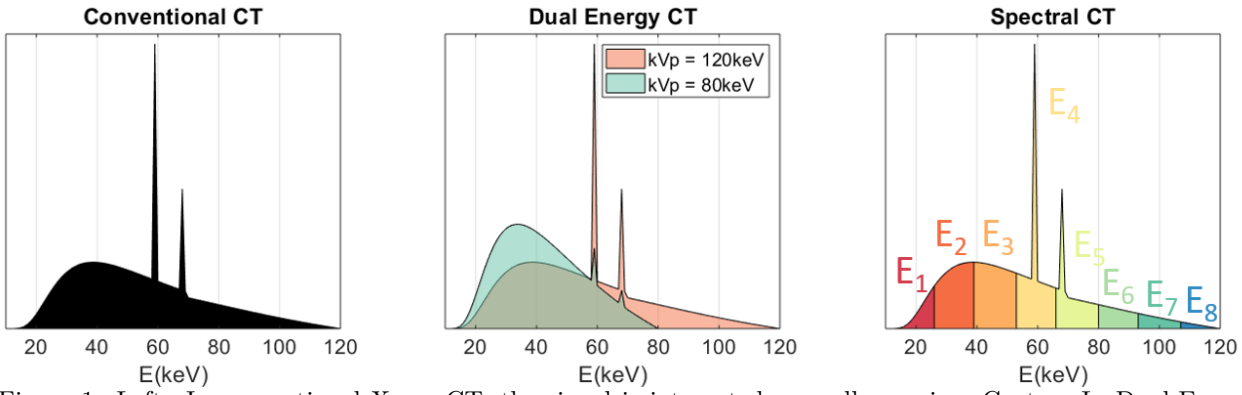

Figure 1: Left. In conventional X-ray CT, the signal is integrated over all energies. Center. In Dual-Energy X-ray CT, two different spectra are used to probe the sample attenuation at a low- and high- mean energy. Right. In Spectral X-ray CT, single photon counting detectors discriminate the incoming radiation in distinct energy bins with mean energy depending on the set energy thresholds.

2. THEORY AND METHODS

In this section, we define the system-independent physical properties we have used to characterize materials and the methods we have adopted in this work to estimate them from SCT measurements.

2.1 Dual-Energy X-ray CT Characterization

As described in the Lambert-Beer's law,[17] X-ray CT measures the Linear Attenuation Coefficient (LAC) of materials. However, LAC is a function of the energy and therefore conventional CT, which use acquisitions with energy integrating detectors, is not a robust method for the characterization of materials since it depends on the source spectrum and polychromatic effects such as beam hardening that cause distortions in the reconstruction. Alvarez and Macovski showed in 1976 that the LAC could be approximated as linear combination of a dual set of basis functions:[4]

$$\mu(E) = a_1 f_{ph.abs.}(E) + a_2 f_{KN}(E), \tag{1}$$

where $f_{ph.abs.}(E) = 1/E^3$ models the photoelectric absorption interactions of photons with matter, and $f_{KN}(E)$ is the Klein-Nishina function, which approximately models the incoherent (Compton) scattering interactions of photons with matter:

$$f_{KN}(E = E'/511\text{keV}) = \frac{1+E}{E^2}\left[\frac{2(1+E)}{1+2E} - \frac{1}{E}\ln(1+2E)\right] + \frac{1}{2E}\ln(1+2E) - \frac{1+3E}{(1+2E)^2}. \tag{2}$$

The coefficients a_1 and a_2 are proportional to the physical parameters of bulk density ρ and atomic number Z, which are energy-independent. Based on this concept, Azevedo et al. presented a method[6] using Dual-Energy X-ray CT for the system-independent characterization of materials into their features of electron density (ρ_e)

and effective atomic number (Z_e). For a compound material, consisting of a number n_i of N distinct elements i, the electronic density is defined as:

$$\rho_e = \frac{\sum_{i=1}^{N} n_i Z_i}{\sum_{i=1}^{N} n_i A_i}\rho, \tag{3}$$

where $A(Z)$ is the atomic mass (g/mole) of the element Z. To approximate the atomic number of such a compound Azevedo et al.[6] used the effective atomic number, Z_e, defined as a non-integer atomic number that corresponds to an artificial element, for which the interactions are assumed to be modeled by the X-ray attenuation cross sections. The cross sections for the artificial element Z_e are obtained by a linear interpolation between the cross section of the two adjacent elements in the periodic table:

$$\sigma_e(Z_e, E) = (1-\epsilon)\sigma_e(Z', E) + \epsilon\sigma_e(Z'+1, E). \tag{4}$$

Therein, Z' is the lower adjacent element, $Z' = floor(Z)$ and ϵ is the difference, $\epsilon = Z' - Z$. In terms of the effective atomic number and electronic density presented above, we express the LAC of a material m as:

$$\mu^m(E) = \rho_e^m \sigma_e(Z_e^m, E). \tag{5}$$

In their study, Azevedo et al.[6] demonstrated system-independence of the method and very good accuracy and precision for a set of standard materials with $Z_e < 15$ with well-known physical parameters.

2.2 Spectral X-ray CT Characterization

We briefly describe the method presented in detail by Busi et al.[16] to estimate the effective atomic number and electron density from SCT acquisitions. The measured raw data undergoes a spectral detector correction algorithm presented by Dreier et al.,[18] which corrects for the spectral distortions caused by the interactions between photons and the PCDs. This step is followed by the spectral scattering corrections method, from Monte Carlo X-ray simulations, presented by Busi et al.[19] The energy resolved sinograms are converted into attenuation using Lambert-Beer's law, and reconstructed using Livermore Tomography Tools (LTT) software[20] using the filtered back projection algorithm. The energy-dependent LACs are obtained by taking the mean values in the manually segmented regions respective to each material, for each energy bin. The respective variance of the mean values in the segmented regions is calculated as well, as it will be used in the feature estimation step. At this stage, an automated energy thresholding is used to disregard energy bins in which the reconstructions are corrupted by photon starvation caused by highly dense materials. The estimation of the physical parameters is performed by solving a constrained minimization of the squared distance between the measured LAC, $\tilde{\mu}(E)$, and its relative theoretical definition $\mu(E)$, parametrized by ρ_e and Z_e as in eq. (5) :

$$\underset{\{\rho_e, Z_e\}}{\arg\min} \sum_{k=i}^{f} \lambda_{E_k} |\tilde{\mu}(E_k) - \rho_e \sigma_e(Z_e, E_k)|^2. \tag{6}$$

Therein, λ_{E_k} are the energy weights, computed as the reciprocal of the variance (s^2) of each material's LAC in their ROI, $\lambda_{E_k} = 1/s^2(\tilde{\mu}_{E_k})$. These can be interpreted as the weight given to each energy bin E_k into the estimation of the material's features. The minimization process in this work was performed with MATLAB®'s routine function FMINCON with solution boundaries $\rho_e = 0 - 15$ e$^-$mol/cm^3 and $Z_e = 1 - 99$ and initial guesses $\rho_e^0 = 1$ e$^-$mol/cm^3 and $Z_e^0 = 7$. No particular dependency on the starting values was observed.

3. EXPERIMENTS

3.1 Instrumental setup

The instrumentation used for the characterization of the materials into their physical properties was designed for SCT measurements and briefed in Table 1. The X-ray beam was generated by a Hamamatsu source with a tungsten anode and the acceleration voltage and filament current set to 160kV and 0.5mA, respectively. For these operating parameters the focal spot was 75μm. The detector was made up of two 1D PCD Multix-ME100[21] modules, composed of 1×128 pixels of size 0.8×0.8 mm^2 and each with 128 energy bins of width 1.1 keV, evenly

distributed between 20 and 160 keV. The energy resolution of the detector under high X-ray fluxes is 6.5% (8 keV at 122 keV).[22] A 2−mm−thick aluminum filter was placed in front of the source to reduce the beam hardening effects and to suppress the photons with energy below the spectral range of the detector. The characteristic X-ray peaks of the tungsten target are smeared due to the limited detection energy resolution,[18,23] resulting in a smoother spectrum compared to what is theoretically expected. For all the SCT scans performed, the total acquisition time per scan was 30 minutes with the rotation stage continuously rotating. Each scan was rebinned into 5 seconds frames to form 360 projections evenly distributed between 0° and 359°. The source to detector distance (SDD) was set to 1115 mm whereas the source to object distance (SOD) was set to 575 mm.

Table 1: Experimental parameters.

Source parameters	160 keV, 0.5 mA
Focal spot	75 μm
Number of pixels	1×256 1D array
Pixel size	0.8×0.8 mm^2
Detector's resolution	6.5%(8 keV) at 122 keV
Number of energy bins	128 (1.1 keV width)
Number of projections	360
Exposure time per projection	5 seconds
SDD	1115 mm
SOD	575 mm

3.2 Characterization results

We used the SCT characterization method described in Section 2.2 to estimate the physical parameters of a set of 73 different materials listed in Table 3 in Appendix A. The results are displayed in a ρ_e/Z_e chart, in Fig 2. The choice of the materials in this work focus on the threat detection in airport luggage. It consists of a varied selection of organic innocuous compounds, mostly in water solutions, and a selection of explosive or precursor threat materials. We found a good contrast in the two physical parameters of ρ_e and Z_e for threat and innocuous materials, except for a few materials. Ethanol 96% (index: 25) for example, will have a high chance of being detected as a false positive for its proximity to acetone (index: 3). Among the threats, the hydrazine solution in water (index: 7) and nitromethane (index: 12) are also challenging, due to their similarity with water (index: 48).

3.3 Singular Value Decomposition analysis

We estimate material physical parameters from their LAC using the model in Eq. 5. To confirm that this model matches with the experimental findings, we performed a Singular Value Decomposition (SVD) analysis procedure, similar to the one proposed by Eger et al.[24] for synthetic data. We constructed a matrix $\mathcal{M}$ with the linear attenuation coefficients measured of all the materials listed in Appendix A. The matrix $\mathcal{M}$ has dimensions $(E_b \times N_{mat})$ where E_b is the number of energy bins for which the LAC is probed and N_{mat} is the number of materials. The SVD decomposition aims to find a set of linearly independent vectors that can express the LAC, and can be expressed as:

$$\text{SVD}(\mathcal{M}) \equiv M = USV^T, \tag{7}$$

where U is a $(E_b \times N_{mat})$ matrix where each column i compose the set of linearly independent vectors $U_i(E)$, S is a $(N_{mat} \times N_{mat})$ diagonal matrix where the magnitude of each element $S_{i,i}$ describes the relative contribution of the corresponding vector U_i to the model. The first singular values $S_{i,i}$ and the first six singular vectors U_i are shown in Fig. 3. A qualitative look at these vectors indicate the two dominant singular vectors, U_1 and U_2 are corresponding to the basis functions for incoherent scattering and photoelectric absorption, as in Eq. 1. These observations were confirmed by finding a linear proportionality between U_1 and the Klein-Nishina function f_{KN}, and a linear trend of the inversion $1/\sqrt[3]{U_2(E)}$. The remaining singular vectors are dominated by noise components and the oscillations in the measured LAC due to the poor spectral resolution of the detector around

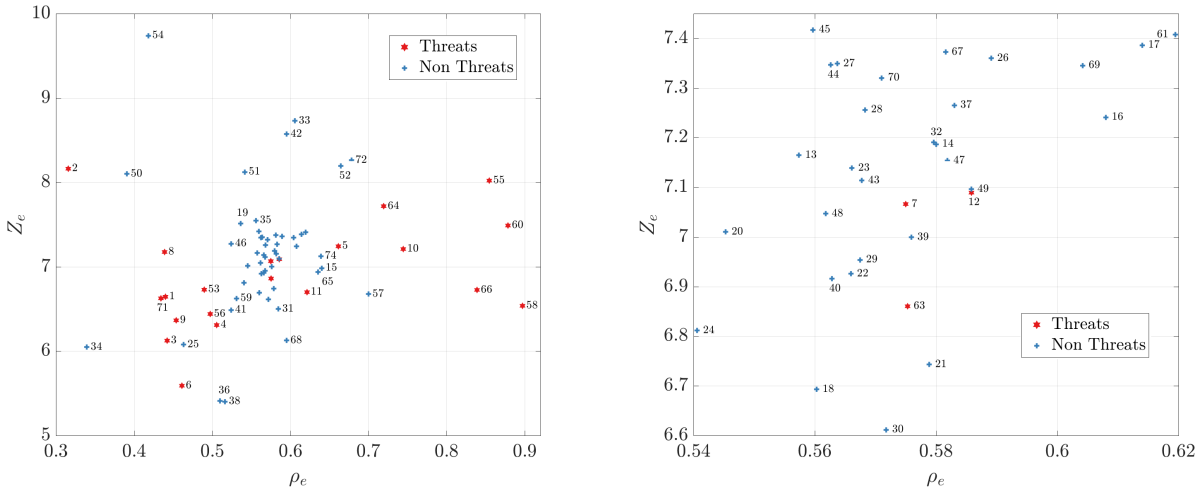

Figure 2: Charts of the effective atomic number and electron density (Z_e,ρ_e) of the materials scanned, estimated through the SRZE method. The numbers labeling the data points are referring to the index in Table 3 in Appendix A. Note that to avoid overlap of the material labelled indexes, a magnified version of the left frame is displayed in the right frame.

the characteristic peaks of the X-ray source, as indicated by the wiggles around the energy of the K_{α_1} (59.3 keV) and K_{β_1} (67.2 keV) tungsten emission lines. The third singular vector U_3, displays a sharp rise and consecutive relaxation, and is required to fully represent all the materials LACS. One would find the same behavior of the third significant singular vector, when running the same procedure on standard reference LAC curves from NIST database.[25] We found, however, that the first two vectors are sufficient to approximate all the materials studied. This was confirmed by calculating the autocorrelation values of the singular vectors, which were below the value of 0.5[26] except for $U_{1,2,3}$ and a few more $U_{4,5,6}$, as seen in Fig. 3 (b), with the same behavior as U_3 but different modulation of the peaks.

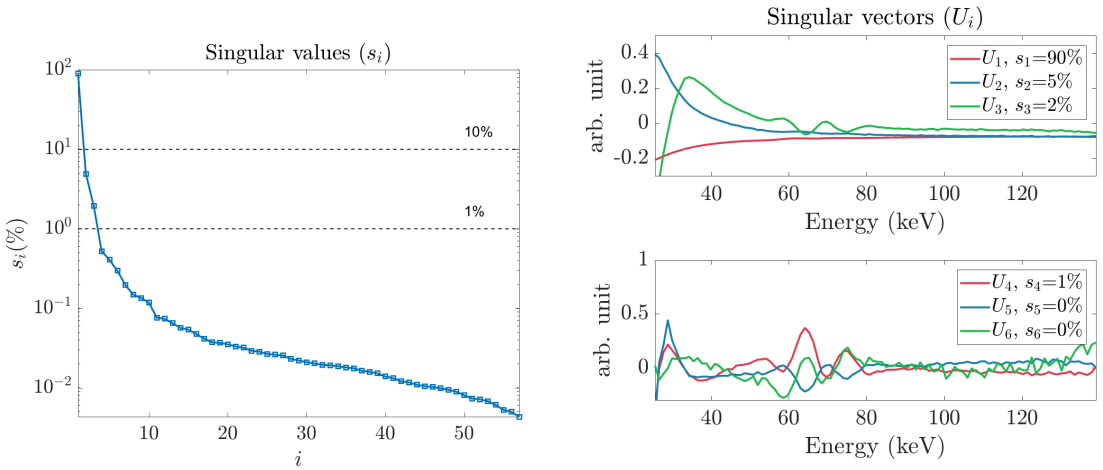

(a) (b)

Figure 3: Singular Value Decomposition analysis of the reference materials LACs. (a) Singular values of the diagonal i-elements (blue-squares). Note logarithmic scale in the y-axis. (b) Singular vectors U_i respective of the diagonal singular values s_i. The scale is in arbitrary units.

4. CLASSIFICATION BENCHMARKING

4.1 Materials and prediction models

In this work, we have tested three different methods for the material classification from SCT data acquisitions. In the first method, we used as the material's feature the energy integrated LAC, $\tilde{\mu}(E')$, obtained by summing the signal over all the 128 energy channels of the detector. The effective energy (E') corresponding to $\tilde{\mu}$ was calculated using the source spectrum as measured by the flat field acquisition (i.e. without the sample) as a model for the detector's response. The second method, utilizes as the material's feature the energy-dependent LAC, i.e. the attenuation coefficient probed at the 128 energy values corresponding to the specifics of the detector ($\mu(E_k)$ with $k = 1, 2, 3, ..., 128$). In the third method, we used the SRZE characterization method described in Section 2. For each of these methods, a look-up table library of materials features such as the one in Appendix A, has been built by using single slice fan-beam SCT of individual materials in ideal condition (i.e. without metal artifacts and center-offset).

In the following scans, we have measured 30 samples composed of four glass bottles filled with different materials (found in Appendix A) and aluminum pin of 4mm diameter placed in a sample holder. Of these samples, 10 of them were with the sample holder centered with the sample's rotation stage, 10 of them were with an offset between the sample holder and rotation stage centers, and the remainder 10 with an aluminum slab of 10×30 mm as well. Examples of the CT reconstructions of the different groups are shown in Fig. 4.

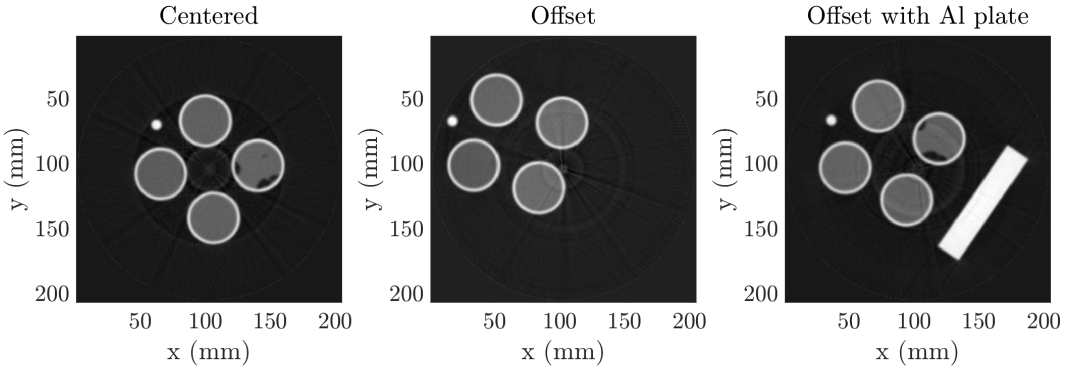

Figure 4: Reconstruction examples of the three types of dataset reproduced. Left: the samples are placed centered in respect to the center of rotation. Center: the samples are placed offset in respect to the center of rotation. Right: the samples are placed offset in respect to the center of rotation and an aluminum plate 10×30 mm wide is inserted to provoke metal artifacts and photon starvation.

For each of the four materials in the samples, we have benchmarked the classification accuracy, as the ratio between successful predictions and total cases, of the three methods. The prediction models in the equations below have been used for the material classification to find the labels (i.e. the type of materials) from the ground truth library obtained using SRZE method listed in Table 3 in Appendix A. A similar library has been constructed for the other two methods.

- Integrated LAC discrimination:

$$label = \arg\min_{label} \sqrt{(\mu^{est} - \hat{\mu}^{label})^2}. \tag{8}$$

- Spectral LAC discrimination:

$$label = \arg\min_{label} \sqrt{\sum_{k=1}^{128} \left(\mu_{E_k}^{est} - \hat{\mu}_{E_k}^{label}\right)^2}. \tag{9}$$

- SRZE discrimination:

$$label = \arg\min_{label} \sqrt{w_{Z_e}\left(\frac{Z_e^{est} - \hat{Z}_e^{\,label}}{<\hat{Z}_e^{\,label}>}\right)^2 + w_{\rho_e}\left(\frac{\rho_e^{est} - \hat{\rho}_e^{\,label}}{<\hat{\rho}_e^{\,label}>}\right)^2}. \quad (10)$$

The hat sign refers to the values stored in the libraries whereas the <> operator corresponds to the mean, applied to all reference values of Z_e and ρ_e. That is done to have the physical parameters in the same scale and with same importance. The weights w_{ρ_e} and w_{Z_e} are assigned to the individual features to tune the significance given to each of them. In this work both have been set to $w = 0.5$.

4.2 Results

The results of the benchmarking are reported in Table 2 for the different prediction methods and sample groups. In the material classification, the prediction is successful when the individual material label is found correctly,

Table 2: The accuracy results (%) obtained for the different sample groups. In the exact material classification, the prediction is successful when the specific materials are classified correctly. In the binary classification, the discrimination is only performed between threats and innocuous materials.

Material classification

	Integrated LAC ($\tilde{\mu}$)	Spectral LAC ($\mu(E)$)	SRZE (ρ_e/Z_e)
Centered	24.0%	72.0%	72.0%
Offset	28.0%	68.0%	72.0%
Offset with Al plate	40.0%	38.3%	58.3%
Mean	30.7%	59.4%	67.4%

Binary classification (Threat/Innocuous)

	Integrated LAC ($\tilde{\mu}$)	Spectral LAC ($\mu(E)$)	SRZE (ρ_e/Z_e)
Centered	60%	100%	100%
Offset	64%	98%	100%
Offset with Al plate	75%	66.7%	78.3%
Mean	66.3%	88.2%	92.8%

whereas in the binary classification the discrimination is only done between innocuous and threat materials. Both the spectral characterization methods (LAC and SRZE) show an overall improved prediction accuracy when compared to integrated LAC method (which is corresponding to conventional integrating detectors). Samples with metal artifacts induced by the aluminum plate show a significant decrease in the accuracy of the direct LAC discrimination method, whereas the accuracy increases with the SRZE method. That is due to the energy thresholds selection step of the SRZE method, which allows data affected by photon starvation induced by the Aluminum plate to be disregarded. We remark that such a relatively low accuracy in the exact material classification was expected as most of the innocuous materials in the library are water-based compounds and some of them are varieties of the same specimens (e.g. 5 types of beer, 4 sun lotions etc.). On the other hand, the SRZE method shows perfect accuracy in the binary classification for samples without the aluminum plate. Nevertheless, the relatively low result obtained in the presence of metal artifacts suggests a demand for a further optimization of the data pre-processing step, possibly with the introduction of a metal artifact removal step.

5. CONCLUSIONS

We have demonstrated feasibility of material characterization into system-independent physical parameters (ρ_e, Z_e) using spectral X-ray CT. We have shown that the spectral methods have overall superior accuracy in the material classification, when compared to the conventional CT techniques. Spectral LAC method shows a 28.7% and 21.9% increase in material and binary overall mean classification, respectively. The SRZE method shows a

36.7% and 26.5% increase in material and binary overall mean classification, respectively. The SRZE method is free of calibration steps and system-independent, which makes it suitable for a standard method estimation of a material's physical properties ρ_e, Z_e. Moreover, the SRZE method presents higher robustness in the presence of high-Z materials due to the capability to omit photon starved data. Further developments in the metal artifact removal algorithms for SCT, and advances in the hardware technologies of the PCD, decreasing their spectral distortions, should increase the screening of threats even further, using this method.

APPENDIX A. MATERIALS ESTIMATED FEATURES LIBRARY

The library of materials, for which the physical parameters were estimated, includes innocuous materials, which are commonly found in checked-in luggage, and explosive or precursor materials, which are aimed to be screened by the SCT inspection. Note that it is composed of mostly organic and liquid materials without a k-edge discontinuity and with $6 \leq Z_e \leq 10$. Table 3 provides a summary of all the materials scanned by themselves, their type and their estimated physical parameters, using the SRZE method described in Section 2. This table was used as the ground truth for material classification when the materials are scanned in groups of 4.

Table 3: The list of all the 73 materials scanned and processed through the SRZE method, and their estimated physical parameters $\rho_e(\mathrm{e}^-\mathrm{mol/cm}^3)$ and Z_e.

Index	**Material label**	**Type**	Z_e	ρ_e
1	2-Butanone	Threat	6.64	0.440
2	2,4-Dinitrotoluene	Threat	8.16	0.316
3	Acetone	Threat	6.12	0.442
4	Ethylenediamine	Threat	6.31	0.506
5	H_2O_2 50%	Threat	7.24	0.661
6	Hexamethylenetetramine	Threat	5.59	0.461
7	Hydrazine solution	Threat	7.07	0.575
8	Methanol	Threat	7.17	0.439
9	N,N-Dimethylhydrazine	Threat	6.36	0.454
10	Nitric acid 65%	Threat	7.21	0.744
11	Nitrobenzene	Threat	6.70	0.621
12	Nitromethane	Threat	7.09	0.586
13	Wine	Innocuous	7.16	0.557
14	Cream Liquor	Innocuous	7.19	0.580
15	Balsamic Vinegar	Innocuous	6.98	0.640
16	Bromhexin DAK	Innocuous	7.24	0.608
17	Baby Shampoo	Innocuous	7.39	0.614
18	Aftersun Lotion 1	Innocuous	6.69	0.560
19	Brandy	Innocuous	7.51	0.537
20	Hand cream	Innocuous	7.01	0.545
21	Sun Lotion 1	Innocuous	6.74	0.579
22	Body Lotion 1	Innocuous	6.93	0.566
23	Beer 1 (Wheat)	Innocuous	7.14	0.566
24	Ethanol 40%	Innocuous	6.81	0.541
25	Ethanol 96%	Innocuous	6.08	0.463
26	Shampoo	Innocuous	7.36	0.589
27	Beer 2 (Brown Ale)	Innocuous	7.35	0.564
28	Porto Wine	Innocuous	7.26	0.568
29	Aftersun Lotion 2	Innocuous	6.95	0.567
30	Sun Lotion 2	Innocuous	6.61	0.572
31	Neutral Hand Soap	Innocuous	6.50	0.585
32	Sun Lotion 3	Innocuous	7.19	0.580
33	Sun Baby Lotion	Innocuous	8.73	0.606

Continued on next page

Table 3 – *Continued from previous page*

Index	Material label	Type	Z_e	ρ_e
34	Antiperspirant	Innocuous	6.05	0.340
35	Beer 3 (Pale Ale)	Innocuous	7.55	0.556
36	Olive Oil	Innocuous	5.41	0.510
37	Alcohol Drink	Innocuous	7.27	0.583
38	Rapeseed Oil	Innocuous	5.40	0.516
39	Simple Eye Makeup Remover	Innocuous	7.00	0.576
40	Body Lotion 2	Innocuous	6.92	0.563
41	Sugar	Innocuous	6.49	0.524
42	Sun lotion 4	Innocuous	8.57	0.595
43	Hairspray 1	Innocuous	7.11	0.568
44	Beer 4 (IPA Ale)	Innocuous	7.35	0.563
45	Beer 5 (Danish Christmas Beer)	Innocuous	7.42	0.560
46	Whiskey	Innocuous	7.27	0.524
47	Beautifying Anti-Blemish Care	Innocuous	7.15	0.582
48	Water	Innocuous	7.05	0.562
49	Energy Drink	Innocuous	7.10	0.586
50	Hairspray 2	Innocuous	8.10	0.391
51	Shaving Foam	Innocuous	8.12	0.542
52	Toothpaste 1	Innocuous	8.19	0.665
53	Ammonia Nitrate	Threat	6.73	0.490
54	Book	Innocuous	9.74	0.419
55	C4 Simulant	Threat	8.02	0.855
56	C4	Threat	6.44	0.497
57	Chocolate	Innocuous	6.68	0.700
58	Comp B	Threat	6.54	0.897
59	Crystal Sugar	Innocuous	6.63	0.531
60	DVD Bomb Simulant	Threat	7.49	0.878
61	Hard Cheese	Innocuous	7.41	0.619
62	Marzipan	Innocuous	6.47	0.648
63	Nitromethane	Threat	6.86	0.575
64	PETN Simulant	Threat	7.72	0.719
65	Peanut Butter	Innocuous	6.94	0.636
66	PETN	Threat	6.73	0.839
67	Shampoo	Innocuous	7.37	0.582
68	Soap Bar	Innocuous	6.13	0.595
69	Soft Cheese	Innocuous	7.35	0.604
70	Sun Cream	Innocuous	7.32	0.571
71	TNT (chunks)	Threat	6.63	0.434
72	Toothpaste 2	Innocuous	8.26	0.678
74	Vinegar	Innocuous	7.13	0.639

ACKNOWLEDGMENTS

The author would like to thank Innovation Fund Denmark for funding the project.

REFERENCES

[1] Wells, K. and Bradley, D., "A review of X-ray explosives detection techniques for checked baggage," *Applied Radiation and Isotopes* **70**(8), 1729–1746 (2012).

[2] Brooks, R. A. and Di Chiro, G., "Beam hardening in x-ray reconstructive tomography," *Physics in medicine & biology* **21**(3), 390 (1976).
[3] De Man, B., Nuyts, J., Dupont, P., Marchal, G., and Suetens, P., "Metal streak artifacts in x-ray computed tomography: a simulation study," *IEEE Transactions on Nuclear Science* **46**(3), 691–696 (1999).
[4] Alvarez, R. E. and Macovski, A., "Energy-selective reconstructions in x-ray computerised tomography," *Physics in Medicine & Biology* **21**(5), 733 (1976).
[5] Ying, Z., Naidu, R., and Crawford, C. R., "Dual energy computed tomography for explosive detection," *Journal of X-ray Science and Technology* **14**(4), 235–256 (2006).
[6] Azevedo, S. G., Martz, H. E., Aufderheide, M. B., Brown, W. D., Champley, K. M., Kallman, J. S., Roberson, G. P., Schneberk, D., Seetho, I. M., and Smith, J. A., "System-independent characterization of materials using dual-energy computed tomography," *IEEE Transactions on Nuclear Science* **63**(1), 341–350 (2016).
[7] Champley, K. M., Azevedo, S. G., Seetho, I. M., Glenn, S. M., McMichael, L. D., Smith, J. A., Kallman, J. S., Brown, W. D., and Martz, H. E., "Method to extract system-independent material properties from Dual-Energy X-ray CT," *Submitted to IEEE Transactions on Nuclear Science (2018)* (2018).
[8] Silva, A. C., Morse, B. G., Hara, A. K., Paden, R. G., Hongo, N., and Pavlicek, W., "Dual-energy (spectral) CT: applications in abdominal imaging," *Radiographics* **31**(4), 1031–1046 (2011).
[9] Shikhaliev, P. M., "Energy-resolved computed tomography: first experimental results," *Physics in Medicine & Biology* **53**(20), 5595 (2008).
[10] Rebuffel, V., Rinkel, J., Tabary, J., and Verger, L., "New perspectives of X-ray techniques for explosive detection based on CdTe/CdZnTe spectrometric detectors," *Proc. of the Int. Symp. on Digital Industrial Radiology and Computed Tomography* **2** (2011).
[11] McCollough, C. H., Leng, S., Yu, L., and Fletcher, J. G., "Dual-and multi-energy CT: principles, technical approaches, and clinical applications," *Radiology* **276**(3), 637–653 (2015).
[12] Anderson, N., Butler, A., Scott, N., Cook, N., Butzer, J., Schleich, N., Firsching, M., Grasset, R., De Ruiter, N., Campbell, M., et al., "Spectroscopic (multi-energy) CT distinguishes iodine and barium contrast material in mice," *European radiology* **20**(9), 2126–2134 (2010).
[13] Fornaro, J., Leschka, S., Hibbeln, D., Butler, A., Anderson, N., Pache, G., Scheffel, H., Wildermuth, S., Alkadhi, H., and Stolzmann, P., "Dual-and multi-energy CT: approach to functional imaging," *Insights into imaging* **2**(2), 149–159 (2011).
[14] Roessl, E. and Proksa, R., "K-edge imaging in x-ray computed tomography using multi-bin photon counting detectors," *Physics in Medicine & Biology* **52**(15), 4679 (2007).
[15] Schlomka, J., Roessl, E., Dorscheid, R., Dill, S., Martens, G., Istel, T., Bäumer, C., Herrmann, C., Steadman, R., Zeitler, G., et al., "Experimental feasibility of multi-energy photon-counting k-edge imaging in pre-clinical computed tomography," *Physics in Medicine & Biology* **53**(15), 4031 (2008).
[16] Busi, M., Mohan, K. A., Dooraghi, A. A., Champley, K. M., Olsen, U. L., and Martz, H. E., "Method for System-Independent Material Characterization from Spectral X-ray CT," *Accepted by NDT&E International* (2019).
[17] Swinehart, D., "The beer-lambert law," *Journal of chemical education* **39**(7), 333 (1962).
[18] Dreier, E. S., Kehres, J., Khalil, M., Busi, M., Gu, Y., Feidenhans, R., and Olsen, U. L., "Spectral correction algorithm for multispectral CdTe x-ray detectors," *Optical Engineering* **57**(5), 054117 (2018).
[19] Busi, M., Olsen, U. L., Knudsen, E. B., Frisvad, J. R., Kehres, J., Dreier, E. S., Khalil, M., and Haldrup, K., "Simulation tools for scattering corrections in spectrally resolved x-ray computed tomography using McXtrace," *Optical Engineering* **57**(3), 037105 (2018).
[20] Champley, K., "Livermore tomography tools (LTT) technical manual, LLNL-SM-687016, pages 1-165, 2016,"
[21] Gorecki, A., Brambilla, A., Moulin, V., Gaborieau, E., Radisson, P., and Verger, L., "Comparing performances of a CdTe X-ray spectroscopic detector and an X-ray dual-energy sandwich detector," *Journal of Instrumentation* **8**(11), P11011 (2013).
[22] Brambilla, A., Ouvrier-Buffet, P., Rinkel, J., Gonon, G., Boudou, C., and Verger, L., "CdTe linear pixel x-ray detector with enhanced spectrometric performance for high flux x-ray imaging," *IEEE Transactions on Nuclear Science* **59**(4), 1552–1558 (2012).

[23] Dooraghi, A. A., Fix, B. J., Smith, J. A., Brown, W. D., Azevedo, S. G., and Martz, H. E., "Characterization of a spectroscopic detector for application in x-ray computed tomography," in [*Developments in X-Ray Tomography XI*], **10391**, 103911G, International Society for Optics and Photonics (2017).

[24] Eger, L., Do, S., Ishwar, P., Karl, W. C., and Pien, H., "A learning-based approach to explosives detection using multi-energy x-ray computed tomography," in [*2011 IEEE International Conference on Acoustics, Speech and Signal Processing (ICASSP)*], 2004–2007, IEEE (2011).

[25] Chantler, C. T., "Theoretical form factor, attenuation, and scattering tabulation for Z= 1–92 from E= 1–10 eV to E= 0.4–1.0 MeV," *Journal of Physical and Chemical Reference Data* **24**(1), 71–643 (1995).

[26] Haldrup, K., "Singular value decomposition as a tool for background corrections in time-resolved xfel scattering data," *Philosophical Transactions of the Royal Society B: Biological Sciences* **369**(1647), 20130336 (2014).